Aix*Marseille université
Socialement engagée

NL/NNT

THÈSE DE DOCTORAT

Soutenue à Aix-Marseille Université

Le 10 Mars à Marseille par

Mostafa TAHA

Modelling fire-induced flows using Lattice Boltzmann methods

Discipline
Sciences pour l'Ingénieur

Spécialité
Mécanique et physique des fluides

École doctorale
ED 353 : Sciences pour l'Ingénieur : Mécanique, Physiques, Micro et Nanoélectronique.

M2P2 : Laboratoire de Mécanique, Modélisation et Procédés Propres

Composition du jury

Arnaud TROUVE Department of Fire protection Engineering, University of Maryland, USA.	Rapporteur
Bénédicte CUENOT Centre Européen de Recherche et de Formation Avancée en Calcul Scientifique (CERFACS), France.	Rapporteure
Bart MERCI Department of Flow, Heat and Combustion Mechanics, Ghent University, Belgium.	Examinateur
Lucie MERLIER Centre d'Energétique et de Thermique de Lyon (CETHIL), Claude Bernard Lyon 1 University, France.	Examinatrice
Olivier VAUQUELIN Institut Universitaire des Systems Thermiques Industriels (IUSTI), Aix Marseille University, France.	Président
Pierre BOIVIN Laboratoire de Mécanique, Modélisation et Procédés Propres (M2P2), Aix Marseille University, France.	Directeur de thèse
Aymeric LAMORLETTE Institut Universitaire des Systems Thermiques Industriels (IUSTI), Aix Marseille University, France.	Co-Directeur de thèse
Jean-Louis CONSALVI Institut Universitaire des Systems Thermiques Industriels (IUSTI), Aix Marseille University, France.	Co-Encadrant de thèse

M2P2 cnrs Ecole Doctorale ED 353 Sciences Pour l'Ingénieur Centrale Marseille

To my beloved family ...

«لا يَزَالُ المَرْءُ عَالِمَاً مَا طَلَبَ العِلْمَ ، فَإِذَا ظَنَّ أَنَّهُ قَدْ عَلِمَ فَقَدْ جَهِل»

One is a scholar as long as he keeps seeking knowledge, the moment he thinks that he has learned it all, he is ignorant

Je soussigné, Mostafa Taha, déclare par la présente que le travail présenté dans ce manuscrit est mon propre travail, réalisé sous la direction scientifique de Pierre Boivin, Aymeric Lamorlette et Jean-Louis Consalvi, dans le respect des principes d'honnêteté, d'intégrité et de responsabilité inhérents à la mission de recherche. Les travaux de recherche et la rédaction de ce manuscrit ont été réalisés dans le respect à la fois de la charte nationale de déontologie des métiers de la recherche et de la charte d'Aix-Marseille Université relative à la lutte contre le plagiat.

Ce travail n'a pas été précédemment soumis en France ou à l'étranger dans une version identique ou similaire à un organisme examinateur.

Fait à Marseille le 20 Janvier 2023

Mostafa Taha

I, undersigned, Mostafa Taha, hereby declare that the work presented in this manuscript is my own work, carried out under the scientific direction of Pierre Boivin, Aymeric Lamorlette, and Jean-Louis Consalvi, in accordance with the principles of honesty, integrity and responsibility inherent to the research mission. The research work and the writing of this manuscript have been carried out in compliance with both the french national charter for Research Integrity and the Aix-Marseille University charter on the fight against plagiarism.

This work has not been submitted previously either in this country or in another country in the same or in a similar version to any other examination body.

Marseille, 20 January 2023

Mostafa Taha

Acknowledgements

First of all, I would like to thank the members of the jury for their effort to assess and evaluate the present work. During the last three years I was hosted by the M2P2 lab as it was my second home. I would like to thank the administration of the lab and its secretary that sought always to provide for me and my colleagues the best environment for work and produce. It was not been feasible without you all, Michel, Sadia, Sophie, Marine and Elena.

Despite of the tough circumstances that the whole world suffered from, my supervisors kept supporting and pushing me forward. It was not an easy ride, but we were able to do our best to get the best possible outcome. So thank you Pierre, Aymeric and Jean-Louis for the support both at the scientific level alongside the personal level. I evolved a lot during these three years, the environment that you three provided enabled me to learn and sharpen my skills and knowledge.

To all my professors along my study years since I joined the engineering track, thanks you all for the effort that you do and keep doing. Your honesty to transfer knowledge for the next generations is priceless and I am indebted to all and each one of you.

I would like to thank the senior researchers in M2P2, Song, Jérome, Tayyab, Said, Alejandro and Gauthier. Thank you all for your non-reluctant continuous insights that were always brilliant and enlightening.

To my family, that without their support I would not be able to reach this stage in my life. Your unconditional love and support can not be paid back.

As they say, gems are precious but true friends are priceless. For my old loyal friends who were always there: Ahmed Yousef, Fayed, Amr Hossam, Mohamed Said, Bagoury, Ragab, Ahmed Salah, Samir, Hodaib, Mohamed Sayed and Haytham.

My five-year stay in France made me encounter friends that became a family: Anne-Charlotte, Noha, Taslim. From M2P2 also I can not miss Giacomo, Iko, Heesik, Xenia, Amir, Marchello, Karthik, Dhruba, Gabriel, Felix and the list goes on.

During my stay in Marseille I was volunteering regularly at the local Red-Cross. I am grateful to great people I met there: Angelo, Christine, Ingrid, Jean-Pascal, Nathalie, Philippe, Maylis, Florence, Ilhame and the others.

I am extremely grateful to the destiny that made me encounter those people and to have always their support. Thank you all for everything.

Liste de publications et participation aux conférences

Liste des publications réalisées dans le cadre du projet de thèse :

1. Mostafa Taha, Song Zhao, Aymeric Lamorlette, Jean-Louis Consalvi, and Pierre Boivin. Lattice boltzmann modeling of buoyancy-driven turbulent flows. Physics of Fluids, 34(5):055131, 2022.

2. Mostafa Taha, Song Zhao, Aymeric Lamorlette, Jean-Louis Consalvi, and Pierre Boivin. Turbulent fire modelling using lattice boltzmann method. (En preparation)

Participation aux conférences au cours de la période de thèse :

1. ECCOMAS CONGRESS (European Congress on Computational Methods in Applied Sciences and Engineering), 2021 Paris, France.

2. ECCOMAS CONGRESS (European Congress on Computational Methods in Applied Sciences and Engineering), 2022 Oslo, Norway.

3. IACM Computational Fluids Conference (CFC), 2023 Cannes, France.

Abstract

Due to their attractive computational cost, their capacities for massively parallel computing, and the ease to deal with complex geometries using multi-level Cartesian grids, Lattice Boltzmann methods (LBM) have attracted growing interest both in the academic and industrial spheres in the past decade. In this Phd work, and for the first time, a pressure-based hybrid LBM is developed to simulate with high fidelity buoyant flows characteristics of unwanted fires. Both compressible and low-mach formulations are considered and are coupled with state-of-the-art turbulence and combustion models in order to correctly predict the unsteady behaviour and characteristics of such flows. The consistency, the implementation and the robustness of the proposed LBM method are verified through 1-D and 2-D canonical test cases, involving the 1-D pressure column and the 2-D Rayleigh-Bénard and Rayleigh-Taylor instabilities. The LBM model is then applied to Large Eddy Simulation (LES) of the near and far fields of buoyant plumes, each region being characterised by its own dynamics. The LES of plume-like region (i.e. far-field) shows the capability of the model to reproduce the characteristic behaviour of the far-field region of a forced plume. Axial and radial profiles of velocity and temperature agreed well with experimental, theoretical and numerical data. The LES of large-helium plume is then performed to assess the capability of the model to reproduce the dynamics of the near-field region. Different subgrid-scale turbulence models were considered in these simulations and it was found, consistently with previous studies, that results are more sensitive to the grid resolution than to the turbulence model. Having a well resolved grid at the base of the plume is crucial to capture the formation of buoyancy driven instabilities that grow to generate the buoyancy-generated turbulence and govern the plume dynamics. The puffing mechanism was correctly predicted and the axial and radial profiles of velocity and helium mass fraction were consistent with the experimental data and previous numerical simulations based on classical solver of the Navier-Stokes equation. Finally, LES of a purely-buoyant large-scale methane fire was performed by using the Eddy dissipation concept (EDC) as combustion model and a simplified radiant fraction-based radiation model. The solver was able to correctly predict the fire dynamics. These test cases showed that the developed LBM model is fully capable of simulating with fidelity buoyant flows associated with fire applications at lower computational cost than classical solvers of Navier-Stokes equations.

Keywords: LBM, Buoyant Flows, Combustion, Fire, Turbulence, LES.

Resumé

En raison de leur coût de calcul attractif, leurs capacités pour le calcul massivement parallèle, et la facilité à traiter des géométries complexes en utilisant des maillages cartésiens à plusieurs niveaux, les méthodes de Boltzmann sur réseau (LBM) ont connu un intérêt accru dans les domaines universitaire et industriel lors de la dernière décennie. Dans ce travail de doctorat, et pour la première fois, une méthode de Boltzmann sur réseau hybride à base de pression est développée pour simuler des écoulements contrôlés par les forces de flottabilité caractéristiques des incendies avec haute fidélité. Les formulations compressibles et à faible nombre de Mach sont considérées et sont couplées avec des modèles de turbulence et de combustion à l'état de l'art afin de prédire correctement le comportement instationnaire et les caractéristiques de ces écoulements. La cohérence, la mise en œuvre et la robustesse de la LBM proposée sont vérifiées par des cas test canoniques 1-D et 2-D, impliquant la colonne de pression 1-D et les instabilités 2-D de Rayleigh-Bénard et Rayleigh-Taylor. Le modèle LBM est ensuite appliqué à la simulation aux grands échelles (LES) des champs proche et lointain de panaches contrôlés par les forces de flottabilité, chacune de ces régions étant caractérisée par sa propre dynamique. La LES de la région de type panache (c.-à-d. champ lointain) montre la capacité du modèle à reproduire le comportement caractéristique de la région de champ lointain d'un panache forcé. Les profils axiaux et radiaux de vitesse et de température concordent bien avec les données expérimentales, théoriques et numériques. La simulation d'un panache d'hélium de grande taille est ensuite effectuée pour évaluer la capacité du modèle à reproduire la dynamique de la région en champ proche. Différents modèles de turbulence de sous-maille sont comparés dans ces simulations et il a été constaté, comme dans les études précédentes, que les résultats sont plus sensibles à la résolution spatiale qu'au modèle de turbulence. Il est essentiel d'avoir un maillage bien résolu à la base du panache pour saisir la formation d'instabilités entraînées par la flottabilité qui se développent pour générer des structures turbulentes et régir la dynamique du panache. Le mécanisme de "puffing" a été correctement prédit et les profils axiaux et radiaux de la vitesse et de la fraction massique d'hélium correspondaient aux données expérimentales et aux simulations numériques antérieures fondées sur le solveur classique de l'équation de Navier-Stokes. Enfin, une simulation aux grandes échelles d'un feu de méthane à grande échelle purement contrôlé par les forces flottabilité a été réalisée en utilisant le modèle EDC comme modèle de combustion et un modèle simplifié de rayonnement utilisant la fraction rayonnée. Le solveur a pu prédire correctement la dynamique du feu. Ces cas de test ont montré que le modèle LBM développé est entièrement capable de simuler avec fidélité les écoulements associés à des applications incendie et ce à un coût de calcul inférieur aux solveurs classiques des équations de Navier-Stokes.

Mot-cles: LBM, Ecoulements Flottants, Combustion, Feu, Turbulence, LES.

Table of Contents

List of Figures

List of Tables

Nomenclature

Acronyms

BGK	Bhatnagar-Gross-Krook
CFD	Computational Fluid Dynamics
CFL	Courant-Friedrichs-Levy
CPU	Central Processing Unit
DDF	Double Distribution function
DES	Detached Eddy Simulation
DNS	Direct Numerical Simulation
EDC	Eddy Dissipation Concept
EOS	Equation Of State
FD	Finite Difference
FFT	Fast Fourier Transform
FV	Finite Volume
HPC	High Performance Computing
HRR-$\mathcal{P}$	Hybrid Regularized Recursive Pressure-based
LBE	Lattice Boltzmann Equation
LBM	Lattice Boltzmann Method
LES	Large Eddy Simulation
MRT	Multi-Relaxation Time
NS	Navier-Stokes
PDE	Partial Differential Equation

PIV	Particle Image Velocimetry
RANS	Reynolds Averaged Navier-Stokes
RMS	Root Mean Square
SGS	Subgrid Scale
SRT	Single Relaxation Time
TKE	Turbulent Kinetic Energy
TRT	Two Relaxation Time

Non-Dimensional Numbers

At	Atwood Number
Fr	Froude Number (flow inertia / external force)
Le	Lewis Number (thermal diffusion / mass diffusion)
Ma	Mach Number (velocity / speed of sound)
Pr	Prandtl Number (molecular viscosity / thermal diffusion)
Ra	Rayleigh Number (buoyancy force / viscosity force)
Re	Reynold Number (inertial force / viscosity force)
Ri	Richardson Number
Sc	Schmidt Number (molecular viscosity / mass diffusion)

Operators

$\overline{(.)}$	Reynolds averaged variable
$\widetilde{(.)}$	Favre averaged variable

Subscripts/Superscripts

0	reference value
∞	ambient condition
α	variable in direction α
η	quantity associated with Kolmogorov scale
c	centerline value of the variable
col	collision
eq	equilibrium
h	hydrodynamic quantity
i	variable in lattice direction i
k	variable associated with species k
neq	non-equilibrium
t	total quantity /quantity associated with turbulence
th	thermodynamic quantity
s	sensible thermodynamic quantity
sgs	subgrid scale quantity

Symbols Definition

Romanian Letters

A_i	NASA polynomial coefficient	
C_p	heat capacity at constant pressure	(J/kg/K)
C_v	heat capacity at constant volume	(J/kg/K)
C_s	Smagorinsky constant	(-)

c_i	discrete velocity in direction i	(m/s)
c_s	speed of sound	(m/s)
$\mathcal{D}_k$	diffusion coefficient of species k	(m^2/s)
e	internal energy	(J/kg)
e_s	sensible energy	(J/kg)
e_t	total energy	(J/kg)
F_α	external force	(N)
f	distribution function/ frequency	(-)/Hz
$\boldsymbol{g}$	gravitational acceleration vector	(m/s^2)
$\mathcal{H}$	hermite polynomials	(-)
h	absolute enthalpy	(J/kg)
h_t	total enthalpy	(J/kg)
h_s	sensible enthalpy	(J/kg)
k	wave number	(1/m)
N_{sp}	number of species	(-)
p	pressure	(pascal)
p^h	hydrodynamic pressure	(pascal)
p^{th}	thermodynamic pressure	(pascal)
q_α	heat flux in direction α	(watt/m^2)
$\mathcal{R}$	universal gas constant (=8.31451)	(J/mol/K)
$S_{\alpha\beta}$	Strain tensor	(1/s)
s	stoichiometric ratio	(-)
T	temperature	(K)

t	time	(s)
u_α	velocity at direction α	(m/s)
$V_{k,\alpha}$	species diffusion velocity for species k in direction α	(m/s)
$\mathcal{W}$	mixture molecular weight	(kg/mol)
X_k	molar fraction of species k	(-)
x_α	cartesian coordinate in direction α	(m)
Y_k	mass fraction of species k	(-)

Greek Letters

α	heat diffusion coefficient / entrainment coefficient	$(m^2/s)/(-)$
$\gamma = \frac{C_p}{C_v}$	specific heat ratio	(-)
$\Delta h^0_{f,k}$	enthalpy of formation of species k	(J/kg)
$\delta_{\alpha\beta}$	kronecker delta	(-)
δx	grid size	(m)
δt	time step	(s)
ϵ	dissipation rate of turbulent energy	(m^2/s^3)
θ	reduced temperature	(-)
λ	heat conductivity	(watt/m/K)
μ	dynamic viscosity	(kg/m/s)
ν	kinematic viscosity	(m^2/s)
$\boldsymbol{\xi}$	particle velocity vector	(m/s)
$\Pi_{\alpha\beta}$	viscous shear stress tensor	(pascal)
ρ	Density	(kg/m^3)

τ	relaxation time	(s)
Ω_i	collision operator	(-)
ω_i	weighting factor i	(-)
$\dot{\omega}_k$	reaction rate of species k	(1/s)

Chapter 1

Introduction

Contents

1.1 Study context

Throughout the history, man has been trying to control fire, as it provided warmth, lighting and protection from predators. Afterwards, it represented a critical technology enabling the evolution of humans throughout the history. Nowadays, fire moves nearly everything around us: factories, power plants, vehicles, heating systems, etc. Such a powerful source of energy has its risks and hazards as unwanted fires can rage naturally as in wild fires or accidentally as in industrial contexts. Those unwanted fires can be in some scenarios hard to control which may cause huge losses to human life and material properties. Moreover, those fires, in most cases, will emit harmful pollutants to the atmosphere of unburned hydrocarbons and soot.

Consequently, there is a great interest in profound understanding of fire behaviour and dynamics in order to assess and mitigate the potential risks. Such understanding has been widely used in engineering design of fire protection systems such as fire

detection, fire extinguishing and venting, smoke control systems, fire heating of structural elements of buildings or indoor/outdoor thermal radiation risks [56, 98, 161, 197]. The fire phenomenon includes numerous coupled complex physics as buoyancy-driven flows, buoyancy generated turbulence, turbulent combustion, radiation heat transfer, solid/liquid fuel evaporation, soot formation and interactions between structural materials and fire. Researchers were invested to explore experimentally fires and the associated physics long time ago, but because of the restrictions and difficulties related to experiments, specially for large-scale fires, as well as the exponential growth of the calculation resources, numerical CFD simulations became an essential research mean [1, 160]. Nonetheless, fire simulations using computational fluid dynamics is a daunting task as it requires resolving several length and time scales, from the small ones of combustion and turbulence to the large ones of global mass and energy transport. In addition, the modelling effort to be able to simulate such physics is significant. It is also important to ensure the consistency and the integrity of the CFD solver while adding the necessary models to capture the associated phenomena.

1.2 Fire related characteristics

Fire related flows are within the buoyancy-driven regime with the fuel injection velocity, u_{inj}, being significantly lower than that induced by the gravitational acceleration. This results in Froude number, $\mathrm{Fr} = u_{inj}/gL$ where L is a characteristic length scale of the problem, typically in the range $10^{-6} - 10^{-2}$ [56]. The purely buoyant fire plume generated by a pool fire represents a canonical scenario for fire applications and has been widely investigated experimentally [29, 44, 46, 100, 107, 159, 198, 229, 230]. The fire plume can be divided into two regions: the far-field region and the near-field one, each region being characterised by its specific properties and dynamics. The combustion process takes place in the near-field region of fire plumes. Nevertheless, the dynamics of both regions can be reproduced by considering simplified configurations without the complexities associated with combustion.

Far-field region

The far field of axisymmetric fire plume is non-reactive, turbulent and exhibits a self-similar behaviour characteristic of buoyancy-driven free plume in quiescent and unstratified atmosphere. This kind of flows is encountered in a wide range of industrial and environmental applications, including thermal plumes that arise due to the convective

heating on Earth's surface [169, 172, 258], dispersal of volcanic eruptions [26, 61, 193], sea ice plumes [210, 253], smoke stacks [23], and cooling tower plume dispersion [75], and, as such, has been widely investigated, in particular through forced plumes or buoyant jets that represent a canonical configuration to study these flows. They are generated by releasing the plumes from a source with an initial momentum. The flow can be then decomposed into three regions: (i) a region featuring a jet-like behaviour near the source, (ii) a transitional region and (iii) further downstream, the far-field fully-developed buoyancy-driven plume [32].

The first far-field plume theories [171, 201, 206] assumed a turbulent flow, a point source of buoyancy, the Boussinesq approximation and a dynamic similarity of the mean and turbulent motion at all elevations. Morton *et* al. [171] developed an integral formulation by assuming both "top-hat" radial profiles for both velocity and temperature/density and a point source, and by introducing an entrainment coefficient, α, defined as the ratio of radial velocity at the edge of the plume to the vertical velocity within the plume. Their model predicts correctly the scaling laws for the plume radius, that increases linearly with height, z, as well as for both velocity and temperature rise above the ambient that decay as $z^{-1/3}$ and $z^{-5/3}$, respectively. The weak plume formulation of Morton *et* al. [171] was extended to "strong plumes" by removing both the Boussinesq and the point source assumptions through the introduction of a virtual origin and, by considering more realistic Gaussian profiles for both velocity and temperature [97]. This was in conjunction with experiments on fire plumes above the flames [99] which provided expressions for plume radius and centerline velocity and temperature consistent with experimental data [81, 187, 207]. Another important feature of buoyant plumes is that the radial profiles of dimensionless velocity and temperature exhibit a self-similar behaviour with $\eta = r/z$ as a self-similar variable, where r is the radial coordinate [45, 81, 173, 187, 207]. Progress was also made in the understanding of the role of buoyancy on the entrainment process and the flow behaviour. In particular, Saeed *et* al. [203] found that buoyancy not only contributes to enhance the mean kinetic energy budget but also the momentum flux.

Near-field region

The near field flow in fire plumes is more complex than the far field. It exhibits a rapid transition from laminar to fully turbulent regime in the few first inlet diameters and a puffing motion characterised by a repetitive shedding of these coherent vortices [25, 29, 30, 270]. This periodic motion results from the formation and the growth of non-dissipative non-linear laminar instabilities near the edge of the pan that develops

to become energy containing turbulent structures [228]. The resulting turbulence is called "buoyancy-generated turbulence" [55] and results from a combination of vorticity generation and vorticity transport [228]. These structures develop periodically to form energy containing large-scale toroidal vortices that govern the flow pattern, the air entrainment as well as the mixing and combustion processes.

It was found experimentally [183, 227] that a large-scale lazy plume resulting from the release of helium in air mimics the same dynamics and structure that present in large-scale fires without the complexities associated with combustion and radiation. This makes this test case appealing for a numerical prospective as it allows to isolate a certain aspect from all the others for a profound understanding.

1.3 Fire related flow simulations

The numerical simulations of the flows described previously require an accurate modelling of buoyancy-induced turbulence. In the case of fire simulations, the underlying physics has also to be modelled. This includes turbulent combustion, heat transfer to the surroundings including the heat feedback to the condensed fuel surface, the formation of soot that drives the radiative heat transfer, and the condensed fuel decomposition. The proper modelling and description of those phenomena and coupling them together is a considerable challenge for CFD modelling. As a general rule, all numerical studies exist in the literature were based on the classical Navier-Stokes solvers and, to the authors' best knowledge, no attempt to consider LBM was reported.

Direct numerical simulation (DNS) is extremely costly in studying those categories of phenomena because of the wide range of time and length scales that need to be resolved. Other affordable techniques may be utilised such as Reynolds-Averaged Navier-Stokes (RANS) and Large-Eddy Simulation (LES). In RANS simulations, turbulence models have to be adapted to take into account the "buoyancy-generated turbulence" [22, 40, 55, 174, 237, 259]. On the other hand, LES became the standard simulation technique over the two last decades, in particular the development of two fire simulators, namely Fire Dynamics Simulator (FDS) [160] and FireFoam [1].

Numerous LES of far and near-field regions of fire plumes were reported in the literature. LES of the far-field of thermal plumes [11, 189, 265, 267] used different numerical modellings (i.e. mesh, numerical scheme, turbulence model, etc) to capture the dynamics of the far-field region, also called plume-like region, and to reproduce the reference experimental data of Shabbir and George [207] as well as the theoretical correlations of Morton *et* al. [171]. On the other side, LES was also used to inves-

tigate the instabilities generated in the near-field region [50, 145, 154, 255]. In these studies, the focus was mainly on studying the mechanism behind the puffing motion and its source. Furthermore, LES of medium and large-scale fire plumes were also performed [49, 104, 150, 261] with the objectives to provide insights on the modelling of the dynamics [4, 49, 104, 142, 143, 150–152, 261], of the the combustion in well and under-ventilated scenarios [135, 144, 239, 240, 252, 260, 266], of the soot production [178] and of the radiative heat transfer [179–181].

1.4 LBM as a CFD tool

Lattice Boltzmann Methods (LBM) are a powerful tool for the simulation of fluid dynamics [35]. Due to its attractive computational cost [20], its capacities for massively parallel computing and the ease to deal with complex geometries using multi-level Cartesian grids, these methods have attracted growing interest both in the academic and industrial spheres in the past decade [88, 126, 216].

LBM being initially designed to tackle isothermal flows, extension to thermal flows is today an active topic of investigation in the community. In achieving that goal, the numerical stability of the collision operator, at the heart of the method, used to be a major issue. The single relaxation time Bhatnagar-Gross-Krook model [13], probably the most popular model, lacks stability for shear flows, but more recent models such as multiple relaxation collision [106] or regularized kernels [108, 148] significantly improved stability. Another issue is the resolution of energy or temperature equation, which cannot be straightforwardly achieved on low-order lattices [126]. Two main options are available in the literature: the first is the double distribution function (DDF) where a second distribution function is added, whose main order corresponds to either temperature, energy, or enthalpy (see, e.g. [102, 202], for recent studies). A second option is to couple directly LBM with a scalar (temperature, energy, enthalpy) transport equation, solved in a coupled finite difference solver. This second option was found attractive as it allows, for a reasonable cost [20], to include an arbitrary number of additional scalar equations. Following recent successful applications to compressible [41, 64, 65, 70, 71, 87], atmospheric [37, 68, 109, 165, 166] or reactive flows [12, 221, 223–225], the second option, often referred to as hybrid LBM, is retained for this study.

1.5 Thesis objectives

This research work aims to develop a numerical model based on LBM to simulate fire-induced flows. The development will be based on the ProLB code [2], which is a parallel C++ CFD code based on LBM using a hybrid strategy where continuity and momentum are solved with the lattice Boltzmann equation coupled with the standard Navier-Stokes scalar equations (e.g. energy and species). The code has both compressible [64] and low-Mach approximation [242] formulations. The strategy is to consider scenarios of gradual incremental complexity:

- At first the gravity source term is added and then validated through canonical test cases, mainly, 1-D pressure column, 2-D Rayleigh Bénard and 2-D Rayleigh Taylor.
- Afterwards, the far-field characteristics will be investigated through LES. The forced plume studied experimentally by Shabbir and George [207] will be simulated and the results will be compared to the experimental data.
- Then, the near-field region of large-scale helium plume is studied. Different turbulence models and mesh resolutions are explored and the numerical results will be compared to the experimental data of O'Hern *et* al. [183, 227].
- Finally, the Eddy dissipation combustion model (EDC) and a simplified radiation model are added to be able to finally simulate fire. The 1-m diameter methane pool fire studied by Tieszen *et* al. [229, 230] will be investigated and compared to the experimental data.

The work will demonstrate the advantage of using LBM as high-fidelity simulation tool, yet, with lower computation cost.

1.6 Organization of the manuscript

Figure 1.1 depicts the global plan of the manuscript:

- Chapter 2 introduces the macroscopic Navier-Stokes equations and the transport and thermodynamics properties.
- Chapters 3-4 explains the Lattice Boltzmann theory and the physics behind, as well as the algorithm followed in the code.

- Chapter 5 validates the constructed numerical model through canonical test cases.
- Chapter 6 introduces the filtered equations of Navier-Stokes and the concept behind Large eddy simulation, moreover, different sub-grid models will be shown which will be used afterwards.
- Chapter 7 studies the far-field region of forced plume and the results will be compared to experimental data.
- Chapter 8 investigates the near-field region of large-scale helium plume and the results will be examined against experimental data.
- Chapter 9 introduces the EDC combustion model and then Sandia's 1-m diameter methane pool fire will be simulated. Qualitative and quantitative assessment of the results will be done in comparison to experimental data.
- Finally in Chapter 10 the conclusion about our study will be drawn and the perspectives for future work and improvements will be suggested.

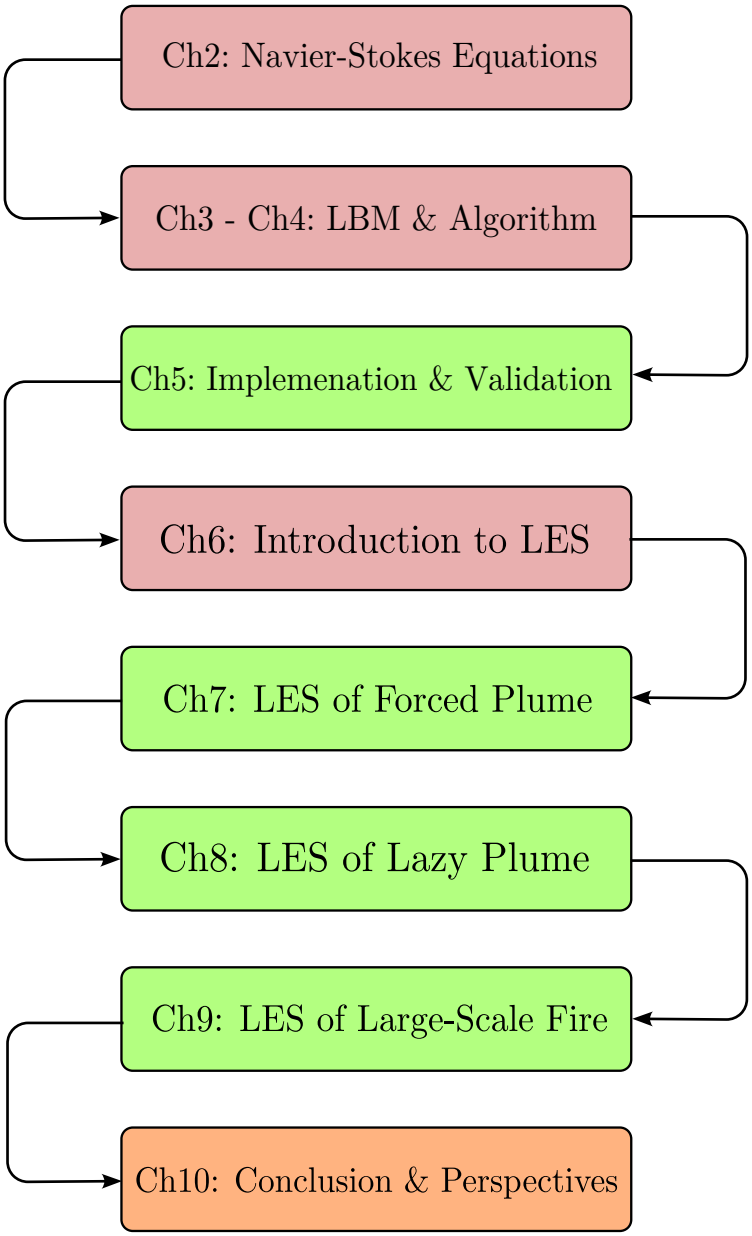

Figure 1.1: Planning of the dissertation

Chapter 2

Macroscopic equations for fire modelling

Contents

This chapter covers in details the governing equations of compressible multi-component reactive fluids, as well as the thermodynamics of gases, the transport properties, and the chemical kinetics for fire-induced flows.

2.1 Primitive variables

Combustion process involves multiple species interacting via multiple chemical reactions. Species are represented by mass fractions Y_k for $k = 1$ to N_{sp} where N_{sp} is the number of species in the gas mixture. The mass fraction Y_k is defined as:

$$Y_k = m_k/m, \tag{2.1}$$

where m_k is the mass of species k in a given volume V and m is the total mass of the

gas in that volume. Hence, the primitive variables for three-dimensional compressible multi-component reactive flows are:

- The density $\rho = m/V$,
- The three components of the velocity field u_α where $\alpha = 1, 2, 3$,
- One variable representing energy (or pressure/enthalpy/entropy/temperature),
- The mass fraction Y_k of all the species constituting the gas mixture.

In practice, only $5 + N_{sp} - 1$ variables are solved for, as the mass conservation imposes that the sum of all mass fractions must equal unity:

$$\sum_{k=1}^{N_{sp}} Y_k = 1. \tag{2.2}$$

The previous identity enables us to calculate the mass fractions of one species by knowing the others which in other words decreases the number of unknowns to $5 + N_{sp} - 1$. Those unknowns need now to be solved simultaneously through the system of coupled partial differential equations of Navier-Stokes introduced in the next section.

2.2 Navier-Stokes macroscopic equations

The equations that governs the dynamics of multi-component fluids in nature are called Navier-Stokes (NS) equations. They describe the conservation laws: mass conservation, Newton's second law of motion, first principle of thermodynamics and balance of species mass fraction. The flow mass, momentum, total energy and species conservation equations in the conservative form using *Einstein notation* are introduced as [191]:

$$\textbf{Mass:} \quad \frac{\partial \rho}{\partial t} + \frac{\partial \rho u_\alpha}{\partial x_\alpha} = 0 \tag{2.3}$$

$$\textbf{Momentum:} \quad \frac{\partial \rho u_\alpha}{\partial t} + \frac{\partial (\rho u_\alpha u_\beta + \delta_{\alpha\beta} p)}{\partial x_\beta} = \frac{\partial \Pi_{\alpha\beta}}{\partial x_\beta} + \rho F_\alpha, \tag{2.4}$$

$$\textbf{Energy:} \quad \frac{\partial \rho e_t}{\partial t} + \frac{\partial u_\alpha (\rho e_t + p)}{\partial x_\alpha} = -\frac{\partial q_\alpha}{\partial x_\alpha} + \frac{\partial \Pi_{\alpha\beta} u_\alpha}{\partial x_\beta} + \rho u_\alpha F_\alpha, \tag{2.5}$$

$$\textbf{Species:} \quad \frac{\partial \rho Y_k}{\partial t} + \frac{\partial \rho u_\alpha Y_k}{\partial x_\alpha} = -\frac{\partial}{\partial x_\alpha}(\rho Y_k V_{k,\alpha}) + \dot{\omega}_k, \tag{2.6}$$

where ρ is the mass volume (i.e. density), t denotes the time, u_α is the velocity vector with the subscript α denoting the direction also it is the dummy index for *Einstein notation*, x_α is the position vector and $\delta_{\alpha\beta}$ is the Kronecker delta symbol: $\delta_{\alpha\beta} = 1$ if $\alpha = \beta$, 0 otherwise. p is the static pressure and $\Pi_{\alpha\beta}$ represents the viscous stress tensor described as [127] based on the Newtonian approximation[1]:

$$\Pi_{\alpha\beta} = \mu \left(\frac{\partial u_\alpha}{\partial x_\beta} + \frac{\partial u_\beta}{\partial x_\alpha} - \delta_{\alpha\beta} \frac{2}{3} \frac{\partial u_\gamma}{\partial x_\gamma} \right). \tag{2.7}$$

It is worth mentioning that the contribution of the so called *bulk viscosity*[2] in the viscous stress tensor was neglected and that the above tensor is traceless, more details about the origin of this viscous stress tensor may be found in Ref. [18, 205, 233]. The scalar μ is the molecular dynamic viscosity which, following the Newtonian assumption, is independent from the strain rate. Non-Newtonian fluids is another complexity which is out of our scope. Finally in the momentum equation, we have the source term at the right hand side F_α which represents the body force on the fluid.

As for the energy equation, e_t is the total energy defined as:

$$e_t = e + \frac{1}{2} u_\alpha u_\alpha, \tag{2.8}$$

where e is the internal energy described as:

$$e = h - \frac{p}{\rho}, \tag{2.9}$$

where h is the enthalpy. The term q_α signifies the heat flux and can be divided into two parts:

$$q_\alpha = -\lambda \frac{\partial T}{\partial x_\alpha} + \sum_{k=1}^{N_{sp}} \rho h_k Y_k V_{k,\alpha}, \tag{2.10}$$

where the first part is a heat diffusion term (i.e. heat transfer by conduction) expressed by *Fourier's law* ($\lambda \partial T / \partial x_\alpha$), λ represents the molecular heat conductivity. The second term ($\rho \sum_{k=1}^{N_{sp}} h_k Y_k V_{k,\alpha}$) represents the heat flux associated with the species diffusion with different enthalpies which is specific to multi-component fluids. This term vanishes if all the species of the mixture have the same partial sensible enthalpy or that

[1] Isaac Newton stated that shear stress is proportional to the strain rate, i.e. velocity gradients.

[2] Bulk viscosity: represents the property which is responsible for energy dissipation in a fluid of uniform temperature during a change of volume at a finite rate. This viscosity becomes significant in compressible flows which is not the case in our study.

the mixture is composed of only one species. There is another contribution that could be considered called *Dufour effect* [59, 60][3]. However, This effect will be neglected all around our work. The term $(\partial \tau_{\alpha\beta} u_\alpha / \partial x_\beta)$ represents the viscous heating source term. At last, $(\rho u_\alpha F_\alpha)$ is the power induced by the external force F_α.

Finally regarding the species equation, Y_k represents the mass fraction of species k. The term $\rho Y_k V_{k,\alpha}$ constitutes the species mass flux, with $V_{k,\alpha}$ being the species diffusion velocity for species k in the direction α such that $\sum_{k=1}^{N_{sp}} Y_k V_{k,\alpha} = 0$ ensuring global mass conservation. The species mass flux is modelled by *Hirschfelder and Curtiss approximation* equipped with a correction term ensuring global mass conservation:

$$\rho Y_k V_{k,\alpha} = -\rho \mathcal{D}_k \frac{\mathcal{W}_k}{\mathcal{W}} \frac{\partial X_k}{\partial x_\alpha} + \underbrace{\rho V_\alpha^c Y_k}_{\text{correction term}}, \tag{2.11}$$

where for each species k: $\mathcal{D}_k$ is the molecular diffusion coefficient, $\mathcal{W}_k$ is the molecular weight of species and X_k is the molar fraction. $\mathcal{W}$ is the average molecular weight and V_α^c the correction velocity introduced in order to ensure the conservation of total mass (i.e. ensuring $\sum_{k=1}^{N_{sp}} Y_k V_{k,\alpha} = 0$) which can be evaluated by:

$$V_\alpha^c = \sum_{k=1}^{N_{sp}} \mathcal{D}_k \frac{\mathcal{W}_k}{\mathcal{W}} \frac{\partial X_k}{\partial x_\alpha}. \tag{2.12}$$

Note that *Soret effect* [84][4] will be neglected in our work. The source term in the species conservation equation $\dot{\omega}_k$ is called the reaction rate, to be detailed later in Sec. 2.3. The Navier-Stokes system of equations is *under-determined* and needs a closure. In our work we consider only perfect gases, thus, the equation of state of ideal gases will be used as a thermodynamic closure that links between pressure, density and temperature:

$$p = \rho \frac{\mathcal{R}}{\mathcal{W}} T, \tag{2.13}$$

where $\mathcal{R} = 8.314\,\mathrm{J/mol/K}$ is the universal perfect gas constant. Refer to Sec. 2.4.1 for more details about the equation of state.

A small note regarding the energy equation, the choice of the variable for which we solve the energy equation is crucial and it depends mainly on the application in hand. The transition between energy forms is straight forward and they can all be found with thorough explanation in Ref. [191]. For reactive flows in open configurations, the

[3] *Dufour effect* is heat transfer caused by concentration gradients.
[4] *Soret effect* is molecular species diffusion due to temperature gradients.

natural variable to handle combustion is the enthalpy h. The transformation from total Energy to enthalpy conservation equation is detailed in Appendix A.1, and it results in the conservation equation of enthalpy:

$$\frac{\partial \rho h}{\partial t} + \frac{\partial \rho u_\alpha h}{\partial x_\alpha} = \frac{Dp}{Dt} - \frac{\partial q_\alpha}{\partial x_\alpha} + \Pi_{\alpha\beta}\frac{\partial u_\alpha}{\partial x_\beta}, \tag{2.14}$$

Throughout this manuscript, we neglect the pressure work in the energy equation $\frac{Dp}{Dt} = \frac{\partial p}{\partial t} + u_\alpha \frac{\partial p}{\partial x_\alpha} \approx 0$, which is a reasonable approximation for low-Mach number flows which is the case in our application for buoyancy-driven flows and fire simulations [191]. Furthermore, the primitive form (i.e. non-conservative form) was used throughout our work for both enthalpy and species conservation equations so that we end up with the following form for enthalpy:

$$\rho\frac{\partial h}{\partial t} + \rho u_\alpha \frac{\partial h}{\partial x_\alpha} = -\frac{\partial q_\alpha}{\partial x_\alpha} + \Pi_{\alpha\beta}\frac{\partial u_\alpha}{\partial x_\beta}, \tag{2.15}$$

and with the following form for species:

$$\rho\frac{\partial Y_k}{\partial t} + \rho u_\alpha \frac{\partial Y_k}{\partial x_\alpha} = -\frac{\partial}{\partial x_\alpha}(\rho Y_k V_{k,\alpha}) + \dot{\omega}_k. \tag{2.16}$$

In the next section, the chemical kinetics of reactive flows will be introduced and the species reaction rate source term $\dot{\omega}_k$ will be elaborated.

2.3 Reactive Flows

Combustion is simply the exothermic chemical process that includes fuel and oxidizer, under specific conditions, to produce heat and products. If $\mathcal{M}_k$ denotes any given chemical species k. For N number of species reacting through M number of chemical reversible reaction, the overall equation that describes the change from reactants to products can be written in the general form:

$$\sum_{k=1}^{N} \nu'_{kj}\mathcal{M}_k \rightleftharpoons \sum_{k=1}^{N} \nu''_{kj}\mathcal{M}_k \qquad \text{for} \quad j = 1, M \tag{2.17}$$

where ν'_{kj} and ν''_{kj} are the molar stoichiometric coefficient of species k in reaction j.

Recalling mass conservation:

$$\sum_{k=1}^{N} \nu'_{kj} \mathcal{W}_k \rightleftharpoons \sum_{k=1}^{N} \nu''_{kj} \mathcal{W}_k \quad \text{or} \quad \sum_{k=1}^{N} \nu_{kj} \mathcal{W}_k = 0 \qquad \text{for} \quad j = 1, M \tag{2.18}$$

where $\nu_{kj} = \nu''_{kj} - \nu'_{kj}$. To keep it simple, mass reaction rate will be only used. For species k, the total reaction rate $\dot{\omega}_k$ is the sum of rates $\dot{\omega}_{kj}$ produced by M reactions:

$$\dot{\omega}_k = \sum_{j=1}^{M} \dot{\omega}_{kj} = \mathcal{W}_k \sum_{j=1}^{M} \nu_{kj} \mathcal{Q}_j, \tag{2.19}$$

where $\mathcal{Q}_k$ is the progress rate of reaction j given as:

$$\mathcal{Q}_j = \frac{\dot{\omega}_{kj}}{\mathcal{W}_k \nu_{kj}}, \tag{2.20}$$

The description of the species reaction rate $\dot{\omega}_k$ is the main target of combustion modelling, more details will be given in Chapter 9. Adding all reaction rates $\dot{\omega}_{kj}$ of all species:

$$\sum_{k=1}^{N} \dot{\omega}_{kj} = \sum_{j=1}^{M} \left(\mathcal{Q}_j \underbrace{\sum_{k=1}^{N} \mathcal{W}_k \nu_{kj}}_{=0 \text{ (mass cons.)}} \right) = 0 \tag{2.21}$$

which shows that total mass is conserved. The progress rate $\mathcal{Q}_j$ of reaction j is defined as:

$$\mathcal{Q}_j = K_{fj} \prod_{k=1}^{N} [X_k]^{\nu'_{kj}} - K_{rj} \prod_{k=1}^{N} [X_k]^{\nu''_{kj}} \tag{2.22}$$

where K_{fj} and K_{rj} are , respectively, the forward and the reverse rates of reaction j. Here, the kinetic rates of reaction are expressed in terms of molar concentrations $[X_k] = \rho Y_k / \mathcal{W}_k$. The rates of reaction K_{fj} and K_{rj} are not strait forward to obtain and constitute a fundamental problem of combustion modelling. Those constants are usually

modelled using the empirical *Arrhenius law* describing the forward rate of reaction:

$$K_{fj} = A_{fj} T^{\beta_j} \exp\left(-\frac{E_j}{\mathcal{R}T}\right) = A_{fj} T^{\beta_j} \exp\left(-\frac{T_{aj}}{T}\right) \tag{2.23}$$

A_{fj} is the pre-exponential constant, β_j is the temperature exponent and E_j is the activation energy (or equivalently can be expressed via the activation temperature $T_{aj} = E_j/\mathcal{R}$). Those constants must be defined in order to express the progress rate $\mathcal{Q}_j$ of each reaction, and this is a difficult task because it necessitates performing experiments.

In the next section, we give more details about the thermodynamics and transport properties of a gas mixture.

2.4 Multi-component gas properties

2.4.1 Thermodynamic properties

Dalton's law describes the relation between total pressure p and the partial pressures p_k in a multi-component gas as follows:

$$p = \sum_{k=1}^{N_{sp}} p_k \qquad where \qquad p_k = \rho \frac{\mathcal{R}}{\mathcal{W}_k} T, \tag{2.24}$$

where $\rho_k = \rho Y_k$ and $\mathcal{W}_k$ are the density and the molecular weight of species k, respectively. Since the density ρ of the multi-species gas is:

$$\rho = \sum_{k=1}^{N_{sp}} \rho_k, \tag{2.25}$$

the equation of state will read:

$$p = \rho \frac{\mathcal{R}}{\mathcal{W}} T, \tag{2.26}$$

where $\mathcal{W}$ is the average molecular weight of the gas mixture given by:

$$\frac{1}{\mathcal{W}} = \sum_{k=1}^{N_{sp}} \frac{Y_k}{\mathcal{W}_k} = \sum_{k=1}^{N_{sp}} X_k \mathcal{W}_k, \tag{2.27}$$

There are other quantities introduced as alternatives to the mass fraction Y_k to describe the composition of a multi-component gas and also to measure their concen-

trations:

- The mole fraction X_k which is the ratio of the number of moles of species k in a volume V to the total number of the mole in the same volume, $X_k = \frac{\mathcal{W}}{\mathcal{W}_k} Y_k$.
- the molar concentration $[X_k]$ is the number of moles of species k per unit volume, $[X_k] = \rho \frac{Y_k}{\mathcal{W}_k} = \rho \frac{X_k}{\mathcal{W}}$.

Thermodynamic properties of a multi-component system are linked to the internal energy e_k or enthalpy h_k of each species. In the context of our study and as a common practice in combustion codes, enthalpy is the natural variable for combustion, hence, the enthalpy h will be used throughout our work. The enthalpy h_k for each species k in a multi-component gas is described as:

$$h_k = \underbrace{\int_{T_0}^{T} C_{p,k}(T) \cdot dT}_{\text{Sensible}} + \underbrace{\Delta h^{\circ}_{f,k}}_{\text{Chemical}}, \tag{2.28}$$

where $C_{p,k}$ is the heat capacity at constant pressure for species k, and $\Delta h^{\circ}_{f,k}$ is the mass enthalpy of formation of species k at a reference temperature T_0. In theory, the T_0 can take any value, and a value $T_0 = 0$ seems a logical choice, but collecting experimental data on formation enthalpies at 0 K is cumbersome. Hence, the standard reference state used to gather the formation enthalpies is usually $T_0 = 298.15$ K, those values are well documented and tabulated in the text books [191]. So the enthalpy h can be written as:

$$h = \sum_{k=1}^{N_{sp}} h_k Y_k = \sum_{k=1}^{N_{sp}} (\int_{T_0}^{T} C_{p,k} \cdot dT + \Delta h^{\circ}_{f,k}) Y_k = \int_{T_0}^{T} C_p \cdot dT + \sum_{k=1}^{N_{sp}} \Delta h^{\circ}_{f,k} Y_k \tag{2.29}$$

where C_p is the heat capacity at constant pressure of the gas mixture. Internal energy by definition is:

$$\begin{aligned} e = h - \frac{p}{\rho} &= \int_{T_0}^{T} C_p(T) \cdot dT - \frac{\mathcal{R}T}{\mathcal{W}} + \sum_{k=1}^{N_{sp}} \Delta h^{\circ}_{f,k} Y_k \\ &= \underbrace{\int_{T_0}^{T} C_v(T) \cdot dT - \frac{\mathcal{R}T_0}{\mathcal{W}}}_{\text{Sensible}} + \sum_{k=1}^{N_{sp}} \underbrace{\Delta h^{\circ}_{f,k} Y_k}_{\text{Chemical}} = \sum_{k=1}^{N_{sp}} e_k Y_k, \end{aligned} \tag{2.30}$$

where C_v is the heat capacity at constant volume of the gas mixture. C_p and C_v can be written in terms of the component of the gas as:

$$C_p = \sum_{k=1}^{N_{sp}} C_{p,k} Y_k, \tag{2.31}$$

$$C_v = \sum_{k=1}^{N_{sp}} C_{v,k} Y_k. \tag{2.32}$$

The relation between C_p and C_v is given by the relation:

$$C_p - C_v = \frac{\mathcal{R}}{\mathcal{W}}. \tag{2.33}$$

The thermodynamic properties of a gas are function in temperature, and in practice (i.e. in CFD codes) they are usually tabulated as temperature functions in the form of polynomials for each species, NASA polynomials [63, 101, 215]. The heat capacities $C_{p,k}$ and the enthalpy h_k are written as function of temperature as:

$$\frac{C_{p,k}(T)}{\mathcal{R}} = A_1 + A_2 T + A_3 T^2 + A_4 T^3 + A_5 T^4, \tag{2.34}$$

$$\frac{h_k(T)}{\mathcal{R}} = A_1 + A_2 \frac{T}{2} + A_3 \frac{T^2}{3} + A_4 \frac{T^3}{4} + A_5 \frac{T^4}{5} + \frac{A_6}{T}, \tag{2.35}$$

where A_i are the polynomial coefficients can be found in [63, 158]. It is worth mentioning that there are two sets of coefficients depending on the local temperature of the fluid. In the situations where temperature is required, a newton iterative procedure is needed [77] due to the non-explicit nature of the polynomials.

Throughout our work, the non-reactive test cases have temperature levels that do not exceed 600 K, which allows us to assume a constant C_p. On the other hand for reactive cases, this assumption is no longer valid and C_p must be temperature dependant.

2.4.2 Transport properties

The diffusion terms in Navier-Stokes equations are associated with some properties of the fluid: The viscosity μ for the momentum equation in the stress tensor via *Newton's law*, the thermal conductivity λ for the heat equation following *Fourier's law*, and the

diffusion coefficient of species k in the rest of the mixture $\mathcal{D}_k$ which is used in *Fick's law*.

Diffusion process includes binary diffusion coefficient $\mathcal{D}_{kj}$ which requires the resolution of a system giving diffusion velocities. This is not practical, as solving the diffusion problem in a multi-species gas is a considerable problem in itself. Hence, simplified laws like *Fick's law* are used in practice and this is the approach we used in our work.

Those properties can be obtained using different methods for multi-component fluids. Mixture average properties can be found in many commercial software [121], but this will result in an additional cost to solve for the detailed transport properties. A simplified approach is to define some non-dimensional numbers that link those properties together. The Prandtl number, Pr, compares momentum and heat diffusion:

$$\mathrm{Pr} = \frac{\nu}{\alpha} = \frac{\nu}{\lambda/(\rho C_p)} = \frac{\mu C_p}{\lambda} = \frac{\text{Viscous effect}}{\text{Thermal diffusion effect}}, \tag{2.36}$$

where $\nu = \mu/\rho$ is the kinematic viscosity and $\alpha = \lambda/(\rho C_p)$ is the thermal diffusivity coefficient. The Schmidt number, Sc_k, compares the momentum and species k molecular diffusion:

$$\mathrm{Sc}_k = \frac{\nu}{\mathcal{D}_k} = \mathrm{PrLe}_k = \frac{\text{Viscous effect}}{\text{Molecular diffusion effect}} \tag{2.37}$$

where Le_k is the Lewis number which compares the the diffusion speed of heat and species k. Although the Lewis number Le_k is a local quantity, in most cases it changes insignificantly from one point to another, hence, it can be considered constant. Lewis number reads:

$$\mathrm{Le}_k = \frac{\mathrm{Sc}_k}{\mathrm{Pr}} = \frac{\lambda}{\rho C_p \mathcal{D}_k} = \frac{\alpha}{\mathcal{D}_k} = \frac{\text{Thermal diffusion effect}}{\text{Molecular diffusion effect}}, \tag{2.38}$$

Having defined the non-dimensional numbers that link all the transport properties, one property needs to be determined in order to deduce the others. The molecular viscosity μ can be described using the well-known power law which links the molecular viscosity to temperature for gases:

$$\mu = \mu_0 (\frac{T}{T_0})^{\beta}, \tag{2.39}$$

where μ_0 and T_0 is the reference molecular viscosity and temperature, respectively, based on the mixture of the gas, β is constant and equals to 3/2. After determining the molecular viscosity μ, the thermal conductivity λ can be found through Prandtl number Pr while the diffusion coefficient $\mathcal{D}_k$ of species k is calculated via Sc_k.

2.5 Buoyancy forcing term

The forcing term ρF_α in the momentum equation (Eqn. 2.4) would represent gravity if $F_\alpha = \boldsymbol{g}$ with $\boldsymbol{g}$ being the gravitational acceleration. Hence, the gravity forcing term can be written in this following form:

$$\rho F_\alpha = \rho \boldsymbol{g} = (\rho_0 + \Delta\rho)\boldsymbol{g}, \tag{2.40}$$

where $\Delta\rho$ is the difference between the local density ρ and the ambient one denoted by ρ_0, such that $\Delta\rho = \rho - \rho_0$. The pressure gradient and the buoyancy terms $-\nabla p + (\rho_0 + \Delta\rho)\boldsymbol{g}$ are usually written as $-\nabla p^* + \Delta\rho\boldsymbol{g}$ where $p^* = p + \rho_0 \boldsymbol{g} z$ where z is the elevation. If not mentioned otherwise, the z-direction will be always the vertical direction representing elevation. The change from p to p^* is called pressure shift. Finally, the star superscript can be dropped and the source term in the momentum equation can be written as a buoyancy term:

$$\rho F_\alpha = (\rho - \rho_0)\boldsymbol{g}. \tag{2.41}$$

2.6 Low-Mach number approximation

Equations 2.3-2.4 represented the fully compressible Navier-Stokes equations which will be used in a part of our work. However, this set of equations is over powerful for our study cases where the Mach number is much lower the compressibility limit of 0.3 [6]. Hence, a small modification can be done to benefit from the absence of compressibility effects which start to be significant beyond Mach number of 0.3. The low-Mach number approximation (derivation can be found in the literature [147, 186, 199]) describes large variations in temperature and density, due to volumetric heat addition or having different species, without requiring a simultaneous description of acoustics oscillations appearing because of the elastic properties of the fluid.

In the context of large-scale fires/plumes, the time scale associated with this type of flows is gigantic compared to the acoustic time scale, in other words, the time step

required to capture sound waves is much smaller than the one necessary to predict the relatively slow dynamics of fires/plumes. The low-Mach number approximation allows for larger time steps suitable for fire applications while filtering out the insignificant sound waves. In fact, the use of fully compressible equations here is not necessary as acoustics do not play any important role in our application and a low-Mach formulation would be sufficient, allowing for lower computation cost.

The essence of the low-Mach number approximation is rather simple, the pressure p will be divided into two parts, a thermodynamic pressure p^{th} and a hydrodynamic pressure p^h as:

$$p = p^{th} + \kappa p^h, \tag{2.42}$$

where κ is the expansion parameter for p chosen as $\kappa = \gamma \mathrm{Ma}^2$. Only two equations will be impacted by this pressure splitting, the first equation is the momentum equation where the pressure gradient term will only contain the hydrodynamic part p^h of the pressure leading to:

$$\frac{\partial \rho u_\alpha}{\partial t} + \frac{\partial (\rho u_\alpha u_\beta + \delta_{\alpha\beta} p^h)}{\partial x_\beta} = \frac{\partial \Pi_{\alpha\beta}}{\partial x_\beta} + \rho F_\alpha, \tag{2.43}$$

the second equation to be impacted is the thermodynamic closure (i.e. equation of state) where the pressure will be constant and equals the thermodynamics part p^{th} leading to:

$$p^{th} = \rho \frac{\mathcal{R}}{\mathcal{W}} T, \tag{2.44}$$

those two modified equations alongside the other unchanged conservation equations constitute the low-Mach Navier-Stokes equations.

Summary In this chapter, we introduced the governing equations of Navier-Stokes that describe the behaviour of any three-dimensional compressible multi-component reactive flow. Also, the thermodynamic and transport properties of gases were briefly explained. Moreover, we introduced the low-Mach number approximation which can help reduce the overall computational cost. In the next two chapters we will introduce the Lattice-Boltzmann method and the algorithm used in our solver to simulate Navier-Stokes equations.

Chapter 3

LBM for isothermal flows

"The quantum behaviour of a system reduces to classical behaviour when the system becomes large enough." ***Niels Bohr***

Contents

3.1 Introduction

Lattice Boltzmann method (LBM) is based on the kinetic theory of gases on the molecular level which is a statistical description of the particles. The method is directly linked to the lattice gas automaton (LGA) rose in the late 80's by Frisch *et* al. [76]. The LBM works from the particles point of view but is capable of recovering the macroscopic description of fluid mechanics (i.e. Navier-Stokes equations). The advantage of LBM is its efficiency with lower computational cost compared to the standard Navier-Stokes solvers. Moreover, it is easy to implement and is highly parallelized, as it operates locally. For those reasons, LBM became popular in the last decade, and more fields of application are being invaded by this method such as: reactive flows, compressible flows, multi-phase flows, turbo-machinery, etc. In this chapter we introduce the basics of athermal LBM and we prove the link to the macroscopic Navier-Stokes equations. Moreover, discretized LBM will be given as well as the source term to account for gravity.

3.2 Statistical mechanics & kinetic theory of gases

The kinetic theory of particles stands in the heart of the LBM method, thus, it is indispensable to have a solid background on this field, knowing the concepts and terminology related to this topic. Note that, the terms molecule and particle signify the same thing.

Boltzmann Distribution

In 1859, Maxwell recognized that dealing with large number of molecules is extremely complex and that the use of Newton's second law for huge number of molecules is out of realization, as tracing the trajectory of each molecule is out of hand for a macroscopic system. The idea of averaging seemed encouraging at that time, as Maxwell argued that the knowledge of the instantaneous position and velocity is not important. Instead, the so-called *distribution function* is the cardinal parameter that represents the impact of the molecules. In other words, what percentage of molecules in a certain location of a container has a specific range of velocities, at a given instance in time. Molecules of a gas have a wide range of velocities and they collide with each other continuously, the fast molecules transfer momentum to the slower ones, resulting in a conservation of momentum. For a gas in thermal equilibrium, the distribution function is not a function in time, as the gas is distributed uniformly in its container. Appendix B.1

shows the detailed derivation of *Maxwell* distribution function:

$$f(c) = 4\pi(\frac{m}{2\pi kT})^{\frac{3}{2}} c^2 e^{-\frac{mc^2}{2kT}}, \tag{3.1}$$

The extension of *Maxwell* distribution function was done by Ludwig Eduard Boltzmann (1844 - 1906) for arbitrary large systems. He is the first one to realize the deep connection between the thermodynamics concept of entropy and the statistical analysis of possible states of large system, which states that the increase of entropy of a system with time is a change in macroscopic variables to those values corresponding to the largest possible number of the microscopic arrangements. Boltzmann demonstrated that possible microscopic states for a certain level of energy are way greater for the macroscopic values corresponding to thermal equilibrium. This theory resulted in the *Boltzmann* distribution (see Appendix B.2 for derivation):

$$f(c) = \left(\sqrt{\frac{m}{2\pi kT}}\right)^3 e^{-\frac{m(c_x^2+c_y^2+c_z^2)}{2kT}} = \left(\frac{m}{2\pi kT}\right)^{3/2} e^{-\frac{mc^2}{2kT}} \tag{3.2}$$

The above equation is similar to the *Maxwell* distribution function (Eqn. 3.1), it needs only to be multiplied by the factor $4\pi c^2$ (which is the surface area of a sphere in the phase space) to account for the density of velocity states available to particles. As a matter of fact, integrating Eqn. 3.1 over a sphere surface in the phase space will yield to the above equation.

3.3 The Boltzmann equation

Boltzmann was the one who succeeded to develop statistical mechanics, which explains and predicts how the properties of molecules (microscopic properties) determine the global (macroscopic) properties of matter such as viscosity, thermal conductivity, thermal diffusion, and species diffusion flux (for multi-component media). The distribution function (probability of finding particles within a certain range of velocities at a certain range of locations at a given time) replaces tagging each particle, as in molecular dynamic simulations.

3.3.1 Boltzmann transport equation

The fundamental variable in the kinetic theory of particles is the distribution function $f(\boldsymbol{x}, \boldsymbol{\xi}, t)$, which explains the statistical description of a system. The Boltzmann

transport equation can be derived following Appendix B.3 and reads:

$$\frac{\partial f}{\partial t} + \frac{\partial f}{\partial \boldsymbol{x}} \cdot \boldsymbol{\xi} + \frac{\boldsymbol{F}}{\rho} \cdot \frac{\partial f}{\partial \boldsymbol{\xi}} = \Omega(f), \tag{3.3}$$

where $\boldsymbol{x}$ denotes the particle positions, $\boldsymbol{\xi}$ represents the particles velocity, $\boldsymbol{F}$ is the external body force and $\Omega(f)$ is the collision operator. This collision operator Ω needs to be determined to solve the Boltzmann equation. It would have been easy if Ω could be expressed explicitly, but the burden is that Ω is a function of f and the previous equation represents an integro-differential equation, which is difficult to resolve. For systems where there are no external forces, the Boltzmann equation can be written as follows:

$$\frac{\partial f}{\partial t} + \boldsymbol{\xi} \cdot \nabla f = \Omega(f), \tag{3.4}$$

it should be mentioned that $\boldsymbol{\xi}$ and ∇f are vectors. The concept on which the distribution function was established made it directly connected to the macroscopic variables, like density ρ and velocity $\boldsymbol{u}$, through the moments of this distribution function. These moment are merely the integrals of f, weighted with $\boldsymbol{\xi}$, over the entire velocity space. For instance, the mass density can be found as the zeroth moment of f:

$$\rho(\boldsymbol{x}, t) = \int f(\boldsymbol{x}, \boldsymbol{\xi}, t) d^3\xi, \tag{3.5}$$

this integration is done over the entire velocity space which consequently considers all the contribution to the density of particles of all the possible velocities at position $\boldsymbol{x}$ and time t. Furthermore, we can also consider the contribution of $\boldsymbol{\xi} f$ to the momentum density. Considering all the possible velocities, we find the macroscopic momentum density as the first moment:

$$\rho(\boldsymbol{x}, t)\boldsymbol{u}(\boldsymbol{x}, t) = \int \boldsymbol{\xi} f(\boldsymbol{x}, \boldsymbol{\xi}, t) d^3\xi, \tag{3.6}$$

With the same idea, we are capable of recovering the total energy density ρe_t of the particles by the second moment:

$$\rho(\boldsymbol{x}, t) e_t(\boldsymbol{x}, t) = \frac{1}{2} \int |\boldsymbol{\xi}|^2 f(\boldsymbol{x}, \boldsymbol{\xi}, t) d^3\xi, \tag{3.7}$$

the resulting total energy contains two parts of energies; the energy contained in the

bulk motion of the fluid $\frac{1}{2}\rho|\boldsymbol{u}|^2$, and the internal energy e due to the haphazard thermal motion of the gas molecules. The latter part of energy can be found as the second moment:

$$\rho(\boldsymbol{x},t)e(\boldsymbol{x},t) = \frac{1}{2}\int |\boldsymbol{v}|^2 f(\boldsymbol{x},\boldsymbol{\xi},t)d^3\xi, \tag{3.8}$$

where we introduce a new velocity called the relative velocity $\boldsymbol{v}$ which is the deviation of the particle velocity from the local mean velocity:

$$\boldsymbol{v}(\boldsymbol{x},t) = \boldsymbol{\xi}(\boldsymbol{x},t) - \boldsymbol{u}(\boldsymbol{x},t). \tag{3.9}$$

Those expressions, for the gas energy, account only for the translational energy of the molecules (i.e.the energy as a result of their motion at velocity $\boldsymbol{\xi}$). In the more strenuous kinetic theory of polyatomic gas, it is of great importance to consider the other degrees of freedom, such as molecular vibrational and rotational energies.

3.3.2 Collision operator

Regarding the collision operator Ω, for whatever form it will take, it must achieve two things: First, ensuring that the distribution function evolves locally towards its equilibrium f^{eq}. Secondly, conserving mass, momentum and energy. These conservation constraints may be represented by the moments of the collision operator as follows:

$$\text{mass conservation :} \quad \int \Omega(f)d^3\xi = 0, \tag{3.10}$$

$$\text{momentum conservation :} \quad \int \boldsymbol{\xi}\Omega(f)d^3\xi = \boldsymbol{0}, \tag{3.11}$$

$$\text{total energy conservation :} \quad \int |\boldsymbol{\xi}|^2\Omega(f)d^3\xi = 0, \tag{3.12}$$

$$\text{internal energy conservation :} \quad \int |\boldsymbol{v}|^2\Omega(f)d^3\xi = 0. \tag{3.13}$$

The original Boltzmann's collision operator is daunting to calculate, because this operator is in the form of intricate and cumbersome double integral over velocity space. It considers all the possible outcomes of two-molecules collisions for any inter-molecular forces. However, considering that the outcome of two particles colliding does not impact significantly the values of many measured quantities [27], it is possible to have a simplified approximated collision operator without promoting significant error to the

outcome of the solution. Subsequently, Bhatnagar, Gross and Krook (BGK) [13] introduced a simplified model for collision operator which will be widely used afterwards in LBM, the operator named **BGK collision operator** and it reads:

$$\Omega(f) = -\frac{1}{\tau}(f - f^{eq}). \tag{3.14}$$

The **BGK** operator is the simplest possible collision operator given the previous constraints. This particularity of this operator is that it can capture the relaxation of the distribution function f towards the equilibrium distribution f^{eq}. The parameter τ is the relaxation time, which defines the characteristic speed of equilibration from the state f to f^{eq}. The value of τ is crucial because it determine the transport properties of the fluid such as viscosity, heat diffusion, and species diffusion.

The essence of this **BGK** collision operator proclaims that when a gas left for an adequate duration of time, the distribution function $f(\boldsymbol{x}, \boldsymbol{\xi}, t)$ will reach an equilibrium distribution $f^{eq}(\boldsymbol{x}, \boldsymbol{\xi}, t)$ which is isotropic in velocity space around $\boldsymbol{u}$, and if we considered a reference frame that move at a speed $\boldsymbol{u}$ the equilibrium distribution can be expressed as $f^{eq}(\boldsymbol{x}, |\boldsymbol{v}|, t)$. The f^{eq} would take the form:

$$f^{eq}(\boldsymbol{x}, |\boldsymbol{v}|, t) = \rho \left(\frac{1}{2\pi r T}\right)^{\frac{3}{2}} e^{-\frac{|v|^2}{2rT}}, \tag{3.15}$$

This equilibrium distribution is often called the *Maxwell-Boltzmann distribution*. This equation is still in the continuous form and need to be discretized before using it in CFD codes. But before discretizing the Boltzmann equation, we have to expand the distribution function f first using the so called *Hermite polynomials* (HPs) which facilitates discretizing the Boltzmann equation in velocity, space and time. The details of these polynomials and the expansion procedure can be found in details in Appendix B.4. To recover the hydrodynamic behaviour we need to expand the distribution function up to the second order. The expansion of f^{eq} using the Hermite polynomials, up to second order, results in:

$$\begin{aligned} f^{eq}(\boldsymbol{x}, \boldsymbol{\xi}, t) &\approx \omega(\boldsymbol{\xi})\rho \left[1 + \xi_\alpha u_\alpha + u_\alpha u_\beta(\xi_\alpha \xi_\beta - \delta_{\alpha\beta})\right], \\ &= \omega(\boldsymbol{\xi})\rho Q(\boldsymbol{\xi}). \end{aligned} \tag{3.16}$$

Here, and for the sake of simplicity, we have assumed the flow to be isothermal,

where the density ρ and the pressure p are connected through:

$$p = c_s^2 \rho, \tag{3.17}$$

where c_s is a reference velocity (speed of sound) $c_s = \sqrt{r_0 T_0}$ associated with a reference temperature T_0 and a reference gas constant r_0.

3.3.3 External forces incorporation

The external force is what gives particularity to our work. External forces play an intrinsic role in hydrodynamic problems. Gravitational acceleration $\boldsymbol{g}$ is one of the external fields that may affect the flow and therefore it is paramount to include this into our LBM scheme to account this force. The gravitational acceleration will act as a body force in Eqn. 3.3 when multiplied by the density ρ:

$$\boldsymbol{F} = \rho \boldsymbol{g}. \tag{3.18}$$

This term appears in the momentum conservation equation of Navier-Stokes and works as a momentum source term. Other external forces, like radial and Coriolis forces in rotational flows, the electromagnetic forces in charged or magnetic particles either by affecting each others or force by external electromagnetic field. Moreover, forces also can be used to model multi-phase, multi-component flows or used even for immersed boundary conditions.

The projection of the external force using *Hermite polynomials* can be found in Appendix B.5. The resulting forcing term expanding to second order reads:

$$\mathcal{F} = -\frac{\boldsymbol{F}}{\rho} \cdot \frac{\partial f}{\partial \boldsymbol{\xi}} = w(\boldsymbol{\xi}) \left(\xi_\alpha + \left(\xi_\alpha \xi_\beta - \delta_{\alpha\beta} \right) u_\beta \right) F_\alpha. \tag{3.19}$$

where F_α is the applied force field. We refer to [127] for Chapman-Enskog analysis of the Boltzmann equation including the forcing term (not included here), moreover, they analyse the errors that may appear in the presence of incorrect force modelling.

3.4 Velocity-discretized Boltzmann equation

Up till now, we are dealing with the continuous form of the Boltzmann equation. Previously, we used the Hermite polynomials to expand $f^{eq}(\boldsymbol{x}, \boldsymbol{\xi}, t)$ and $f(\boldsymbol{x}, \boldsymbol{\xi}, t)$ after projecting them on Hermite basis for the valid reasons mentioned previously. In order

to discretize the velocity space, we ought first to introduce a suitable velocity set $\boldsymbol{\xi}_i$, of a size q, which ensures the conservation laws for the macroscopic quantities through the f^{eq} as in continuous form. This is realized using the *Hermite-Gauss quadrature* rule, which states:

$$\int f^{(N),eq}(\boldsymbol{\xi})\mathcal{H}^{(M)}(\boldsymbol{\xi})d^d\xi = \sum_i^n f_i^{(N),eq}(\xi_i)\mathcal{H}_i^{(M)}(\xi_i), \tag{3.20}$$

where M is the order of the Hermite polynomials, N is the truncation order of the expansion of f^{eq} in Eqn. B.27 and n is the number of *abscissa* needed to discretize velocity, at least $n = (N+1)/2$ *abscissa* and associated discretized weights w_i to correctly calculate the moments.

Hence, we can now employ the *Gauss-Hermite quadrature* to calculate moments and coefficients of Hermite series expansion for the equilibrium distribution function:

$$\begin{aligned} a^{(n),eq} = \int f^{eq}(\boldsymbol{\xi})\mathcal{H}^{(n)}(\boldsymbol{\xi})d^d\xi &= \rho\int \omega(\boldsymbol{\xi})Q(\boldsymbol{\xi})\boldsymbol{\mathcal{H}}^{(n)}(\boldsymbol{\xi})d^d\xi \\ &= \rho\sum_{i=1}^{n} w_i Q(\boldsymbol{\xi}_i)\boldsymbol{\mathcal{H}}^{(n)}(\boldsymbol{\xi}_i) \end{aligned} \tag{3.21}$$

This is the discretized Hermite expansion with n being the required number of abscissae. In the light of velocity space discretization, we define an n quantities associated with the chosen velocity set ξ_i and representing the equilibrium distribution function:

$$f_i^{eq}(\boldsymbol{x}, \boldsymbol{\xi}_i, t) = w_i\rho(\boldsymbol{x}, t)Q(\boldsymbol{\xi}_i) \tag{3.22}$$

So instead of having a continuous function $f^{eq}(\boldsymbol{\xi})$, we only account for a finite set of quantities $f_i^{eq} = f_i^{eq}(\boldsymbol{\xi}_i)$. Based on Eqn. 3.16, expanded to the second order using Hermite polynomials, the velocity-discretized f^{eq} will read:

$$f_i^{eq} = w_i\rho\left[1 + \xi_{i,\alpha}u_\alpha + \frac{1}{2}u_\alpha u_\beta(\xi_{i,\alpha}\xi_{i,\beta} - \delta_{\alpha\beta})\right] \tag{3.23}$$

The first three moments of the velocity-discretized distribution function $f^{eq}(\boldsymbol{\xi}_i)$ recover the same macroscopic quantities as the continuous one $f^{eq}(\boldsymbol{\xi})$. However, instead of using integration to calculate the moments in the case of $f^{eq}(\boldsymbol{\xi})$, it will be a summation over the chosen velocity set for $f^{eq}(\boldsymbol{\xi}_i)$.

There are plenty of abscissae that can be found in [127], they contain a factor of

$\sqrt{3}$ so it is logical and convenient to get rid of it by introducing a new lattice velocity $\boldsymbol{c}_i = \boldsymbol{\xi}_i/\sqrt{3}$, also we define $c_s = 1/\sqrt{3}$ as the reference lattice speed of sound for our chosen velocity set. This change of variables enables an exact propagation (i.e. streaming) by having all the population f_i arriving exactly at the neighbouring node after one time step δt. After having a velocity set with integer abscissae, we are able to write the form for the discrete equilibrium distribution function f_i^{eq}:

$$\boxed{f_i^{eq} = w_i \rho \left(1 + \frac{c_{i,\alpha} u_\alpha}{c_s^2} + \frac{u_\alpha u_\beta (c_{i,\alpha} c_{i,\beta} - c_s^2 \delta_{\alpha\beta})}{2c_s^4}\right)} \tag{3.24}$$

where c_s is the *speed of sound* which links the pressure and density. With the same manner, we can discretize the distribution function $f(\boldsymbol{\xi})$ exactly as the equilibrium distribution function $f(\boldsymbol{\xi})$, along with changing from $\boldsymbol{\xi}_i$ to $\boldsymbol{c}_i$:

$$f_i(\boldsymbol{x}, t) = \frac{w_i}{\omega(\boldsymbol{c}_i)} f(\boldsymbol{x}, \boldsymbol{c}_i, t) \tag{3.25}$$

$\omega(\boldsymbol{c}_i)$ is added to satisfy the the Gauss-Hermite rule:

$$\begin{aligned} a^{(n)}(\boldsymbol{x}, t) &= \int f(\boldsymbol{x}, \boldsymbol{c}, t) \boldsymbol{\mathcal{H}}^{(n)}(\boldsymbol{c}) d^d c = \int \frac{\omega(\boldsymbol{c})}{\omega(\boldsymbol{c})} f(\boldsymbol{x}, \boldsymbol{c}, t) \boldsymbol{\mathcal{H}}^{(n)}(\boldsymbol{c}) d^d c \\ &\approx \sum_{i=1}^{q} \frac{w_i}{\omega(\boldsymbol{c_i})} f(\boldsymbol{x}, \boldsymbol{c}_i, t) \boldsymbol{\mathcal{H}}^{(n)}(\boldsymbol{c}_i) = \sum_{i=1}^{q} f_i(\boldsymbol{x}, t) \boldsymbol{\mathcal{H}}^{(n)}(\boldsymbol{c}_i). \end{aligned} \tag{3.26}$$

we now have q functions of $f_i(\boldsymbol{x}, t)$, each one of them is associated to one discrete velocity $\boldsymbol{c}_i$. So finally we can write down the discrete-velocity Boltzmann equation "without" external force:

$$\frac{\partial f_i}{\partial t} + c_{i,\alpha} \frac{\partial f_i}{\partial x_\alpha} = \Omega_i(f_i), \qquad i = 0, \ldots, q-1. \tag{3.27}$$

That being said, the macroscopic moments (density, momentum and energy) are

now computed from finite sums:

$$\begin{aligned}\rho &= \sum_i^q f_i = \sum_i^q f_i^{eq},\\ \rho \boldsymbol{u} &= \sum_i^q f_i \boldsymbol{c}_i = \sum_i^q f_i^{eq} \boldsymbol{c}_i,\\ \rho e_t &= \frac{1}{2}\sum_i^q f_i \boldsymbol{c}_i \boldsymbol{c}_i = \frac{1}{2}\sum_i^q f_i^{eq} \boldsymbol{c}_i \boldsymbol{c}_i,\end{aligned} \tag{3.28}$$

Similarly, the force term can be discretized in the velocity space, we can write the discrete form of the force term starting from Eqn. 3.19:

$$\begin{aligned}\mathcal{F}_i(\boldsymbol{x}, t) &= -\frac{w_i}{\omega(\boldsymbol{c}_i)}\frac{\boldsymbol{F}}{\rho}\cdot\frac{\partial}{\partial \boldsymbol{c}_i} f(\boldsymbol{x}, \boldsymbol{c}_i, t)\\ &= \boxed{w_i\left(\frac{c_{i,\alpha}}{c_\mathrm{s}^2} + \frac{\left(c_{i,\alpha}c_{i,\beta} - c_\mathrm{s}^2\delta_{\alpha\beta}\right)u_\beta}{c_\mathrm{s}^4}\right)F_\alpha.}\end{aligned} \tag{3.29}$$

The first three moments of this force term will read:

$$\begin{aligned}\sum_i^q \mathcal{F}_i &= 0,\\ \sum_i^q \mathcal{F}_i c_{i,\alpha} &= F_\alpha,\\ \sum_i^q \mathcal{F}_i c_{i,\alpha} c_{i,\beta} &= F_\alpha u_\beta + u_\alpha F_\beta.\end{aligned} \tag{3.30}$$

The zeroth-order moment denotes a mass source which is zero in our study. As for the first-order moment, it is a momentum source. Finally, the second-order moment given an energy source describing the power flux that the body force exert on the fluid.

The second-order moment plays an important role as it removes the undesirable spurious term, given by $F_\alpha u_\beta + u_\alpha F_\beta$, that would appear at the viscous stress tensor level [89, 129, 141]. In the case of incompressible flow this error would vanish and the second-order moment will be zero, i.e. $\sum_i \mathcal{F}_i c_{i\alpha} c_{i\beta} = 0$. Hence, the force term should only be expanded up to the first order in the velocity space.

The discrete-velocity Boltzmann equation "with" a forcing term will then read:

$$\frac{\partial f_i}{\partial t} + c_{i,\alpha}\frac{\partial f_i}{\partial x_\alpha} = \Omega_i + \mathcal{F}_i, \quad i = 0, \ldots, q-1. \tag{3.31}$$

The previous equation is called the *Lattice Boltzmann* (LB) equation. More details about velocity sets used to discretize the Boltzmann equation can be found in Appendix B.6. Our LBM solver ProLB is based on the D3Q19 velocity set (i.e. lattice).

3.5 Chapman-Enskog expansion

It is about the right moment to demonstrate the validity of the Boltzmann equation to simulate fluid mechanics and to illustrate how one can retrieve the macroscopic Navier-Stokes equations starting from the Boltzmann equation. That being said, Appendix B.7 introduces the famous Chapman-Enskog expansion to prove the righteousness of using Boltzmann equation as a base for CFD simulations.

3.6 Spatial and Temporal discretization

What we achieved until now is discretizing the Boltzmann equation in the velocity space, yet, we still need a final step to have a fully discretized equation that can be implemented as a solver. This final step is discretization in both space and time. Although the most common form of space discretization in the classical LBM is uniform structured grids. Overall, the original LB algorithm assumes that the population f_i travels with speed $\boldsymbol{c}_i$ from one lattice to another. So after one time step δt, all the population should arrive exactly at the neighbouring node. This is achieved when the change of variables was introduced in the previous section (i.e. $\boldsymbol{c}_i = \boldsymbol{\xi}_i/\sqrt{3}$).

Now, we recall the velocity-discretized LB equation from the previous section:

$$\frac{\partial f_i}{\partial t} + c_{i,\alpha}\frac{\partial f_i}{\partial x_\alpha} = \Omega_i + \mathcal{F}_i, \tag{3.32}$$

Some comments about the previous equation:

1. The equation is a linear first order hyperbolic partial differential equation (PDE).
2. It is an advection equation with a source term.
3. The left-hand side of the equation represents the advection (streaming).

4. The right-hand side term represents the collision process, the source term in addition to the external force.

For more details and insights about the discretization of the left hand side of this equation, we refer to Ref. [127]. We briefly give here some hints about how this equation can be discretized. One of the powerful methods to handle such PDE is the *method of characteristics/trajectories*. This method benefits from the characteristic lines/trajectories associated with the space of PDE's independent variables, so it enables us to obtain the exact integration between t and δt. This can be applied on the left hand side of equation 3.32 which is linear to give the *exact* propagation step. Such that we can have:

$$f_i(\boldsymbol{x} + \boldsymbol{c}_i\delta t, t + \delta t) - f_i(\boldsymbol{x}, t) = \int_t^{t+\delta t} (\Omega_i + \mathcal{F}_i) d\zeta \tag{3.33}$$

where ζ is the characteristic line/trajectory in space and time (a consequence of *method of characteristic*). However, the right hand side is non-linear and can be approximated to attain a desired level of precision. This integral can be calculated in various ways [127, 236], here we will discuss only two approximations.

First-order integration

The integration of the collision and forcing terms can be approximated by the *rectangular* method using one point:

$$\int_t^{t+\delta t} (\Omega_i + \mathcal{F}_i)\, \mathrm{d}\zeta = \left[\Omega_i(\boldsymbol{x}, t) + \mathcal{F}_i(\boldsymbol{x}, t)\right] \delta t + \mathcal{O}\left(\delta t^2\right). \tag{3.34}$$

Using this first-order approximation with the **BGK** collision operator, the discretized LB equation gives:

$$f_i\left(\boldsymbol{x} + \boldsymbol{c}_i\delta t, t + \delta t\right) - f_i(\boldsymbol{x}, t) = -\frac{\delta t}{\tau}\left(f_i - f_i^{\mathrm{eq}}\right) + \mathcal{F}_i\delta t \tag{3.35}$$

The previous formula is first-order accurate in time and can not be considered a second-order; When considering the free-force formula, the first-order approximation is actually a second-order accurate in time if we just shifted $\delta t/2$ in the viscosity-relaxation relation $\nu = c_s^2\left(\tau - \frac{\delta t}{2}\right)$ instead of $\nu = c_s^2\tau$ [127]. Unfortunately, this manoeuvre is not valid in the presence of an external force. So we will end up with first-order accuracy which will lead to a non-accurate macroscopic solution, the analysis of these errors and

their impact can be found in [127]. Hence, in order to solve this and to have an accurate solution we perform a second order space-time discretization.

Second-order integration

The *trapezoidal* discretization is more accurate, when applied to the integration of the collision operator we will have:

$$\int_t^{t+\delta t} (\Omega_i + \mathcal{F}_i)\, \mathrm{d}\zeta = \left(\frac{\Omega_i(\boldsymbol{x}, t) + \Omega_i\left(\boldsymbol{x} + \boldsymbol{c}_i \delta t, t + \delta t\right)}{2} + \frac{\mathcal{F}_i(\boldsymbol{x}, t) + \mathcal{F}_i\left(\boldsymbol{x} + \boldsymbol{c}_i \delta t, t + \delta t\right)}{2} \right) \delta t + \mathcal{O}\left(\delta t^3\right) \tag{3.36}$$

The second-order accuracy is here attained but with an implicit formulation, this can be overcome to recover explicit form by introducing a subtle change of variables [47,93]:

$$\overline{f}_i = f_i - \frac{(\Omega_i + \mathcal{F}_i)\, \delta t}{2} \tag{3.37}$$

this change of variable results in:

$$\overline{f}_i\left(\boldsymbol{x} + \boldsymbol{c}_i \delta t, t + \delta t\right) - \overline{f}_i(\boldsymbol{x}, t) = \left[\Omega_i(\boldsymbol{x}, t) + \mathcal{F}_i(\boldsymbol{x}, t)\right] \delta t. \tag{3.38}$$

substituting the collision operator with **BGK** model we can write down:

$$\overline{f}_i\left(\boldsymbol{x} + \boldsymbol{c}_i \delta t, t + \delta t\right) - \overline{f}_i(\boldsymbol{x}, t) = -\frac{\delta t}{\tau + \delta t/2} \left(\overline{f}_i - f_i^{\mathrm{eq}} - \tau \mathcal{F}_i\right) \tag{3.39}$$

rearranging the right-hand side to reach the final form:

$$\boxed{\overline{f}_i\left(\boldsymbol{x} + \boldsymbol{c}_i \delta t, t + \delta t\right) - \overline{f}_i(\boldsymbol{x}, t) = -\frac{\delta t}{\overline{\tau}} \left(\overline{f}_i - f_i^{\mathrm{eq}}\right) + \left(1 - \frac{\delta t}{2\overline{\tau}}\right) \mathcal{F}_i} \tag{3.40}$$

where the bar can be dropped. This is the explicit second-order accurate discretization of LB equation with BGK collision operating accounting for forcing term. With a redefined relaxation time $\overline{\tau} = \tau + \delta t/2$. Based on the new variable $\overline{f}_i$ the macroscopic

moments reads:

$$\begin{aligned}\rho &= \sum_i^q \overline{f}_i + \frac{\delta t}{2}\underbrace{\sum_i^q \mathcal{F}_i}_{=0} = \sum_i^q \overline{f}_i, \\ \rho \boldsymbol{u} &= \sum_i^q \overline{f}_i \boldsymbol{c}_i + \frac{\delta t}{2}\underbrace{\sum_i^q \mathcal{F}_i \boldsymbol{c}_{i\alpha}}_{\mathcal{F}_\alpha} = \sum_i^q \overline{f}_i \boldsymbol{c}_i + \frac{\delta t}{2} F_\alpha.\end{aligned} \tag{3.41}$$

The density is not impacted with the force term because the forcing term does not incorporate a mass source. The momentum has an additional term that accounts for the additional forcing term on the momentum conservation equation.

The equilibrium population f^{eq} is not changed by the addition of the forcing term, however, the velocities used to calculate f^{eq} has a new definition that accounts for the external force in the momentum equation.

The forcing term scheme introduced is one of many other ways the tries to incorporate the forcing term, the scheme introduced is named *Guo scheme* referring to Guo *et* al. [89]. They scrutinized the derivation and gave deeper discussions along side Huang *et* al. [105]. Ginzburg *et* al. [83] discussed other equivalent ways of introducing forcing in the LB equation.

3.7 General LBM solver algorithm

The previous sections provided in detail the Boltzmann equation and we proved how it represents the Navier-Stokes equation, also we demonstrated how we can discretize this equation in the velocity space as well as in the time and space domains to get the LB equation. In this section we will show how this equation can be implemented and used in a CFD solver.

3.7.1 Non-dimensionalization of variables

It is of a great importance to understand the dimensions implicated in the LB equation and their conversions, and how to transfer from physical units to lattice units. Both unit systems are linked through a reference length scale L_0, and physical sound speed $c_{s,phy}$ for space and time, a reference density ρ_0 for mass and a reference temperature T_0.

It is a common practice that LBM solvers are built such that $\delta x^* = 1$, $\delta t^* = 1$ and $\rho_0^* = 1$ (called *lattice* units), so that we have our conversion factors for length, time, and density equal the dimensional values for lattice constant δx, time step δt and density ρ. The physical units can be retrieved from the lattice units (superscript *) as:

$$\begin{aligned} &\delta x = L_0/N_i, \qquad \delta t = t/N_t, \\ &u = u^* \frac{\delta x}{\delta t}, \end{aligned} \tag{3.42}$$

LB simulations are performed entirely in *lattice* units, so it is fundamental to master how to go from one to the other. The physical relaxation time τ and the dimensionless relaxation time τ^* is connected through the conversion factor δt because τ has the dimensions of time:

$$\tau = \tau^* \delta t, \tag{3.43}$$

The viscosity is one of the most important parameters in the simulation since it is related directly to the relaxation time τ. So a typical problem is to relate the physical kinematic viscosity ν to the non-dimensional relaxation parameter τ^*, they can be related as:

$$\nu = \nu^* \frac{\delta x^2}{\delta t} = c_s^{*2}(\tau^* - \frac{1}{2})\frac{\delta x^2}{\delta t} \tag{3.44}$$

3.7.2 collision & streaming

The LBM algorithm has only two fundamental steps to complete a full time step, those steps are the ***collision*** and the ***streaming***:

$$\begin{aligned} &f_i^{col}(\boldsymbol{x}, t) = f_i(\boldsymbol{x}, t) - \frac{\delta t}{\tau}(f_i - f_i^{eq}) + \left(1 - \frac{\delta t}{2\tau}\right)\mathcal{F}_i \delta t \qquad \text{(Collision)} \\ &f_i(\boldsymbol{x} + \boldsymbol{c}_i \delta t, t + \delta t) = f_i^{col}(\boldsymbol{x}, t) \qquad \text{(Streaming)} \end{aligned} \tag{3.45}$$

the collision step here used the standard **BGK** model which defines the relaxation towards the equilibrium state and it is directly related to the viscosity of the flow, furthermore, the collision step includes the required forcing terms. This step is usually local so it is done at each node independently from the others and it is performed generally before the streaming step. Afterwards, the post-collision particles $f_i^{col}(\boldsymbol{x}, t)$ stream to the neighbouring nodes via $\boldsymbol{x} + \boldsymbol{c}_i \delta t$. Then boundary condition must be dealt with and their related information should be provided. At the end, the macroscopic

variables can be recovered through the moments of the distribution function. By then we can say that a complete time step is done and we start the process again.

This is not a unique algorithm, some steps are interchangeable. Now we have finished explaining all the details related to the LBM and the algorithm by which this method is generally realized. We recall the fact that the LBM method is precise for incompressible or weakly compressible flows, therefore, one of the challenges that faces the LBM is the stability and the accuracy of this method for compressible and thermal flows.

The **BGK** collision operator was used in this chapter for simplicity in order to understand the basics of LBM. Unfortunately, this simple **BGK** operator faces some stability issues and the need of more sophisticated models is fundamental [175]. Numerous collision models were introduced in the literature enhancing stability. Two-relaxation time (TRT) or multi-relaxation time (MRT) based collision operators can be found in the literature [51,52,57,106,131,192,263]. The BGK collision operator can be called a single relaxation time (SRT). It is worth mentioning that at second order, the incompressible macroscopic mass and momentum conservation equations are identical for TRT, SRT, MRT but these models differ for high-order approximations. Also we can find cumulant models [80]. Cascade LB models also are proposed in the literature [91]. Another approach that can be found is the regularized models [132, 133, 149, 157], where their idea was to mitigate the non-hydrodynamics moments of the distribution function (also called ghost modes) so that an infinitely fast relaxation to equilibrium is realized. The latter strategy will be adopted in our solver ProLB and will be introduced next.

The LBM model adopted thereafter was mainly developed by Farag *et* al. [64] where they used a **pressure based hybrid regularized recursive** LB algorithm (shortly **HRR**-$\mathcal{P}$) for the sake of addressing compressible flows (which can be applied to thermal flows as well). Some modifications were added to this model to accommodate to our specific application of fire-induced flows, mainly, the gravity forcing term. The **HRR**-$\mathcal{P}$ model was proven in the literature to be capable of handling various configurations in various flow regimes. The details of this model and the algorithm used in the solver will be introduced next.

3.8 LB Formulation for isothermal HRR-$\mathcal{P}$ model

We introduce the **HRR**-$\mathcal{P}$ model as a general model that works for both isothermal and thermal flows, it is sufficient to set the parameter θ to unity in order to have a fully isothermal algorithm.

The **HRR**-$\mathcal{P}$ model introduced by Farag *et* al. [64] to solve compressible flows, uses a modified equilibrium distribution function via Hermite polynomials expansion of the *Maxwell-Boltzmann* distribution function Eqn. 3.15. A regularized collision operator was used instead of the pure **BGK** to further enhance the stability and the precision by having an accurate ghost mode damping properties with an explicit control of the artificial hyperviscosity. [8] proved using linearized spectral analysis that this scheme can mitigate the spurious ghost modes [256].

While pressure based and density based models yield to the same macroscopic equations in the low-Mach athermal limit (i.e. isothermal $\theta = 1$). Handling pressure directly via an evolution equation instead of the equation of state, is known to reduce the spurious pressure oscillations in flows containing large density variations as reported in [3, 118]. The model is developed by expanding the *Maxwell-Boltzmann* distribution 3.15 to the fourth order, then replace the third and fourth order terms by means of recursive regularization to set the viscous stress tensor correctly. The model is applied over a standard lattice of $D3Q19$ with the distribution function f_i that implies:

$$\begin{aligned}
&\sum_i f_i^{eq} = \rho = p/c_s^2, \\
&\sum_i c_{i,\alpha} f_i^{eq} + \frac{\delta t}{2} F_\alpha = \rho u_\alpha, \\
&\sum_i c_{i,\alpha} c_{i,\beta} f_i^{eq} = \rho u_\alpha u_\beta + \rho c_s^2 \delta_{\alpha\beta},
\end{aligned} \tag{3.46}$$

We follow a single relaxation time (SRT) evolution equation equipped with the **BGK** collision operator and considering the external force. The collision is based on the following modified pressure based fourth order equilibrium distribution [64]:

$$f_i^{\mathrm{eq},19r} = \omega_i \left\{ a^{(0),\mathrm{eq}} + \frac{\mathcal{H}_{i,\alpha}^{(1)}}{c_s^2} a_\alpha^{(1),\mathrm{eq}} + \frac{\mathcal{H}_{i,\alpha\beta}^{(2)}}{2c_s^4} a_{\alpha\beta}^{(2),\mathrm{eq}} + \frac{\mathcal{H}_{i,\gamma}^{(3r)}}{6c_s^6} a_\gamma^{(3r),\mathrm{eq}} + \frac{\mathcal{H}_{i,\delta}^{(4r)}}{24c_s^8} a_\delta^{(4r),\mathrm{eq}} \right\}, \tag{3.47}$$

The superscript $19r$ signifies the 19 discrete velocities and the recursive process. We explain in Appendix B.4 that the equilibrium distribution function f_i^{eq} needs only to be expanded to the second order to recover the macroscopic laws of hydrodynamics. Nonetheless, the third order expansion is crucial as the stress tensor recovered with lower orders is not sufficient enough to accurately define the momentum equation. Thus, the third order term allows us to constitute a correct stress tensor as shown through Chapman-Enskog in Appendix B.7. The fourth order term is included in order

to enhance the isotropicity of the lattice.

The previous equation was expanded using Hermite polynomials, for the D3Q19r lattice, we have 19 discrete polynomials defined in details in Appendix B.8. Although, all lattices retrieve consistent Navier-Stokes dynamics in the continuum limit, they are expected to behave differently at discrete level. Indeed, a study done by [248] demonstrated that some truncation terms (the non-linear momentum advection corrections) does not have rotational invariance in $D3Q15$ and $D3Q19$ in the contrary of $D3Q27$. This lack of isotropy may lead to problems whenever non-linear phenomena contribute significantly (e.g. in simulating high Reynolds number flows and turbulence). However, $D3Q27$ requires more memory when compared to $D3Q19$. Another study addressing this issue [209], where they studied different velocity sets, i.e. lattices, and performed truncation error analysis, and they deduced that the differences between the studied lattice lie in the structure of their non-linear truncation errors. They showed that the lattices $D3Q15$ and $D3Q19$ introduce spurious angular dependencies via non-linear truncation errors which was not the case for the $D3Q27$, and they emphasized on the superiority of the $D3Q27$ to cope with the rotational invariance principal in 3D hydrodynamic problems specially when convection is not negligible (our case). Further investigations have been done to assess the impact of the lattice on turbulent flows [117,217], and they confirmed the same thing. So a choice had to be made to compromise between accuracy and required memory. Hence, the $D3Q19$ lattice equipped with correction fourth order terms to enhance the isotropy of the $D3Q19$ lattice to be able to tackle problems that include axisymmetry, e.g. round thermal plumes, and the turbulence naturally involved in fire-induce flows.

3.9 The isothermal HRR-$\mathcal{P}$ algorithm

In the present work, a regularization strategy is followed and an additional step for regularization is adopted from [66, 108, 133]. The algorithm follows exactly the study of Farag *et* al. [64]. The algorithm is illustrated in Fig. 3.1. Starting from knowing the post collide population at time step t, we introduce an intermediate population f_i^* calculated by ***streaming step*** from neighbours:

$$f_i^*(\boldsymbol{x}, t+\delta t) = f_i^{col}(\boldsymbol{x} - \boldsymbol{c}_i \delta t, t), \tag{3.48}$$

Then a ***Regularized collision step*** is performed, where the collide population at time $t+\delta t$ is obtained by several steps: first, updating the macroscopic variables to

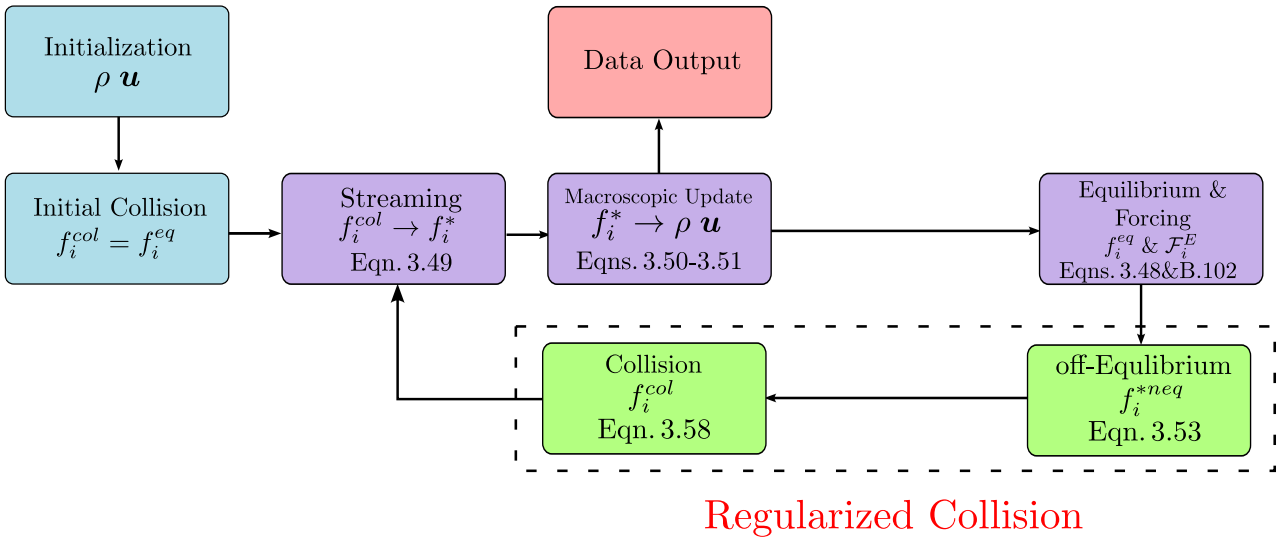

Figure 3.1: Flow chart of the HRR algorithm

have them at $t + \delta t$. Density and velocity are reconstructed from the post-streaming population f_i^* as:

$$\rho(\boldsymbol{x}, t + \delta t) = \sum_i f_i^*(\boldsymbol{x}, t + \delta t), \tag{3.49}$$

$$(\rho u_\alpha)(\boldsymbol{x}, t + \delta t) = \sum_i c_{i,\alpha} \left(f_i^*(\boldsymbol{x}, t + \delta t) + \frac{\delta_t}{2} \mathcal{F}_i^g \right). \tag{3.50}$$

where F_i^g is the gravity forcing term indispensable for scrutinizing buoyancy-driven flows, defined as:

$$\mathcal{F}_i^g = \omega_i \left[\frac{\rho g_\alpha \mathcal{H}_{i,\alpha}^{(1)}}{c_s^2} + \frac{(\rho u_\alpha g_\beta + \rho u_\beta g_\alpha) \mathcal{H}_{i,\alpha\beta}^{(2)}}{2 c_s^4} \right], \tag{3.51}$$

where g_α is the gravity acceleration in the direction α. Secondly, the off-equilibrium tensors is constructed using the formula:

$$f_i^{*neq}(\boldsymbol{x}, t + \delta t) = f_i^*(\boldsymbol{x}, t + \delta t) - f_i^{eq}(\boldsymbol{x}, t + \delta t) + \frac{\delta t}{2} \mathcal{F}_i^E(\boldsymbol{x}, t + \delta t), \tag{3.52}$$

where f_i^{eq} is the equilibrium distribution calculated from ρ, u, θ at time $t + \delta t$ using Eqn. 3.47, also F_i^E is a forcing term given by Eqn. B.102 in Appendix B.9. Note that, f_i^{eq}

and F_i^E are calculated from available data at $t+\delta t$. The second order non-equilibrium tensor is estimated by:

$$a_{\alpha\beta}^{*(2),neq}(\boldsymbol{x},t+\delta t)=\sum_i \mathcal{H}_{i,\alpha\beta}^{(2)}(\boldsymbol{c}_i)f_i^{*neq}(\boldsymbol{x},t+\delta t), \tag{3.53}$$

Furthermore, we impose a traceless tensor by removing its trace [64]. The viscous stress tensor then reads:

$$a_{\alpha\beta}^{(2),\mathrm{neq}}\equiv\sigma\left[a_{\alpha\beta}^{*(2),\mathrm{neq}}-\frac{\delta_{\alpha\beta}}{3}a_{\gamma\gamma}^{*(2),\mathrm{neq}}\right]+(1-\sigma)a_{\alpha\beta}^{*\mathrm{neq,FD}}, \tag{3.54}$$

where σ is a free parameter while $a_{\alpha\beta}^{*\mathrm{neq,FD}}$ can be evaluated directly from a second order finite difference (FD) scheme of:

$$a_{\alpha\beta}^{*\mathrm{neq,FD}}=-\rho c_s^2\overline{\tau}(u_{\alpha\beta}+u_{\beta\alpha}-\frac{2}{3}u_{\gamma\gamma}\delta_{\alpha\beta}), \tag{3.55}$$

where $\overline{\tau}$ is the relaxation time linked to the dynamic viscosity as:

$$\overline{\tau}=\frac{\mu}{\rho c_s^2}+\frac{\delta t}{2}. \tag{3.56}$$

Finally, we perform the collision step following:

$$f_i^{col}\left(\boldsymbol{x},t+\delta t\right)=f_i^{\mathrm{eq}}\left(\boldsymbol{x},t\right)+\left(1-\frac{\delta t}{\overline{\tau}}\right)f_i^{\mathrm{neq}}\left(\boldsymbol{x},t\right)+\frac{\delta t}{2}\mathcal{F}_i^E(\boldsymbol{x},t), \tag{3.57}$$

Note that $\mathcal{F}_i^E$ is added to recover a correct non-equilibrium tensor as explained in Appendix B.9, and the non-equilibrium regularized population

$$f_i^{\mathrm{neq}}=\omega_i\left[\frac{\mathcal{H}_{i,\alpha\beta}^{(2)}}{2c_s^4}a_{\alpha\beta}^{(2),\mathrm{neq}}+\frac{\mathcal{H}_{i,\gamma}^{(3r)}}{6c_s^6}a_{\gamma}^{(3r),\mathrm{neq}}\right], \tag{3.58}$$

and the third order off-equilibrium $a_{\gamma}^{(3r),\mathrm{neq}}$ is recursively derived as demonstrated in Eqn. B.104 of Appendix B.10.

At this stage a full time step is accomplished, we repeat again the streaming then collision until we perform the required number of iterations (i.e. time steps).

Summary In this chapter, we introduced the basic global knowledge about LBM method, we proved via CE analysis how the LB equation can be used for Navier-Stokes simulations. We introduced finally the **HRR**-$\mathcal{P}$ algorithm that will be the heart of our solver ProLB and with which we will perform all the simulations in this thesis. Nevertheless, the isothermal assumption was made throughout this chapter and we never mention what to do in the case of thermal flows. That's the goal of the next chapter, we will give the details of how we can simulate thermal flows and how the parameter θ can be calculated when the flow is no longer isothermal.

Chapter 4

LBM algorithm for thermal flows

Contents

4.1 Introduction

The last chapter handled the athermal LBM and gave all the basics necessary to understand the context of LBM. The athermal LBM ($\theta = 1$) with BGK collision operator is widely used to simulate various incompressible flows. However, simulating compressible/thermal flows is limited and faces many issues. The major cause is the equilibrium distribution function used in the LB equation. The Chapman-Enskog scale analysis

required expanding the distribution function f in terms of Knudsen number ϵ, which is proportional to the Mach number, and which should be limited to small values for accuracy and stability [127], hence, the Mach number. The athermal model implies that pressure is related to density though the equation of state (EOS) $p = c_s^2\rho$, where c_s is constant. This equation of state is not capable of working with thermal or compressible flow where temperature changes and affects density and thus pressure. The logical candidate to replace this limited EOS is the ideal gas law, which is rigorous despite its simplicity. In the context of fire simulations and buoyancy driven flows, we are encountered with different physics that requires a model that covers beyond the iso-thermal (athermal) flows. According to the momentum equation in Navier-Stokes equations, the buoyancy force appears when there is a density deficit in the flow, this deficit maybe caused by different manners:

- Temperature difference in a gas with one species.
- Uniform temperature but with different species having different molecular weights.

So it is compulsory to add energy and species equations to the model in order to be able to simulate this complex multi-physics system. Comprehending energy equation in the LBM system is a hot topic and many approaches have been introduced in the LBM community. This topic is still open to find efficient and accurate technique to incorporate the energy equation in our LBM system. Some of the proposed approaches to include energy/species equations to the LB system are:

- ***Multi-speed***: One of the proposed approaches is the ***multi-speed*** lattice. This method is based on extending the velocity set in order to include more discrete velocity. The additional discrete velocities create high order lattices in addition to adding higher order terms in the discrete equilibrium distribution function. By doing this, we are able to recover correctly the conservation of mass, momentum and energy purely by LBM. This technique has been used in the literature and validated through thermal flow test cases, such as Couette flow with heat transfer [5, 244], two dimensional Rayleigh-Bénard [194] and some additional thermal test cases [34, 119].

  The multi-speed methods are considered to inherit all the basic advantages of the LB method. Nevertheless, they are hyper costly in comparison to the other available approaches in the LB framework [43]. The high cost is clearly due to the high number of discrete velocities (e.g. D3Q121). Consequently, it is not considered affordable in terms of computational cost for the industrial applications where accurate results are required but in the minimum possible time.

- ***DDF***: Another approach is the ***double distribution function (DDF)*** which uses two distribution functions. It uses one distribution function f to recover mass and momentum equations and the other g for the energy equation, e.g. $\sum_i g = e$. Each distribution function is solved independently of the other with different relaxation times, macroscopic variable recovery and lattice descriptions. More details about this method and the associated application can be found abundantly in the literature [71, 90, 93, 138, 195, 196].

  Nevertheless, this method is under questioning, as its cost may be high which contradicts the original purpose of developing LBM, specially when using higher order lattices (more discrete velocities). Also, their stability and accuracy may vary depending on the application. A great care as well should be given to the coupling issue between the distribution functions.

- ***Hybrid***: The strategy of hybridization includes the energy equations by using the standard single distribution function to calculate the mass and momentum conservation while the energy and species conservation equations are solved using a classical finite difference (FD) or a finite volume (FV) applied to the macroscopic equations of Navier-Stokes. Achieving a fully compressible thermal CFD solver necessitates a full coupling between mass, momentum, energy and species.

  Early trials to attain hybridization were reported by [73, 74, 130]. The hybrid approach has been used to model hydrodynamics in the Boussinesq approximation [131] where temperature was regarded as passive scalar which does not impact the LB system (i.e. no full coupling).

  Instability in hybrid LBM is a serious issue and many studies tried to figure out a solution to deal with the spurious currents and correct the coupling between the two solvers. One of the propositions suggests the usage of a forcing term in the framework of hybrid LB thermal models in order to deal with the spurious source term [139]. Moreover, simulations of highly compressible flows were presented in [177] and robustness was tested.

  Feng *et* al. [67] proposed a method using Hybrid Regularized Recursive (HRR) collision operator based on [108]. They succeeded to perform simulations of high subsonic thermal simulation with variable density. The stability showed significant improvement compared to the original recursive regularized approach proposed by [148]. In this method also, they have corrected the Galilean invariance defect on standard lattice through correction term based on Hermite-polynomials, which is computed using finite difference and added eventually as a forcing term.

More advancement then reported in [200] where the model was able to correctly predict the hydrodynamic physics of Navier-Stokes with ideal gas, covering all the flow regimes from subsonic to supersonic. Recently, Farag *et* al. [64] proposed a similar method to [67] where the equilibrium distribution function was modified and they showed the stability and the robustness of the model against various compressible test cases.

Having said that, the ***hybrid*** approach is the one adopted throughout our study and on which the ProLB solver is based. We have already explained in details the **HRR**-$\mathcal{P}$ algorithm for isothermal flows in Sec. 3.9 where we imposed $\theta = 1$ to get isothermal solution. In the next section, we will show the modifications needed when $\theta \neq 1$ for thermal flows. We define the thermal parameter θ for thermal multi-species flows as:

$$\theta = \frac{rT}{c_s^2} = \frac{\mathcal{R}T}{c_s^2} \sum_k^{N_{sp}} \frac{Y_k}{W_k}. \tag{4.1}$$

All the configurations to be studied fall within the low-Mach regime, hence, the low-Mach number approximation will be also incorporated, which was introduced recently by Wang *et* al. [242].

4.2 LB Formulation for thermal HRR-$\mathcal{P}$ model

The model is typical to the one introduced in Sec. 3.9 with the difference that the thermal parameter θ is no longer unity and is calculated through Eqn. 4.1 via the coupling with energy and species conservation equations. The model is applied over a standard lattice of $D3Q19$ with the distribution function f_i that implies:

$$\begin{aligned}
&\sum_i f_i^{eq} = \rho\theta = p/c_s^2, \\
&\sum_i c_{i,\alpha} f_i^{eq} + \frac{\delta t}{2} F_\alpha = \rho u_\alpha, \\
&\sum_i c_{i,\alpha} c_{i,\beta} f_i^{eq} = \rho u_\alpha u_\beta + \rho\theta c_s^2 \delta_{\alpha\beta},
\end{aligned} \tag{4.2}$$

we notice the change in the zeroth order moment where it is no longer the density but instead it is a pseudo pressure $\rho\theta$ which is the essence of the pressure based method. Moreover, on contrast to the density based models where the thermal effects appears in

the high order moment through the parameter θ, this model is regarded as an athermal equilibrium with a modified zeroth order moment $a^{(0),\text{eq}} = \rho\theta = p/c_s^2$.

4.2.1 The thermal HRR-$\mathcal{P}$ algorithm

Fig. 4.1 shows the modifications to the isothermal algorithm explained in Sec. 3.9. The thermal parameter θ is updated each time step after updating energy and species equations.

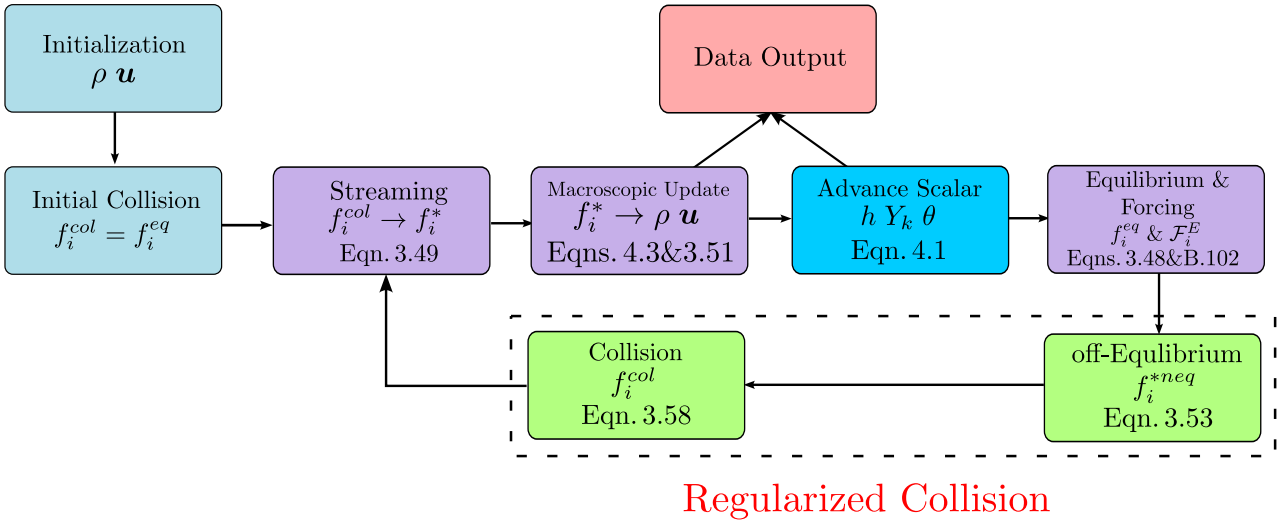

Figure 4.1: Flow chart of the HRR algorithm

As we said earlier, the zeroth order moment is no longer density, hence, to recover density from the post-streaming population f_i^* we use the following formula instead of Eqn. 3.49:

$$\rho(\boldsymbol{x}, t+\delta t) = \sum_i f_i^*(\boldsymbol{x}, t+\delta t) - (\rho\theta)(\boldsymbol{x}, t) + \rho(\boldsymbol{x}, t). \tag{4.3}$$

Note that no change is needed to update velocity. The scalar transport equations (i.e. energy and species) can be then advanced in time using finite difference discretization. Having updated both density and energy, the reduce temperature θ may now be calculated using the thermodynamic closure (Eqn. 4.1) to have $\theta(t+\delta t)$.

4.2.2 Density reconstruction

The equilibrium distribution function f_i^{eq} has been modified (Eqn. 3.47) in order to have a pressure based solver, consequently, the way of how we recover density (Eqn. 4.3) was

adjusted, as the zeroth order moment of the distribution function is no longer the density but a pseudo pressure $\sum_i f_i = \rho\theta$. Hence, a correction was introduced to the zeroth order moment in order to recover density (i.e. mass equation). Owing to the change in the zeroth order moment, the corresponding conservation equation recovered from Eqn. 3.47 reads:

$$\frac{\partial \rho\theta}{\partial t} + \frac{\partial \rho u_\alpha}{\partial x_\alpha} = 0, \tag{4.4}$$

inducing a pressure equation in the low-Mach limit [95]. The momentum conservation equation remains the same because the first and the second moments of $f_i^{eq,19r}$ are still physically consistent. In particular, the first order moment of Eqn. 3.47 will read:

$$\frac{\partial \rho u_\alpha}{\partial t} + \frac{\partial \rho u_\alpha u_\beta}{\partial x_\beta} = -\frac{\partial \theta \rho c_s^2}{\partial x_\alpha} - \frac{\partial a_{\alpha\beta}^{neq}}{\partial x_\beta} + \rho F_\alpha, \tag{4.5}$$

where $a_{\alpha\beta}^{neq}$, as we already explained, is the second order non-equilibrium stress tensor. This gives us a a low-Mach thermal solver, which constitutes a predictor step, and in order to recover a fully compressible solution, it is mandatory to correct both macroscopic moments and density distributions during the modified stream and collision algorithm as we showed previously. That's why the algorithm is regarded as a predictor-corrector approach, where the weakly compressible (i.e. low-Mach) solution of the predictor step is later corrected to recover a fully compressible solution. This approach we used is called *segregated* where both predictor and corrector steps depends only on explicit schemes without any sub-iteration process.

Eqn. 4.3 is the correction equation to recover the conservation of mass equation. By default and without any correction, the step where we update the macroscopic variables should have the zeroth order moment equals to $\rho\theta$:

$$(\rho\theta)^*(\boldsymbol{x}, t+\delta t) = \sum_i f_i^*(\boldsymbol{x}, t+\delta t). \tag{4.6}$$

Reminding that $\rho\theta = p/c_s^2$, it leads to the pressure equation demonstrated at Eqn. 4.4 in the low-Mach limit [95]. The previous equation can be manipulated (subtracting $\rho\theta$ from both sides) to have the following relation:

$$(\rho\theta)^*(\boldsymbol{x}, t+\delta t) - (\rho\theta)(\boldsymbol{x}, t) = \sum_i f_i^*(\boldsymbol{x}, t+\delta t) - (\rho\theta)(\boldsymbol{x}, t), \tag{4.7}$$

the left-hand side of the above equation can be related to the pressure equation Eqn. 4.4 through:

$$(\rho\theta)^*(\boldsymbol{x}, t+\delta t) - (\rho\theta)(\boldsymbol{x}, t) \approx \frac{\partial \rho\theta}{\partial t}\delta_t = -\frac{\partial \rho u_\alpha}{\partial x_\alpha}\delta_t. \tag{4.8}$$

The standard Navier-Stokes mass conservation equation can be now used to correct the prediction step and to recover the density:

$$\begin{aligned}\rho(\boldsymbol{x}, t+\delta t) &\approx -\frac{\partial \rho u_\alpha}{\partial x_\alpha}\delta t + \rho(\boldsymbol{x}, t) \\ &= (\rho\theta)^*(\boldsymbol{x}, t+\delta t) - (\rho\theta)(\boldsymbol{x}, t) + \rho(\boldsymbol{x}, t) \\ &= \sum_i f_i^*(\boldsymbol{x}, t+\delta t) - (\rho\theta)(\boldsymbol{x}, t) + \rho(\boldsymbol{x}, t)\end{aligned} \tag{4.9}$$

which leads to Eqn. 4.3. Nevertheless, this correction, applied to get a correct density field, generates errors that modifies the second order moment of the distribution function. Hence, in order to have a viscous stress tensor as in Eqn. B.99, a correction term (tensor) should be inserted to the forcing term to fix this issue shown in Eqn. B.100. The scheme that we demonstrated has the advantageous property of conserving both mass and momentum [64].

4.3 Turbulence model incorporation

Turbulence modelling in LBM is rather simple, we know a priori that the viscosity is connected to the LBM through the relaxation time $\overline{\tau}$ associated with the BGK collision kernel. Turbulence models add the so called turbulent viscosity or SGS viscosity ν_t to compensate the effects of the non-resolved scales smaller than cell size. Having said that, the relaxation time can then be modified to include this additional viscosity as follows [108, 262]:

$$\overline{\tau} = \frac{\nu + \nu_t}{c_s^2} + \frac{\delta t}{2}, \tag{4.10}$$

ν_t is calculated from the turbulence models presented in Sec. 6.4.2. Generally, the SGS models used in our work depends only on velocity gradients to estimate ν_t which are available simply.

4.4 Coupling LBM - Energy & Species

The coupling between LB and finite difference (FD) solvers is simple and straightforward. Fig. 4.2 depicts how the LB and FD solvers can run simultaneously and exchange information. The communication between the two solver happens only once each time step which keeps the process simple. After initializing all macroscopic variables $(\rho, \boldsymbol{u}, T, Y_k)$, the LB branch advances in time by first calculating f^{eq} and f^{neq} then performing the two main steps, namely collision and streaming, at the end of LB branch we can reconstruct the macroscopic density ρ and velocity vector $\boldsymbol{u}$. Concurrently, in the FD branch, where energy and species equations are being resolved, the advance in time is done using first order Euler time integration which suits the scheme for its simplicity and lower computational cost, at the end of this branch we end up with the updated temperature T and the species mass fraction Y_k. At this point, all the macroscopic variables are updated and a full time step is finished. At this stage, the communication happens and the exchange occurs between the two solvers, the LB branch feeds the FD branch with the updated ρ and $\boldsymbol{u}$, while the FD branch sends the updated T and Y_k through the parameter θ (see Eqn. 4.1). The solver is then ready to perform another time step, and this process will be repeated until the end of the required number of time steps.

4.5 Finite Difference for Energy & Species conservation equations

The FD solver aims to resolve the conservation equation of energy and species to update temperature and species, respectively, in parallel with the LB solver that updates density and velocities. The choice of discretization spatial and temporal schemes is of supreme importance. The choice will be always compromising between computational cost and solution accuracy. In the highlight, low order schemes seem sufficient and constitute good candidates for our model, due to their low computational cost and benefiting from the low dissipation introduced by the LB algorithm. To demonstrate how the spatial and temporal discretization is done, we will take the example of the conservation equation of enthalpy. The same discretization can be done for any other heat variable (energy, enthalpy, entropy) as well as the species equation, all may be discretized in the same manner. We recall the conservation equation of enthalpy without

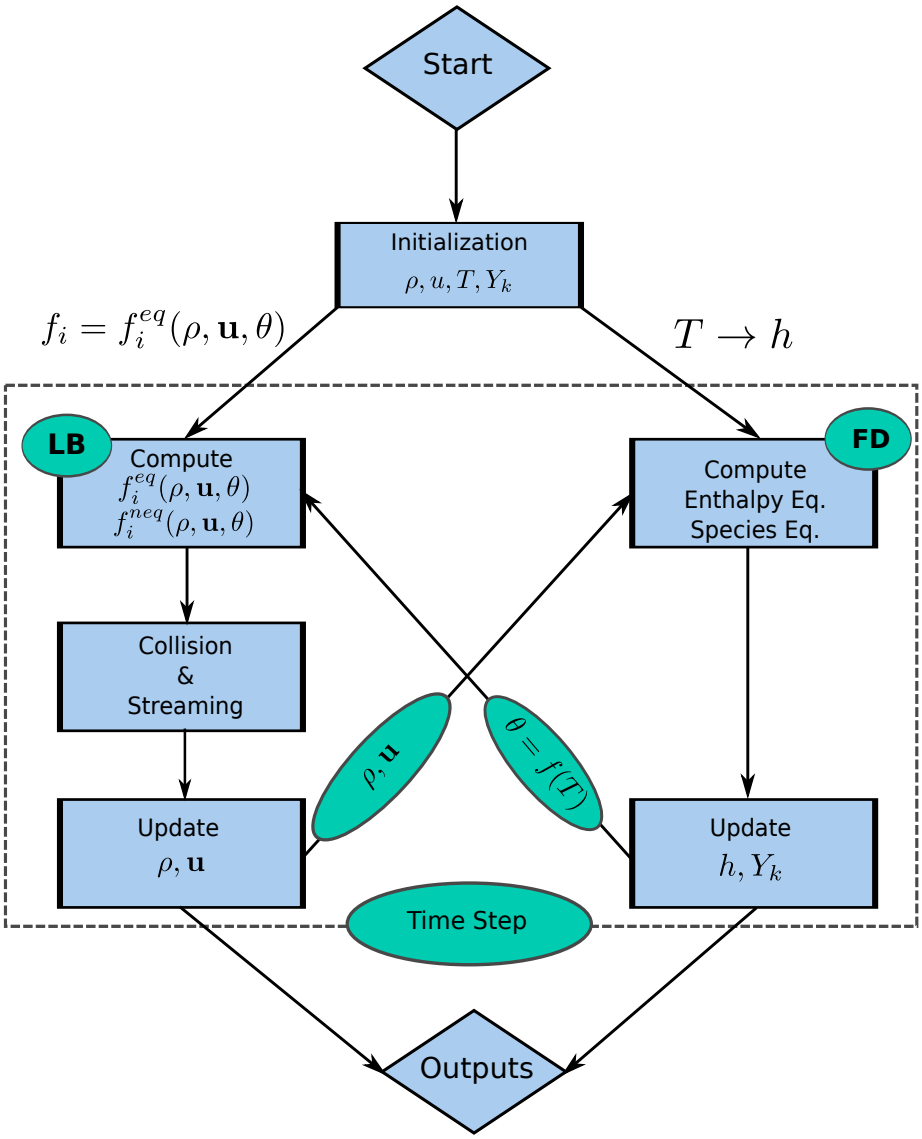

Figure 4.2: Flow chart of Coupling algorithm. Consists of the Lattice-Boltzmann (LB) in the left-hand side and Finite Difference (FD) solver in the right-hand side. Data communication happens once each time step at clearly illustrated.

the viscous heat nor the species diffusion heat flux:

$$\rho\frac{\partial h}{\partial t} + \rho u_\alpha \frac{\partial h}{\partial x_\alpha} = \frac{\partial}{\partial x_\alpha}(\lambda \frac{\partial T}{\partial x_\alpha}), \tag{4.11}$$

other equations can be presented by replacing h and λ with other forms of energy or species mass fraction and diffusion coefficients, respectively, associated with the target transport equation. Note that, the schemes to be demonstrated can be employed also whenever required in the code, e.g. within the LB solver or even when applying the

turbulence SGS model (it contains spatial gradient calculations).

4.5.1 Spatial Discretization

Standard central difference discretization scheme [7] was employed throughout our work to represent the spatial derivatives. The spatial derivatives are discretized as follows:

$\rho u_\alpha \frac{\partial h}{\partial x_\alpha}$: The convection term is treated using an isotropic finite difference scheme, which uses a 19-point stencil (as we use a $D3Q19$ lattice) to estimate the derivative term in three-dimensional space [128, 226]. The lattice description was used to implement the scheme and the isotropic finite difference in lattice units can be introduced as:

$$\rho u_\alpha \frac{\partial h}{\partial x_\alpha} = \rho u_\alpha \left[\frac{1}{c_s^2} \sum_i w_i c_{i,\alpha} h(x_\alpha + c_{i,\alpha}) \right] \tag{4.12}$$

In some scenarios, the isotropic central difference may encounter some stability issues. A simple fixation for this is to combine an up-winding/back-winding scheme alongside the isotropic central one. With a weighting parameter to control the ratio between central and up-winding/down-winding schemes. The upwind/downwind scheme writes:

$$\rho u_\alpha \frac{\partial h}{\partial x_\alpha} = \rho u_\alpha \begin{cases} \frac{h_i - h_{i-1}}{\delta x}, & \text{when} \quad u_\alpha > 0 \\ \frac{h_{i+1} - h_i}{\delta x}, & \text{otherwise} \end{cases} \tag{4.13}$$

where the subscript i is the local grid position and δx is the grid size. Thus, the combination can be realized through the following equation:

$$\rho u_\alpha \frac{\partial h}{\partial x_\alpha} = \sigma^{UP} (\rho u_\alpha \frac{\partial h}{\partial x_\alpha})^{UP} + (1 - \sigma^{UP}) (\rho u_\alpha \frac{\partial h}{\partial x_\alpha})^{CDS}, \tag{4.14}$$

where σ^{UP} is the percentage of up-winding to be used and it has values from zero to unity. The superscript UP and CDS denotes upwind and isotropic finite difference scheme, respectively. Using this formulation allows us to enhance numerical stability. Nonetheless, this comes with the tax of lowering the accuracy as upwind/downwind is a first order scheme, thus, degrading the over all order of accuracy. Upwinding normally introduces numerical diffusion, thus, an attentive care should be given to the amount of upwinding given so as not to affect the solution greatly, specially when dealing with turbulent flows, where turbulent structures might get diffused which might affect the

predicted solution in problems where turbulence is a main actuator in the physics governing the study case. In all the simulations and as a general rule, the values given for upwinding were relatively small $0-10\%$, unless stated otherwise.

$\frac{\partial}{\partial x_\alpha}(\lambda\frac{\partial T}{\partial x_\alpha})$: The diffusion term is estimated also using a central difference scheme that includes three-points stencil in one-dimensional space. The formula can be presented as follows:

$$\frac{\partial}{\partial x_\alpha}(\lambda\frac{\partial T}{\partial x_\alpha}) = \left[\frac{\lambda_{i+1/2}\frac{T_{i+1}-T_i}{\delta x} - \lambda_{i-1/2}\frac{T_i-T_{i-1}}{\delta x}}{\delta x}\right] \tag{4.15}$$

where,

$$\lambda_{i\pm1/2} = \frac{\lambda_i + \lambda_{i\pm1}}{2}. \tag{4.16}$$

Note that the above formulations can be extended to be multi-dimensional. Other potential discretization, such as Lax-Wendroff and Muscle-Hankok schemes can be implemented in the context of the ProLB code [41, 64].

4.5.2 Temporal Discretization

Simple first order Euler time integration is used to compute the temporal derivative term and advance in time, described as follows:

$$\begin{aligned} \frac{\partial h}{\partial t} &= \underbrace{\frac{1}{\rho}\frac{\partial}{\partial x_\alpha}(\lambda\frac{\partial T}{\partial x_\alpha}) - u_\alpha\frac{\partial h}{\partial x_\alpha}}_{\mathcal{RHS}}, \\ h^{(n+1)} &= h^n + \delta t\mathcal{RHS} + \mathcal{O}(\delta t^2), \end{aligned} \tag{4.17}$$

where $n+1$ represents the next time step. It was reported that higher order schemes (e.g. Runge-Kutta) did not provide any considerable enhancements in the accuracy [222]. Consequently, we kept the Euler time integration for all the study cases throughout our work.

4.6 Boundary Conditions

Boundary conditions are one of the most essential aspects when performing numerical simulations. During the computation we require a proper description of the boundary conditions to solve the discretized equations. While defining the boundary conditions

for Navier-Stokes equations is rather simple, it is not that straightforward for LBM, where the inward distribution function to the integration domain need to be determined at the boundaries. Consequently, we need to determine the distribution functions at the boundaries that correspond to the required macroscopic variables. A great care should be given to boundary conditions because it would have an impact on the stability and the accuracy of the solution. In LBM, we can impose the required boundaries via numerous strategies. A popular technique is to directly use the distribution function f_i instead of the standard macroscopic values. There are two types of boundaries as explained in [127], the *link-wise* when the boundary is located on the lattice links alongside the *wet-node* where the boundary is located on the lattice node. For more details and examples on how this can be applied in LBM we refer to [127, 168]. The other strategy is rather simple, which will be used during our work, the boundaries were imposed in the same manner used in standard Navier-Stokes solvers, where we impose directly descriptions linked to macroscopic variables. This could be achieved through applying the boundaries of distribution function by a finite difference reconstruction approach along with the regularization procedure [133, 134]. The desired macroscopic variables are given on the boundary nodes. In addition, the shear stress tensor is computed using the velocity gradients on the boundary nodes. First order FD scheme is used to achieve this. Eventually, these values are used to compute the equilibrium and non-equilibrium function on the missing nodes [67, 69].

The formulation of boundary conditions follows the standard boundary conditions in NS solvers, such as, inlet, outlet, slip wall, non-slip wall or periodic. There are some specificity that will be mentioned at each test case for convenience. Three main types of boundaries can be imposed and utilized: Dirichlet, Neumann and Robin.

1. **Dirichlet**: This boundary imposes a desired value to the targeted macroscopic variable, this could be done directly but it will be harsh, or it can be imposed with taking into account the values of this variable at the nodes near the boundary (by means of interpolation).

2. **Neumann**: This one works rather on the derivative of the variable and imposes the required value for the targeted derivative, the derivative can be approximated using first order or second order FD, we found that first order FD was more stable.

3. **Robin**: It is simply a weighted average between the previous two boundary conditions.

4.7 Low-Mach number approximation

Following the work introduced recently by Wang *et* al. [242] the compressible description of LBM can be adjusted to follow the low-Mach number approximation. The demonstration done here is for the classical athermal (i.e. isothermal) LBM. In the athermal LBM, pressure is just a scaled density,

$$p^{LBM} \equiv \rho c_s^2. \tag{4.18}$$

This pressure is updated each time step following equation 4.3 as follows:

$$\begin{aligned} p^{LBM}(x, t+\delta t) &\equiv c_s^2 \rho(x, t+\delta t) \\ &= c_s^2 \left[\sum_i f_i(x, t+\delta t) - (\rho\theta)(x,t) + \rho(x,t) \right] \\ &\approx p^{LBM}(x,t) - \delta t c_s^2 \frac{\partial \rho u_\alpha}{\partial x_\alpha}(x,t) \\ &= p^{LBM}(x,t) - \delta t \frac{\partial p^{LBM} u_\alpha}{\partial x_\alpha}(x,t) \\ &= p^{LBM}(x,t) - \delta t \left[u_\alpha \frac{\partial p^{LBM}}{\partial x_\alpha}(x,t) - \rho c_s^2 \frac{\partial u_\alpha}{\partial x_\alpha}(x,t) \right]. \end{aligned} \tag{4.19}$$

He *et* al. [93] indicated that under low-Mach number assumption, the equation imitates the acoustic pressure transport, the only difference is that the physical sound speed c in the last term is substituted by the lattice sound speed c_s. This demonstrates that the athermal LBM is in fact an artificial compressibility method where the transport of acoustic pressure fields is modified to suite the time step allowed by the numerical scheme in hand. The extension of the low-Mach number approximation for thermal LBM is now introduced. Note that density gradients can be quite large in low-Mach buoyant plumes, so that the flow dilatation $\partial(\rho u_\alpha)/\partial x_\alpha$ might break the scale balance of Eq. 4.19. For now, the thermal part of the dilatation term $(-\partial\rho/\partial t)$ can be excluded and only apply the "hydrodynamic" part for the hydrodynamic pressure

transport as:

$$\begin{aligned} p^h(x,t+\delta_t) &= p^h(x,t) + c_s^2\Bigg[\sum_i \left\{f_i^{col}(x-c_i\delta t,t) - f_i^{col}(x,t)\right\} \\ &\quad - \rho(x,t+\delta t) - \rho(x,t)\Bigg] \\ &\approx p^h(x,t) - \delta t c_s^2 \frac{\partial(\rho u_\alpha)^h}{\partial x_\alpha} \\ &\approx p^h(x,t) - \delta t\Bigg[u_\alpha \frac{\partial \rho^h c_s^2}{\partial x_\alpha} + \rho^h c_s^2 \frac{\partial u_\alpha}{\partial x_\alpha} \\ &\quad + u_\alpha^h \frac{\partial \rho c_s^2}{\partial x_\alpha} + \rho c_s^2 \frac{\partial u_\alpha}{\partial x_\alpha}\Bigg] \end{aligned} \tag{4.20}$$

In comparison to the theoretical transport equation of the hydrodynamic pressure, the speed of sound is substituted with the lattice sound speed c_s. The stability constraint represented by CFL number is now related to c_s instead of c. Note that we need always to keep a low-Mach property, in other words:

$$\frac{|u|_{max}}{c_s} = \mathrm{Ma} < 0.3, \tag{4.21}$$

Having a mach number lower than 0.3 is the limit beyond which compressibility effect will be significant and the low-Mach number approximation is not valid any more.

Hence, the time step is constraint by the flow maximum velocity and not the speed of sound anymore. Consequently, the time step in the low-Mach solver can be much larger compared to the one of the compressible solver which accelerates the calculation.

Only small modifications to the original algorithm have to be done to take into account the low-Mach number approximation. The reduced temperature under the low-Mach number approximation will be defined as:

$$\theta \equiv \frac{p^h}{\rho c_s^2}. \tag{4.22}$$

The thermodynamic pressure p^{th} is set to be constant, because we are dealing with open system. From which the density is calculated at each time step through our

thermodynamic closure (i.e. equation of state):

$$\rho(x, t + \delta t) = \frac{p^{th}(x, t + \delta t)}{r.T} \tag{4.23}$$

The hydrodynamic pressure p^h, is updated using Eq. 4.20:

$$p^h(x, t+\delta_t) = p^h(x, t)+c_s^2\Big[\sum_i \left\{f_i^{col}(x - c_i\delta t, t) - f_i^{col}(x, t)\right\}-\rho(x, t + \delta t) - \rho(x, t)\Big] \tag{4.24}$$

All in all, the low-Mach algorithm imposes only three major changes compared to the compressible algorithm:

1. Pressure is divided into two part, hydrodynamic p^h and thermodynamic p^{th}. p^h is calculated from the LBM probability distribution function $f_i(x, t)$ (i.e. Eq. 4.20), while p^{th} is constant for open systems.

2. Density is calculated via the equation of state using p^{th}.

3. Hydrodynamic pressure p^h is used to evaluate the equilibrium population, through the modification of θ.

Summary In this chapter we introduced the thermal **HRR**-$\mathcal{P}$ algorithm, how to incorporate energy/species equations and also how to discretize them. In addition, we showed how the algorithm could be slightly modified to include the low-Mach number approximation. Hence, in the next chapter we will validate this algorithm against canonical test cases before addressing the realistic simulations of plumes and fires.

Chapter 5

Numerical model validation

This chapter was a part of the publication:"Taha, M., Zhao, S., Lamorlette, A., Consalvi, J. L., & Boivin, P. (2022). Lattice-Boltzmann modeling of buoyancy-driven turbulent flows. Physics of Fluids, 34(5), 055131."

Contents

In this chapter, the physical model introduced previously will be tested and validated against canonical test cases where buoyancy is involved, mainly 1D pressure column, Rayleigh-Bénard natural convection and the Rayleigh-Taylor instability. Note that the results shown in this chapter are produced using the compressible formulation.

5.1 1-D pressure column

The aim of this test case is to verify that the gravity implementation is able to recover the theoretical pressure column and the applied gravitational acceleration.

5.1.1 Numerical setup

The vertical 1-D domain of a 10 meters height is discretized using uniform 100 cells. In the bottom of the domain, we impose a wall boundary condition, while at the top we impose a pressure outlet boundary condition. The domain is initialized using air at a uniform temperature of $T_0 = 300\,\mathrm{K}$ and a uniform pressure $p_0 = 101\,325\,\mathrm{N\,m^{-2}}$. The simulation will start from the uniform initialization of pressure then the applied gravity field will modify this pressure until it settles on the correct pressure gradient corresponding to the applied gravitational acceleration of $10\,\mathrm{m/\,sec^2}$.

5.1.2 Results

Fig. 5.1 shows the converged pressure profile in comparison to the theoretical famous profile $p(z) = p_0 + \rho g z$ which shows a great agreement. Moreover, the gravity is re-evaluated from the simulation to assure that we got the input value of gravity. The gravity could be calculated knowing the pressure gradient and the density following:

$$\frac{\partial p}{\partial z} = \rho g, \tag{5.1}$$

The same figure (Fig. 5.1) shows the calculated gravity and it matches the input value of $10\,\mathrm{m/\,sec^2}$.

5.2 Rayleigh Bénard

5.2.1 Introduction

The Rayleigh-Benard instability is a configuration involving natural convection and heat transfer [10].

Figure 5.2 depicts the configuration to be simulated. It consists of a square box of dimension $1\,\mathrm{m} \times 1\,\mathrm{m}$ initially filled with quiescent air, and surrounded by adiabatic walls on the left and right, and isothermal top and bottom walls, resp. at $T_C = 299.5\mathrm{K}$ and $T_H = 300.5\mathrm{K}$.

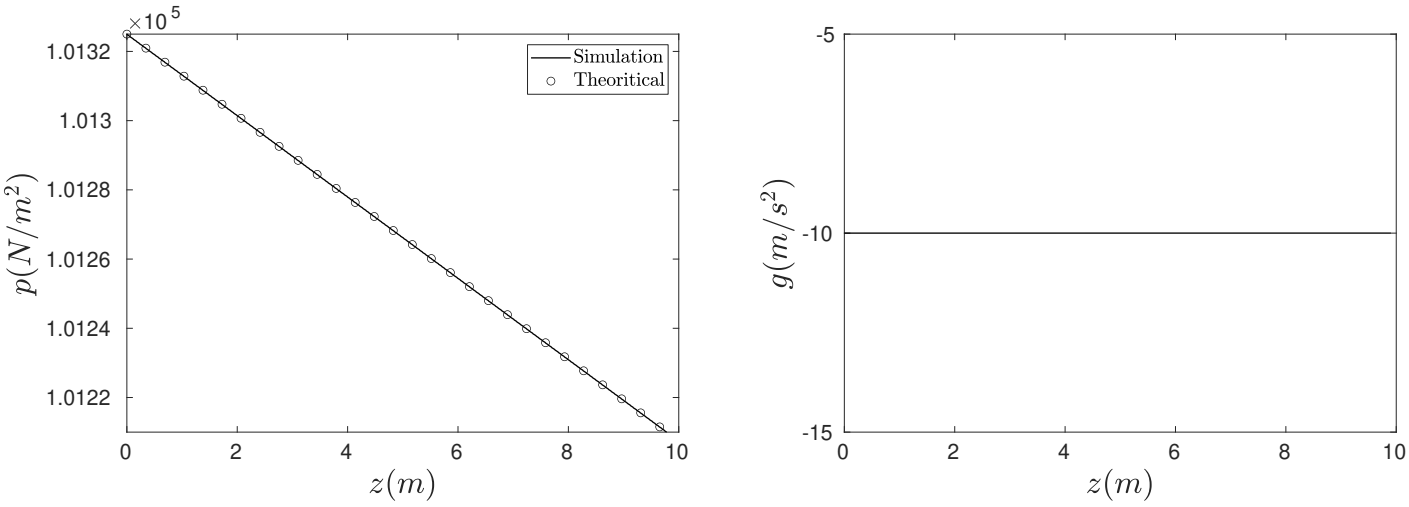

Figure 5.1: 1D gravity pressure column showing: pressure vs altitude (left), and the calculated gravity (right).

The Rayleigh number, Ra, describes, on the one hand, the balance between buoyancy versus viscous forces in the momentum equation and, on the other hand, the balance between conductive versus convective transfer in the energy equation. It is assumed that convective heat transfer takes place with the velocity obtained by the balance in the momentum equation, and it is defined as:

$$\mathrm{Ra} = \frac{g\beta(T_H - T_C)H^3}{\alpha\nu} = \mathrm{Pr}\frac{g\beta(T_H - T_C)H^3}{\nu^2}, \tag{5.2}$$

where $g = 9.81\mathrm{m\,s^{-2}}$ is the gravitational acceleration and $H = 1\,\mathrm{m}$ is the domain size. β is the thermal expansion coefficient that is equal to $1/T_{ref}$ for an ideal gas with isobaric expansion (i.e. at constant pressure). In the present study, T_{ref} is taken equal to T_H. Setting Pr= 0.71, the viscosity can be deduced from the target Rayleigh numbers (Eq. 5.2) of 10^4, 10^5 and 10^6, while the thermal conductivity, λ, in the energy equation is obtained from Eq. (2.36).

5.2.2 Numerical setup

The domain is discretized with a uniform grid with 256×256 cells. The flow is then uniformly initialized as $u_0 = 0$, $T_0 = 300\mathrm{K}$, $\rho_0 = 1.2\,\mathrm{kg\,m^{-3}}$, and $p = p_0 + \rho_0 g y$. The simulation is then carried out until convergence using a time-step, $\delta t = 6.5 \times 10^{-6}\,\mathrm{s}$.

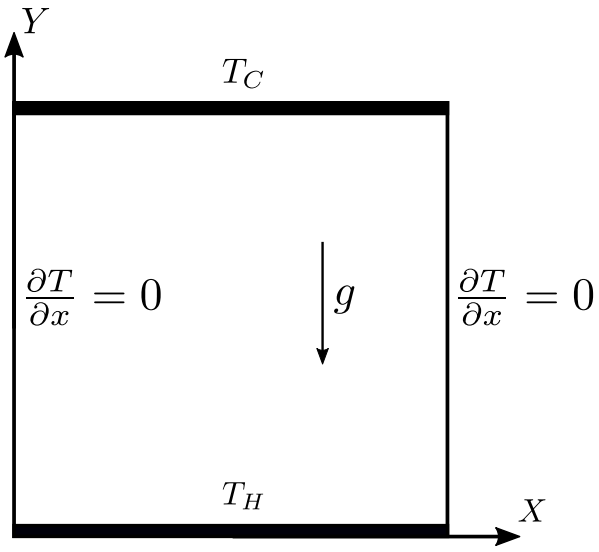

Figure 5.2: Schematic of Rayleigh Benard test case

5.2.3 Results

Figure 5.3 presents temperature contours as well as streamline patterns, showing a good qualitative agreement with the literature (see [184], e.g.): for $\mathrm{Ra} = 10^4$, the flow is symmetric and dominated by the recirculation in the core region with small eddies near the corner. When increasing the Rayleigh number, secondary eddies near the top left and bottom right corners appear and become larger.

The quantitative agreement is shown in Fig.5.4, presenting velocity profiles along the centerlines. The present numerical results are compared with the benchmark solution provided by Ouertatani *et* al. [184]. For further validation, the local Nusselt number Nu is calculated at the bottom wall as:

$$\mathrm{Nu} = \left.\frac{\partial T}{\partial y}\right|_{y=0}. \tag{5.3}$$

It can be observed that both velocity and Nusselt number profiles are in excellent agreement with the reference solutions.

5.3 Rayleigh Taylor

5.3.1 Introduction

The Rayleigh-Taylor instability is another classical test case for buoyancy-driven flows due to its practical and fundamental importance. It was investigated extensively in the

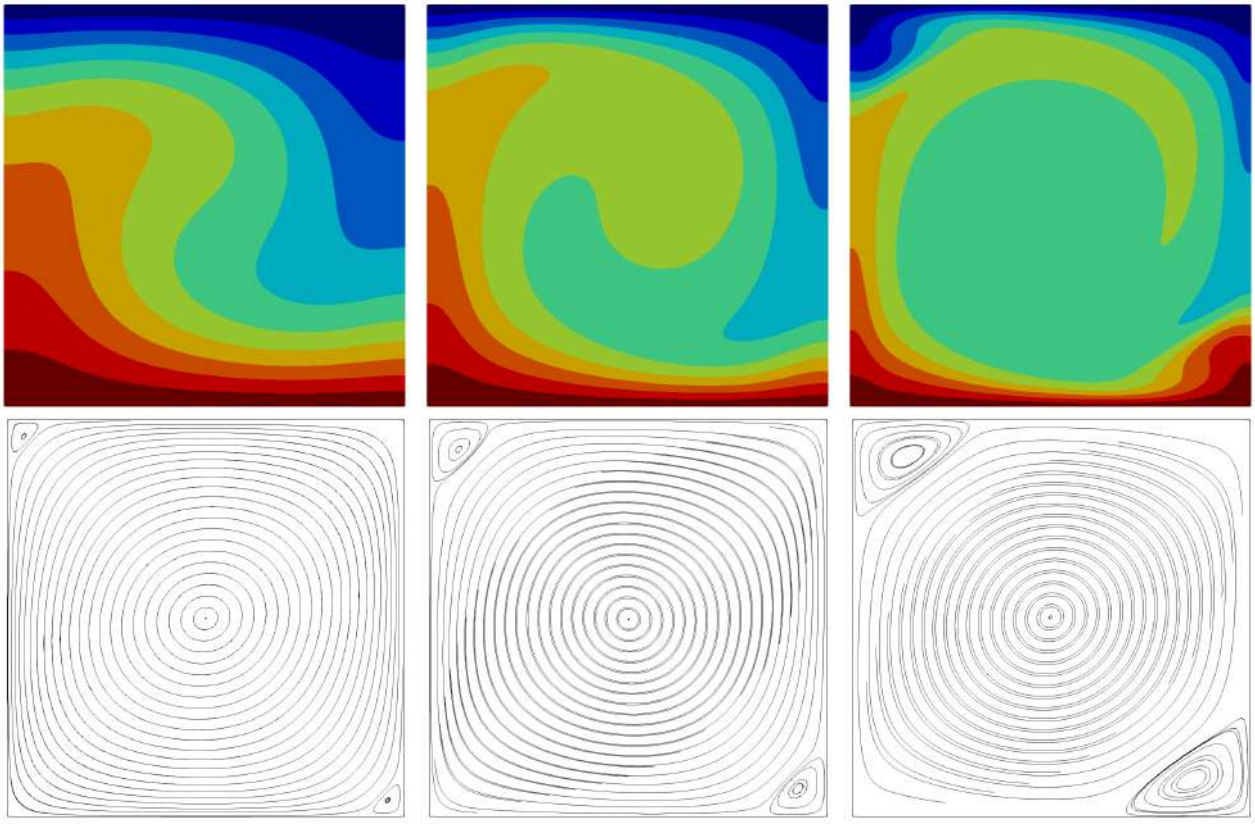

Figure 5.3: Rayleigh-Benard instability: Temperature contours (top) and streamlines (bottom), for three Rayleigh numbers (10^4, 10^5, 10^6), from left to right.

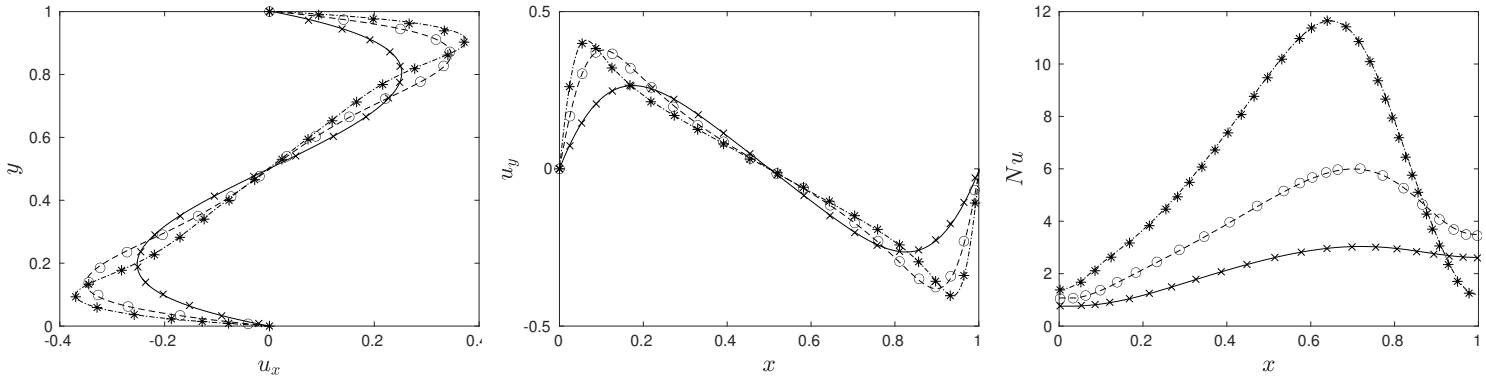

Figure 5.4: Rayleigh-Benard instability. u_x along the vertical centerline, u_y along the horizontal centerline, and Nusselt number along the bottom wall (from top to bottom), for Ra=10^4 (solid), Ra=10^5 (dashed) and Ra=10^6 (dot-dashed). Symbols indicate the reference data [184]

.

literature by different numerical methods [38, 54, 86, 94, 96, 103, 136, 137, 234, 269]. It consists of two layers of fluids of different densities (ρ_H, ρ_L) at rest under gravitational

field, as illustrated in Fig. 5.5.

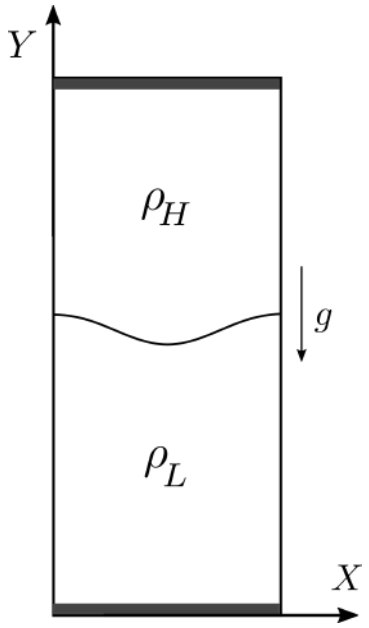

Figure 5.5: Schematic of Rayleigh Taylor instability.

The dynamics of this problem is governed by the Atwood (At) and Reynolds (Re) numbers:

$$\mathrm{At} = \frac{\rho_H - \rho_L}{\rho_H + \rho_L}, \qquad \mathrm{Re} = \frac{U^* L_x}{\nu}, \tag{5.4}$$

where L_x is the dimension of the domain in the horizontal direction and $U^* = \sqrt{gL_x}$ is a reference velocity.

5.3.2 Numerical setup

The investigated configuration was previously studied in the literature [38,94,103] with two target Reynolds numbers of 256 and 2048. The domain size is $L_x \times 4L_x$, discretized with 256×1024 (fine mesh) or 128×512 grid points (coarse mesh). The heavy (index H) and light (index L) fluids are initially separated by a perturbed interface given by the following equation:

$$y_i(x) = \frac{L_x}{10} \cos\left(\frac{2\pi x}{L_x}\right) + 2L_x \tag{5.5}$$

The fluids initial densities are set to $\rho_H = 3\,\mathrm{kg\,m^{-3}}$ and $\rho_L = 1\,\mathrm{kg\,m^{-3}}$, corresponding to At=0.5. The pressure was initialized to account for the gravity field as follows:

$$p = \begin{cases} p_0 + \rho_L g y, & 0 \le y \le y_i(x) \\ p_0 + \rho_L g y_i(x) + \rho_H g (y - y_i(x)), & y_i(x) < y \end{cases} \tag{5.6}$$

where p_0 is the pressure at $y = 0$. Finally, the domain size and gravity are set to $L_x = 0.25\text{m}$ and $g = 20\text{m}\,\text{s}^{-2}$. The fluid viscosity is obtained from the target Reynolds numbers of 256 and 2048.

5.3.3 Results

Figure 5.6 represents the density contours obtained for the two Reynolds numbers of 256 and 2048 using the finer mesh. The diagrams of the right of the figure represents the time evolution of the bubble and spike positions. Numerical predictions are compared to reference numerical simulation [94], showing an excellent agreement.

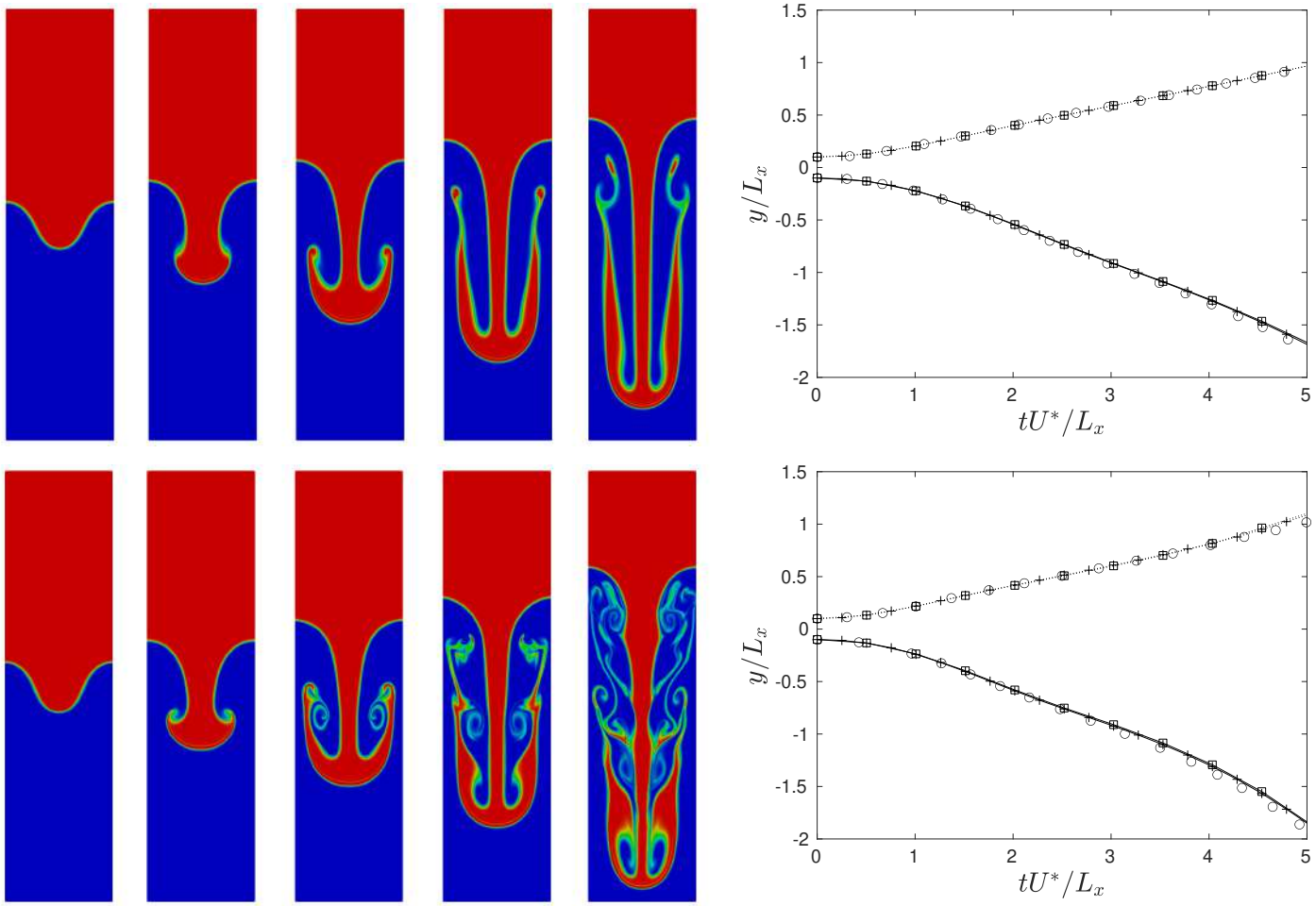

Figure 5.6: Rayleigh-Taylor instability for Re = 256 (top) and Re = 2048 (bottom). Left: Density contours at different normalized times $t.U^*/L = 1, 2, 3, 4, 5$ obtained for the fine mesh. Right: time evolution of the position of both bubble (solid) and spike dashed). (□) indicates the coarse mesh, (+) for the fine mesh, and (∘) for the reference from He *et* al. [94].

To investigate the robustness of the method, simulations were carried out on the coarser mesh. An excellent agreement is also obtained with a maximum error less than 2%.

5.4 Concluding remarks

In this chapter we validated the integrity of our solver including the gravitational forcing term through multiple canonical test cases:

- The 1-D pressure column test case validated the capability of our solver to predict the correct drop of pressure due to elevation because of gravity.
- The 2-D Rayleigh-Bénard test case elaborates the equilibrium between buoyancy, viscosity and heat transfer where the velocity profiles and Nusselt number were validated against reference data over a range of Rayleigh number Ra.
- The unsteady 2-D Rayleigh-Taylor instability test case was run for two different Reynolds numbers Re using different mesh resolutions. The temporal evolution of the positions for the spike and the bubble was in a good agreement with the reference data.

All the above concludes the validity of our model to be capable of taking into account the gravity force and that the code showed robustness by being tested against multiple test cases mainly driven by gravity. It is worth mentioning that the test cases were also validated using the low-Mach number formulation but were not presented. Next, a large eddy simulation of a forced plume will be introduce as our first real physical simulation with the aim to study the far-field behaviour and characteristics of plumes.

Chapter 6

Large Eddy Simulation

"Big whirls have little whirls that feed on their velocity, And little whirls have lesser whirls and so on to viscosity " ***-Lewis Fry Richardson***

Contents

6.1 Introduction

In the previous chapter we successfully implemented and validated the gravity source term in the context of our LBM pressure-based numerical model. The next step is to apply the model to simulate buoyancy-driven flows characteristics of unwanted fires. A fire plumes can be conceptually divided into two regions: 1) the far-field zone where the impact of the source vanishes and buoyancy becomes the main driving force that controls the dynamics of the flow, and 2) the near-field zone where the dynamics is governed by instabilities that grow to generate turbulent structures. In this chapter, the basis of turbulence and of large eddy simulations (LES) that will be used hereafter to simulate fire plumes are presented.

6.2 Turbulence: Kolmogorov Hypothesis

The vast majority of flows encountered in engineering application becomes unstable beyond a certain Reynolds number Re. This non-dimensional number determines whether the flow is laminar or turbulent and compares the inertial to viscous forces and defined as:

$$\mathrm{Re} = \frac{\text{Inertial force}}{Viscous force} = \frac{\rho u L}{\mu} = \frac{uL}{\nu} \tag{6.1}$$

where u and L are the characteristic velocity and length, respectively. Low Reynolds numbers flows are laminar while higher Reynolds numbers flows are observed to be turbulent, in other words, a chaotic and random motion develops in which the velocity and pressure are time dependent within the flow. Fluid particles which are initially separated by a long distance can be brought close together by the eddies (i.e. vortices) existing in turbulent flows. Hence, mass, momentum, heat are exchanged and mixed.

The theory of turbulence introduced by Kolmogorov [122] states that the turbulent kinetic energy transfers from the large scales (i.e. eddies) to the small scales. This process is know as *Energy Cascade* and occurs until it reaches the smallest length scale l_η named Kolmogorov length scale defined as:

$$l_\eta = (\nu^3/\epsilon)^{1/4}, \tag{6.2}$$

where ν is the kinematic viscosity and ϵ is the dissipation rate of the turbulent kinetic energy. The length l_η can be seen as the smallest dimension of the structures of eddies that can be encountered in a turbulent flow. Below this scale, no mechanical energy subsists as it is transformed into thermal energy (i.e. heat) due to the molecular viscosity. Hence, the eddies of length l_η are uniquely defined by the rate of energy dissipation ϵ and the fluid viscosity. The corresponding Kolmogorov time scale can be defined as:

$$\tau_\eta = l_\eta/u_\eta = \nu^{1/2}\epsilon^{-1/2}, \tag{6.3}$$

where $u_\eta = (\epsilon\nu)^{1/4}$ is the velocity scale associated with the dissipative eddies having the length of l_η. Hence, the Reynolds number associated with l_η and u_η reads:

$$\mathrm{Re}_\eta = \frac{l_\eta u_\eta}{\nu} = 1, \tag{6.4}$$

According to Bailly and Comte-Bellot [9] the dissipation rate ϵ was proven experi-

mentally to be:

$$\epsilon = \frac{u'^3}{L_f} \tag{6.5}$$

where u' is the fluctuations and L_f is the integral length scale [1]. This shows that dissipation is in reality set by large structures represented by the two quantities u' and L_f. Small structure must adapt themselves to the amount of energy to be dissipated. As a consequence, small structures are finer for smaller molecular viscosity. It appears that the are two types of scales. One scale which contains the kinetic energy of the flow while the other represented by the smallest structures of the flow, whose associated velocity, time, length scales are summarized below.

$$\text{Eddies bearing kinetic energy} \begin{cases} u' \quad \text{(velocity)} \\ L_f \quad \text{(length)} \\ L_f/u' \ \text{(time)} \end{cases} \qquad \begin{cases} k_t \sim u'^2 \\ \epsilon \sim \frac{u'^3}{L_f} \end{cases}$$

$$\text{Smallest dissipative scales} \begin{cases} u_\eta = \nu^{1/4}\epsilon^{1/4} \ \text{(velocity)} \\ l_\eta = \nu^{3/4}\epsilon^{-1/4} \ \text{(length)} \\ \tau_\eta = \nu^{1/2}\epsilon^{-1/2} \ \text{(time)} \end{cases} \qquad \text{Re}_\eta = \frac{l_\eta u_\eta}{\nu} = 1$$

Hence, Kolmogorov hypothesis [122] described the energy spectrum (for small structures assuming that they contain homogeneous isotropic turbulence HIT) as:

$$E(k) \sim \epsilon^{2/3} k^{-5/3}, \tag{6.6}$$

where k is the wave number associated with the length scale l, $k = 2\pi/l$. This expression was also confirmed experimentally as seen in Fig. 6.1, the expression holds independently from the flow type or the Reynolds number as long as it large enough.

The subject of correctly describing turbulence in numerical simulations is still a challenging research topic because of the associated necessity to compromise between

[1] This is the large length scale where no dissipation appears and it only transfers kinetic energy to the smaller structures which in turn dissipate this energy via viscosity.

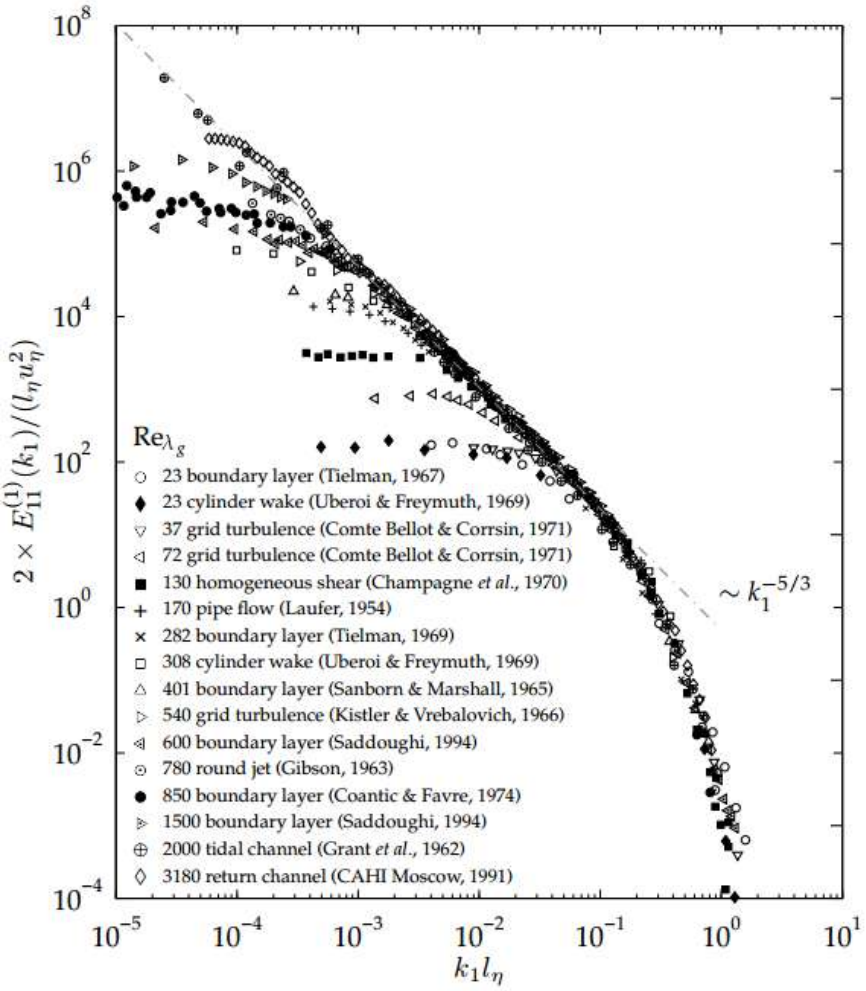

Figure 6.1: Universal equilibrium of spectra for small structures. The figure deals with the one-dimensional spectrum $E_{11}^1 = (k_1)/(l_\eta u_\eta^2)$. Data are collected from many experiments. For all the curves, the emergence of an inertial subrange towards smaller k_1 with increasing Reynolds number is observed. Figure from [9]

cost and accuracy. Now, we will briefly mention the different techniques to simulate turbulent flows as well as the pros and cons for each one of them.

6.3 Computational methods

The choice of the computation technique to be used depends on the requirement of the simulation, the compromise between cost and precision is the main factor leading this decision.

Direct Numerical Simulation (DNS)

Direct Numerical Simulation (DNS) consists in solving the Navier-Stokes equations with a sufficiently high spatial and temporal resolutions in order to capture the smallest turbulent eddies and the fastest fluctuations. The task is excessively time consuming as all the scales forming the turbulent kinetic energy spectrum must be computed. The range of length scales to be covered can be estimated by taking the integral length scale L_f to characterize the larger scales and the Kolmogorov scale l_η to characterize the smaller ones, and then writing the ratio:

$$\frac{L_f}{l_\eta} \sim \frac{L_f}{\nu^{3/4}\epsilon^{-1/4}} \sim \frac{L_f}{\nu^{3/4}(u'^3/L_f)^{-1/4}} \sim \mathrm{Re}_{L_f}^{3/4} \tag{6.7}$$

where $\mathrm{Re}_{L_f} \equiv u' L_f/\nu$. This ratio is proportional to the number of points necessary to build the mesh grid in one direction. The total number of mesh points N_p required to describe all the scales involved in a turbulent spectrum is thus directly linked to the Reynolds number, and more precisely in three dimensions is proportional to:

$$N_p \propto \mathrm{Re}_{L_f}^{9/4}, \tag{6.8}$$

Although the computational resources have evolved during the past decades [14, 21] as shown in Fig. 6.2, it remains extremely expensive to perform DNS for problems with high Reynolds number. For example, in industrial application where high Reynolds number flow are involved, a flow with $\mathrm{Re} \approx 10^5$ will require a mesh with $N_p \approx 10^{11}$ points.

However, DNS can provide comprehensive views of turbulence dynamics, instantaneous results can be generated that are not measurable with instrumentation, and instantaneous turbulence structures can be visualized and probed. For example, pressure–strain correlation terms in Reynolds stress models (RSM) turbulence closure cannot be measured, but accurate values can be computed from DNS. It is also instrumental in validating turbulence models in academic configurations.

Large Eddy Simulation

In Large Eddy Simulation (LES) the equations are obtained via spatial filter applied to the Navier-Stokes conservation equations. Consequently, only the largest scales of the turbulent flow are resolved while the smaller scales dropped by the filter must be taken into account through employing sub-grid models. The number of points required then can be reduced and the constraint of Eqn. 6.8 can thus be relaxed. Many sub-grid

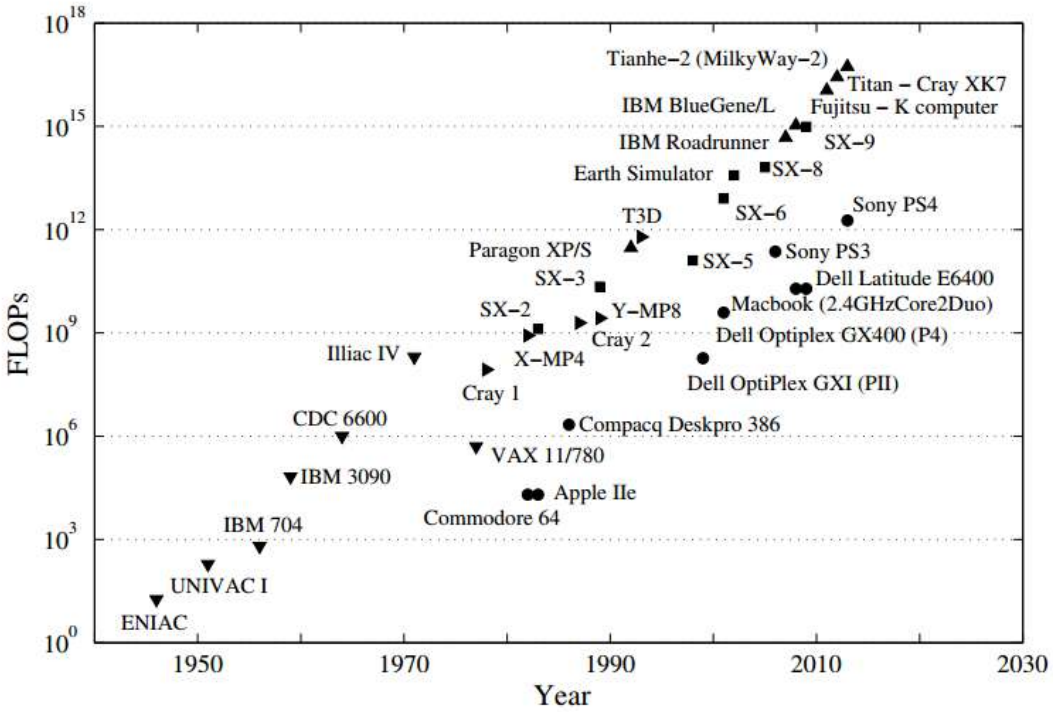

Figure 6.2: Evolution of computational power through time measured by FLOPs (floating point operations per second).Figure from [9], data from [124, 182].

models can be found in the literature; Sagaut [204] provided more details about the different models and their characteristics and classified turbulence models as *functional* or *structural*.

- **Functional models:** they correctly take into account the level of the energy transfers between the resolved scales and the sub-grid modes. However, they do not focus on modelling the sub-grid terms but only their effects (e.g. diffusion or dissipation effects). Consequently, the prediction of the sub-grid structure (i.e. its eigenvectors) is quite poor.

- **Structural models:** The models are based on the scale-similarity hypothesis and globally well predict the structure of the sub-grid shear stress tensor, but are less efficient for dealing with the level of the energy transfers.

And here arises an interest of *mixed* sub-grid models that have good performance on both structural and energy levels. This is done by combining a sub-grid viscosity model for representing the energy cascade mechanism with a scale similarity. The backward cascading (i.e. back-scatter) is implicitly included by the structural model, so there is no need to model such a phenomena when using mixed models.

Reynolds Averaged Navier Stokes (RANS)

In RANS, the mean flow is studied, and the effect of turbulence on the mean flow properties is considered. In this context, the Navier-Stokes equations are averaged in time. When performing time average on the flow equations (or Reynolds average), additional terms appear due to the interaction between different turbulent fluctuations. Those terms are modeled with classical turbulence models, among the most known are the $k-\omega$, $k-\epsilon$ and the Reynolds tress model. In those models, additional transport equations are solved along the Reynolds averaged equations to get the additional terms presenting due to the averaging process. The computing resources required for this type of simulations are modest and, as such, they are widely used in the engineering flow calculations.

Detached Eddy simulations

When dealing with problems requiring a good resolution of the turbulent boundary layer, the calculation cost becomes problematic. Based on the fact that the velocity field at this region can represented better by RANS solutions. A hybrid method called Detached Eddy Simulation (DES) was introduced by Spalart *et* al. [212]. This approach combines the two techniques and benefits from the advantages of both. LES would be applied to the regions that are "Detached" from the wall and reproduce the turbulent structure in the main flow, while the solver shifts to RANS near the walls producing the averaged solution of the boundary layer. This method is advantageous as it requires lower computational resources than pure LES. Nonetheless, it remains more demanding than pure RANS as the grid requires to be sufficiently fine to resolve the turbulent structures in certain regions.

Figure 6.3 depicts the modelling vs resolved scales by each simulation strategies. While RANS models all the turbulence structures, DNS resolves all of them. LES resolves most of the scales and models the rest.

Each of the mentioned strategies have associated pros and cons and can be employed depending on the requirements of the application, in the present thesis, the LES is adopted and the governing equations are demonstrated in the next section.

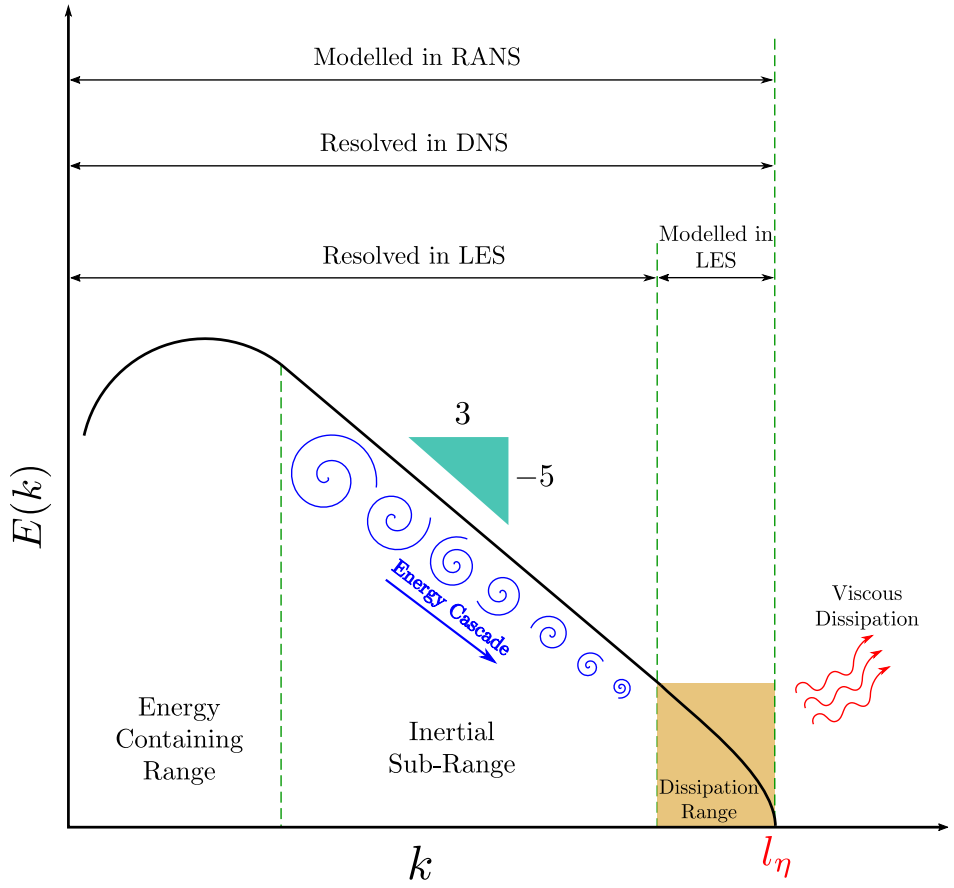

Figure 6.3: Schematic showing the energy spectrum E as a function of the wave number $k = 2\pi/l$ where l is the eddy length scale. The cascade of energy between different scales is also demonstrated.

6.4 Large Eddy Simulation

6.4.1 Filtered Navier-Stokes Equations

The governing equations of LES are deduced from the instantaneous equations of NS through filtering. The filtered quantity $\overline{f}$ are obtained by:

$$\overline{f}(x) = \int f(x')F(x - x')dx', \tag{6.9}$$

where F is the LES filter. The most common filters are the cut-off filters in the spectrum space, box and Gaussian in physical space [191]. After filtering the quantity f can be expressed by its mean value $\overline{f}$ and the residual f' as:

$$f = \overline{f} + f', \tag{6.10}$$

For variable density flows, Favre average can be introduced:

$$\overline{\rho}\widetilde{f}(x) = \int \rho f(x')F(x-x')dx', \qquad \widetilde{f}(x) = \frac{\overline{\rho f}}{\overline{\rho}}, \tag{6.11}$$

For LES simulation, Favre-filtered Navier-Stokes equations are solved, the filtered conservation equations for mass, momentum, species and enthalpy, of compressible multispecies non-reactive flows, are[2]:

$$\textbf{Mass: } \frac{\partial \overline{\rho}}{\partial t} + \frac{\partial \overline{\rho}\widetilde{u}_\alpha}{\partial x_\alpha} = 0, \tag{6.12}$$

$$\textbf{Momentum: } \frac{\partial \overline{\rho}\widetilde{u}_\alpha}{\partial t} + \frac{\partial(\overline{\rho}\widetilde{u}_\alpha\widetilde{u}_\beta + \delta_{\alpha\beta}\overline{p})}{\partial x_\beta} = \frac{\partial \overline{\Pi_{\alpha\beta}}}{\partial x_\beta} + \overline{\rho}F_\alpha - \frac{\partial \tau^{sgs}_{\alpha\beta}}{\partial x_\beta}, \tag{6.13}$$

$$\textbf{Enthalpy: } \overline{\rho}\frac{\partial \widetilde{h}}{\partial t} + \overline{\rho}\widetilde{u}_\alpha\frac{\partial \widetilde{h}}{\partial x_\alpha} = -\frac{\partial \overline{q_\alpha}}{\partial x_\alpha} + \overline{\Pi_{\alpha\beta}}\frac{\partial \widetilde{u}_\alpha}{\partial x_\beta} - \frac{\partial Q^{sgs}_\alpha}{\partial x_\alpha}, \tag{6.14}$$

$$\textbf{Species: } \overline{\rho}\frac{\partial \widetilde{Y}_k}{\partial t} + \overline{\rho}\widetilde{u}_\alpha\frac{\partial \widetilde{Y}_k}{\partial x_\alpha} = -\frac{\partial}{\partial x_\alpha}(\overline{\rho Y_k V_{k,\alpha}}) - \frac{\partial J^{sgs}_{k,\alpha}}{\partial x_\alpha}. \tag{6.15}$$

Once again this system of equations needs a thermodynamic closure represented by the equation of state (assuming perfect gas) to link between the filtered pressure, density and temperature:

$$\overline{p} = \overline{\rho}\frac{\mathcal{R}}{\widetilde{\mathcal{W}}}\widetilde{T}, \tag{6.16}$$

The $\widetilde{u_\alpha} = \overline{\rho u_\alpha}/\overline{\rho}$, $\widetilde{h} = \overline{\rho h}/\overline{\rho}$ and $\widetilde{Y} = \overline{\rho Y}/\overline{\rho}$ are the Favre-filtered velocity, enthalpy and mass fraction, respectively. $\tau^{sgs}_{\alpha\beta} = \overline{\rho u_\alpha u_\beta} - \overline{\rho}\widetilde{u}_\alpha\widetilde{u}_\beta$ is the subgrid scale Reynold stress tensor, $Q^{sgs}_\alpha = \overline{\rho h u_\alpha} - \overline{\rho}\widetilde{h}\widetilde{u}_\alpha$ is the subgrid scale heat flux and $J^{sgs}_{k,\alpha} = \overline{\rho Y u_\alpha} - \overline{\rho}\widetilde{Y}\widetilde{u}_\alpha$ is the subgrid scale of species flux. $\overline{\Pi_{\alpha\beta}}$ is the filtered shear stress tensor given by:

$$\overline{\Pi_{\alpha\beta}} = \overline{\mu}\left(\frac{\partial \widetilde{u}_\alpha}{\partial x_\beta} + \frac{\partial \widetilde{u}_\beta}{\partial x_\alpha} - \delta_{\alpha\beta}\frac{2}{3}\frac{\partial \widetilde{u}_\gamma}{\partial x_\gamma}\right). \tag{6.17}$$

[2]The low-Mach number approximation can be simply introduced similar to Sec. 2.6.

$\overline{q_\alpha}$ is the filtered heat flux given by:

$$\overline{q_\alpha} = -\overline{\lambda}\frac{\partial \widetilde{T}}{\partial x_\alpha} + \sum_{k=1}^{N_{sp}} \overline{\rho Y_k V_{k,\alpha}}\widetilde{h_k} \qquad \text{with} \qquad \overline{\lambda} \approx \frac{\mu \overline{C_p(\widetilde{T})}}{\mathrm{Pr}} \tag{6.18}$$

$\overline{\rho Y_k V_{k,\alpha}}$ is the filtered species diffusion flux expressed by:

$$\overline{\rho Y_k V_{k,\alpha}} = -\overline{\rho}\overline{\mathcal{D}}_k \frac{\mathcal{W}_k}{\widetilde{\mathcal{W}}}\frac{\partial \widetilde{X}_k}{\partial x_\alpha} + \overline{\rho}\widetilde{V}_\alpha^c \widetilde{Y}_k, \tag{6.19}$$

where $\widetilde{V}_\alpha^c$ is the correction velocity to ensure the conservation of mass expressed as:

$$\widetilde{V}_\alpha^c = \sum_k^{N_{sp}} \overline{\mathcal{D}}_k \frac{\mathcal{W}_k}{\widetilde{\mathcal{W}}}\frac{\partial \widetilde{X}_k}{\partial x_\alpha} \qquad \text{with} \qquad \overline{\mathcal{D}}_k = \frac{\overline{\mu}}{\overline{\rho}\mathrm{Sc}_k}, \tag{6.20}$$

The unknown subgrid scale terms $\tau_{\alpha\beta}^{sgs}$, Q_α^{sgs} and $J_{k,\alpha}^{sgs}$ require closure models, those models are called turbulence models, our turbulence model will be introduced next.

6.4.2 Sub-grid scale stress tensor modelling

The most famous closures for the subgrid scale Reynold stress tensor $\tau_{\alpha\beta}^{sgs}$ are based on the concept of turbulent viscosity, named *Boussinesq's hypothesis*. The Reynold stress tensor is then given by:

$$\tau_{\alpha\beta}^{sgs} = \mu_t \left(\frac{\partial \widetilde{u}_\alpha}{\partial x_\beta} + \frac{\partial \widetilde{u}_\beta}{\partial x_\alpha} - \delta_{\alpha\beta}\frac{2}{3}\frac{\partial \widetilde{u}_\gamma}{\partial x_\gamma} \right), \tag{6.21}$$

where $\mu_t = \overline{\rho}\nu_t$ is the turbulent viscosity. Applying the subgrid-scale model numerically comes down to modifying the viscosity μ through the addition of the turbulent viscosity μ_t. Many models can be found in the literature such as the Smagorinsky model [211], the dynamic Smagorinsky model [82], the Sigma model [176], the WALE model [58] and the Vreman model [241].

Smagorinsky model

The Smagorinsky model [211] belongs to the functional models family (see Sec. 6.3). This model is based on the assumption that the Reynolds number is sufficiently high to ensure that energy is transferred from the large to the small scales, which are responsible for dissipation only, and do not transfer any energy. Also it assumes that

turbulence energy generation and dissipation are locally equal (i.e. in equilibrium). It is constructed by a length scale term, a time scale length, and a dimensionless constant C_s called Smagorinsky constant. The turbulent viscosity μ_t is calculated through:

$$\mu_t = \rho(C_s\Delta_m)^2\left|\widetilde{S}\right|, \tag{6.22}$$

where Δ_m is the local mesh size, and $\left|\widetilde{S}\right|$ is the filtered rate of stress tensor written as:

$$\left|\widetilde{S}\right| = \sqrt{2\widetilde{S}_{\alpha\beta}\widetilde{S}_{\alpha\beta}}. \tag{6.23}$$

with $\widetilde{S}_{\alpha\beta}$ defined as:

$$\widetilde{S}_{\alpha\beta} = \frac{1}{2}(\frac{\partial\widetilde{u_\alpha}}{\partial x_\beta} + \frac{\partial\widetilde{u_\beta}}{\partial x_\alpha}), \tag{6.24}$$

The Smagorinsky model exhibits some limitations listed below:

- C_s is a predefined input to the simulation, this constant can not represent correctly various turbulent flows.
- The eddy viscosity does not vanish for pure shear flows nor near-wall regions.
- The backscatter of energy from small scale to large scale is prevented since:

$$(C_s\Delta_m)^2\sqrt{2S_{\alpha\beta}S_{\alpha\beta}} \geq 0 \tag{6.25}$$

- Smagorinsky model is considered too much diffusive.

Vreman model

Vreman eddy-viscosity subgrid scale model was introduced to rectify the drawbacks of the Smagorinsky model [241]. Applying the subgrid-scale model numerically comes down to modifying the viscosity μ through the addition of a turbulent viscosity μ_t obtained as:

$$\mu_t = \rho C\sqrt{\frac{B_j}{\alpha_{\alpha\beta}\alpha_{\alpha\beta}}}, \tag{6.26}$$

with

$$\alpha_{\alpha\beta} = \frac{\partial u_\beta}{\partial x_\alpha}, \tag{6.27}$$

$$\beta_{\alpha\beta} = \Delta_m^2 \alpha_{m\alpha}\alpha_{m\beta}, \tag{6.28}$$

$$B_j = \beta_{11}\beta_{22} - \beta_{12}^2 + \beta_{11}\beta_{33} - \beta_{13}^2 + \beta_{22}\beta_{33} - \beta_{23}^2, \tag{6.29}$$

The constant C is related to the Smagorinsky constant C_s as $C = 2.5C_s^2$. Δ_m is the local mesh size in direction m. The model is simple to implement and compute as it only requires the local filter width (i.e. mesh size) and the first order derivatives of the velocity field.

6.4.3 Sub-grid scale heat and species fluxes

Similarly, the subgrid heat flux Q_j^{sgs} can be modelled in analogy with *Boussinesq's hypothesis* as follows:

$$Q_\alpha^{sgs} \approx -\overline{\lambda}_t \frac{\partial \widetilde{T}}{\partial x_\alpha} + \sum_{k=1}^{N_{sp}} \overline{\rho Y_k V_{k,\alpha}}^{sgs} \widetilde{h}_k, \tag{6.30}$$

where $\overline{\lambda}_t$ is the turbulent heat conductivity that can be linked to the turbulent viscosity μ_t through Pr_t as:

$$\overline{\lambda}_t \approx \frac{\mu_t \overline{C_p(\widetilde{T})}}{\mathrm{Pr}_t} \tag{6.31}$$

The value of turbulent Prandtl number Pr_t can be found experimentally and it depends on the flow type and condition [120]. Finally, the subgrid species flux $J_{k,\alpha}^{sgs}$ will be introduced as:

$$J_{k,\alpha}^{sgs} = -\overline{\rho}\overline{\mathcal{D}}_{k,t} \frac{\mathcal{W}_k}{\widetilde{\mathcal{W}}} \frac{\partial \widetilde{X}_k}{\partial x_\alpha} + \overline{\rho}\widetilde{V}_{\alpha,t}^c \widetilde{Y}_k, \tag{6.32}$$

where $\widetilde{V}_{\alpha,t}^c$ is the correction velocity of the subgrid species flux introduced as:

$$\widetilde{V}_{\alpha,t}^c = \sum_k^{N_{sp}} \overline{\mathcal{D}}_{k,t} \frac{\mathcal{W}_k}{\widetilde{\mathcal{W}}} \frac{\partial \widetilde{X}_k}{\partial x_\alpha} \tag{6.33}$$

and $\overline{\mathcal{D}}_{k,t}$ is the turbulent species diffusion coefficient expressed as:

$$\overline{\mathcal{D}}_{k,t} = \frac{\overline{\mu_t}}{\overline{\rho}\mathrm{Sc}_{k,t}}, \tag{6.34}$$

where $\mathrm{Sc}_{k,t}$ is the turbulent Schmidt number can be found experimentally and its value depends on the flow nature [231].

Summary Having introduced the filtered equations and the SGS closures which are necessary to perform LES, the next chapters will demonstrate the direct application of these equations using Large eddy simulations of buoyant plumes.

Chapter 7

Application to forced plumes

This chapter was a part of the publication:"Taha, M., Zhao, S., Lamorlette, A., Consalvi, J. L., & Boivin, P. (2022). Lattice-Boltzmann modeling of buoyancy-driven turbulent flows. Physics of Fluids, 34(5), 055131."

Contents

7.1 Introduction

In Chapter 5 we were able to validate and verify our solver over multiple canonical test cases. In the present chapter, the far-field region of a forced plume is studied to evaluate the capacity of our solver to reproduce the characteristics of this zone. The CFD modelling of forced plumes was a very active research area. A significant amount of Reynolds-Averaged Navier-Stokes simulations were reported with different formulations of the k-ϵ model [22, 174, 237, 259]. On the other hand, Zhou *et* al. [267] and Yan [265] showed the capability of Large Eddy Simulation (LES) to predict well the self-preserving and spreading of the plume. LES of forced jet were also performed [185] to evaluate the energy-consistent approach for modelling entrainment rate coefficient, α, developed by Kaminski *et* al. [116] and van Reeuwijk and Craske [238]. Direct numerical simulation (DNS) and LES of thermal plumes were also reported [11,31,189,190]. These studies focused mainly on the generation and growth of buoyancy-induced instabilities in the near field that governs the transition from laminar to turbulence. In particular, it was shown that these instabilities have to be fully resolved to capture the dynamics of such purely buoyant thermal plumes [189]. In addition, the DNS was found in good agreement with experimental data in the far field [190].

7.2 Experimental setup

Many experiments were conducted to study and explore thermal buoyant plumes, so first we introduce the experiment of Shabbir and George [207] with whom we mainly compare our results.

7.2.1 Facility

The plume source consists of two bronze discs heated by eight electric heaters (1500 W Watlow fire cartridges). Compressed air was first passed via those heated discs, and then through a set of screens, before being ejected through a 12 : 1 contraction ratio nozzle, this produced a uniform exit velocity profile outside the wall boundary layer. Under usual operating conditions, two hours were necessary for the plume generator to attain thermal equilibrium. Nonetheless, the gathering of the data did not start until the plume had been running for around four hours to ensure the global statistic equilibrium of the environment. The deviation of the temperature at the exit was in the order of magnitude of $\pm 1\,\mathrm{K}$ over the period of the experiment compared to the nominal operating temperature of 568 K.

The plume facility is depicted in Fig. 7.1, the room dimensions containing the experimental facility were $6\,\mathrm{m} \times 6\,\mathrm{m} \times 10\,\mathrm{m}$ and it was completely closed for the whole duration of the experiment to prevent any kind of unconsidered flow disturbances which might arise from the heating, ventilation and air-conditioning system. A flow visualization study was conducted to ensure that there was no plume drifts during the experimenting.

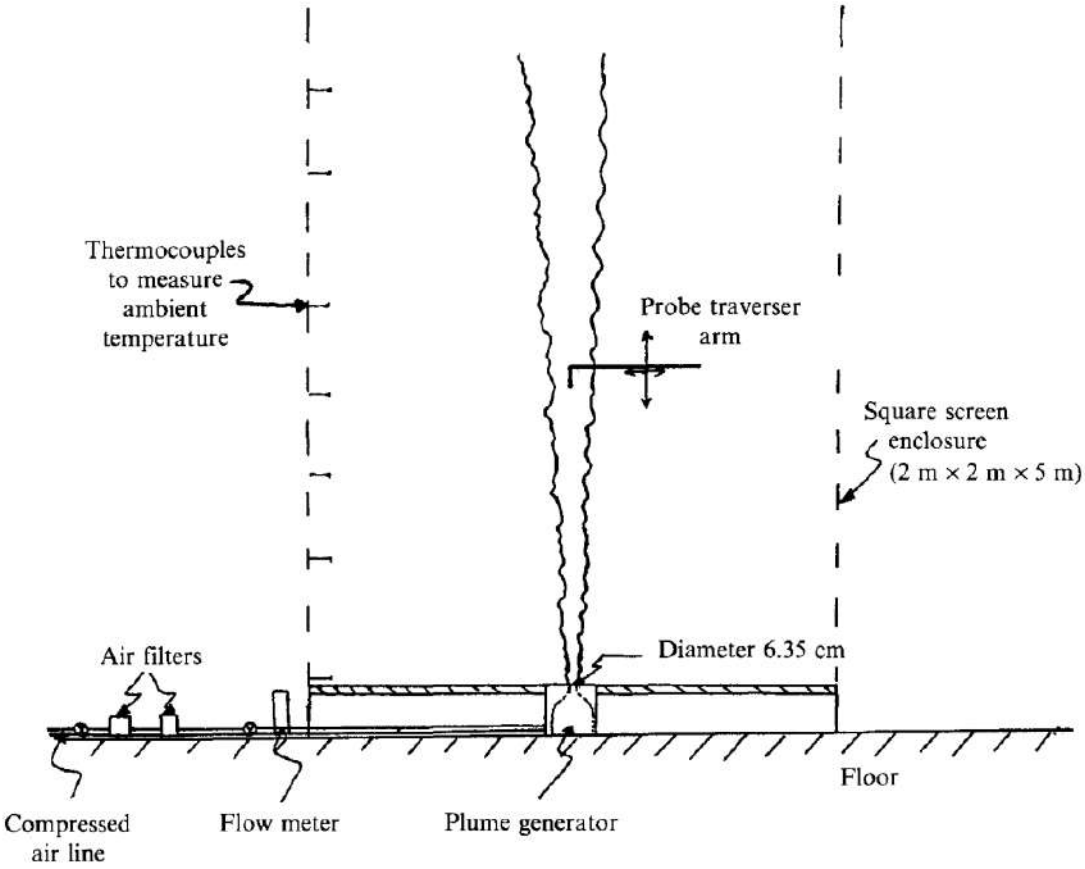

Figure 7.1: Schematic of the experimental facility. Figure from [207].

7.2.2 Instrumentation

Two types of hot wire probes were deployed to measure the velocity and the temperature fields. The first was a two-wire probe, whose leading wire was used as a cold to measure the temperature while the bottom wire was used in the constant temperature mode to measure velocity. The second probe was a coalescence of a cross-wire to measure velocity field and a temperature wire for temperature.

16 thermocouples were exploited in the shape of 4×4 grid in order to verify the axisymmetry of the flow and to locate the plume center. The calibration of the hot wires

was performed at the exit of the plume generator where it is possible to get the desired temperatures and velocities. The reference temperature was obtained using a copper wire thermocouple placed at the exit of the plume generator and the reference velocity was obtained by performing mass balance on a rotameter placed in the inlet inline. The calibration process of the hot-wires was done before and after the experiment. The velocity calibrations were found stable while the temperature wire was found sometimes to deviate significantly.

7.3 Simulation inlet conditions

In this chapter, we present the 3D large eddy simulation of a buoyant plume, generated by a vertical jet of hot air into a quiescent atmosphere. The source conditions correspond to the experiments of Shabbir and George [207], summarized in Table 7.1.

$D(m)$	$T_a(K)$	$T_0(K)$	$U_0(m/s)$	$F_0(m^4/s^3)$	$M_0(m^4/s^3)$	$\mathrm{Re} = \frac{U_0 D}{\nu}$	$\mathrm{Fr} = \frac{U_0^2}{gD}$
0.0635	300	568	0.98	0.0127	0.003	1273	1.54

Table 7.1: Source parameters of the plume

The plume source diameter, D, the exit mean velocity, U_0, the hot air temperature, T_0, and the ambient air temperature, T_a, are 6.35 cm, 0.98 m/ sec, 568 K and 300 K, respectively. The corresponding Reynolds number, Re, based on inflow mean injection velocity, source diameter and kinematic viscosity, is 1273. The specific momentum, M_0, buoyancy, F_0, mass, Q_0, and the Morton length scale, L_M, are defined as:

$$F_0 = 2\pi g \int_0^\infty U_z \frac{\Delta T}{T} r dr, \quad M_0 = 2\pi \int_0^\infty U_z^2 r dr, \quad Q_0 = 2\pi \int_0^\infty U_z r dr, \quad L_M = \frac{M_0^{3/4}}{F_0^{1/2}} \tag{7.1}$$

where r is the radial coordinate. Morton [172] and Morton and Middleton [170] introduced the source parameter Γ_0 that characterizes the plume as being either lazy ($\Gamma_0 > 1$), pure ($\Gamma_0 = 1$) or forced ($0 < \Gamma_0 < 1$):

$$\Gamma_0 = \frac{5 Q_0^2 F_0}{8\sqrt{\pi}\alpha M_0^{5/2}} \tag{7.2}$$

with α the entrainment coefficient explained in details later on. The value of Γ_0 in our simulation is around 0.9, which indicates a forced plume, having a value of Γ_0 near unity says that the plume is forced but not too much, as a result the buoyancy is significant near the source which explains the acceleration zone detailed later.

7.4 Numerical Setup

The computational domain is a box of size 18D×9D×9D. A uniform mesh, composed of 300×150×150 cells, is considered. The simulation was performed on 280 processors using the compressible formulation. The time-step, based on the sound speed, is $\delta t = 4.5 \times 10^{-6}$ s. In accordance with previous LES of this configuration [267], the Vreman turbulence model, described in Sec. 6.4.2, is applied with a constant $C_s = 0.1$, following Vreman's recommendation [241], which was also adopted in the forced plume large eddy simulation by Zhou *et* al. [267]. A turbulent Prandtl number of $\mathrm{Pr}_t = 0.3$ to account for the subgrid heat flux.

The boundary conditions are as follows: at the outlet, a Dirichlet condition is considered for pressure whereas a Neumann condition is applied for other variables with a clip for the axial velocity to prevent any backflow of the plume. Typical inflow/outflow boundary conditions are considered for the vertical sides. At the inlet, temperature and velocity were imposed to represent a plume source.

For the inlet boundary condition, we followed the strategy of Zhou *et* al. [267, 268] to ensure a transition from laminar to turbulence at a very short distance of the exit, consistently with the experimental observations of Shabbir and George [207]. This kind of fluctuations work more as perturbations with artificial nature so they are not divergence free. However, this does not represent an important issue because the associated time scale is large compared to the flow turbulent time scales (the fastest time scale of our injection is around 0.2 s). As a consequence, the impact of this synthetic injection vanishes few diameters away from the inlet where we start performing our analysis. It consists in superimposing azimuthal disturbances:

$$u'(r) = AU_0(r)[(1 - \frac{r}{D})\sum_{n=1}^{N}\sin(2\pi ft/n) + \frac{r}{D}\sum_{n=1}^{N}\sin(2\pi ft/n + \theta)] \tag{7.3}$$

to a mean flow $U_0(r)$ corresponding to a pipe profile:

$$U_0(r) = \frac{1}{2}U_0\left[1 - \tanh(b_2(2r/D - D/2r))\right]. \tag{7.4}$$

A is the amplitude of the forcing and $N = 6$ is the number of the modes. f is the forcing frequency, that is determined by the jet preferred mode corresponding to a Strouhal number, $\mathrm{St} = fD/U_0$, of 0.3, leading to $f = 4.629$ Hz. In the mean pipe flow profile, θ is the azimuthal angle and $b_2 = 6.25$ [167].

Note that Eq. (7.3) was slightly modified from the original formulation [53, 162], which presented a singularity at the center. The forcing amplitude $A = 0.2/\sqrt{3}$, corre-

sponds to a RMS fluctuations of 20% for the axial velocity and $A = 0.01/\sqrt{3}$ corresponds to a RMS fluctuations of 1% for the other two components.

The time-averaged statistics (mean, rms,..) presented hereafter were collected over 15 forcing cycles = 20 s once a statistical steady state was reached. The forcing cycle is defined by the longest period of the sine series in Eq. (7.3) = 1.3 s.

7.5 Results and discussion

7.5.1 Qualitative description

Figure 7.2 illustrates the transition process trough a snapshot of the three dimensional iso-surface for the Q-criterion [111] along with temperature and density fields. The Q-criterion is defined as:

$$Q = \frac{1}{2}(\|\Omega\|^2 - \|S\|^2), \tag{7.5}$$

where S and Ω are the strain rate and the vorticity tensor, respectively:

$$\Omega = \frac{1}{2}(\nabla \mathbf{u} + \nabla \mathbf{u}^T), \tag{7.6}$$

$$S = \frac{1}{2}(\nabla \mathbf{u} - \nabla \mathbf{u}^T), \tag{7.7}$$

The Q-criterion defines the areas where the vorticity magnitude is larger than the magnitude of the strain rate, such that $Q > 0$ indicates the existence of a vortex. The potential core of the plume becomes rapidly turbulent after few diameters from the source which is consistent with the experimental observations of Shabbir and George [207]. The transition occurs due to the growth of azimuthal instabilities that forms large coherent energy containing structures which eventually break down to generate small-scale turbulence.

Figure 7.3 shows the 2D-contours of streamwise vorticity at different heights above the plume source, $z/D = 4, 8, 12, 16$. The forcing introduced at the inlet level triggers an early transition from laminar to turbulent, and it can be clearly noticed that the plume grows downstream of the inlet, with small structures of vortices due to the gravity induced turbulence alongside the entrainment of air.

Figure 7.4 shows the energy spectrum based on the axial velocity at distance $z/D = 4$, it shows the energy cascading reported by the theory of Kolmogorov [122] and that we have the correct power law of $-5/3$ in the inertial range, also the dissipation range was

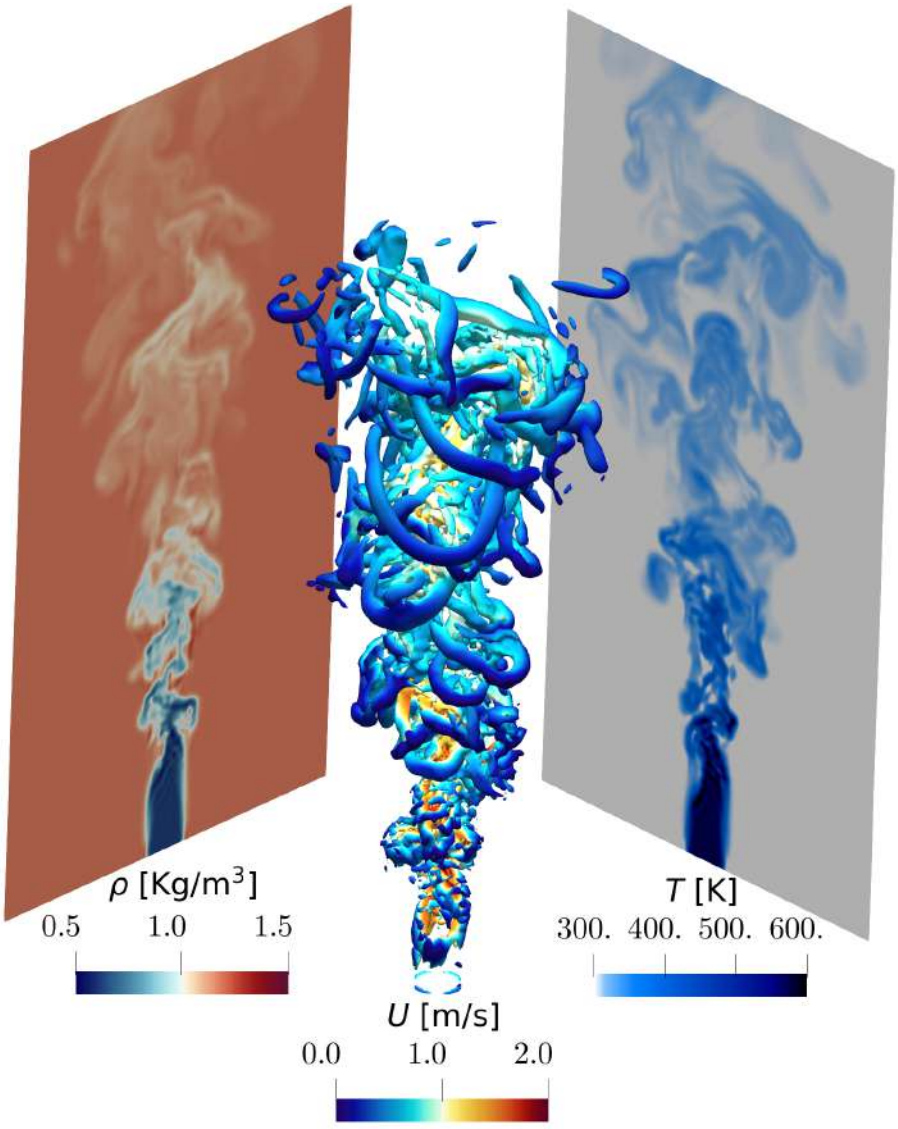

Figure 7.2: Instantaneous 3D Q-criterion coloured by velocity magnitude alongside density and temperature fields

detected at higher frequencies. In addition, in Figure 7.4 the spectrum for temperature fluctuations is shown, the spectrum initially shows the $-5/3$ power law in the so called inertial-convection region. Afterwards, a region is expected where the spectrum decays sharply and follows a -3 power law, which is a unique characteristic of the forced plumes, and it belongs to the inertial-diffusive subrange proposed by Papanicolaou & List [187]. Kostovinos [125] argued experimentally that the slope change from $-5/3$ to -3 is due to strong energy feeding as a result of the large plume vortices driven by buoyancy force. This region cannot be clearly identified on the spectrum of temperature fluctuations in Figure 7.4.

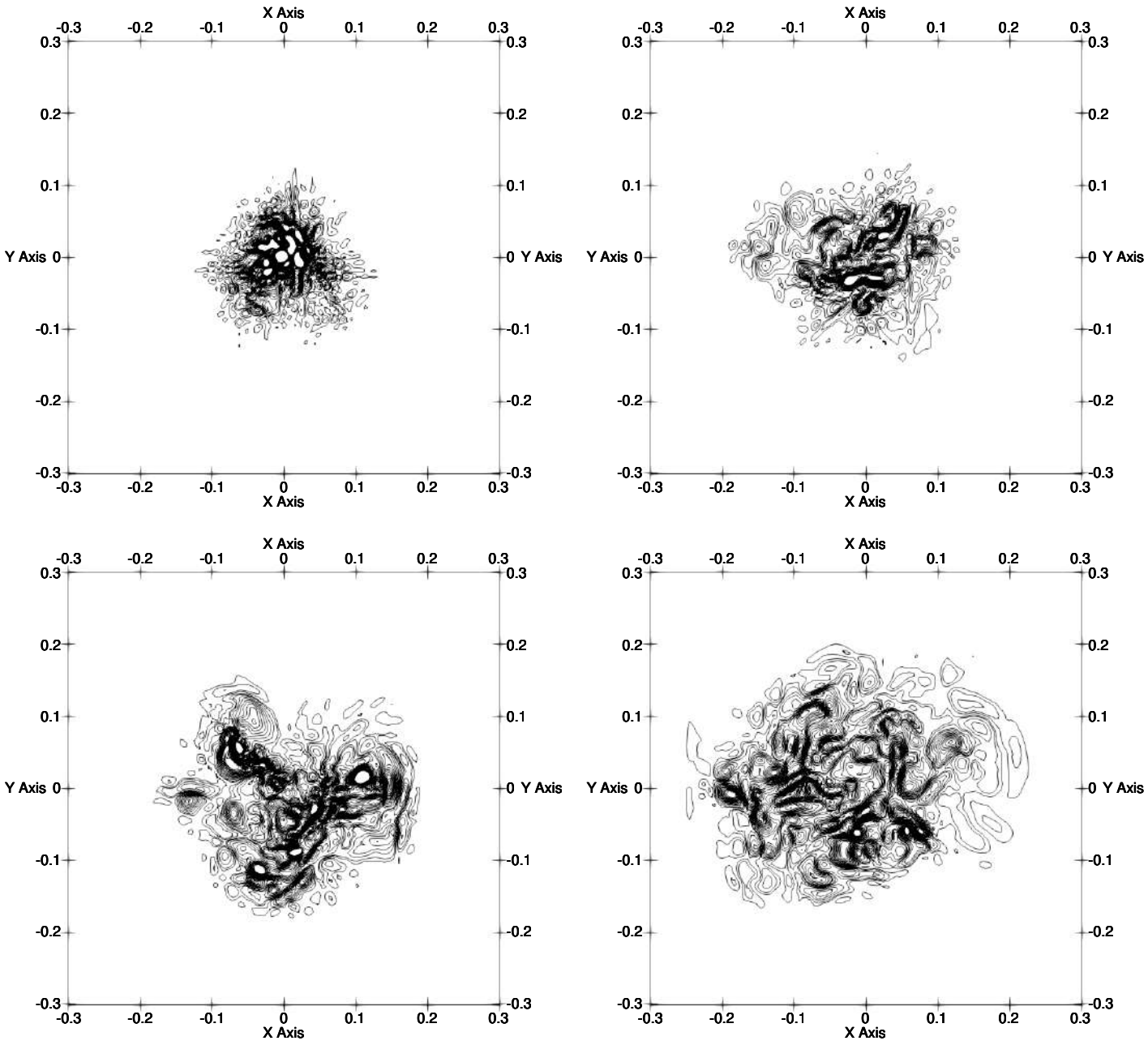

Figure 7.3: Instantaneous streamwise vorticity contours on the X-Y plane at heights: $x/D = 4$ (top-left), $x/D = 8$ (top-right), $x/D = 12$ (bottom-left) and $x/D = 16$ (bottom-right).

7.5.2 Axial mean quantities

Figure 7.5 compares the centerline time-averaged axial velocity U_c, and temperature T_c, to the experimental data of Shabbir and George [207], who proposed the following correlation in the plume-like region, based on the physical analysis of Morton *et* al. [171]:

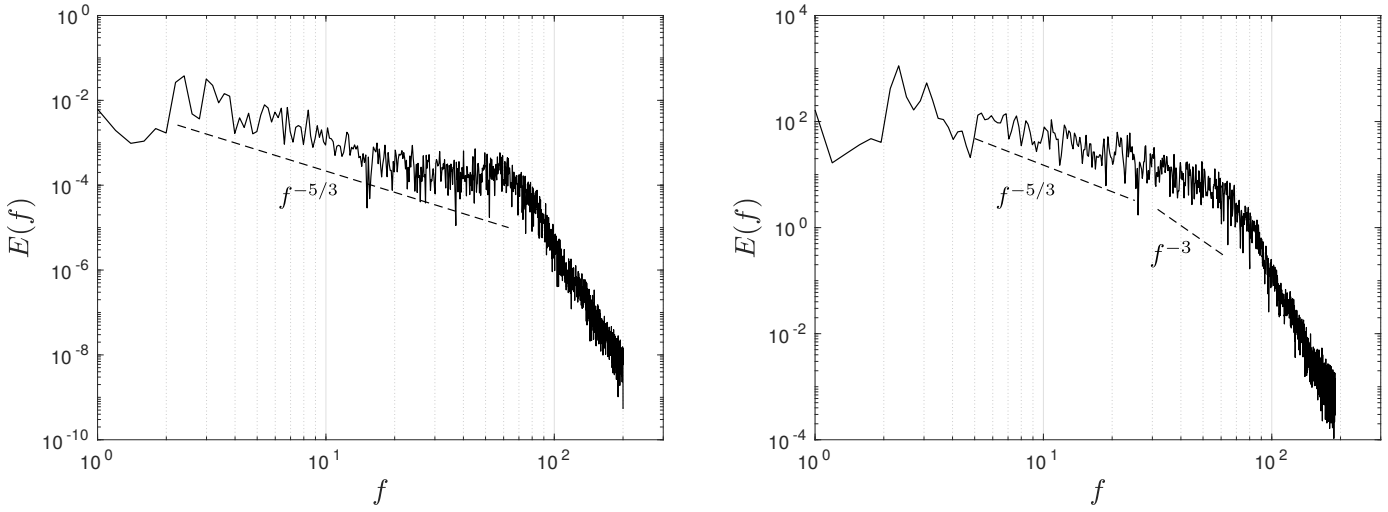

Figure 7.4: Temporal energy spectrum at $z/D = 4$ for axial velocity (left), temperature (right). Dashed lines indicate the expected characteristic slopes.

$$U_c = A_U z^{-1/3} F_0^{1/3}, \qquad \frac{T_a}{T_c} = 1 - A_T z^{-5/3} F_0^{2/3}/g, \tag{7.8}$$

where $A_T = 9.4$ and $A_U = 3.4$ were fitted from the experimental results (see also in Table 7.2).

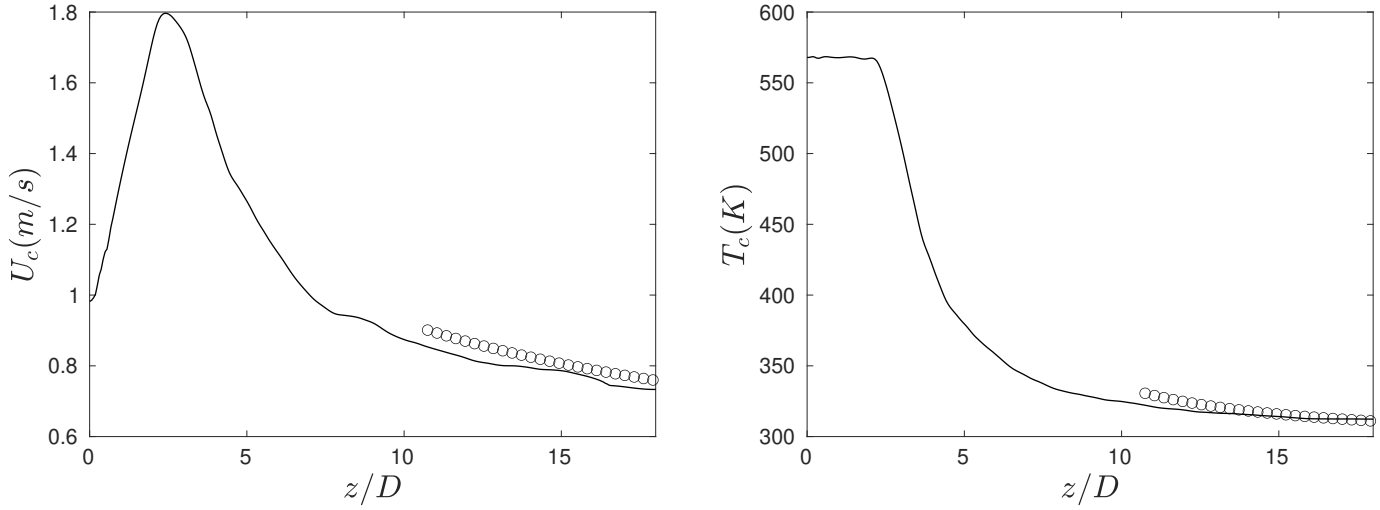

Figure 7.5: Centerline mean axial velocity (left), and Temperature (right) profiles. Solid line for the simulation, symbols for experimental data of Shabbir and George [207]

The centerline velocity in Fig. 7.5 increases rapidly from its initial value at the inlet to a maximum value of about 1.8 at $z/D \approx 2.5$ and then decreases afterwards rapidly to reach values lower than the inflow velocity after about 6 diameters. This behavior

was also observed by Lingens *et* al. [140] who experimentally investigated buoyant jet diffusion flame. The initial acceleration in the near field is due to the large buoyancy force resulting from large temperature (density) difference between the plume core and the ambient. The rapid deceleration after the peak results from the turbulent mixing of the plume with the surrounding fluid, which decreases the temperature. The rapid decrease in temperature downstream the potential core is clearly evidenced in Fig. 7.5. The location of the transition from jet-like to plume-like behaviour can be identified through the rates of decrease which have to scale with $z^{-1/3}$ and $z^{-5/3}$ for velocity and temperature, respectively. The numerical model predicts the transition at $z/D \approx$ 10-11 which is consistent with the experiments of Shabbir and Georges [207] where it was estimated to occur at $z/D = 10.5$. In the plume-like region, the model reproduces quantitatively the evolution of both axial velocity and temperature with z/D, although U_c is on the whole slightly underestimated.

The non-dimensional mean axial velocity $U_c z/\sqrt{M_0}$ is plotted as a function of the non-dimensional axial distance $\xi = z/L_M$ in Fig. 7.6. The transition to the plume-like region (i.e. the slope change) is predicted around $\xi = 4 \sim 5$ which is consistent with the finding of Morton *et* al. [171] who reported that a forced plume will reach a pure plume behaviour for $z/L_M > 5$. In addition, our simulation exhibits a good agreement with the experimental profile obtained from the correlation of Shabbir and George [207] (see Eq. 7.8) in the plume-like region.

Forced plumes becomes plume-like far away from the source in homogeneous environment even if the injected momentum flux is large when the function Γ changes from a value smaller than 1 at the source to a value of 1 in the far field. Four regions were identified in the present simulation: 1) a non-buoyant region where momentum dominates the flow, 2) an acceleration region where the plume is accelerated due to gravity, 3) an intermediate region where influence of initial momentum weakens, and 4) the plume-like region (i.e. self-similarity region) where the plume dynamics is dominated solely by the buoyancy forces. This picture is consistent with the descriptions of Gebhart *et* al. [79] and Chen and Rodi [33] although they did not report the acceleration region (i.e. region 2). Note that the limits of each region in Fig. 7.6 are defined using the velocity inflection points, consistently with the global behaviour of the plume.

7.5.3 Fluctuations quantities

In this section, the axial evolution of the rms values of axial velocity and temperature fluctuations and the cross-correlation between velocity and temperature fluctuations are discussed and compared with experiments [81, 173, 187, 207], for which the fitting

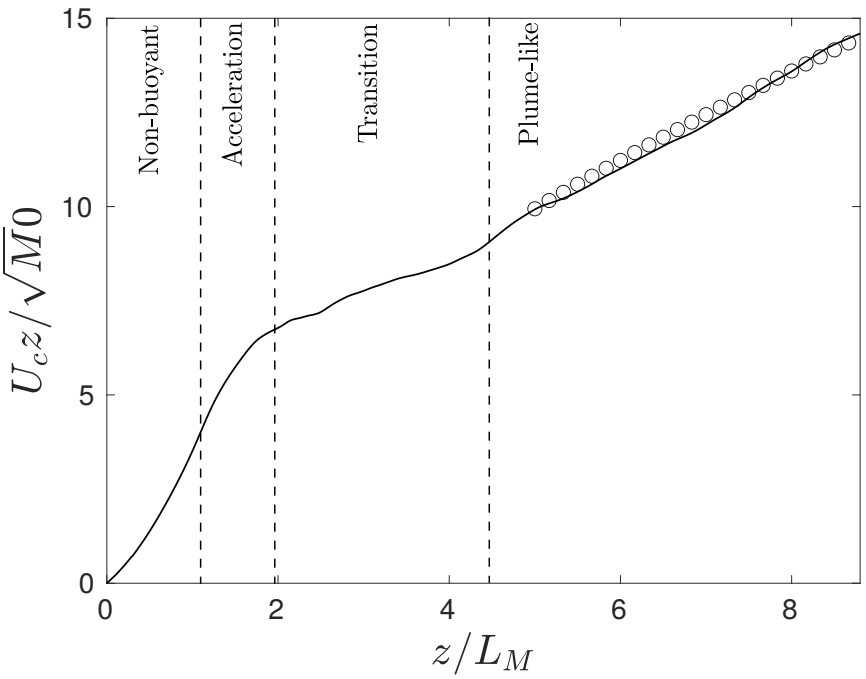

Figure 7.6: Centerline mean non-dimensional axial velocity profile. Solid line for the simulation and symbols for experiment of Shabbir and George [207]

parameters are reported in Table 7.2.

Reference	A_T	A_U	B_T	B_U	$\overline{(T'^2)}^{1/2}/\overline{\Delta T_c}$	$\overline{(u_z'^2)}^{1/2}/\overline{U_c}$	$\overline{u_z'T'}/\overline{(u_z'^2)}^{1/2}\overline{(T'^2)}^{1/2}$
Shabbir & George [207]	9.4	3.4	68	58	0.4	0.33	0.67
George *et* al. [81]	9.1	3.4	65	55	0.38	0.28	0.67
Papanicolaou & List [187]	14.28	3.85	80	90	0.42	0.25	0.51
Nakagome & Hirata [173]	11.5	3.89	48.1	63	0.36	0.25	0.46

Table 7.2: Summary of mean flow parameters and turbulence intensities for different experiments

Figure 7.7 presents the rms values of axial velocity and temperature fluctuations. As expected, the velocity fluctuations are about 20% at vicinity of the inflow plane and corresponds to the imposed disturbance level. The velocity fluctuations decrease in the potential core region of the plume before starting to increase very abruptly in the laminar to turbulence transition region, the initial drop in velocity fluctuations is due to the artificial nature of the fluctuations imposed at the inlet. These artificial fluctuations, without a proper cascade, are dissipated very quickly; however, they constitute the seed for a correct transition to turbulence with a realistic energy cascade in the far field

where we perform our analysis. In the plume-like region, both velocity and temperature fluctuations decrease at a same rate as mean velocity and temperature to ensure constant ratio of $\overline{u'^2}^{1/2}/U_c$ and $\overline{T'^2}^{1/2}/(T_c - T_a)$. The predicted velocity-based turbulence intensity in the plume-like region is lower than those of 0.28 and 0.33 reported by George *et* al. [81] and Shabbir and George [207], respectively. It is in better agreement with those of 0.25 reported by Papanicolaou and List [187] and Nakagome and Hirata [173]. On the other hand, Fig. 7.7 shows that the temperature-based turbulence intensity is also consistent with the available data.

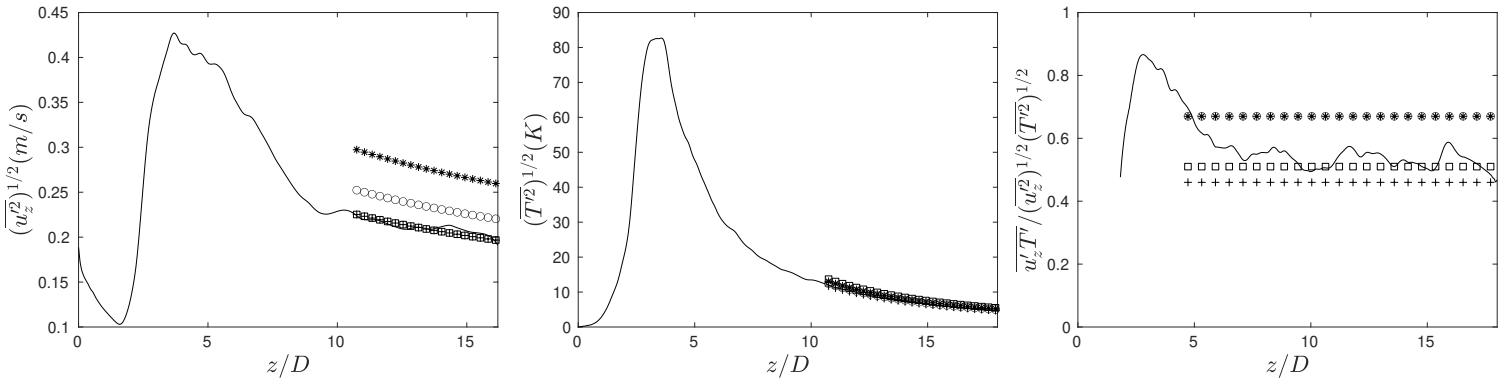

Figure 7.7: Center line profiles of r.m.s of axial velocity (top), temperature (middle), and the cross-correlation of velocity and temperature fluctuations (bottom). Solid line for simulation, (∗) for Shabbir & George [207], (∘) for Geroge *et* al. [81], (□) for Papanicolaou & List [187], and (+) for Nakagome & Hirata [173].

Figure 7.7 shows the evolution of the cross correlation between velocity and temperature fluctuations, $\overline{u'T'}/(\overline{(u'^2)}^{1/2}\overline{(T'^2)}^{1/2}$, along the center line. It can be clearly observed that velocity and temperature fields are positively correlated in this type of flows with a predicted nearly constant value in plume-like region of about 0.55. This value is lower that those reported by George and co-workers [81, 207] in the range 0.6-0.7, averaged to 0.67 (see Table 7.2), and in closer agreement with those of 0.46 and 0.51 reported by Nakagome and Hirata [173] and Papanicolaou and List [187], respectively.

7.5.4 Self-similarity

An important feature of the mean flow in the fully-developed region of turbulent positively buoyant plumes is the "self-similarity" or "self-preserving" behavior. The radial mean velocity and temperature profiles follow a Gaussian shape and become wider as the plume rises. The profiles collapse on the same curve when considering appropriate

dimensionless variables:

$$\frac{U_z}{U_c} = \exp\left(-B_u \frac{r^2}{z^2}\right), \qquad \frac{T - T_a}{T_c - T_a} = \exp\left(-B_T \frac{r^2}{z^2}\right) \tag{7.9}$$

The coefficients B_u and B_T are unknown empirical constants that can be obtained by assuming a linear growth of the plume width b [171]:

$$\frac{b}{z} = \frac{6}{5}\alpha = const, \tag{7.10}$$

The coefficients will then be calculated using $B_u = \sqrt{z/b_u}$ and $B_T = \sqrt{z/b_T}$, where b_u and b_T are the plume width defined by the distance from the centerline to the point at which we have $1/e$ of the centerline values of velocity and temperature, respectively. George *et* al. [81] determined by experiments those coefficients as $B_u = 55$ and $B_T = 65$.

The radial profiles of mean velocity and temperature from our LES at $z/D = 10, 12, 14, 16$ and the profiles of George *et* al. [81] form are plotted in Fig. 7.8. The velocity and the temperature rise above the ambient are normalized by the centreline value. The profiles are plotted versus the non-dimensional radial coordinate $r/(z + z_0)$ where z_0 is the virtual origin of the plume. Empirical relationships were reported to estimate the location of the virtual origin [267]. As pointed out by Yang [265], the location of virtual origin predicted in the simulation can be different from that estimated by empirical formula. Indeed, this location is significantly affected by the transition from laminar to turbulent whose the prediction is a difficult task in LES mainly due to its sensitivity to the plume's source inflow condition. In the present study, the virtual origin was estimated to collapse the radial profiles in the fully developed region to a single dimensionless Gaussian profile following the methodology proposed by Yan [265], giving z_0 set equal to $2.3D$. It can be observed in Fig. 7.8 that the self-similarity is well preserved in the simulation and the predicted self-similarity profiles agree well with those reported by Georges *et* al. [81].

Following Shabbir & George [207], the radial profiles of r.m.s values of axial velocity and temperature and of the cross correlation between velocity and temperature fluctuations are plotted in terms of the similarity variables in Fig. 7.9. The predicted profiles clearly exhibit a self-similar behavior. The agreement with the experimental data is reasonable although, consistently with Fig. 7.7, both r.m.s values of axial velocity fluctuations and the cross correlation between velocity and temperature fluctuations are overall underestimated.

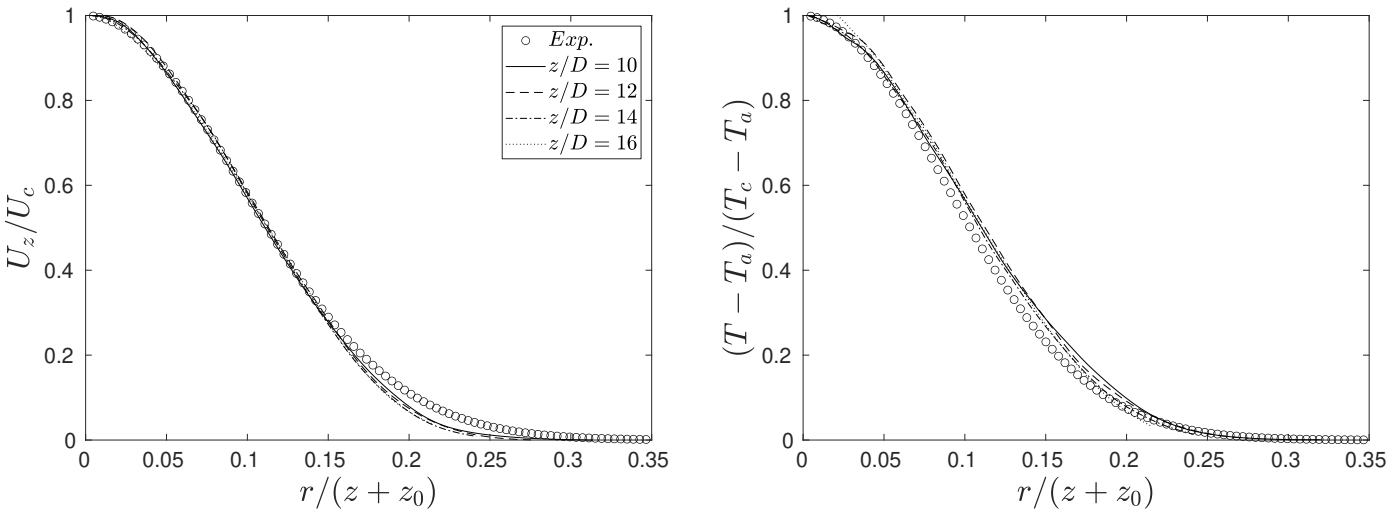

Figure 7.8: Radial profiles of mean axial velocity (left) ,and mean temperature (right) at four axial positions compared to the experiments of George *et* al. [81]

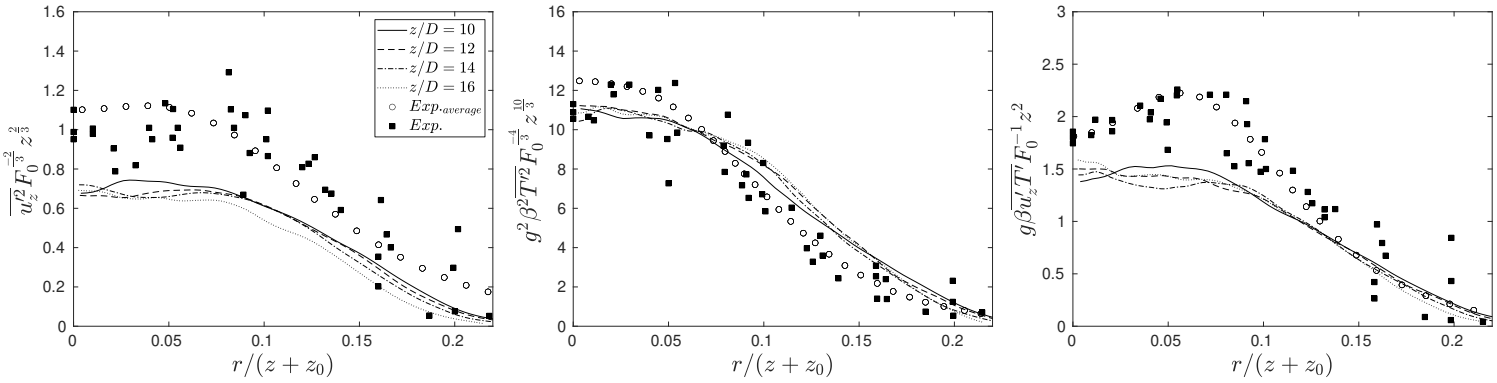

Figure 7.9: Radial profiles at $z/D = 10, 12, 14, 16$ for normalized r.m.s of axial velocity fluctuation (top), r.m.s of temperature fluctuations (middle), and cross correlation of both velocity and temperature fluctuations (bottom).

7.5.5 Entrainment

The mechanism of turbulent mixing which brings air into the buoyant plume is called entrainment. The ideal plume theory is based on both Boussinesq and top-hat radial-profile assumptions and assumes that the mean entrained flux across the edge of the plume E (entrainment rate) is proportional to the local upward velocity W. An air entrainment coefficient is then defined as:

$$\alpha = \frac{E}{bW} \tag{7.11}$$

where E, W, b are know as the top-hat variables of entrainment rate, local vertical

velocity and plume width defined by Turner [235]:

$$b^2W = \int_0^\infty U_z r dr, \qquad b^2W^2 = \int_0^\infty U_z^2 r dr, \qquad E = \frac{d}{dz}(\int_0^\infty U_z r dr) \tag{7.12}$$

The Plume width, b, can be calculated as the value at which velocity or temperature reaches a value of $1/e$ of the centerline value as indicated by Morton *et* al. [171]. This will be referred to as (*method 1*) hereafter. It can be also obtained from Eq. 7.12, as $b^2W/\sqrt{b^2W^2}$. This second method will referred to as (*method 2*) hereafter. Figure 7.10 compares the two methods. The experimental slope obtained by George *et* al. [81] and the numerical prediction obtained by Zhou *et* al. [267] are also plotted in Fig. 7.10. Both the present predicted velocity and temperature half-widths decrease first due to the "necking" process in the near field, as observed experimentally by Cetegen [28], before, as expected, increasing almost linearly in plume region. The two methods provide on the whole consistent predictions that agree with both the experimental slope and the numerical results obtained by Zhou *et* al. [267].

The entrainment coefficient, α, can be calculated using Eq. 7.10. This method requires the knowledge of the width b, along the plume axis. It can be obtained either from temperature and velocity radial profiles (*method 1*) or from Eq. 7.12 (*method 2*), as discussed previously. Another method was adopted by Zhou *et* al. [267] from Eqs. 7.11 and 7.12, leading to $\alpha = E/\sqrt{b^2W^2}$. This method will be referred to as (*method 3*). Figure 7.10 shows that the three methods provide consistent results in the far-field. Our results agrees well with the LES of Zhou *et* al. [267] which settles on a constant value in the far-field, $\alpha = 0.09 - 0.1$. Our predictions of α in the plume region are also close to the value of 0.116 adopted by Morton in his plume model [172] and the experimental value 0.108 reported by George *et* al. [81].

Integrating radially the momentum and energy equations across the flow introduces two fundamental quantities [207]. The first is the momentum flux, M that can be normalized by the inflow momentum flux, M_0 (see Table 7.1):

$$M = 2\pi \int_0^\infty (U_z^2 + \overline{u_z'^2} - \overline{v'^2}) r dr \tag{7.13}$$

The moment flux ratio increases with the height according to the following relationship [48]:

$$\frac{M}{M_0} = k(\frac{x}{L_M})^{4/3} \tag{7.14}$$

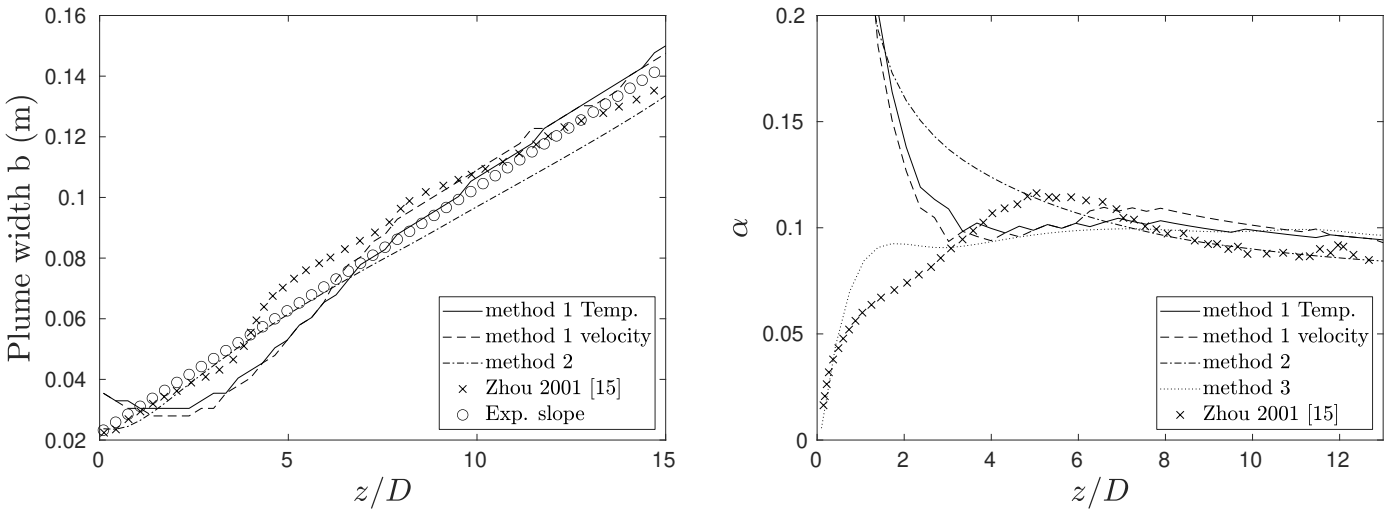

Figure 7.10: Evolution with the height of (left) the plume width and (right) the entrainment coefficient α

Different values of 0.35 [48], 0.34 [207] and 0.29 [187] were reported for the coefficient k. Fig. 7.11 compares our result to these experimental results. Model predictions are in good agreement with the experiments of Shabbir and George [207] and Fisher [48] but overpredict that of Papanicolaou and List [187].

The second is the buoyancy flux F, that has to be conserved conserved along the plume height:

$$F = 2\pi g \int_0^\infty (U_z \frac{\Delta T}{T} + \frac{\overline{u_z' T'}}{T}) r dr \tag{7.15}$$

The buoyancy flux is normalized by its injection value, F_0. Figure 7.11 shows the evolution of F/F_0 along the plume height. The simulated normalized buoyancy flux evolves around unity, consistently with the theory (solid line). It appears clearly by comparing the solid and dashed lines that the turbulent contribution is essential. When it is disregarded, the buoyancy flux decreases with the axial distance and is no more conserved. The turbulence contribution is predicted around $15\% - 20\%$ as also noted by Shabbir & George [207], while George *et* al. [81] and Papanicolaou & List [187] found the contribution to be about 15%.

7.6 Concluding remarks

For the 3D forced plume simulation, which is a critical test case in which the buoyancy is highly coupled with momentum and turbulent mixing, the solver was able to anticipate

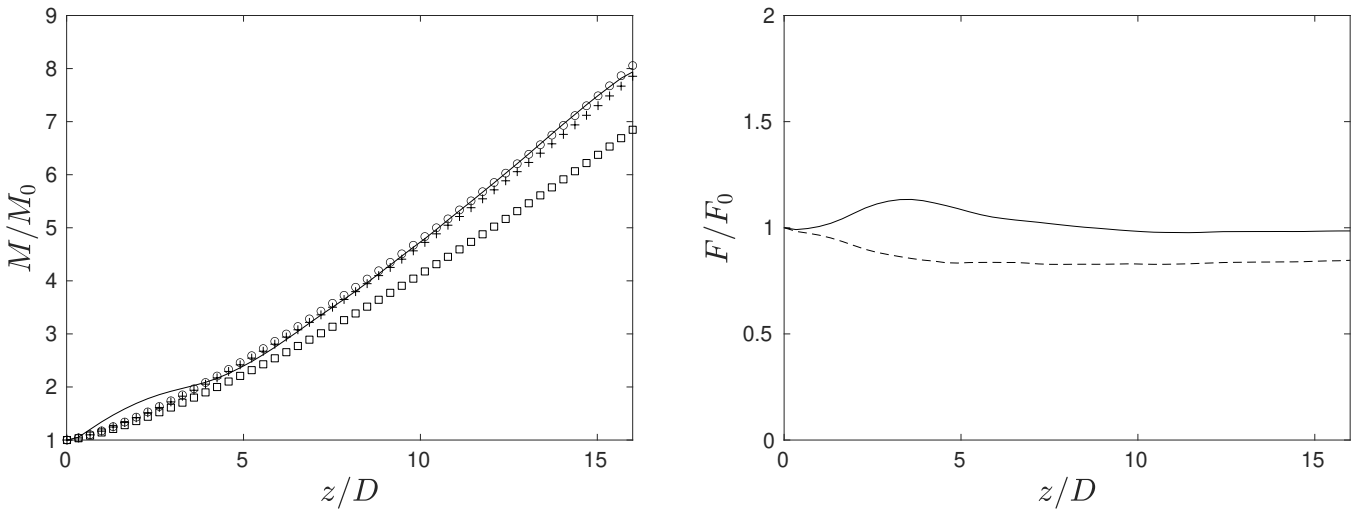

Figure 7.11: Axial profile of momentum flux ratio (left). The solid line represents the present LES, whereas the symbols represent the experimental data of Fischer *et* al. [48] (∘), (+) for Shabbir & George [207] and (□) for Papanicolaou & List [187]. Axial profile of buoyancy flux ratio (right), solid line includes the turbulent heat flux while dash line does not.

the correct physics of a thermal plume from numerous aspects listed below:

- The velocity energy spectrum follows the Kolmogorov theoretical slope of $-5/3$ indicating a proper resolution of the turbulence energy cascading as reported in the literature.
- Axial profiles of mean velocity and temperature were in a good agreement with the experimental data.
- Our forced-plume reaches a plume-like region at around $z/L_m = 4 \approx 5$ which is consistent with the findings in the literature.
- The axial profiles of rms for velocity and temperature also were in a good agreement with the experiments, we should emphasize that we did not take into account the experimental errors which are significant specially for the second order statistics.
- The cross-correlation between velocity and temperature has a high positive value which compares well with the reported values from experiments and indicates a strong coupling between the velocity and temperature fluctuations due to gravity.
- Self similarity profiles in the far field (i.e. plume-like region) were achieved for both mean and rms of velocity and temperature.

- The growth rate of the plume was examined through the spatial evolution of the plume width. The growth of the plume compared very well with experimental and numerical references.
- The entrainment of fluid form the surrounding was correctly predicted by examining the entrainment coefficient α, and the predictions were in a good agreement with the theoretical, experimental and numerical references.
- Integral quantities, mainly buoyancy flux and momentum flux, were compared with the experiments and both were in a good agreement, we emphasize about the finding that the turbulent heat flux participates by around 20% in the total buoyancy flux which is consistent with the experiments.

From all the previous points we can conclude that our solver is capable of reproducing the physics of a thermal plume correctly whether the mean values, the second order statistics or even integral quantities through the plume, and that our code can handle any type of flows with variable densities regardless of their complexity.

In the next chapter, a large helium plume will be simulated in order to study the near-field dynamics which is fundamental for fire applications.

Chapter 8

Application to lazy plumes

Contents

8.1 Introduction

In the previous chapter we assessed the capability of the numerical model to predict the behaviour of the far-field of a forced plume. It was found experimentally [183, 227] that a large-scale helium-air plume mimics the dynamics and structure of large-scale fires. As a consequence, such configuration is particularly interesting to investigate the near-field dynamics of buoyant plumes while avoiding the complexities associated with combustion and radiation.

This particular test case belongs to the list of target problems identified by the workshop MaCFP [24] recently initiated by members of the fire community. The goals of this workshop are to develop and validate predictive models of fire plumes, to identify well-defined target flames that are suitable for modelling, and to archive detailed data sets for these target flames.

Many LES attempted to reproduce the experimental data of the large helium plume investigated experimentally at Sandia [183, 227]. DesJardin *et* al. [50] performed LES of an idealized configuration (i.e. not representing the entire geometrical setup) where he focused on the instability modes and the flow dynamics of a large turbulent helium plume, as a function of mesh resolution with and without subgrid scale (SGS) model. The minimum grid spacing in this study was 1.6 cm, with a maximum spacing of 7.8 cm. The study claimed that a potential problem might be the turbulent energy transfer from small to large scales known as backscatter (i.e. inverse energy transfer). Chung and Devaud [40] used a buoyancy modified $k-\epsilon$ models in Reynolds Averaged Navier Stokes (RANS) as well as conventional eddy-viscosity LES methods with the same idealized configuration but a finer uniform grid resolution of 1.25 cm. Blanquart and Pitsch [17] performed also an LES but on the full geometry of the experimental facility. Burton [25] dealt with the SGS modelling deficiencies identified by Desjardin *et* al. [50] via the use of a nonlinear-LES method, which allows backscatter of energy from small to large scales. Maragkos *et* al. [153, 154] performed LES where they focused on the instability modes. Furthermore, they explored the sensitivity of the simulation to grid resolution, to the SGS model coefficient and also to the turbulent Schmidt number Sc_t, and attributed the discrepancies in his results to a lack of differential diffusion in the simulations. Jatale *et* al. [110] have presented and applied a framework for uncertainty quantification to the 1-m-diameter helium plume using experimental data and LES. Ma *et* al. [145] studied the same helium plume and compared the results of different subgrid scale model for the scalar flux. They concluded that increasing the grid resolution has more effects on the simulation than the choice of the subgrid scale scalar flux. Ahmed and Trouvé [4] quantified the necessary grid resolution to well capture the cyclic thin boundary layer formed near the inlet, which is important to predict correctly the dynamics at this region as well as the global flow characteristics. They argued that a grid resolution on the order of millimetres would be sufficient to capture the dynamics at these small length scales. More recently, Wimer *et* al. [255] used the idealized geometry but employed adaptive mesh refinement (AMR) to locally refine the grid in regions of high density and resolution. All the mentioned studies had good agreement with experimental data, but there were always discrepancies specially

on the values of helium mass fraction.

Experimental setup

Comparisons are made in this study with experiments performed in a large building designed for indoor fire experiments: the Fire Laboratory for Accreditation of Models and Experiments (**FLAME**) at Sandia National Laboratories in Albuquerque, New Mexico. The central FLAME chamber consists of a 6.1 m cubical enclosure with a 2.4 m diameter chimney depicted schematically in Figure 8.1. The plume source is 1 m in diameter surrounded by a 0.51 m wide floor (i.e. the ground plane). The 1-m source diameter is chosen to ensure that the plume would be fully turbulent based on the pool fire fuel burn rate data of Blinov and Khudyakov [19]. The experiment is designed to simulate an unconfined plume within the enclosure with minimal external wind effects and known boundary conditions. Inlet air is injected at the bottom of the facility and is drawn by the accelerating helium plume over the ground plane surrounding the plume source.

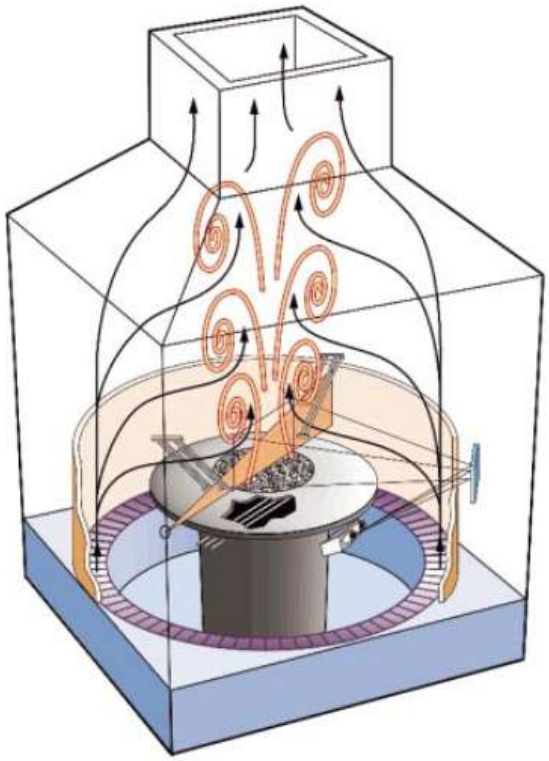

Figure 8.1: Schematic of PIV/PLIF set-up in FLAME facility showing relationship of Plume, Laser illumination, and cameras. Facility details can be found in Tieszen *et* al. [227]. Figure taken from [50].

This flow approximates an external plume on a ground plane, and for the purposes of this study is treated as such (i.e. the entire facility will not be modeled). Helium is supplied from a bottle farm and enters the base of a 3 m tall diffuser that is covered with a 10 cm thick honeycomb with 3 mm nominal cell size. A detailed analysis of the spatial velocity distribution of the plume inlet (using air instead of helium) shows that the inlet velocity profile is uniform to within ±6% [16].

In the experiments, two planar imaging techniques were concurrently applied: particle image velocimetry (PIV) for velocity field measurements and planar laser induced fluorescence (PLIF) for scalar field measurements (mass fraction). Details can be found in O'Hern *et* al [183]. The PIV data is collected by seeding the helium and air flows, while the PLIF data is obtained from laser-induced acetone fluorescence from a small amount of acetone ($1.7 \pm 0.1\%$ vol.) vaporized in the helium to work as a tracer. In addition, $1.9 \pm 0.2\%$ vol. of oxygen was added to quench acetone phosphorescence. The mixture molecular weight was $5.45 \pm 2.7\%$ g mol^{-1}. The PIV data are acquired at 200 images per second while the PLIF data are acquired at 100 images per second. The PIV images are processed with a two-frame cross-correlation technique using the PIV Sleuth software [39].

An iterative interrogation technique was used to extend the dynamic range for these strongly accelerating flows. The interrogation region is 2.1 cm × 2.1 cm. Spatial fluctuations smaller than this dimension are therefore not resolved. PLIF analysis includes film and intensifier correction, normalization for the laser beam intensity profile, absorption correction, scaling, and spatial averaging.

The helium was ejected from the diffuser at an average velocity of 0.325 m/s. The average mixture Reynolds number was $\mathrm{Re} = DU_0/\nu = 3200 \pm 0.6\%$, where D is the inlet diameter of helium, U_0 is the inlet velocity and ν is the kinematic viscosity of the helium/acetone/oxygen mixture. The average mixture Richardson number was $\mathrm{Ri} = (\rho_\infty - \rho_p)gD/(\rho_\infty U_0^2) = 76 \pm 6.5\%$, where ρ_∞ is the surrounding air density, ρ_p is the plume fluid density at the source, g is the gravitational acceleration. It is worth mentioning that the experiment was performed at a low ambient pressure $p_\infty = 80\,900$ Pa (due to the high altitude in which the facility was located) and in an ambient temperature $T_\infty = 285$ K.

The measured velocities from the experiment contain uncertainties in the order of 20%, while their turbulent statistics have uncertainties in the order of 30%. The values of concentrations hold uncertainties in the order of 18%, plus a fixed uncertainties of 5%, while the concentration fluctuations contains uncertainties in the order of 21%. The uncertainties are greater than typical PIV applications, nevertheless, it must be

considered that this is a large-scale application for PIV (i.e 1 m diameter plume). Run-to-run variability also included in the uncertainties and could be found in Ref. [183].

8.2 Numerical setup

The low-Mach number formulation is used for this simulation. The simulation is performed on a Cartesian mesh for a cubic domain sizing $8 \times 8 \times 4\,\mathrm{m}^3$ depicted in Fig. 8.2. Although the study is performed on the near-field region of the helium plume, the boundaries were pushed far from the plume source to mitigate any effects from them. The choice of the domain size as well as the grid resolution is consistent with previous numerical studies [40, 50, 145, 153]. Two meshes were included in our study, and refinements zones were used to reduce the calculation cost. The zones of refinements (Fig. 8.2) are denoted by *ZoneI*, *ZoneII*, *ZoneIII* and *ZoneIV* with grid size reduced in half between two adjacent zones. The coarse mesh contains *ZoneI*, *ZoneII* and *ZoneIII* corresponding to grid size of 8 cm, 4 cm and 2 cm, respectively, resulting in a 2 million-cell mesh. While in the fine mesh, an additional refinement zone is added close to the plume source, indicated by *ZoneVI*, to end up with four levels of refinements with a largest and smallest grid size of 4 cm and 1 cm, respectively, resulting in a 4 million-cell mesh.

Boundary conditions are given in Fig. 8.2. Helium is injected at the center of the bottom plane through a 1 m diameter inlet with a uniform vertical velocity $U^{He}_{inlet} = 0.325\,\mathrm{m/s}$. The helium inlet is surrounded by an annulus solid plate of 0.5 m width beyond which a co-flow of air is injected at a much lower speed $U^{Air}_{coflow} = 0.01\,\mathrm{m/s}$. At the upper outlet plane a Dirichlet boundary condition is used for pressure and Neumann for other variables, with a clip on the streamwise velocity to prevent any backflow from the outlet. The sides are set to a typical In/Out flow.

At every point in the domain, the composition of the fluid corresponds to a mixture of helium and air. The air was treated as a single species without separating Oxygen and Nitrogen, the average molecular weight of the air is taken $W_{air} = 28.9\,\mathrm{g\,mol^{-1}}$. For experimental visualization reasons, the injected helium was not pure, but rather a mixture of 96.4% helium (He), 1.9% oxygen (O_2) and 1.7% acetone (CH_3COCH_3) resulting in an average molecular weight $W_{He} = 5.45\,\mathrm{g\,mol^{-1}}$. The ambient (inlet) temperature and pressure are $T_\infty = 285\,\mathrm{K}$ and $p_\infty = 80\,900\,\mathrm{Pa}$, respectively, in order to match the experimental setup.

The Prandtl number Pr was set to 0.7 while the Schmidt number of helium Sc_{He} is set to 0.2. The dynamic viscosity μ has a constant value of $1.8877 \times 10^{-5}\,\mathrm{kg\,m^{-1}\,s^{-1}}$

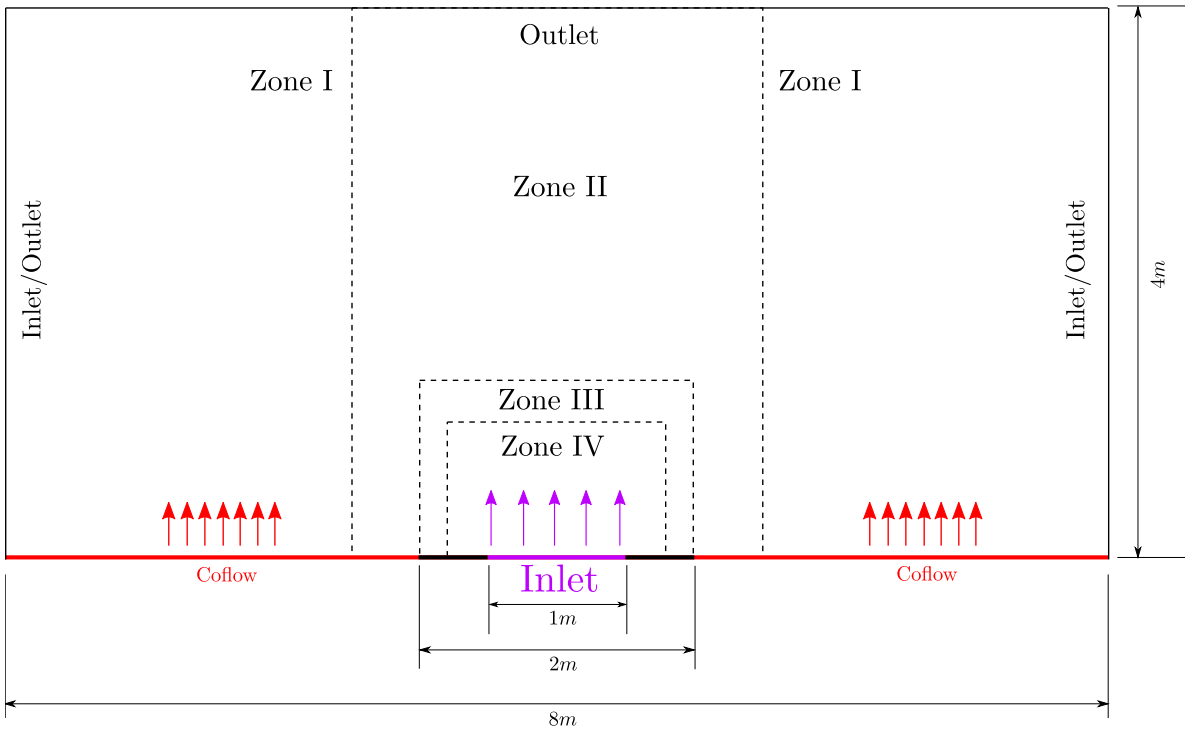

Figure 8.2: Schematic of the computational domain including refinement zones and boundary conditions.

for both air and helium. Resulting in a Reynolds number Re $\simeq$ 3220 and a Richardson number Ri $\simeq$ 75.4, matching the experiment.

In the case of homogeneous isotropic turbulence, the model constant is estimated as $C_s = 0.2$ [191]. However, C_s depends on the flow configuration with values of $C_s \approx 0.1 - 0.2$ often used [78]. In our simulations, the Smagorinsky constant C_s is set to 0.1 as suggested by Maragkos *et* al. [154]. The un-resolved SGS species diffusion fluxes $J^{sgs}_{k,\alpha} = \overline{\rho}(\widetilde{u_\alpha}\widetilde{Y} - \widetilde{u_\alpha Y})$, in the species equation are modelled using the gradient diffusion hypothesis model as:

$$J^{sgs}_{k,\alpha} = -\frac{\mu_t}{\mathrm{Sc}_t}\frac{\partial \widetilde{Y}}{\partial x_\alpha} \tag{8.1}$$

Turbulent Schmidt Sc_t as well as turbulent Prandtl Pr_t are both set to 0.5 as Maragkos *et* al. [154] and Chung *et* al. [40]. Nevertheless, a sensitivity study on the value of Sc_t is done in Sec. 8.5.

The large-eddy simulation is run for 26 s of physical time. The first 13 s are to ensure the evacuation of the initial field and to reach statistically stationary flow conditions, and the other 13 s are used to construct the mean and rms quantities of the plume. The

simulations are performed at a constant CFL number equals to 0.6 such that the time step would depend on the local mesh size. The CFL number is defined as:

$$\mathrm{CFL}_u = \frac{(u + c_{red})\delta t}{\delta x} \tag{8.2}$$

where c_{red} denotes the fictitious reduced speed of sound following the low-Mach number approximation. Consequently, time step is local and depends on the grid size so that time step at each zone will be $\delta t_{ZoneI} \simeq 3.6 \times 10^{-4}$ s, $\delta t_{ZoneII} \simeq 1.8 \times 10^{-4}$ s, $\delta t_{ZoneIII} \simeq 9 \times 10^{-5}$ s and $\delta t_{ZoneIV} \simeq 4.5 \times 10^{-5}$ s. The simulations are parallelized on 128 cores on a Dell PowerEdge C6420 server with 4× 32-core Intel Xeon Gold 6142, 2.6 GHz and 96 GB RAM. The computational cost of the simulation with the finest mesh is compared to other studies in Table 8.1. The proposed LBM numerical model is significantly faster (considering the mesh resolution), demonstrating a clear evidence of the strength and efficiency of LBM.

Reference	mesh	δx_{min}	t_{total}	CPU hours / 1 sec	CPU hours / 1 sec / 1M cells
DesJardin *et* al. [50]	2.5M	1.6 cm	20 sec	700	280
Maragkos *et* al. [154]	1.26M	1.23 cm	30 sec	78	62
Current study	4M	1 cm	26 sec	108	27

Table 8.1: Cost comparison between different numerical studies for the finest mesh.

8.3 Results

8.3.1 Turbulence

Figure 8.3 shows the energy spectrum based on the axial velocity at $z = 0.5$ m. The turbulent kinetic energy decay in the inertial range is correctly reproduced.

8.3.2 Instability modes

Figure 8.4 shows the typical puffing cycle. A puffing cycle can be divided into four distinct phases: In the first phase, instabilities form near the edge of the plume as observed in Fig. 8.4(a). The trigger of these instabilities is the misalignment of pressure and density gradients which generates a localized torque (baroclinic torque). Those instabilities grow and entrain large quantity of the surrounding fluid, forming into a toroidal vortex as shown in Fig. 8.4(b). While this vortex moves upwards more fluid is

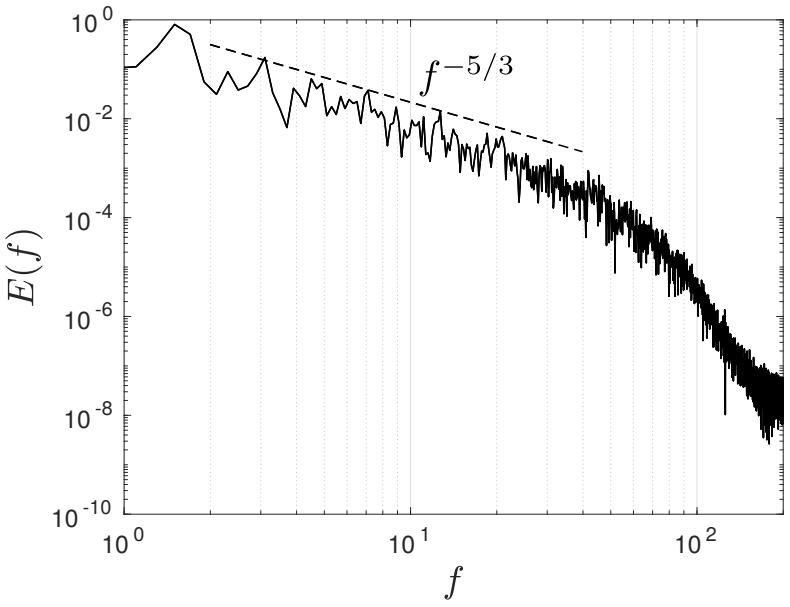

Figure 8.3: Temporal energy spectrum at $z = 0.5\ m$ for axial velocity. Dashed line indicate the expected characteristic slope of $-5/3$ [122].

pumped at the center of the plume causing a large streamwise velocity at the centerline as shown in Fig. 8.4(c). The increase in streamwise velocity at the centerline causes a sharp increase in cross-stream velocity near the base of the plume, as a result of mass conservation, providing a perturbation of the mixing layer for the next cycle (Fig. 8.4(d)).

In the experiment [183] they used honeycomb source which suppress turbulence in the inlet flow causing the flow to be laminar, as a result our inflow condition is laminar and we do not introduce any turbulence injection. Nevertheless, strong instabilities are observed at the helium-air interface near the plume source, and it is important to capture those small dynamics as explained in the introduction based on the study of Ahmed and Trouvé [4]. The lack of turbulence source and the deflection of the low velocity helium at the edges of the source, points out that vorticity from plume source is not the responsible for the formation of those structures. Instead, they are generated by buoyancy-driven (gravitational and baroclinic) vorticity generation. Thus, Rayleigh-Taylor and Kelvin-Helmholtz instabilities are triggered, near the base of the plume, and at last they will form the toroidal structures [50, 183] as shown in Fig. 8.4(d).

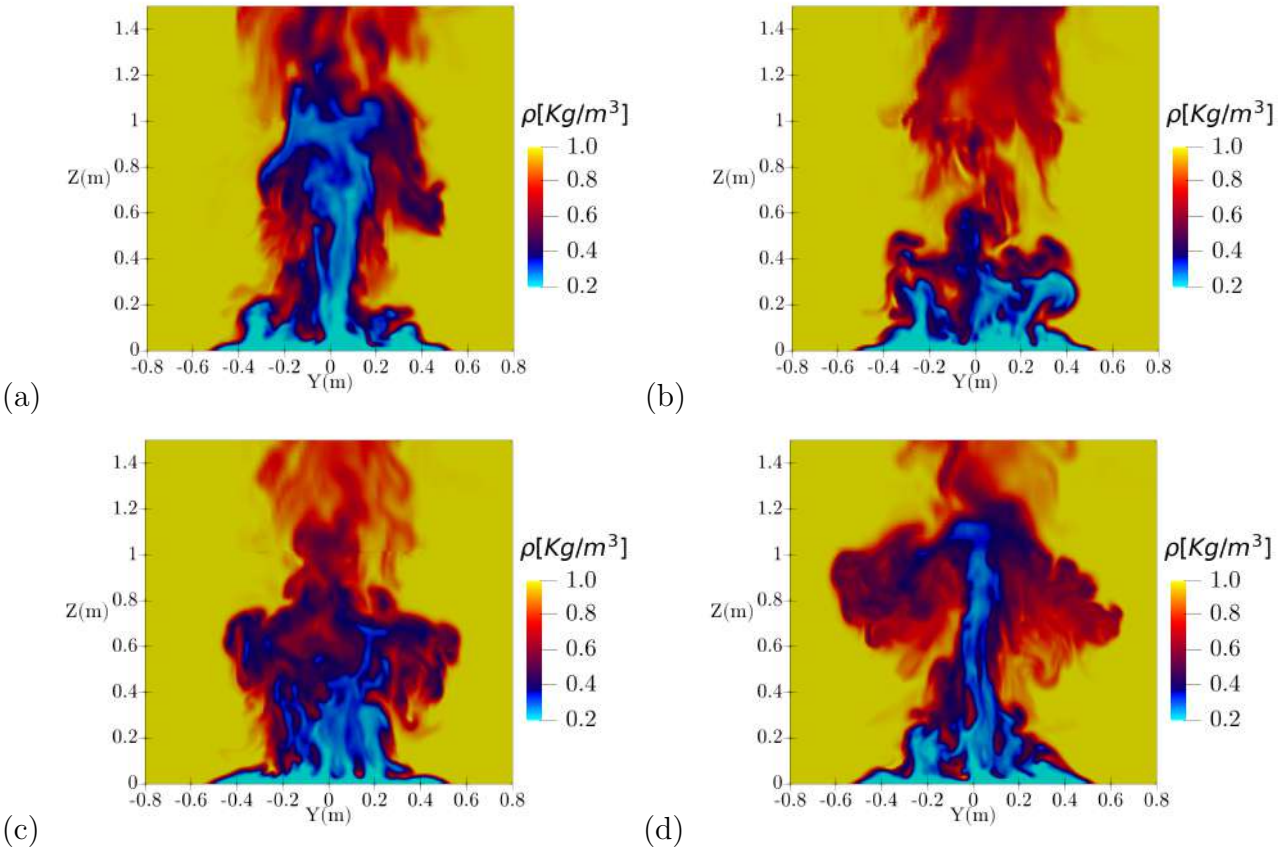

Figure 8.4: Instantaneous iso-contours of density showing a complete puffing cycle. 4 instances were captured which extend for around 0.7 sec which is the periodic time of a puffing cycle.

8.3.3 Vortex dynamics

A better understanding can be attained from the analysis of the vorticity equation (derivation in Appendix A.2), in order to reveal how vorticity is generated and transported downstream by convection and diffusion. The vorticity equation writes:

$$\frac{D\boldsymbol{\omega}}{Dt} = \underbrace{(\boldsymbol{\omega}\cdot\nabla)\mathbf{u}}_{\text{vortex stretching}} - \underbrace{\boldsymbol{\omega}(\nabla\cdot\mathbf{u})}_{\text{dilatation term}} + \underbrace{\frac{1}{\rho^2}(\nabla\rho\times\nabla p)}_{\text{baroclinic torque}} + \underbrace{\frac{\rho_0}{\rho^2}(\nabla\rho\times g)}_{\text{gravitational torque}} + \underbrace{\nabla\times(\frac{1}{\rho}\nabla\cdot\tau)}_{\text{viscous diffusion}} \tag{8.3}$$

On the right hand side of Eq. (8.3), five different physical mechanisms affect the vorticity transport. Those five terms are identified as vortex stretching, dilatation term, baroclinic torque, gravitational torque and viscous diffusion [113]. In incompressible flows, only the first term prevails. Vortex stretching represents the enhancement of vorticity by stretching, it is an essential mechanism by which turbulent energy is trans-

ferred to smaller scales. The dilatation term represents the effects of vorticity field expansion which causes a decrease in vorticity magnitude. Gravitational torque generates vorticity due to the misalignment of gravity and density gradients, while baroclinic torque generates vorticity as a result of non-aligned pressure and density gradients. In buoyancy-driven flows, both the baroclinic and gravitational torque terms are the principal mechanisms generating flow vorticity [112, 113]. The DNS [114] demonstrated that the gravitational torque is fundamental mechanism promoting cross-stream vorticity. LES studies [50, 154] observed that during typical puffing cycle, the maximum gravitational torque is located at the base of the plume. The same behaviour can be observed in the current study, as seen in Fig. 8.5 where the maximum value of gravitational torque is observed at the base of the plume. The contribution of the baroclinic torque has similar importance. Maximum values can be located in zones where large pressure and density gradients exist as observed in Fig. 8.6 near the base of the plume. Both torques trigger the instabilities at the base and then nurture its growth. For large plumes and pool fires, this vortex destabilizes rapidly forming secondary azimuthal, or "finger-like" instabilities that can be detected in Figs. 8.5 and 8.6, which were also observed experimentally [29, 245]. Those secondary instabilities create streamwise vorticity that promote the breakdown of large scale toroidal structures and improves the local mixing eventually. Capturing these instabilities and mechanisms is therefore a prerequisite for pool fire simulation because the combustion process for this type of flows is controlled mainly by the mixing process of fuel and oxidizer.

8.3.4 Puffing frequency

The puffing mechanism is a crucial phenomenon to predict. Fires are diffusion flames where fuel and oxidizer are separate unlike premixed flames. As a result, the combustion process is mainly controlled by the mixing of reactants. The puffing mechanism is a fundamental mixing mechanism in large-scale fires. Consequently, the correct prediction of the frequency of this motion is one of the goals of this study, and in this section we will investigate the effect of different modelling parameters on the predicted puffing frequency.

Mesh resolution and SGS model effects on the puffing cycle of the helium plume are studied. Figure 8.7 shows the temporal signal of the centerline streamwise velocity at $z = 0.5\,\mathrm{m}$. The signal extends over 5 s of physical time, from 13 to 18 s, in order to be compared with the experimental one. The puffing frequency is defined as the number of puffing cycles, a maximum peak of streamwise velocity followed by a minimum trough, which can be identified in the examined timeline. It is worth mentioning that results

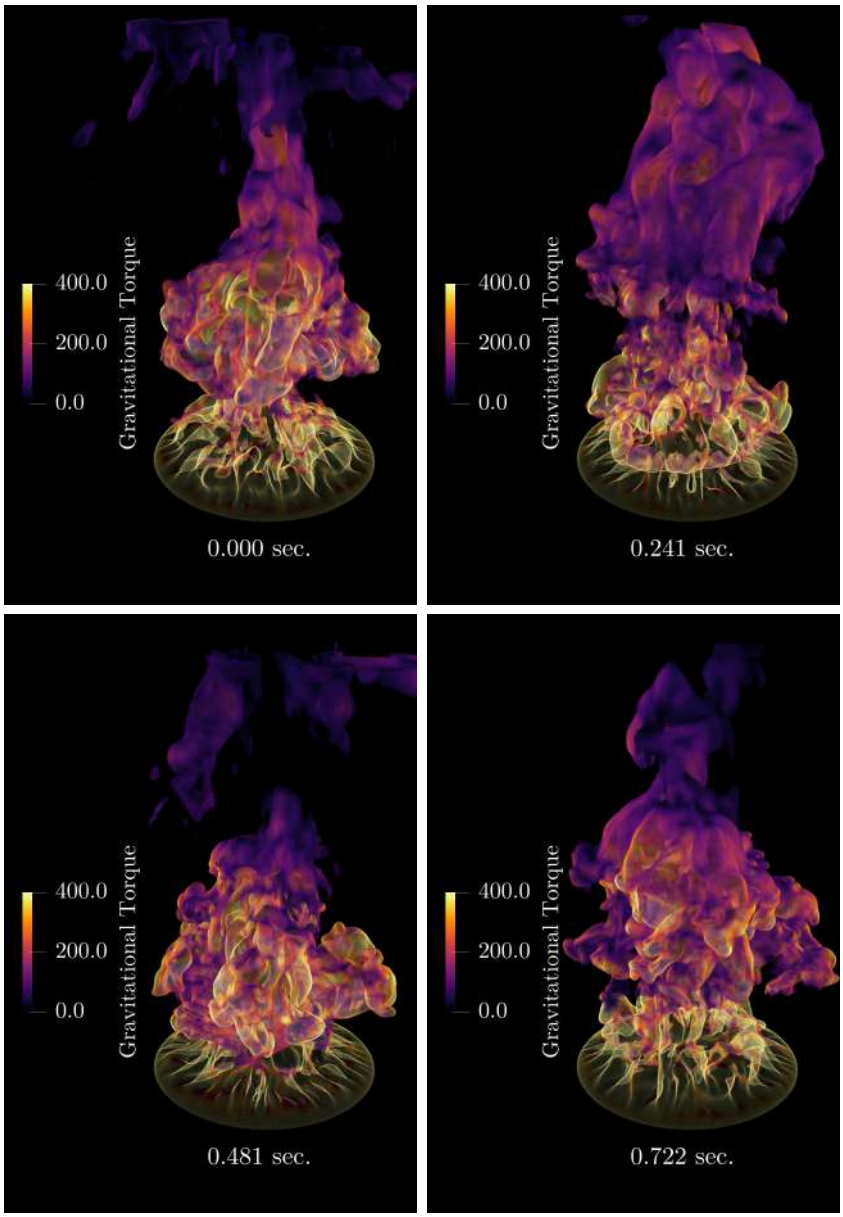

Figure 8.5: Instantaneous iso-volume of density coloured by gravitational torque magnitude showing a complete puffing cycle. From left to right 4 different instances were captured which extend over around 0.7 sec which is the periodic time of a puffing cycle.

revealed a small phase shift compared to the experiment, probably because we do not have the exact same initialization as in the experiment. Thus, the simulation time signals in Fig. 8.7 have been shifted along the time axis to match the first peak of the experimental signal for the sake of clearer comparison.

Maragkos *et* al. [154] reported that for the coarse mesh and without the SGS model, higher frequency modes are more obvious and the puffing cycle is hardly identified. On the contrary, when examining Fig. 8.7, the puffing cycle can be identified for both

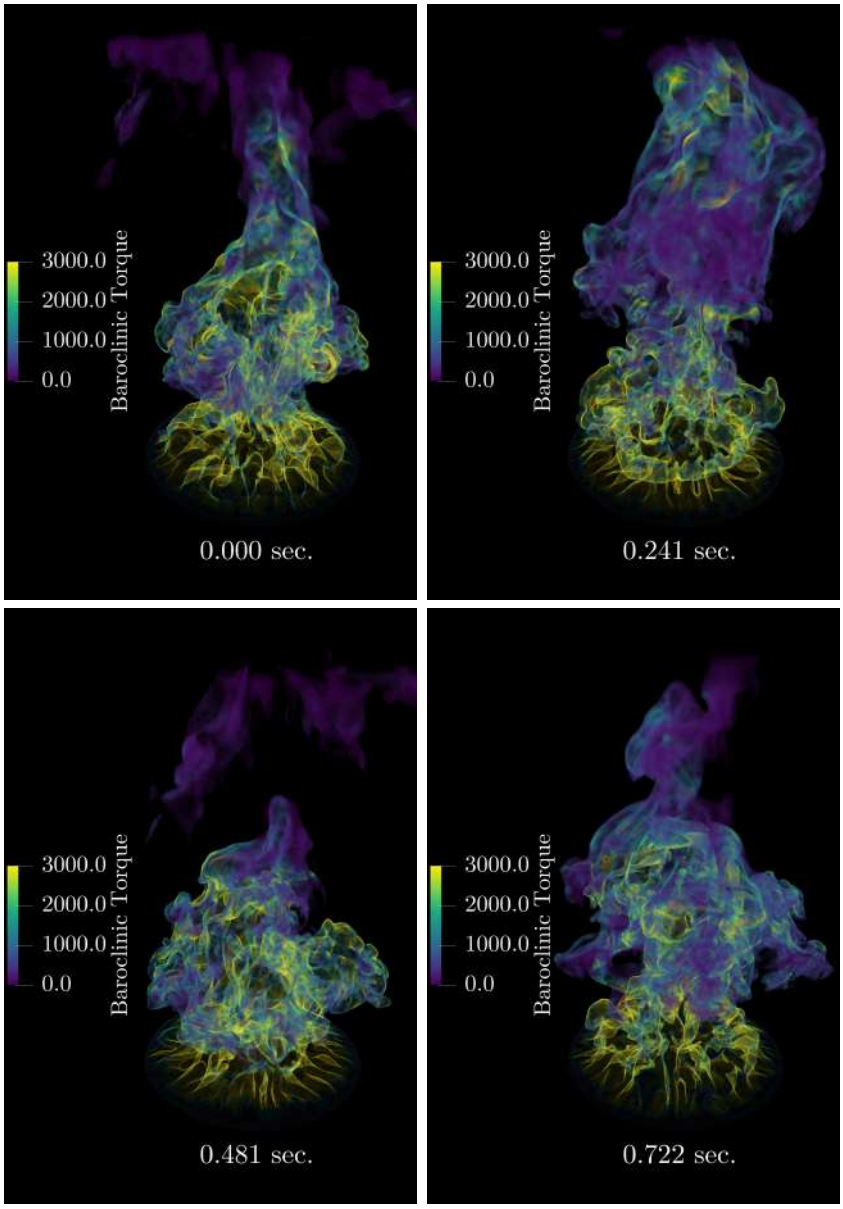

Figure 8.6: Instantaneous iso-volume of density coloured by baroclinic torque magnitude showing a complete puffing cycle. From left to right 4 different instances were captured which extend over around 0.7 sec which is the periodic time of a puffing cycle.

meshes and for all turbulence models, which is inline with the findings of DesJardin *et* al. [50]. However, using a turbulence model damps the higher frequency modes and makes the cycle more distinguishable. The dynamic range (defined as the difference between maximum and minimum values) of the time trace of our simulation agrees well with the experimental readings when using SGS models where as the absence of SGS model introduces some overshoots and high-order fluctuations in the time trace as seen in Fig. 8.7. DesJardin *et* al. [50] had a higher dynamic range than the experiment even

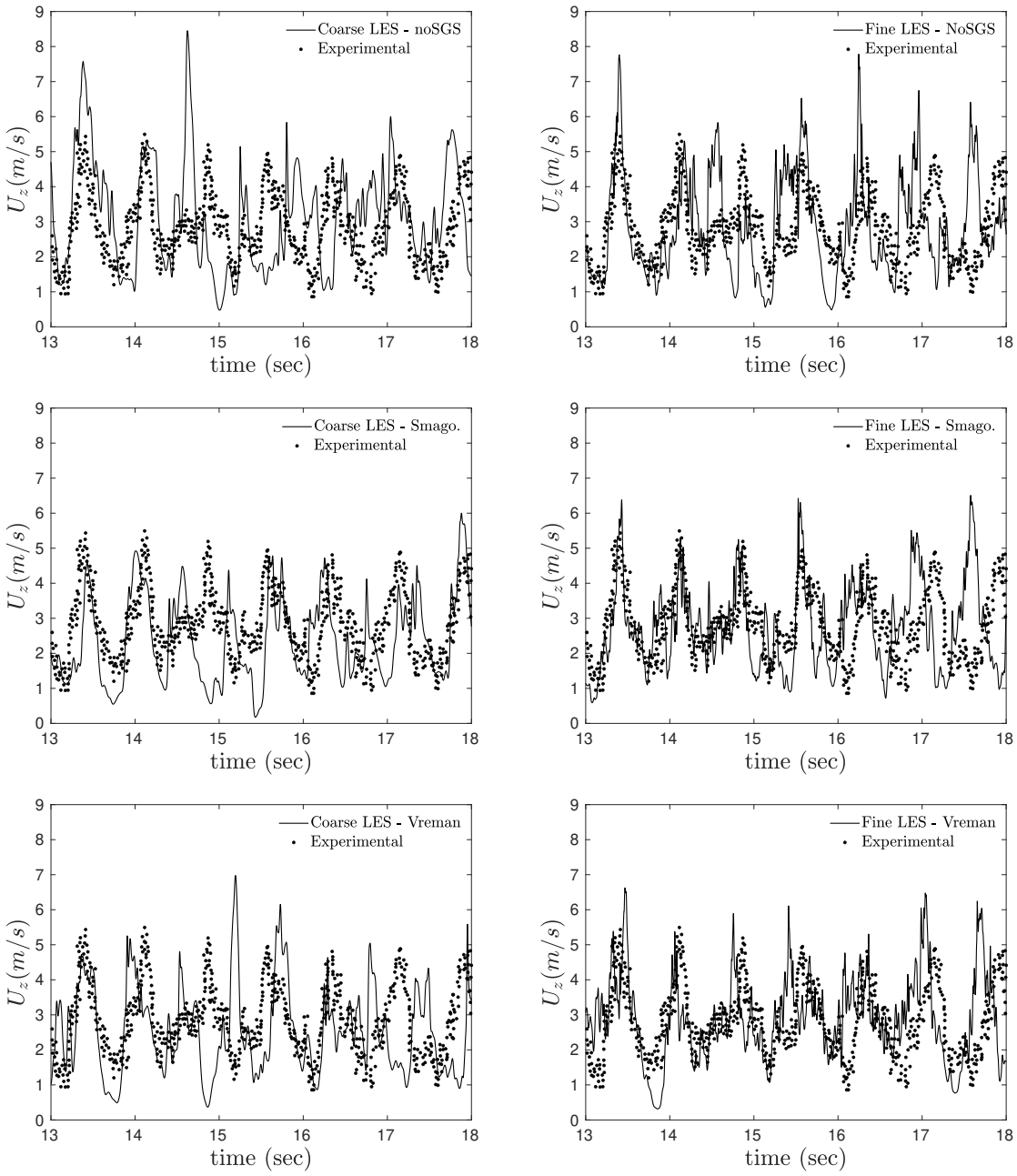

Figure 8.7: Time series of centerline streamwise velocity at $z/D = 0.5$ in a window of 5 s compared to the experiment.

with SGS model, while Maragkos *et* al. [154] obtained a decent agreement in terms of the dynamic range of the time trace.

The number of cycles observed in the 5-sec window depended on the resolution of the mesh regardless of the SGS model applied. For the coarse mesh a total number of around 9 cycles are identified versus the 7 cycles from the experiment [183]. While for the fine mesh we could find 7 cycles, which agrees with the experiments and shows the

impact of the mesh resolution on predicting the puffing phenomenon. Indeed, having finer mesh enables us to correctly predict the instabilities generated near the inlet which is the main trigger of the puffing motion. The same conclusion was made by Maragkos *et* al. [154], DesJardin *et* al. [50] and Ma *et* al. [145] where they emphasized on the importance of the mesh resolution on predicting the correct puffing frequency, increasing the LES grid resolution will improve the frequency estimation.

Figure 8.8 shows the power spectrum of the centerline streamwise velocity at $z = 0.5\,\mathrm{m}$ using Fast Fourier transform (FFT). As the puffing frequency is affected only by the grid resolution, the two diagrams are relative to the coarse grid (left panel) and the the fine grid (right panel). The predicted puffing frequency is 1.69 Hz for the coarse grid and 1.39 Hz for the fine grid whereas the observed experimental frequency was $1.37 \pm 0.1\,\mathrm{Hz}$. Consequently, the result of the coarse mesh overestimates the frequency. While refining the mesh improves the predictions to match the experimental value. It should be also pointed out that the predicted puffing frequency on the fine mesh is consistent with the experimental correlation proposed by Cetegen and Kasper [30] $f = 0.8\mathrm{Ri}^{0.38} U_p/D_p = 1.34\,\mathrm{Hz}$ from measurements of helium-air plumes for $\mathrm{Ri} < 100$. It should be pointed out that Ri is a modified Richardson number defined as $\mathrm{Ri}_1 = (\rho_\infty - \rho) g D_p/(\rho_\infty U p^2) \simeq 76$. Furthermore, the results are inline with the experimental correlation given by Cetegen and Ahmed [29] for buoyant diffusion flames (i.e. pool fire) of various fuels $f = 1.5/\sqrt{D_p} = 1.5\,\mathrm{Hz}$. The disparity from the previous correlation can be attributed to the fact that it was suggested for diffusion flames which is not our case.

Ma *et* al. [145] presumed that to be able to perfectly predict this puffing motion and its frequency, the mesh must be sufficiently small near the inlet to resolve the boundary layer as it is the source of the instability that triggers the puffing mechanism. This conclusion was also discussed afterwards by Ahmed and Trouvé [4].

8.3.5 Statistics of velocity and mass fraction

The mean values and high order statistics (i.e. rms) are discussed in the present study. In all the figures the data with bars represents the experimental results of O'Hern *et* al. [183] including the experimental uncertainties as explained in Sec. 8.1. Furthermore, we added the results of the LES presented by Marakgos *et* al. [154], DesJardin *et* al. [50] and Ma *et* al. [145] for more comparison.

Figure 8.9 shows the centerline mean and rms profiles of the streamwise velocity up to $z = 0.8\,\mathrm{m}$ above the helium source. For the mean profiles, all cases stay within the experimental uncertainties at all locations along the plume axis. Best agreement

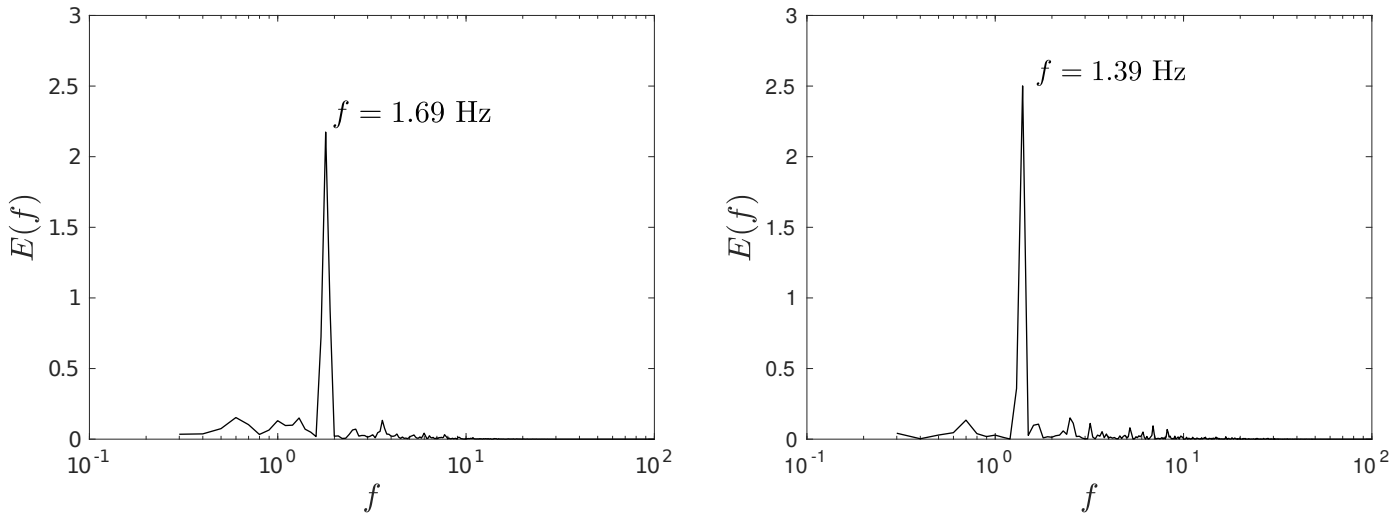

Figure 8.8: Power spectrum of the centerline streamwise velocity U_z for (left) the coarse mesh and (right) the fine mesh. The principle frequency (i.e. puffing frequency) is indicated on the figures. The sampling time ts to construct the power spectrum is taken to be each 10 time steps that is $ts_{coarse} = 9 \times 10^{-4}$ sec and $ts_{fine} = 4.5 \times 10^{-4}$ sec for the coarse and fine mesh, respectively.

spotted on the fine mesh using Smagorinsky model. Nonetheless, the rms profile is harder to match but we still have a good agreement being within the experimental uncertainties. There is an overestimation near the inlet for simulations performed on the coarse grid. Best agreement is achieved through simulations on the fine mesh regardless of the turbulence model, the best among them is where no SGS model is incorporated. The results are also consistent with the findings of Maragkos *et* al. [154].

The mean and rms profiles of helium mass fraction on the centerline up to a height of $z = 0.8\,\mathrm{m}$ are demonstrated in Fig. 8.10. The mean Y_{He} profiles shows less satisfactory agreement, the decay of the mean values are slow compared to the experiment beyond $z = 0.3\,\mathrm{m}$. The same exact behaviour was detected by Maragkos *et* al. [154]. The rms Y'_{He} profile is over-predicted at all the heights, however, we show a better estimation of Y'_{He} than Marakgos *et* al. [154]. It worth noting that the use of SGS model enhances the results and decreases the discrepancies to the experimental data.

The radial profiles of mean streamwise velocity at several downstream locations ($z = 0.2\,\mathrm{m}$, $0.4\,\mathrm{m}$ and $0.6\,\mathrm{m}$ above the inlet) are presented in Fig. 8.11. All our simulations show a satisfactory agreement with the experimental data and fall within the experimental uncertainties, except at height $z = 0.2\,\mathrm{m}$ where we can notice slight violations of the simulations performed on the coarse mesh at few radial locations. The

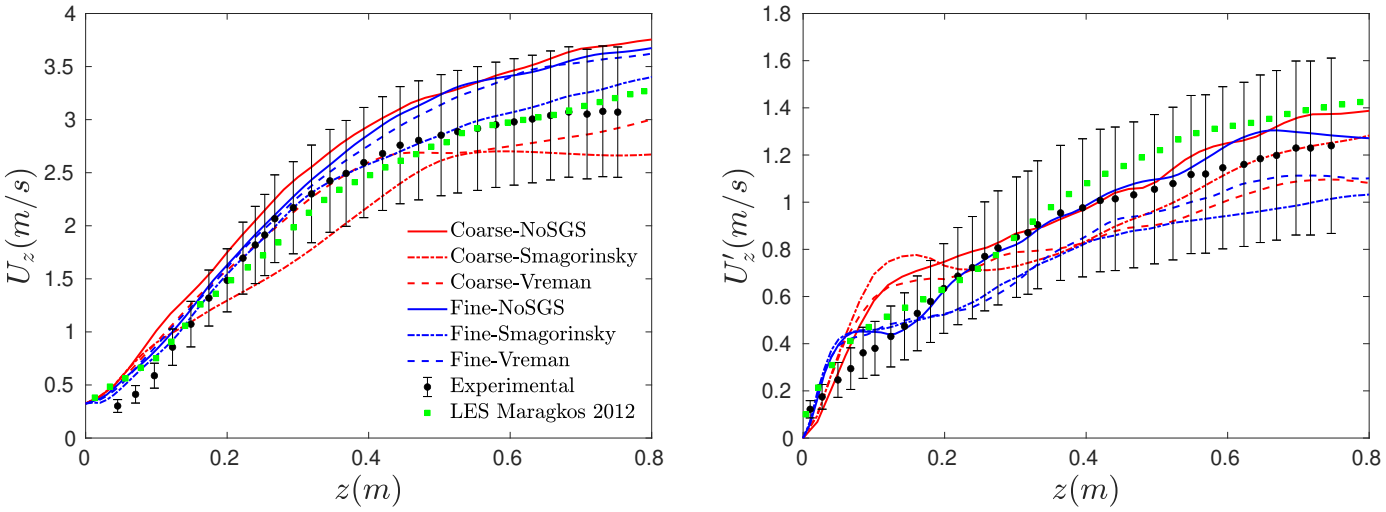

Figure 8.9: Comparison of mean (left) and rms (right) of centerline streamwise velocity. The experimental data includes the respective uncertainties reported in the experimental study [183]. The numerical results of Maragkos *et* al. [154] are also added.

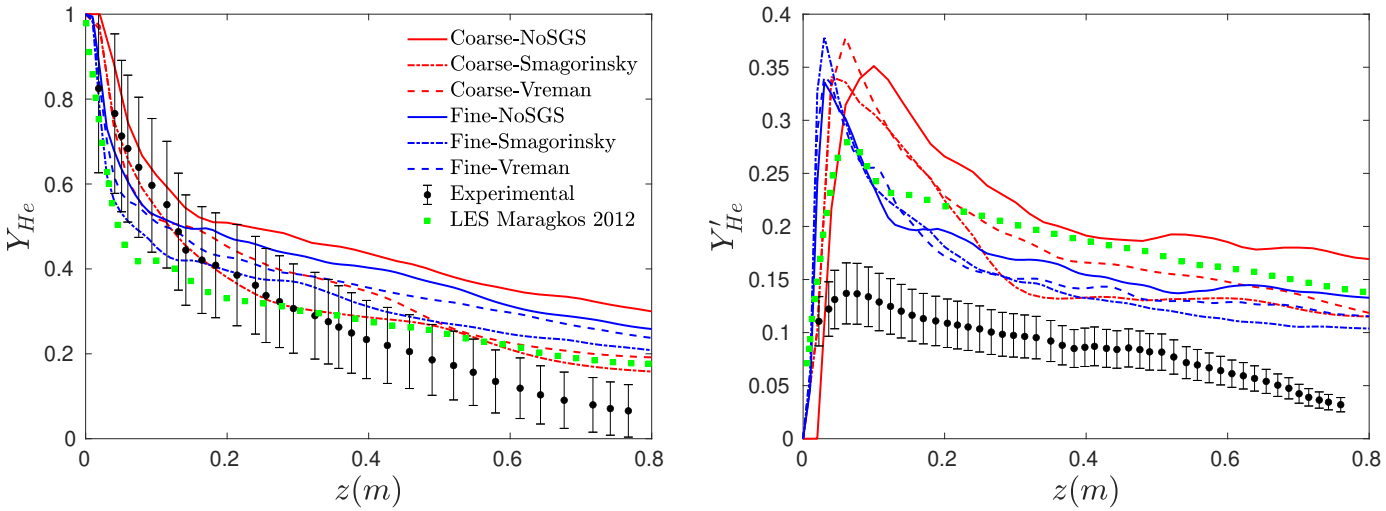

Figure 8.10: Comparison of mean (left) and rms (right) of centerline helium mass fraction. The experimental data includes the respective uncertainties reported in the experimental study [183]. The numerical results of Maragkos *et* al. [154] are also added.

results are also inline with the numerical results [50, 145, 154]. We should mention that all the radial profiles are azimuthally averaged all around the plume.

Figure 8.12 shows rms values of the streamwise velocity at different heights. The results are inline with experimental data, the results are enhanced for the fine mesh, particularly when applying turbulence models. At $z = 0.2\,\mathrm{m}$, the rms is overestimated at the radial position $r = 0.25\,\mathrm{m}$ which was the same finding of Maragkos *et* al. [154].

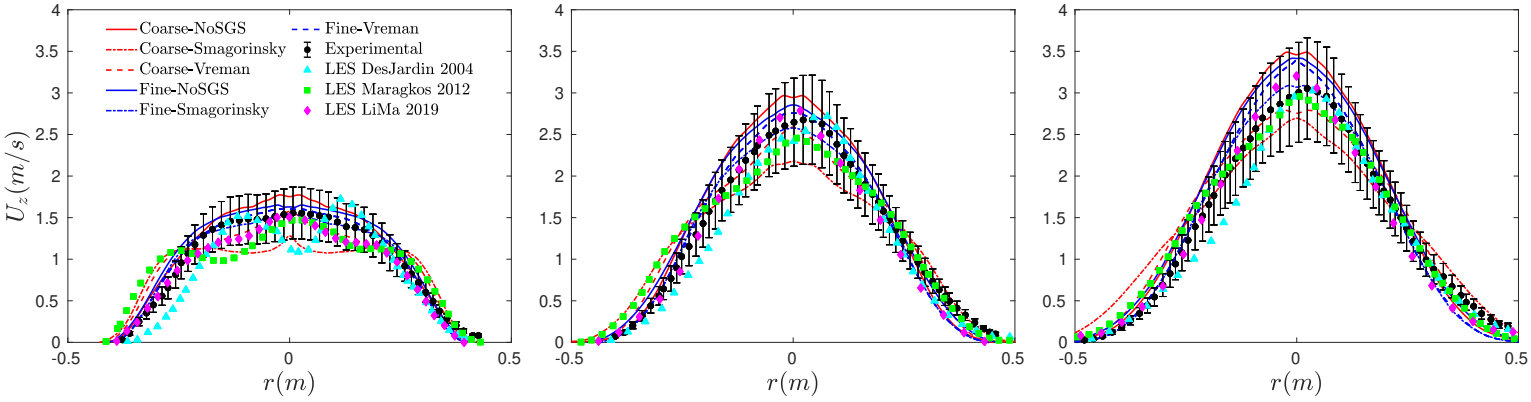

Figure 8.11: Comparison of mean radial profiles of streamwise velocity for different resolutions and different turbulence models at heights $z = 0.2\,\mathrm{m}$ (left), $z = 0.4\,\mathrm{m}$ (middle) and $z = 0.6\,\mathrm{m}$ (right). The experimental data includes the respective uncertainties reported in the experimental study [183]. Numerical data are also presented [50,145,154].

Desjardin *et* al. [50] overpredicted the centerline rms values at all heights.

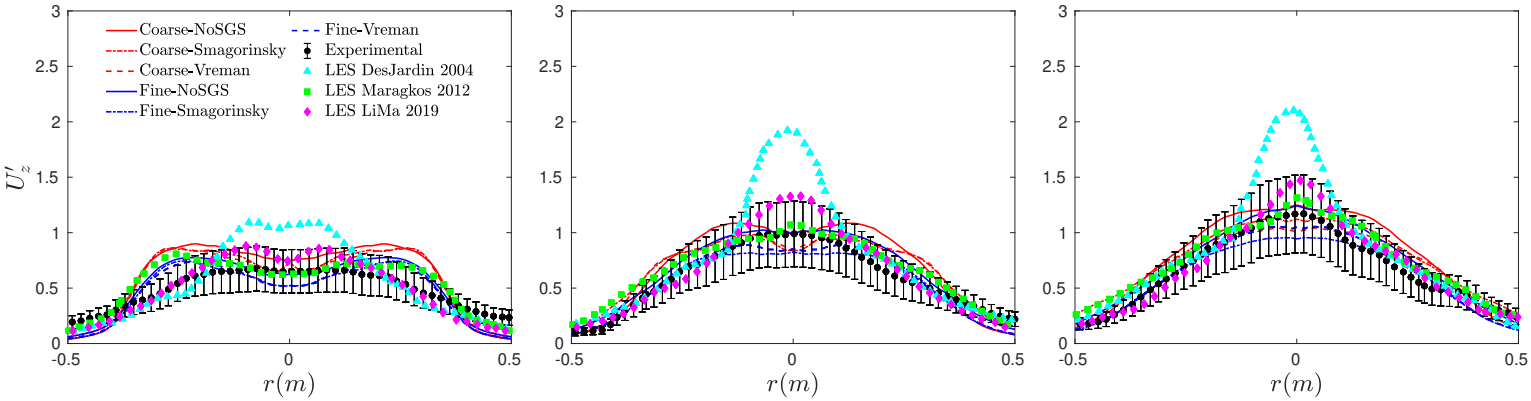

Figure 8.12: Comparison of rms radial profiles of streamwise velocity for different resolutions and different turbulence models at heights $z = 0.2\,\mathrm{m}$ (left), $z = 0.4\,\mathrm{m}$ (middle) and $z = 0.6\,\mathrm{m}$ (right). The experimental data includes the respective uncertainties reported in the experimental study [183]. Numerical data are also presented [50,145,154].

The cross-stream velocity is presented in Fig. 8.13. Our results show a good overall agreement with the experimental data, the profiles are more satisfactory when the resolution is increased. The effect of the SGS model is not significant in this case specially when using the fine mesh. Maragkos *et* al. [154], DesJardin *et* al. [50] and Ma *et* al. [145] reported an overestimation on the left hand side of the plume as seen in Fig. 8.13. While keeping in mind that the experimental data are not perfectly symmetric, we have the same behaviour at $z = 0.2\,\mathrm{m}$ but the disparities in our results are lower. Afterwards farther downstream, the agreement becomes better, even better than

the previous numerical studies. The application of SGS models did not increase the cross-stream velocity as reported by Maragkos *et* al. [154], on the contrary, the SGS has no significant effect on the discrepancies between our simulations and the experimental data.

A rise of the cross-stream velocity indicates an increased entrainment from the surrounding fluid which will result in a surge in the streamwise velocity following the conservation of mass. So accurate predictions of the cross-stream velocities is crucial, as in these type of flows, entertainment controls the mixing (as elaborated in a previous work [220]) which is a fundamental parameter in pool fires where the combustion process is mainly controlled by mixing (i.e. diffusion flame) as will be seen in Chapter 9.

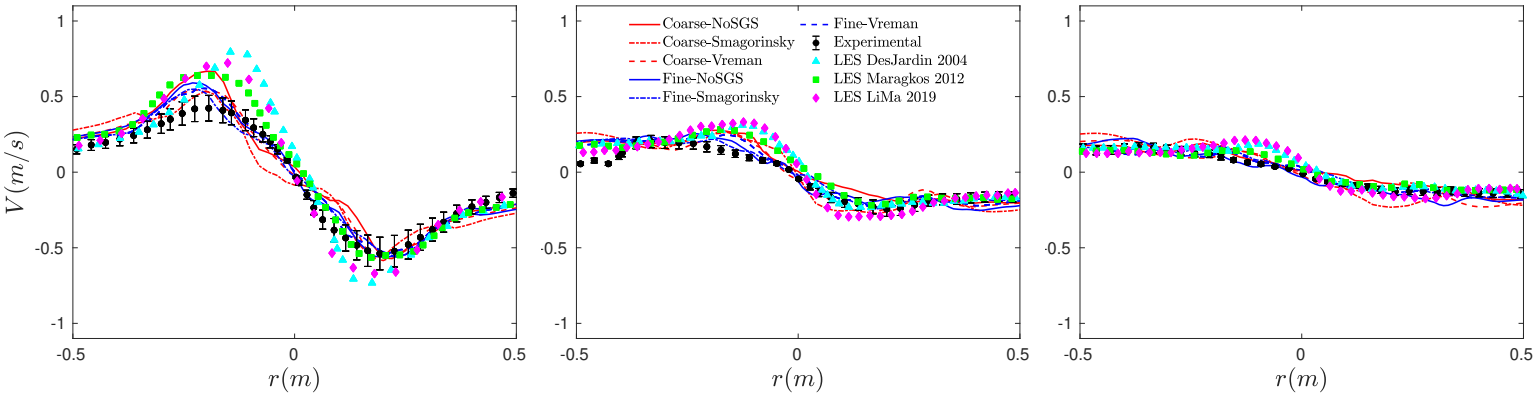

Figure 8.13: Comparison of mean radial profiles of cross-stream velocity for different resolutions and different turbulence models at heights $z = 0.2\,\mathrm{m}$ (left), $z = 0.4\,\mathrm{m}$ (middle) and $z = 0.6\,\mathrm{m}$ (right). The experimental data includes the respective uncertainties reported in the experimental study [183]. Numerical data are also presented [50,145,154].

Figure 8.14 demonstrates the rms values of the cross-stream velocity at different heights. The results agree with the experiment falling within the uncertainties except at some radial locations where we exhibit a slight overestimation. Our simulations showed a bimodal pattern for the rms of the cross-stream velocities, coherent with what was remarked by Chung *et* al. [40], DesJardin *et* al. [50] and Maragkos *et* al. [154]. This bimodal pattern disappears gradually with elevation. There is no clear conclusion that can be drawn about the effect of the mesh resolution nor the SGS model, all the simulations are almost similar with slight disparities.

The radial profiles of mean helium mass fraction at different heights are presented in Fig. 8.15. Global slight overestimation can be observed specially at $z = 0.2\,\mathrm{m}$ at the left side of the plume. Generally speaking, applying SGS model improves the profiles by decreasing the gap with the experimental data. The discrepancies of the centerline value increase with height consistently with the overestimation in the axial profile seen

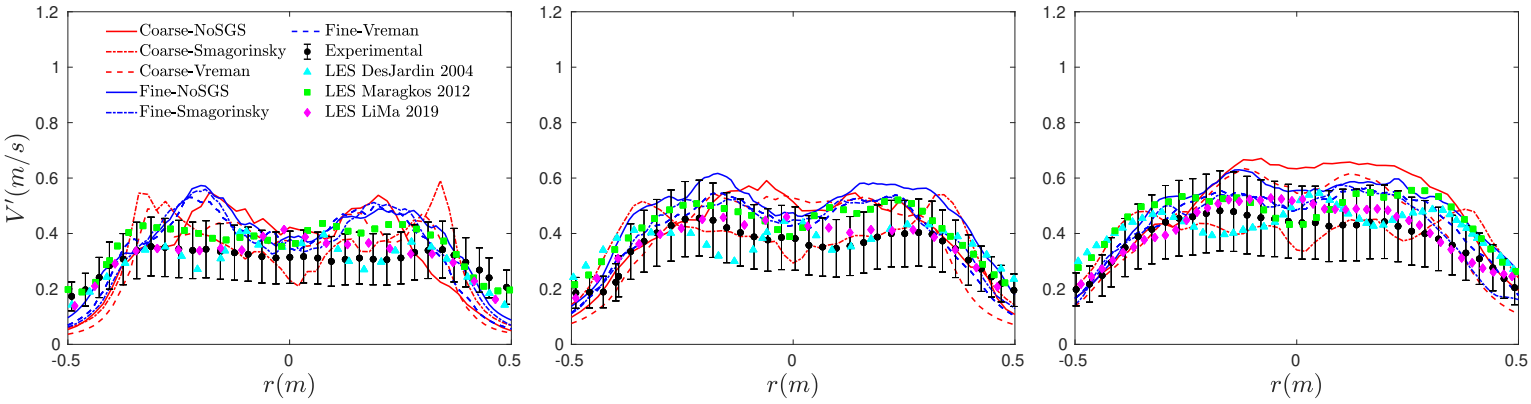

Figure 8.14: Comparison of rms radial profiles of cross-stream velocity for different resolutions and different turbulence models at heights $z = 0.2\,\mathrm{m}$ (left), $z = 0.4\,\mathrm{m}$ (middle) and $z = 0.6\,\mathrm{m}$ (right). The experimental data includes the respective uncertainties reported in the experimental study [183]. Numerical data are also presented [50,145,154].

in Fig. 8.10. The profiles align better with the experiment farther from the centerline. The LES of Maragkos *et* al. [154] is in a better agreement in comparison with the experimental data.

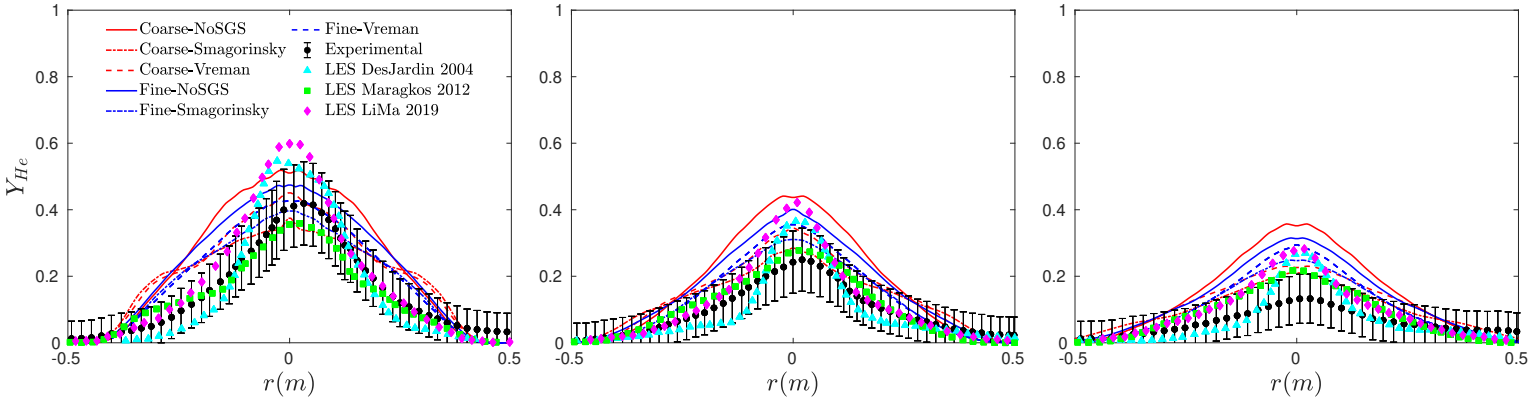

Figure 8.15: Comparison of mean radial profiles of helium's mass fraction for different resolutions and different turbulence models at heights $z = 0.2\,\mathrm{m}$ (left), $z = 0.4\,\mathrm{m}$ (middle) and $z = 0.6\,\mathrm{m}$ (right). The experimental data includes the respective uncertainties reported in the experimental study [183]. Numerical data are also presented [50, 145, 154].

Figure 8.16 shows the radial profiles of the rms values of helium mass fraction. Globally, a significant over-prediction from the experimental data is observed close to the plume inlet for all the simulation, disparities reduce farther downstream the source. Obviously, activating SGS models improves the estimation a bit but still overestimated. The results are consistent with the findings of the previous numerical studies

[50, 145, 153].

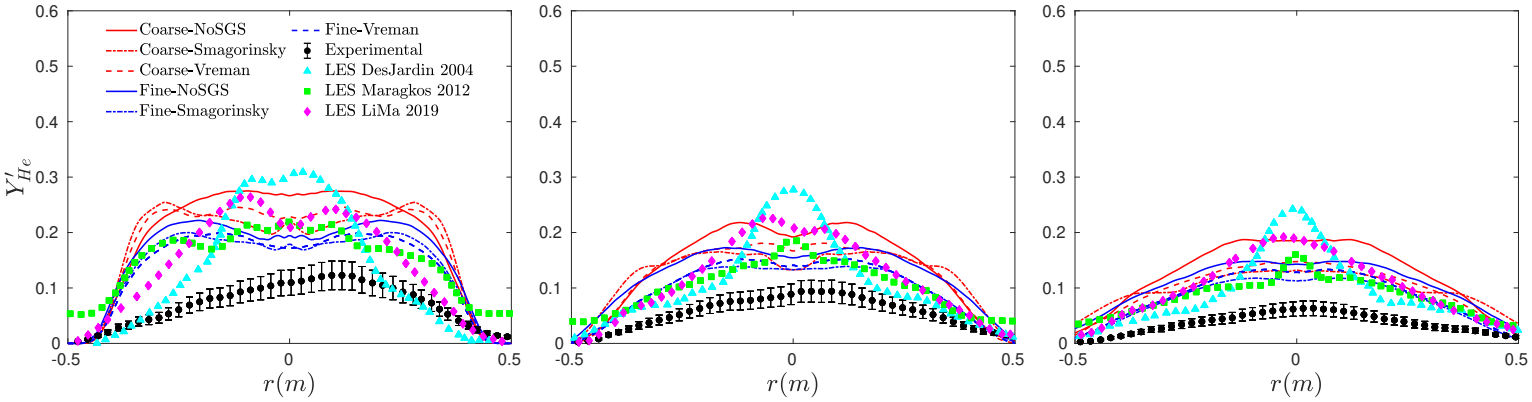

Figure 8.16: Comparison of rms radial profiles of helium's mass fraction for different resolutions and different turbulence models at heights $z = 0.2\,\mathrm{m}$ (left), $z = 0.4\,\mathrm{m}$ (middle) and $z = 0.6\,\mathrm{m}$ (right). The experimental data includes the respective uncertainties reported in the experimental study [183]. Numerical data are also presented [50, 145, 154].

8.4 LES resolution

The ratio between the SGS and the laminar viscosity, μ_t/μ, is shown in Fig. 8.17 and Fig. 8.18. It is observed that the ratio μ_t/μ for the fine mesh is 2-2.5 times smaller when compared to the coarse mesh. Furthermore, in all the profiles, the Smagorinsky model adds more viscosity than the Vreman model. Fig. 8.18 shows that the maximum radial value of μ_t/μ is found at the edges of the plume where maximum shear occurs. By examining Fig. 8.17 one can conclude that fluctuations increase further downstream the inlet, and the value μ_t/μ increases correspondingly. Maragkos *et* al. [154] showed more or less the same levels of the SGS viscosity μ_t.

8.5 Sc_t sensitivity analysis

The turbulent Schmidt number Sc_t is used to calculate the SGS species flux via $\mathrm{Sc}_t = \nu_t/\mathcal{D}_{k,t}$. In our main results in the previous sections, we used a value $\mathrm{Sc}_t = 0.5$ to match the work of Maragkos *et* al. [154]. It is of a great interest to examine the impact of Sc_t on the results. The sensitivity analysis on Sc_t will be conducted on the fine mesh while keeping the Smagorinsky constant $C_s = 0.1$ with Vreman model as our SGS model. Four values of Sc_t will be compared 0.1, 0.2, 0.5 (the baseline case), and ∞. Based on

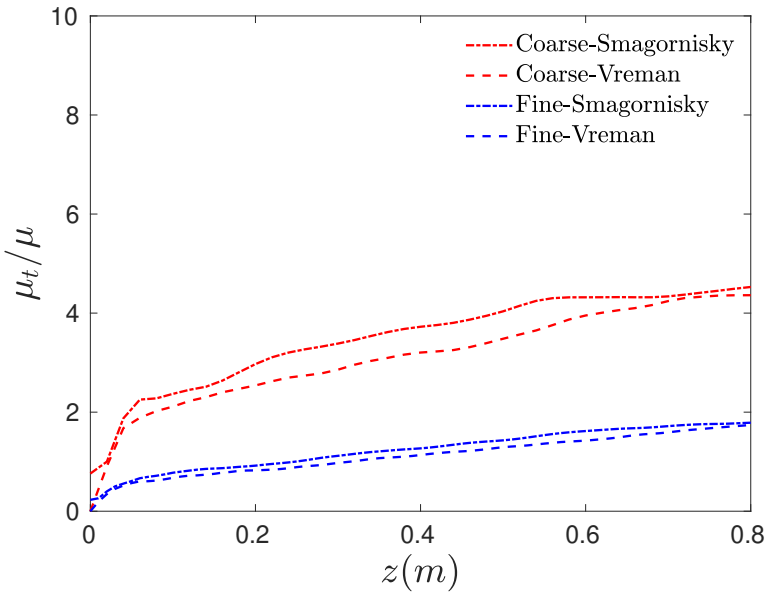

Figure 8.17: Centerline profile of the ratio between SGS to laminar viscosity,μ_t/μ.

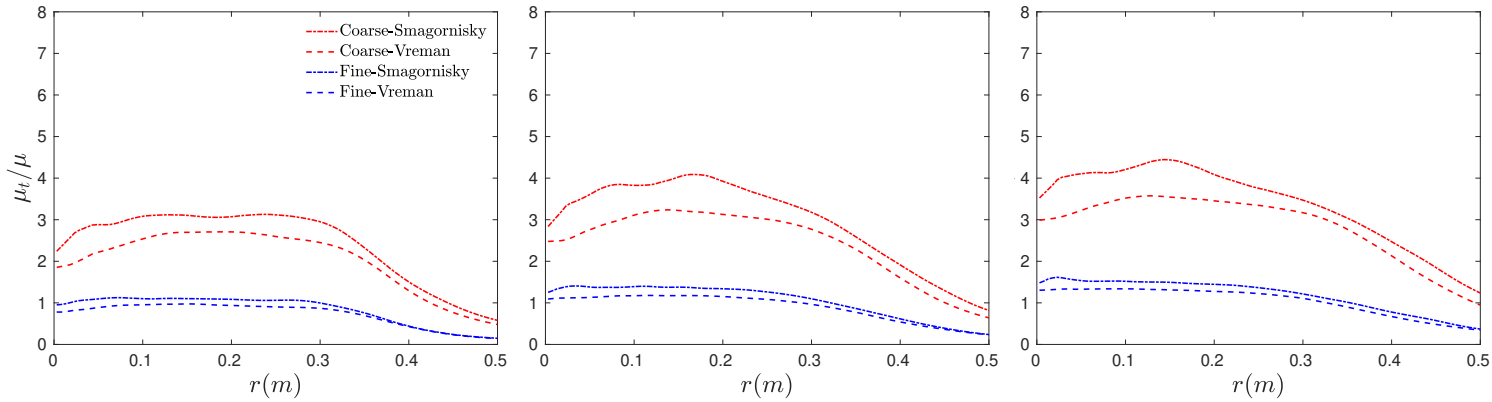

Figure 8.18: Radial profiles of ratio between SGS and laminar viscosity, μ_t/μ for different resolutions and different turbulence models at heights $z = 0.2\,\mathrm{m}$ (left), $z = 0.4\,\mathrm{m}$ (middle) and $z = 0.6\,\mathrm{m}$ (right).

the definition $\mathrm{Sc}_t = \nu_t/\mathcal{D}_{k,t}$, the value $\mathrm{Sc}_t = \infty$ means that we have no SGS species diffusion flux.

The puffing frequency, not shown here, was not affected by the change of Sc_t. Fig. 8.19 shows that the centerline profiles of the streamwise velocity U_z are all within the experimental uncertainties for all values of Sc_t except for $\mathrm{Sc}_t = 0.1$ which generally underestimates U_z. In addition, the centerline rms profiles of U_z are in agreement with the experimental data for all values of Sc_t.

The profiles of centerline mean and rms helium mass fraction Y_{He} show more inter-

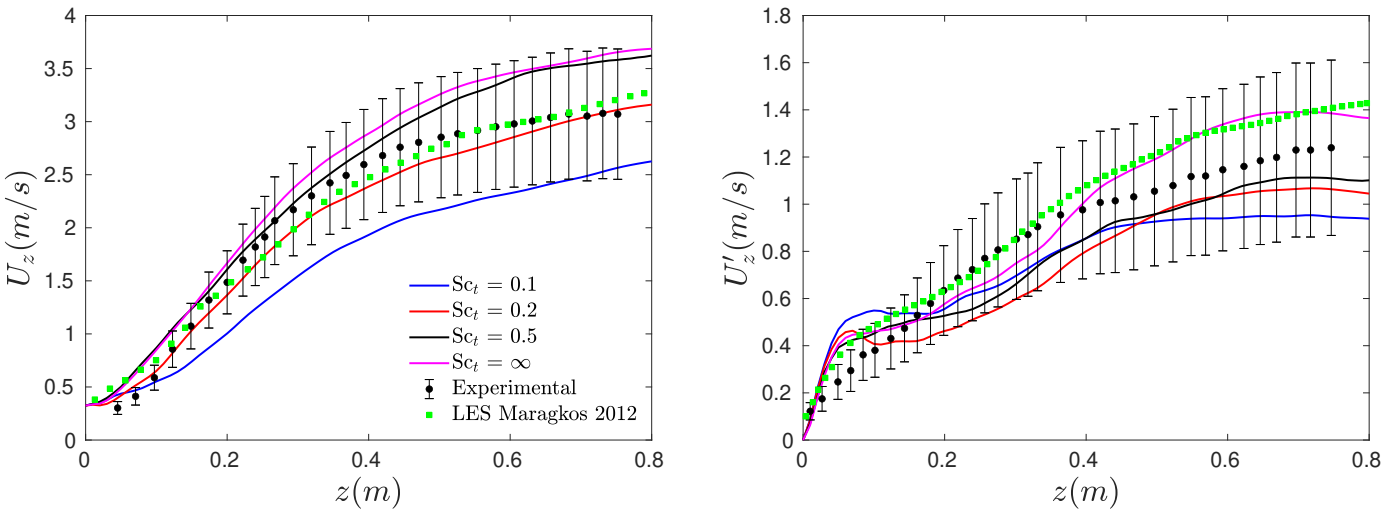

Figure 8.19: Comparison of mean (left) and rms (right) of centerline streamwise velocity for different Sc_t. The experimental data includes the respective uncertainties reported in the experimental study. The numerical results of Maragkos *et* al. [154] are also added.

esting results. Figure 8.20 shows a considerable enhancement for both mean and rms of helium mass fraction when decreasing the value Sc_t. Indeed, the reduction of the turbulent Schmidt number Sc_t will increase the SGS species diffusion flux. It also worth mentioning that the peak near the inlet of the plume presenting in the rms profiles is independent from the value of Sc_t used as the flow is still laminar in this region. These findings contradict the one proposed by Maragkos *et* al. [153], that changing Sc_t has no significant impact on their results.

Figure 8.21 demonstrates the radial profiles of U_z at different heights for the different values of Sc_t. An overall good agreement is observed for all values of Sc_t, except for $\mathrm{Sc}_t = 0.1$ that underestimates U_z near the centerline.

The rms radial profiles of U_z are shown in Fig. 8.22. As deduced before, changing Sc_t does not impact the rms values of U_z, causing all the simulations to lie within the experimental uncertainties.

The mean radial profiles of helium mass fraction Y_{He} show an improvements when decreasing Sc_t, as seen in Fig. 8.23. Enhancements also can be clearly noticed for rms radial profiles of Y_{He} in Fig. 8.24 when decreasing Sc_t. Nevertheless, we still slightly overestimate these profile, yet, consistent with the previous numerical studies [50, 145, 154].

In the light of the previous sensitivity analysis, we recommend using a value of $\mathrm{Sc}_t = 0.2$, as it improved the numerical predictions. This quantification of Sc_t is

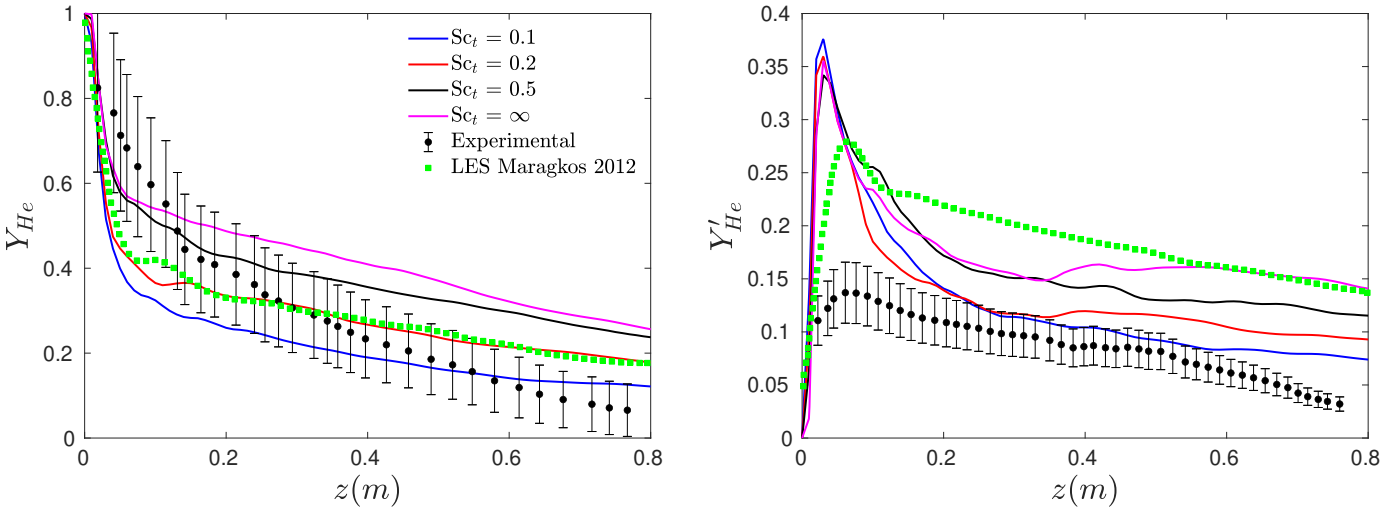

Figure 8.20: Comparison of mean (left) and rms (right) of centerline helium mass fraction for different Sc_t. The experimental data includes the respective uncertainties reported in the experimental study. The numerical results of Maragkos *et* al. [154] are also added.

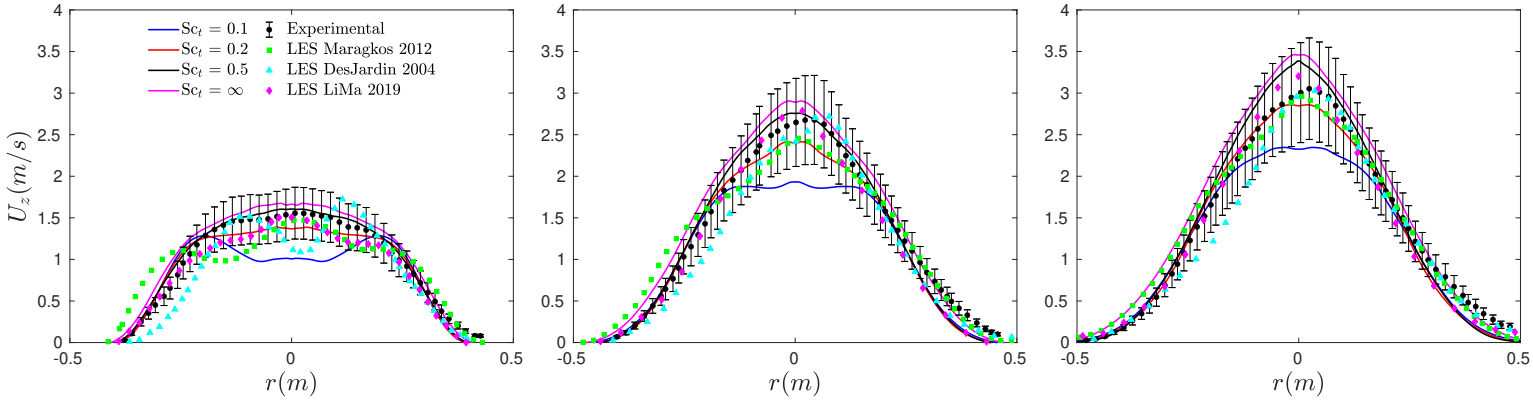

Figure 8.21: Comparison of mean radial profiles of streamwise velocity Uz for different Sc_t at heights $z = 0.2\,\mathrm{m}$ (left), $z = 0.4\,\mathrm{m}$ (middle) and $z = 0.6\,\mathrm{m}$ (right). The experimental data includes the respective uncertainties reported in the experimental study [183]. Numerical data are also presented [50, 145, 154]

not universal, it is only for our setup and our solver, it compensates the lack of grid resolution near the inlet, which should be on order of millimetres [4].

8.6 Concluding remarks

Our pressure-based LBM numerical model with low-Mach number approximation was used to study the near-field region of a buoyant helium plume, and we conclude the

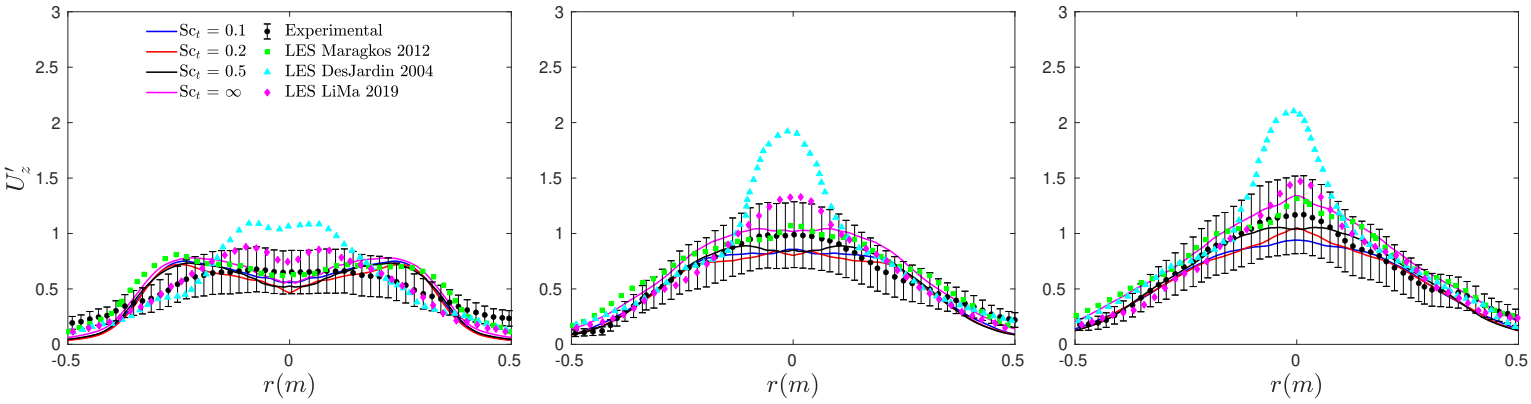

Figure 8.22: Comparison of rms radial profiles of streamwise velocity Uz for different Sc_t at heights $z = 0.2\,\mathrm{m}$ (left), $z = 0.4\,\mathrm{m}$ (middle) and $z = 0.6\,\mathrm{m}$ (right). The experimental data includes the respective uncertainties reported in the experimental study [183]. Numerical data are also presented [50, 145, 154]

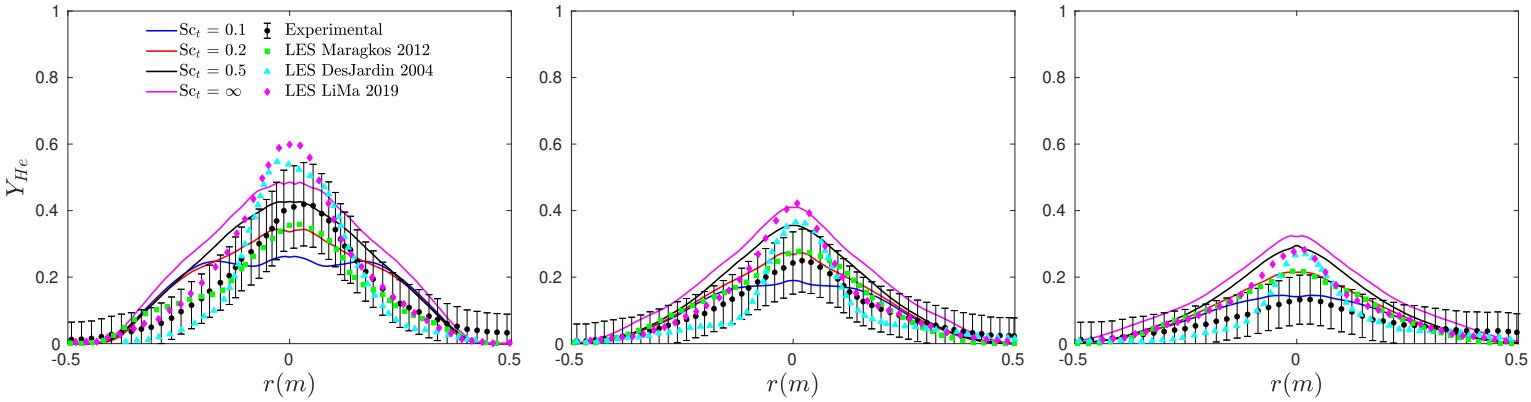

Figure 8.23: Comparison of mean radial profiles of helium's mass fraction Y_{He} for different Sc_t at heights $z = 0.2\,\mathrm{m}$ (left), $z = 0.4\,\mathrm{m}$ (middle) and $z = 0.6\,\mathrm{m}$ (right). The experimental data includes the respective uncertainties reported in the experimental study [183]. Numerical data are also presented [50, 145, 154]

following:

- The velocity energy spectrum follows the Kolmogorov theoretical energy cascade slope of $-5/3$.
- The mechanism creating the puffing cycle of the plume was analysed qualitatively and quantitatively. The instabilities generated near the base of the plume is mainly due to the baroclinic and gravitational torque.
- Regarding the frequency of the puffing cycle, the mesh resolution has the predominant effect on predicting the puffing frequency. The coarse mesh overestimated

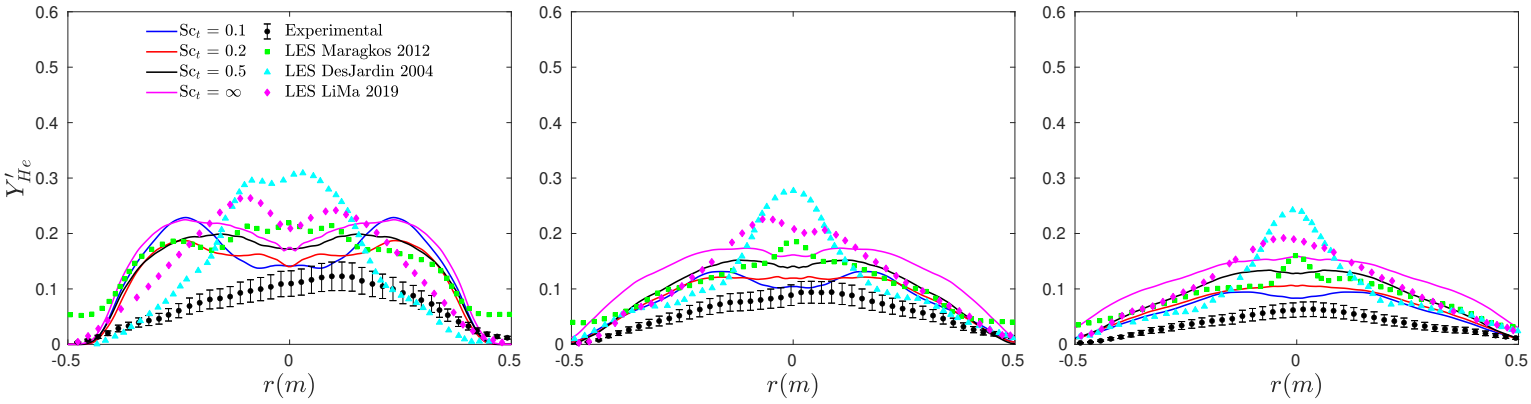

Figure 8.24: Comparison of rms radial profiles of helium's mass fraction Y for different Sc_t at heights $z = 0.2\,\mathrm{m}$ (left), $z = 0.4\,\mathrm{m}$ (middle) and $z = 0.6\,\mathrm{m}$ (right). The experimental data includes the respective uncertainties reported in the experimental study [183]. Numerical data are also presented [50, 145, 154]

the puffing frequency $f_{coarse} = 1.69\,\mathrm{Hz}$, while the fine mesh had better prediction for this frequency $f_{fine} = 1.39\,\mathrm{Hz}$ which is consistent with the experiment $f_{exp} = 1.37 \pm 0.1\,\mathrm{Hz}$. The SGS model did not have any significant effect on prediction the puffing frequency.

- The mean and rms profiles of streamwise and cross-stream velocities agreed well with experimental and other numerical studies. The best agreement for the mean and rms values of the velocity components was obtained with the finer mesh using SGS models.

- The profiles of mean and rms values of helium mass fraction were less satisfactory as we had some slight overestimations at certain zones. However, it is inline with previously published results [40, 50, 145, 154].

- The SGS models has a lower impact on the fine grid than on the coarse one. Moreover, Smagorinsky model adds more viscosity than Vreman model.

- The sensitivity analysis over Sc_t proposes a lower value of $\mathrm{Sc}_t = 0.2$ which would enhance the results.

Increasing mesh resolution is a next step as discussed by Ahmed and Trouvé [4]. Solving the boundary layer at the plume base will give better solution on the instabilities which are the main driving mechanism of the dynamics of this flow configuration.

All in all, the quality of the results is satisfactory when compared to the previously published results in the literature [40, 50, 145, 154] where they used well-established

CFD packages based on Navier-Stokes, yet, our solver showed better efficiency and lower computational cost. This gives the green light for more exploitation of the ProLB code, that's why the next chapter will introduce a reactive flow simulation of a large-scale fire.

Chapter 9

Application to pool fires

Contents

9.1 Introduction

The objective of this chapter is to assess the capability of our numerical model to simulate fire plumes. This is a further step of sophistication as these simulations involve turbulent diffusion flames and, as such, a combustion and a radiation model. As considered in both FDS and FireFoam [150], the Eddy dissipation concept (EDC) will be considered. For ease of simplicity, a simple radiant fraction model will be implemented as radiative model. The 1-m diameter methane fire, experientially investigated at the Fire Laboratory for Accreditation of Models and Experiments (**FLAME**) at Sandia National Laboratories in Albuquerque, New Mexico by Tieszen *et* al. [229, 230], will be simulated using our proposed model. The combustion modelling for fires is presented in the next section.

9.2 Turbulent non-premixed combustion

In the context of fire, the combustion process is by nature a turbulent diffusion flame (i.e. non-premixed flame) where fuel and oxidizer are separated and combustion happens after mixing. Most mechanisms in premixed flames can be found in non-premixed flames such as flame-generated vorticity, viscous effects and flame stretching. However, other specific characteristics associated with diffusion flames make it harder to understand and to describe if compared to premixed flames. To start, the reacting species have to reach, by molecular diffusion, the flame front before reaction. This diffusion of species will definitely be impacted by turbulence, and their diffusion speeds may be strongly modified by turbulent motions. Here, the reaction rate is limited by the species molecular diffusion/mixing. Consequently, in many combustion models for diffusion flames, the chemical reaction is assumed to be fast or infinitely fast compared to other transport processes.

There exist some specific features associated with non-premixed flames that make it a little bit challenging to model compared to premixed flames. First, there is no flame propagation, in other words, flame exists where fuel and oxidizer encounter. This characteristic is useful in terms of safety, however, it has some ramifications on the interaction chemistry/turbulence. The lack of propagation speed makes the diffusion flame unable to impose its dynamics on the flow field and is more sensitive to turbulence. Moreover, diffusion flames are more sensitive to stretch than turbulent premixed flames where its more likely for a diffusion flame to quench by turbulent fluctuations and the flamelet assumptions are not valid as often as in turbulent premixed flames.

Combustion modelling for fires

The aim of combustion modelling is simply to describe the species production term (i.e. combustion source term) in the species conservation equation. The modelling process depends mainly on the flame regime, category and nature, a good understanding of the combustion process and its dynamics is crucial to employ a well-suited model that meets the needs of the field of interest. Fire modelling has been evolving for quite a long time and various models have been proposed for the underlying combustion chemistry. However, due to the assumption made during the development of the model, there still lacks a universal model that is suitable for all combustion scenarios in different combustion systems and fires.

Combustion models based on mixture fractions are widely used by assuming the Shvab Zel'dovic formulation, irreversible infinitely fast chemistry and the Burke-Schumann

flame structure [191, 254]. The probability density function (PDF) approach is also adopted to take into account the effect of turbulence on combustion [243]. The eddy dissipation concept (EDC) is another common model incorporated in fire CFD codes such as FDS [160] and FireFoam. Magnussen and Hjertager [146] introduced the first version of the EDC which is an extension of the eddy break up model (EBU) of Spalding [213,214] which was originally developed to deal with premixed flames. Differently, the reaction rate in EDC is controlled by the mixing rate of fuel and oxidizer instead of the mixing rate of unburned and burned gas in EBU. Afterwards, Magnussen [62] included the significance of the fine structures into EDC where chemical reactions are assumed to occur in these fine structures and the extended model is formulated in a way that both finite rate chemistry and infinite fast chemistry can be used. It worth mentioning that the EDC model was originally proposed in the framework of RANS where the effects of turbulence are considered through additional transport equations. However, the known limitations of RANS turbulence modelling restrain the predictions of the EDC model as it depends primarily on the accuracy of fuel-air mixing prediction for which LES deemed to be more convenient. Hence, modifications should be introduced to the EDC model to function in LES framework where it will be more suitable to capture fine details of the combustion process.

The EDC model introduced by Magnussen and Hjertager [146] simply reads:

$$\dot{\omega}_F = C_{\mathrm{EDC}}\overline{\rho}\frac{1}{\tau_t}\min\left(\widetilde{Y_F}, \frac{\widetilde{Y_O}}{s}\right) \tag{9.1}$$

where $\dot{\omega}_F$ is the fuel mass consumption rate per unit volume (i.e. Kg m^{-3} s^{-1}), C_{EDC} is the model constant, $\overline{\rho}$ is the averaged density, τ_t is the turbulent/mixing time scale, $\widetilde{Y_F}$ and $\widetilde{Y_F}$ are the filtered mass fraction of fuel and oxidizer respectively and finally s is the stoichiometric oxygen-to-fuel mass ratio. The main parameter that controls and defines the dynamics of the EDC model is the turbulent/mixing time scale τ_t. In its original form, the EDC model deals with RANS variables which includes turbulent kinetic energy k and dissipation rate ϵ. Indeed, in RANS framework it is required to solve additional transport equations related to turbulence as a closure (e.g. k-epsilon or k-omega models). Therefore, the turbulent/mixing time scale τ_t can be calculated by:

$$\tau_t = \frac{k}{\epsilon}. \tag{9.2}$$

Calculating τ_t is rather simple in RANS framework as we update explicitly k and ϵ at each time step through their conservation equations. Unfortunately, those tur-

bulent related variables are solved implicitly in LES and there is no direct access to them. Following the work of Yaga *et* al. [264], the C_{EDC} is set to 4.0 whereas the eddy characteristic time τ_t is estimated by considering the Kolomogorov scale as:

$$\tau_t = \left(\frac{\nu}{\epsilon}\right)^{\frac{1}{2}}, \tag{9.3}$$

where we recall that ν is the kinematic molecular viscosity. Assuming local equilibrium between production and dissipation of turbulent kinetic energy (same hypothesis adopted while deriving Smagorinsky SGS model), eddy dissipation rate ϵ is written as follows:

$$\epsilon = 2\nu_t \widetilde{S_{ij}} : \widetilde{S_{ij}}, \tag{9.4}$$

where ν_t is kinematic turbulent viscosity and $\widetilde{S_{ij}}$ is the strain rate, both described in Sec. 6.4.2. The eddy characteristic time scale will then be:

$$\tau_t = \left(\frac{\nu}{2\nu_t \widetilde{S_{ij}} : \widetilde{S_{ij}}}\right)^{\frac{1}{2}}. \tag{9.5}$$

Note the term $\widetilde{S_{ij}} : \widetilde{S_{ij}}$ is an inner product and should calculated as follows:

$$\widetilde{S_{ij}} : \widetilde{S_{ij}} = \widetilde{S_{11}}^2 + \widetilde{S_{22}}^2 + \widetilde{S_{33}}^2 + 2\left(\widetilde{S_{12}}^2 + \widetilde{S_{13}}^2 + \widetilde{S_{23}}^2\right). \tag{9.6}$$

The model is now completed and we emphasize that we have a direct access to the model parameters at every time step. As a summary, to calculate this model we only require density, velocity gradients (to calculate the strain rate), turbulent viscosity, the mass fractions of fuel and oxidizer.

Other sophisticated variations and enhancements for this model can be found in the literature [36, 115, 232]. FDS and FireFoam deals differently with the calculation of the mixing time scale τ_t as detailed and investigated by Maragkos and Merci [150]. Yet, the simplest model explained previously will be kept in our study as a first attempt, improvements can come in the future.

As for radiation, it represents an essential element in large-scale fire simulations and is an inevitable source term as it reduces the resulting burning temperature. Nevertheless, a simplified model will be used in our study to account for radiation where a constant heat loss is subtracted from the heat release rate which results in a decrease in the flame temperature levels.

In the next sections we will be investigating the Sandia's 1-m diameter methane fire [229, 230].

9.3 Sandia's 1-m diameter methane fire

This configuration and the associated experiments carried out by Tieszen *et* al. [229,230] constituted a solid test case for numerical methods and models validation. The LES performed by Ferraris *et* al. [72] aimed to investigate the possibility to use the Conditional Source Estimation (CSE) as a model of low computational cost for large-scale fire simulations. Black *et* al. [15] employed the RANS technique with two approaches to handle turbulence, a steady RANS solution with a model for buoyancy-generated turbulence, and an unsteady RANS with models based on a temporal filter width. DesJardin *et* al. [49] applied a combination of flamelet modelling and an alternative closure for the conditional dissipation rate, based on a transport equation of the mixture fraction filtered probability density function. Xin *et* al. [261] used this test case to validate their FDS solver for large scale fires. In addition, Pasdarshahri *et* al. [188] used OpenFoam to perform LES with one-equation turbulent model. Hu *et* al. [104] developed an LES model coupled with detailed chemistry based on laminar flamelet approach to explore the influence of chemical kinetics on the vortical structures of large-scale fires. Marakgos and Merci [150] used two fire simulators, FDS and FireFoam, to examine the predictive capabilities of the turbulence and combustion models and also to comprehend the impact of how the mixing time scales are evaluated, in the framework of the Eddy dissipation concept. Koo *et* al. [123] investigated the impact of different combustion models on the predictions and explored the effect of modelling the full geometry of the experimental facility. They concluded that adopting a simplified geometry is adequate for this test case. Recently, Han *et* al. [92] focused on the sub-grid scale turbulence chemistry interaction (TCI) where they employed a consistent LES/transported probability density function (TPDF) approach, which is combined with tabulated chemistry based on a radiation flamelet/progress variable (RFPV) approach.

9.3.1 Experimental setup

This experiment was carried out at the Fire Laboratory for Accreditation of Modelling by Experiment (FLAME) facility at Sandia National Laboratories in Albuquerque, New Mexico, reported by Tieszen *et* al. [229, 230]. It is worth noting that this facility is the same as that used for the helium plume experiment. Hence, the details of the

experimental setup can be found in Section 8.1. Particle Imaging Velocimetry (PIV) was used for velocity field measurements of CH4 fire plumes with different heat release rates ranging from 1.56 to 2.61 MW. Nonetheless, no measurements for temperature were performed. The uncertainty of the measured quantities was in order of 20% and 30% for the mean and rms statistics, respectively.

As mentioned by Maragkos and Merci [150], the high uncertainty reported in the fire experiments can be justified by, contrary of typical combustion experiments, the relatively larger domains whose ambient conditions are harder to control, the large scale fuel inlet diameter for which it is harder to impose the desired fuel source conditions (e.g. turbulence intensity) and also the inevitable significant presence of radiation and soot formation (specially in hydrocarbons) which complicates the measurement process of certain quantities such as surface or in-depth temperatures in case of flame spread. Another reason for which this test case is important, is that it is a part of the the MaCFP Working Group (http://www.iafss.org/macfp/) which emphasizes on making systematic progress in fire modelling based on fundamental understanding of fire phenomena [24, 163, 164].

Numerous tests were conducted during the experimental study [229, 230] where the fuel inlet conditions were varied to cover a wide range of fire regimes. TEST-24 is chosen as a reference for our numerical study and whose inlet and boundary conditions are summarized in Table 9.1.

Fuel	CH_4
Fuel inlet velocity (m/s)	$0.097 \pm 3\%$
Fuel mass flux (kg/m^2s)	$0.053 \pm 3\%$
Heat release rate (MW)	$2.07 \pm 8\%$
Ambient pressure (kPa)	81.0 ± 0.2
Ambient temperature (K)	290 ± 3

Table 9.1: Initial and boundary condition of TEST-24 in the experiments [229, 230]

9.3.2 Numerical Setup

The low-Mach number formulation is used for this simulation. The computational domain is a $4 \times 4 \times 7\,m^3$ box, on which a uniform Cartesian grid was constructed,

equipped with refinement zones for cost reduction. The largest and smallest mesh sizes in the computational domain are $\delta x_{max} = 4$ cm and $\delta x_{min} = 2$ cm, resulting in a 6-million cell mesh. The configuration of the 1 m diameter methane fire was simplified such that the fuel (methane) enters the domain through a 1 m diameter inlet surrounded by a 0.51 m wide steel plate (representing ground plane). Fig. 9.1 presents the simplified configuration with 3D iso-surface of vorticity magnitude coloured by temperature.

Methane is injected at the ambient temperature and pressure, $\mathrm{T}_{inlet} = 285\,\mathrm{K}$ and $\mathrm{P}_{inlet} = 81.0\,\mathrm{kPa}$, respectively. Uniform bulk inlet velocity for methane is $U_{inlet}^{CH_4} = 0.097\,\mathrm{m/s}$ corresponding to TEST-24 conditions (see Table 9.1). In addition, a co-flow air stream is injected outside the annular plate with a uniform velocity of $U_{coflow}^{Air} = 0.14\,\mathrm{m/s}$. The value of the co-flow velocity was taken following the numerical studies of Han *et* al. [92] and Koo *et* al. [123]. Boundary conditions of the sides and the outlet are identical to the ones used in the helium study in Chapter 8. Velocities with negative values were forced to zero at the outlet to prevent flow rentering the domain (reverse flow), which might trigger numerical instabilities and pollute the results. The steel plate was modelled as an adiabatic non-slip wall.

The EDC combustion model coefficient $C_{EDC} = 4.0$ [150] with a single step irreversible chemical reaction of methane:

$$\mathrm{CH_4} + 2(\mathrm{O_2} + 3.76\mathrm{N_2}) \rightarrow \mathrm{CO_2} + 2\mathrm{H_2O} + 7.52\mathrm{N_2} \tag{9.7}$$

The NASA polynomials of the participating species are summarized in Appendix A.3.

The unresolved turbulent stress is modelled using Vreman model (Sec. 6.4.2) with $C_s = 0.1$ [150]. In order to resolve the filtered heat and species fluxes, a value of 0.7 is assigned to both turbulent Prandtl (Pr_t) and Schmidt (Sc_t) numbers [150]. The molecular Prandtl number (Pr) is set to 0.7, while the molecular Schmidt numbers of the species are summarized in Table 9.2. The molecular viscosity follows a power law because the simulation will exhibit high levels of temperature, due to combustion, which impacts the viscosity significantly.

CH_4	O_2	CO_2	H_2O
0.7275	0.8325	1.0425	0.6225

Table 9.2: Molecular Schmidt number Sc for different species

The simulation is run over 27 physical seconds. The first 7 seconds are thought sufficient to evacuate the initial solution then the remaining 20 seconds are used to

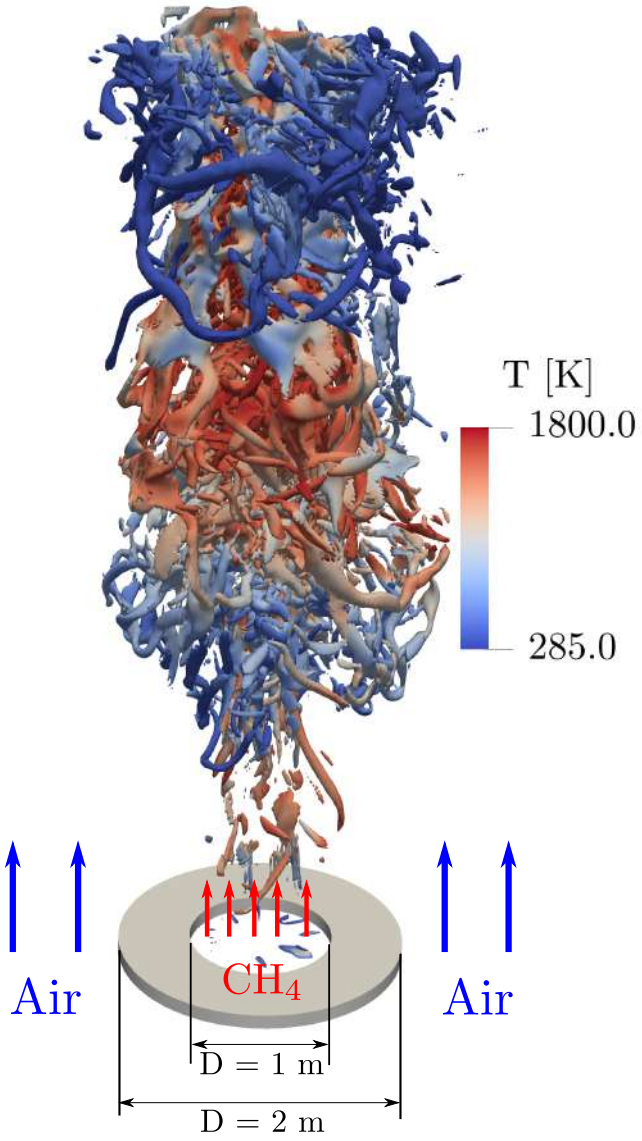

Figure 9.1: The simplified configuration of the Sandia 1-m diameter methane pool fire. The 3D contour shows iso-surface of vorticity magnitude at 25% of the maximum value coloured by temperature.

construct the statistics for quantitative comparisons. The time step is local and depends on the local mesh size while keeping a constant CFL number (CFL ≈ 0.7). This gives a minimum time step in the finest zone $\delta t_{min} \simeq 2.0 \times 10^{-4}$ sec. The simulation is parallelized on 128 cores on a Dell PowerEdge C6420 server with 4× 32-core Intel Xeon Gold 6142, 2.6 GHz and 96 GB RAM producing a calculation time of $\sim$ 1050 CPU hours.

9.3.3 Results and discussion

Figure 9.2 shows the instantaneous field of density, temperature, velocity and CO_2 mass fraction at middle plane. The flame is stabilized and attached to the methane exit due to the low injection velocity. The flow is observed laminar near the base but it rapidly becomes turbulent downstream.

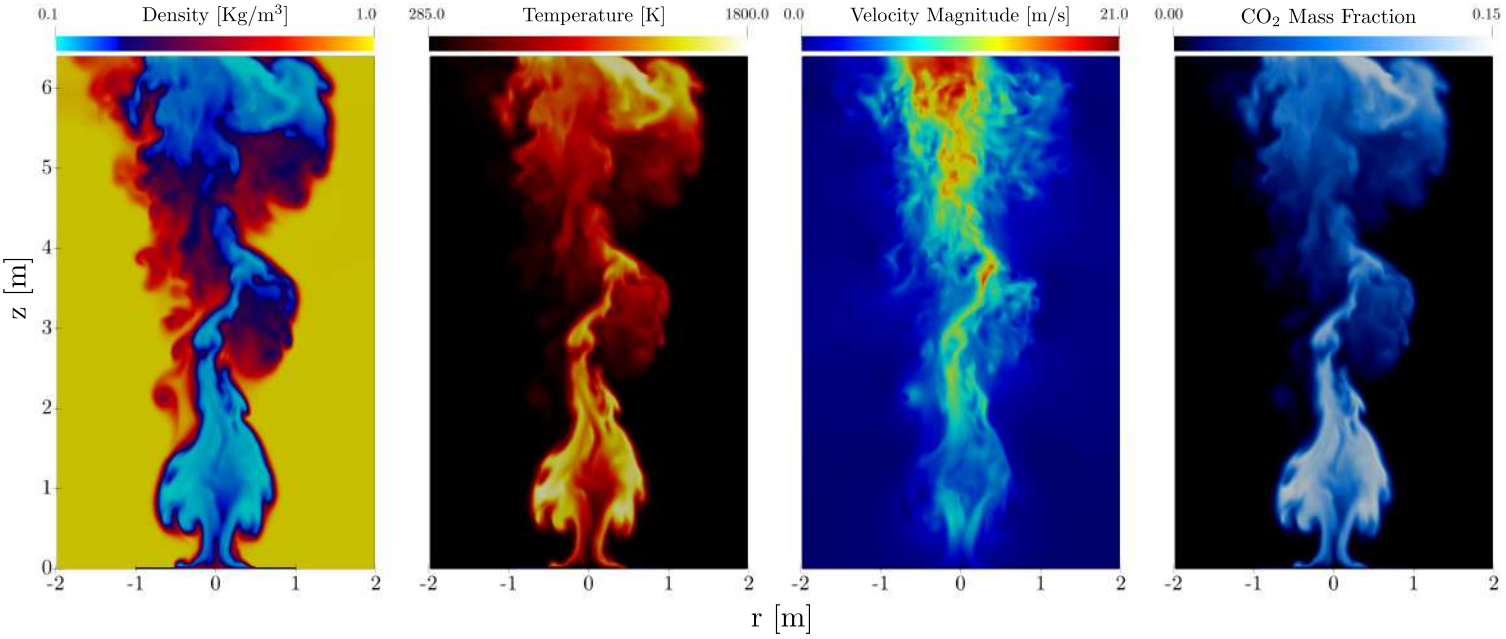

Figure 9.2: The instantaneous fields of density, temperature, velocity and CO_2 mass fraction at the middle plane of the domain.

Turbulence: Energy Cascade

Figure 9.3 shows the energy spectrum based on the axial velocity at $z = 0.5\,\mathrm{m}$. The spectrum exhibits the theoretical energy cascade characteristic reported by the theory of Kolmogorov [122] and that we have the correct power law of $-5/3$ in the inertial range, also the dissipation range was detected at higher frequencies.

Pool fire dynamics: Instability modes

Large scale pool fires exhibit a particular behaviour where a periodic shedding of large toroidal vortices pulsates at a specific frequency and is proportional to the square root of the diameter [29]. The "puffing" mechanism is fundamental for fires as it controls the mixing between fuel and oxidizer which conducts the combustion process. Figure 9.4 shows the different stages of a puffing cycle (four distinct stages); at first, instabilities are

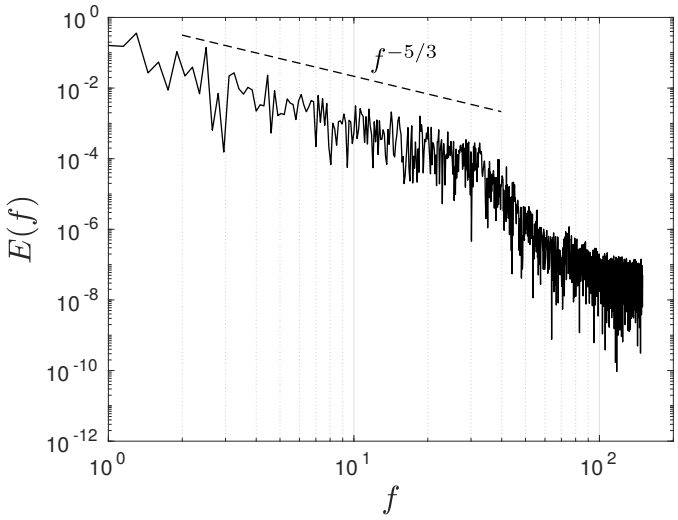

Figure 9.3: Temporal energy spectrum at $z = 0.5\ m$ for axial velocity. Dashed line indicate the expected characteristic slope of $-5/3$ [122].

generated near the edges of the plume at the fire base due to baroclinic and gravitational torques; afterwards, those instabilities grow towards the center of the source; then, large toroidal vortex is formed due to Rayleigh-Taylor instability which self-propagates and entrains a large amount of surrounding air; finally, the destruction of this toroidal vortex because of the creation of secondary instabilities and Kelvin-Helmholtz instabilities that grow causing a non-linear breakdown of the toroidal vortex. These stages are then repeated at every cycle and the frequency of this motion was quantified experimentally and numerical correlations were proposed.

Extensive experiments covering different scenarios and regimes of fires concluded that the puffing frequency depends only on the fire source diameter regardless of the fuel type. Correlations can be found in the literature that predicts the puffing frequency such as the one given by Cetegen and Ahmed [29]:

$$f = 1.5\sqrt{D}\ \text{Hz}, \tag{9.8}$$

and the one given by Zukoski [270]:

$$f = 0.5\left(\frac{g}{D}\right)^{\frac{1}{2}}\ \text{Hz} \tag{9.9}$$

Figure 9.5 shows Fast Fourier transform (FFT) performed on the time signal of axial velocity at $z = 0.5\,\text{m}$ in order to identify the principle frequency of puffing. Our simulation predicts a puffing frequency of ~ 1.32 Hz which underestimates the

Figure 9.4: Snapshots of heat release rate iso-volume through out 1 second depicting a complete puffing cycle.

experimental values of 1.57 Hz while the correlation of Cetegen gives 1.5 Hz and the correlation of Zukoski estimates 1.57 Hz.

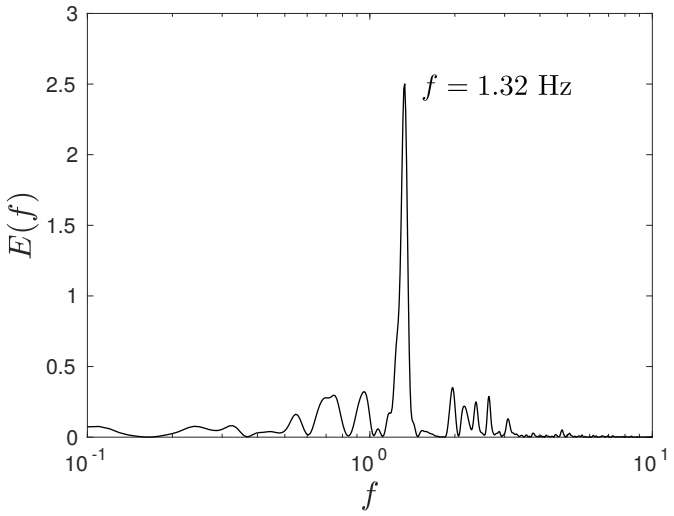

Figure 9.5: Fast Fourier transform (FFT) based on the axial velocity at $z = 0.5\,\mathrm{m}$ showing the puffing frequency.

Mean and RMS profiles

The axial profiles of axial velocity and temperature are demonstrated in Fig. 9.6. The velocity U_z in the near-field region is in quite good agreement with the experiment. On the other, comparisons with the McCaffrey correlations suggest that it is underestimated in the far-field region. The rate of decrease of the temperature is the far field is consistent with the correlation of McCaffrey. However, the quantitative comparison suggests that the temperature is overestimated estimated.

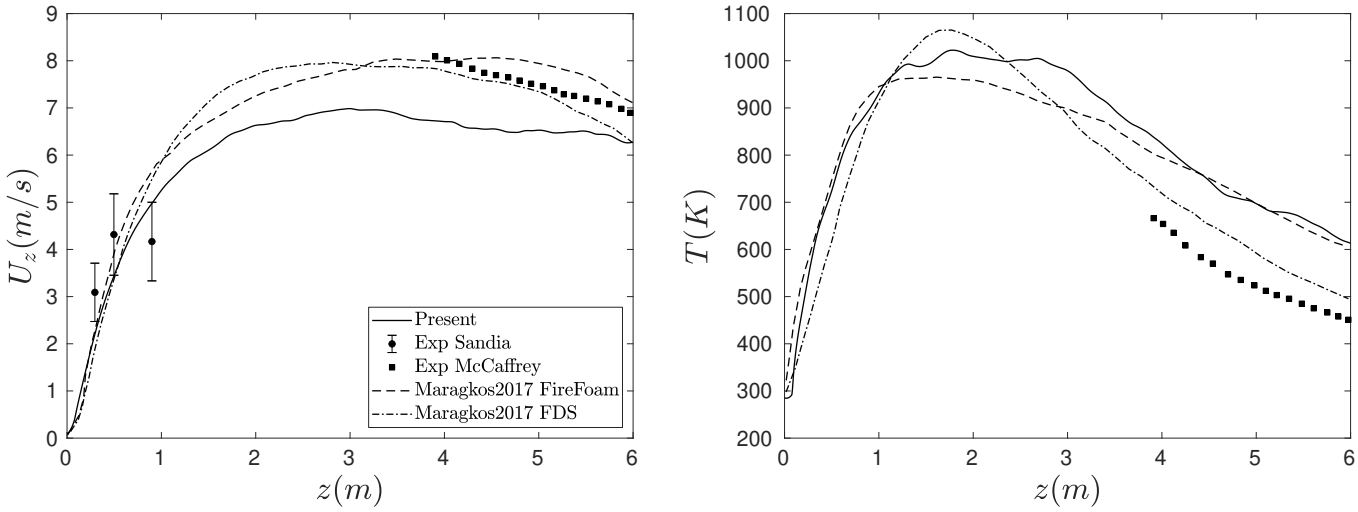

Figure 9.6: Centerline profiles of (left) mean streamwise velocity U_z and (right) temperature T compared to experimental and numerical data

Fig. 9.7 shows the radial profiles of axial velocity at different elevations downstream the inlet $z = 0.3, 0.5, 0.9\,\mathrm{m}$ and we can observe a decent agreement with the experimental data remaining within the experimental uncertainties.

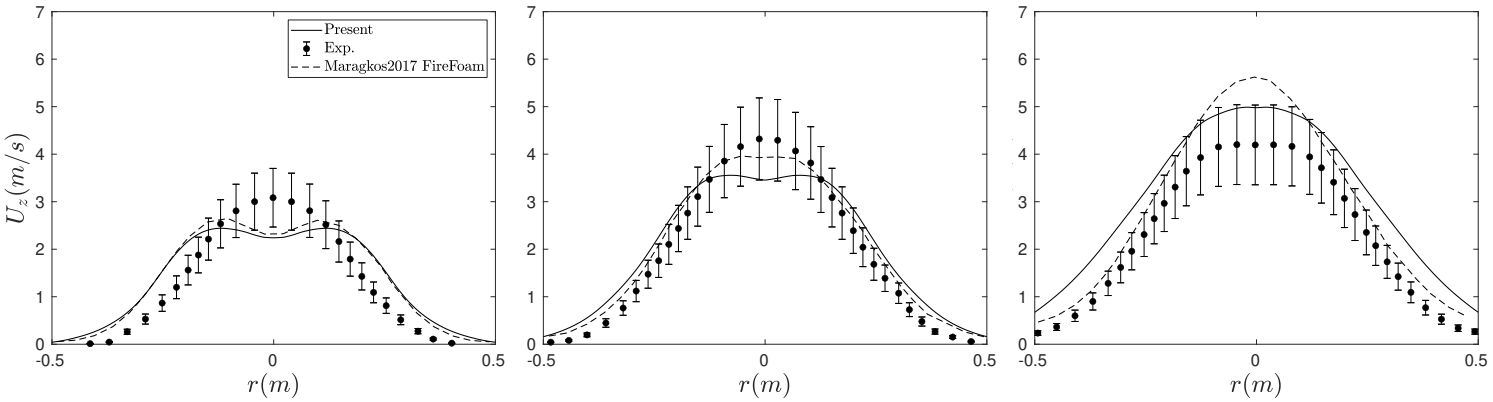

Figure 9.7: Radial profiles of streamwise velocity U_z at $z = 0.3\,\mathrm{m}$ (left), $z = 0.5\,\mathrm{m}$ (middle) and $z = 0.9\,\mathrm{m}$ (right). Comparison is done with experimental and numerical data [150, 229]

Fig. 9.8 depicts the radial profiles of horizontal velocity which may be considered as indicator on the entrainment of air from the ambient environment outside the fire core. We can clearly notice a good agreement with the experimental and numerical data indicating a good prediction of the entrained air towards the fire core.

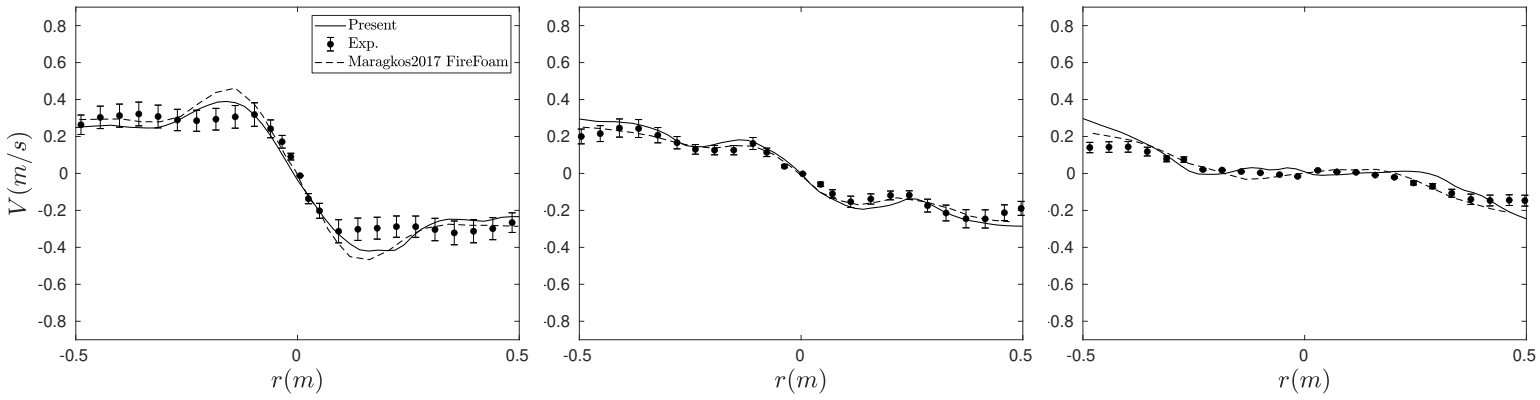

Figure 9.8: Radial profiles of horizontal velocity at $z = 0.3\,\mathrm{m}$ (left), $z = 0.5\,\mathrm{m}$ (middle) and $z = 0.9\,\mathrm{m}$ (right). Comparison is done with experimental and numerical data [150, 229]

The rms of velocity was represented by the turbulent kinetic energy (TKE) which

combines the three component of velocity fluctuations using the following formula:

$$\mathrm{TKE} = \frac{1}{2}\left(\overline{u_x'^2} + \overline{u_y'^2} + \overline{u_z'^2}\right) \tag{9.10}$$

Fig. 9.9 shows the turbulent kinetic energy at different heights which clearly agrees well with experimental and numerical data, yet, disparities grows larger further downstream the fire base (i.e. at $z = 0.9$ m).

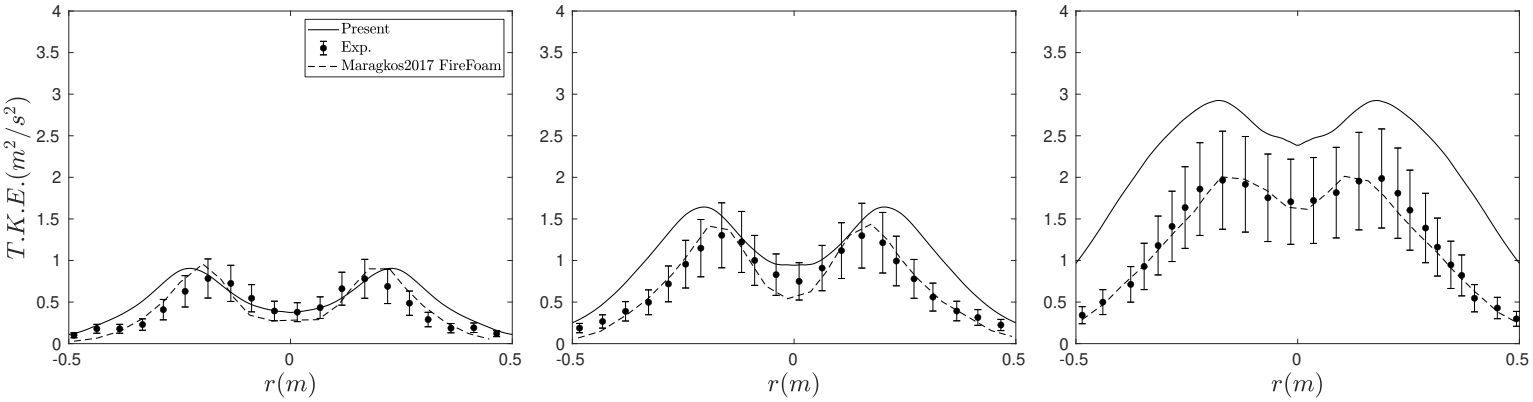

Figure 9.9: Radial profiles of turbulent kinetic energy (TKE) at $z = 0.3$ m (left), $z = 0.5$ m (middle) and $z = 0.9$ m (right). Comparison is done with experimental and numerical data [150, 229]

Flame height

The good prediction of flame height is of great interest for fire application. A common criteria which is followed to determine the average flame height is to determine the elevation at which there is a 500 - 600 K difference between the centerline and the surrounding air temperatures [56]. In our study a 550 K difference is sought following Maragkos and Merci [150]. Our LES estimates a height of 5.2 meters which is slightly higher than the reported value of 4.8 m [155].

9.4 Conclusion

In this chapter we were able to incorporate, for the first time, the EDC combustion model into an LBM environment to simulate fires. The radiation was simplified to be a constant removal of energy proportional to the heat release rate:

- The spectrum of turbulent kinetic energy followed the $-5/3$ slope of Kolmogorov.

- The puffing frequency was underestimated compared to the experimental values.
- We found a satisfactory agreement with the experimental data at the near-field region for the mean values. At this region, radial profiles of velocity components agreed well with the experiment falling within the experimental uncertainties.
- For high order statistics (rms values), our turbulent kinetic energy had some discrepancies compared to experimental data specially when going further downstream.
- The predicted flame height had the same order of magnitude of the reported values, yet, slightly overestimated.

The next chapter will conclude the work done throughout this manuscript, and give some insights and openings for future work.

Chapter 10

Conclusion and Perspectives

10.1 Conclusion

The objective of this thesis was to develop a numerical model based on Lattice Boltzmann method capable of simulating fire-induced flows with high fidelity but with lower computational cost as compared to standard Navier-Stokes solvers. The hybrid pressure-based solver was introduced and detailed in Chapter 4 including both compressible and low-Mach formulations. This model was exhaustively verified and validated in Chapter 5 through canonical test cases of incremental complexity:

- The 1-D pressure column was solved (Sec. 5.1) and the atmospheric pressure gradient could be recovered. The gravity was recalculated through the resolved pressure and density and its value matches the input value. This test case verified that the gravity forcing term is well implemented and that the input value of gravitational acceleration acts correctly throughout the simulation.

- The 2-D Rayleigh-Bénard was also investigated (Sec. 5.2). The steady state axial and vertical velocity profiles as well as the Nusselt number at different Rayleigh numbers agreed well with the reference solution. This test case examined the equilibrium between buoyancy, viscosity and thermal diffusion. The results proved the consistency of the implemented model and that the coupling between the different phenomena is correct.

- The 2-D Rayleigh-Taylor was our last test case of validation (Sec. 5.3). The temporal evolution of the position of both bubble and spike is compared for different Reynolds numbers and they were inline with the reference solution. This test case demonstrated the behaviour of our model in unsteady scenarios. Moreover, this

test case is of a particular importance for buoyant plumes as it has been explained in Chapter 8.

The LBM model was then applied to the LES of forced plume, in Chapter 7, to study the characteristics of far-field region. The main results can be summarised as follows:

- The energy spectrum followed the Kolmogorov theoretical slope of $-5/3$ indicating a proper resolution of the turbulence energy cascade as reported in the literature.
- Axial profiles of velocity and temperature agreed well with the experimental data. The transition to plume-like region at $z/L_m = 4 \sim 5$ inline with the experiments.
- The cross-correlation between velocity and temperature had a high positive value which compared well with the experimental ones and indicated a strong coupling due to gravity.
- Self similarity profiles in the far-field (i.e. plume-like region) were correctly predicted for both velocity and temperature.
- The growth of plume compared very well with experimental and numerical references. Moreover, the entrainment of fluid form the surrounding was correctly predicted.

Afterwards, LES of 1-m diameter helium plume, investigated experimentally at Sandia National Laboratories [230], was performed in Chapter 8. The investigation resulted in the following key points:

- The energy spectrum follows the Kolmogorov theoretical slope of $-5/3$ indicating energy cascading.
- The mesh resolution had the predominant effect on predicting the puffing frequency. In particular, a grid resolution of about 1 cm is required to reproduce accurately the puffing frequency. Conversely, the SGS models do not affect the prediction of the puffing frequency.
- The mean and rms profiles of streamwise and cross-stream velocities agreed well with experimental and other numerical studies. The best agreement for the mean and rms values of the velocity components was obtained with the finer mesh using SGS models.

- The profiles of mean and rms values of helium mass fraction were less satisfactory, exhibiting similar discrepancies as observed in previous numerical studies [40, 50, 145, 154].
- The sensitivity analysis over turbulent Schmidt number Sc_t had shown an improvement of the results when reducing its value down to 0.2.

As a final phase, the numerical model was tested in Chapter 9 to simulate the Sandia's 1-m diameter methane pool fire. We ended up with the following findings:

- The energy spectrum follows the Kolmogorov theoretical slope of $-5/3$ indicating energy cascading.
- The puffing frequency was also consistent with the experiment and with the other experimental correlations.
- Radial profiles of velocity components near-field region agreed well with the experimental results.
- Radial profiles of turbulent kinetic energy had some discrepancies compared to experimental data specially further downstream.
- The predicted flame height had the same order of magnitude of the reported values, yet, slightly overestimated.

The global conclusion of this work is that the proposed hybrid pressure-based LBM model was proved to be able to reproduce efficiently the unwanted fire dynamics and characteristics with a lower cost than the conventional Navier-Stokes solvers. However, improvements and additional models have to be incorporated to be able to simulate more complex fire scenarios and configurations.

10.2 Perspectives and future works

Mesh convergence should be sought at first for the helium plume simulation introduced in Chapter 8, to ensure the correct resolution of the gravity currents being the source of the instabilities driving this type of flows. The natural continuity of this work is to implement state-of-the art turbulent combustion and radiation models to have a better description of the combustion process and the heat transfer mechanisms responsible for fire growth. The combustion model has to capture the extinction/re-ignition process that occur in under-ventilated fires. On the other hand, the development of the

radiation model includes three steps: (i) a proper modelling of the radiative property of the combustion products, (ii) the implementation of a radiative transfer equation solver, and (iii) the modelling of subgrid-scale turbulence radiation interactions that were found to be non-negligible in fire scenario [179, 180]. The third point is highly related to the choice of the combustion model. On the other hand, in order to limit the computational cost, an important work has to be made on the Radiative Transfer Equation (RTE) solver that is known from the literature to be computationally demanding.

The steps to validate these models can be made through the target scenarios included in the MaCFP workshop [24]. As a first step, the large-scale methane fire, introduced in Chapter 9, has to be re-simulated. The second step is to consider a turbulent liquid pool fire where liquid evaporation modelling adds another layer of sophistication. Two experimental setups in the MaCFP workshop are well designed for this purpose: the first one is the 30-cm diameter methanol pool fire investigated experimentally at the University of Waterloo [246, 247], and the second one is a more recent experimental investigation performed at the National Institute of Standards and Technology (**NIST**) by Sung *et* al. [218,219] which involves a 1-m diameter methanol fire. The last step is to investigate the capability of the combustion model to capture extinction processes. The canonical line-fire configuration with controlled co-flow investigated at the university of Maryland (UMD) [249–251] can be considered for this purpose.

Bibliography

[1] Firefoam. http://code.google.-com/p/firefoam-dev/.

[2] Prolb. http://www.prolb-cfd.com/.

[3] Rémi Abgrall and Smadar Karni. Computations of compressible multifluids. *Journal of computational physics*, 169(2):594–623, 2001.

[4] Mohamed M Ahmed and Arnaud Trouvé. Large eddy simulation of the unstable flame structure and gas-to-liquid thermal feedback in a medium-scale methanol pool fire. *Combustion and Flame*, 225:237–254, 2021.

[5] Frank J Alexander, Shiyi Chen, and JD Sterling. Lattice boltzmann thermohydrodynamics. *Physical Review E*, 47(4):R2249, 1993.

[6] John David Anderson. *Modern compressible flow: with historical perspective*, volume 12. McGraw-Hill New York, 1990.

[7] John David Anderson and John Wendt. *Computational fluid dynamics*, volume 206. Springer, 1995.

[8] Thomas Astoul, Gauthier Wissocq, Jean-François Boussuge, Alois Sengissen, and Pierre Sagaut. Analysis and reduction of spurious noise generated at grid refinement interfaces with the lattice boltzmann method. *Journal of Computational Physics*, 418:109645, 2020.

[9] Christophe Bailly and Geneviève Comte-Bellot. *Turbulence*. Springer International Publishing, 2015.

[10] P Bergé and M Dubois. Rayleigh-bénard convection. *Contemporary Physics*, 25(6):535–582, 1984.

[11] K. Bhaganagar and S. R. Bhimireddy. Numerical investigation of starting turbulent buoyant plumes released in neutral atmosphere. *Journal of Fluid Mechanics*, 900:A32, 2020.

[12] Karthik Bhairapurada, Bruno Denet, and Pierre Boivin. A lattice-boltzmann study of premixed flames thermo-acoustic instabilities. *Combustion and Flame*, 240:112049, 2022.

[13] Prabhu Lal Bhatnagar, Eugene P Gross, and Max Krook. A model for collision processes in gases. i. small amplitude processes in charged and neutral one-component systems. *Physical review*, 94(3):511, 1954.

[14] Joel Birnbaum and R Stanley Williams. Physics and the information revolution. *Physics Today*, 53(1):38–43, 2000.

[15] Amalia R Black. Numerical predictions and experiment results for a 1m diameter methane fire. In *ASME International Mechanical Engineering Congress and Exposition*, volume 42215, pages 429–435, 2005.

[16] Thomas K Blanchat. Characterization of the air source and the plume source at flame. Technical report, Sandia National Lab.(SNL-NM), Albuquerque, NM (United States); Sandia ..., 2001.

[17] Guillaume Blanquart and Heinz Pitsch. Large-eddy simulation of a turbulent buoyant helium plume. *Bulletin of the American Physical Society*, 53:245–252, 2008.

[18] Jiri Blazek. *Computational fluid dynamics: principles and applications*. Butterworth-Heinemann, 2015.

[19] VI Blinov and GN Khudyakov. Diffusion burning of liquids. Technical report, Army Engineer Research and Development Labs Fort Belvoir VA, 1961.

[20] Pierre Boivin, Muhammad Tayyab, and Song Zhao. Benchmarking a lattice-boltzmann solver for reactive flows: Is the method worth the effort for combustion? *Physics of Fluids*, 33:017703, 2021.

[21] Alfred E Brenner. The computing revolution and the physics community. *Physics Today*, 49(10):24–30, 1996.

[22] C. P. Brescianini and M. Delichatsios. New evaluation of the k-epsilon turbulence model for free buoyant plumes. *Num. Heat Transf. A: Fundamentals*, 43:731–751, 2003.

[23] Gary A Briggs. Chimney plumes in neutral and stable surroundings. *Atmospheric Environment (1967)*, 6(7):507–510, 1972.

[24] A Brown, Morgan Bruns, M Gollner, J Hewson, Georgios Maragkos, A Marshall, R McDermott, Bart Merci, T Rogaume, S Stoliarov, et al. Proceedings of the first workshop organized by the iafss working group on measurement and computation of fire phenomena (macfp). *Fire safety journal*, 101:1–17, 2018.

[25] GC Burton. Large-eddy simulation of a turbulent helium-air plume using the nles method. *Center for turbulence research, Stanford University and NASA-Ames research center, Stanford, CA*, 2009.

[26] G Carazzo, E Kaminski, and S Tait. On the rise of turbulent plumes: Quantitative effects of variable entrainment for submarine hydrothermal vents, terrestrial and extra terrestrial explosive volcanism. *Journal of Geophysical Research: Solid Earth*, 113(B9), 2008.

[27] Carlo Cercignani. Are there more than five linearly-independent collision invariants for the boltzmann equation? *Journal of statistical physics*, 58(5):817–823, 1990.

[28] B. M. Cetegen. Behavior of naturally unstable and periodically forced axisymmetric buoyant plumes of helium and helium-air mixtures. *Phys. Fluids*, 9:3742–3753, 1997.

[29] Baki M Cetegen and Tarek A Ahmed. Experiments on the periodic instability of buoyant plumes and pool fires. *Combustion and flame*, 93(1-2):157–184, 1993.

[30] Baki M Cetegen and Kent D Kasper. Experiments on the oscillatory behavior of buoyant plumes of helium and helium-air mixtures. *Physics of fluids*, 8(11):2974–2984, 1996.

[31] C. H. Chen and K. Bhaganagar. New findings in vorticity dynamics of turbulent buoyant plumes. *Physics of Fluids*, 33:115104, 2021.

[32] C. J. Chen and W. Rodi. *Vertical buoyant jets: a review of experimental data*. Pergamon, 1980.

[33] Ching Jen Chen and Wolfgang Rodi. Vertical turbulent buoyant jets: a review of experimental data. *Nasa STI/Recon Technical Report A*, 80:23073, 1980.

[34] Feng Chen, Aiguo Xu, Guangcai Zhang, Yingjun Li, and Sauro Succi. Multiple-relaxation-time lattice boltzmann approach to compressible flows with flexible specific-heat ratio and prandtl number. *EPL (Europhysics Letters)*, 90(5):54003, 2010.

[35] Shiyi Chen and Gary D Doolen. Lattice boltzmann method for fluid flows. *Annual review of fluid mechanics*, 30(1):329–364, 1998.

[36] Zhibin Chen, JX Wen, Baopeng Xu, and Siaka Dembele. Large eddy simulation of fire dynamics with the improved eddy dissipation concept. *Fire Safety Science*, 10:195–808, 2011.

[37] Isabelle Cheylan, Song Zhao, Pierre Boivin, and Pierre Sagaut. Compressible pressure-based lattice-boltzmann applied to humid air with phase change. *Applied Thermal Engineering*, page 116868, 2021.

[38] Daniele Chiappini, Gino Bella, Sauro Succi, Federico Toschi, and Stefano Ubertini. Improved lattice boltzmann without parasitic currents for rayleigh-taylor instability. *Communications in Computational Physics*, 7(3):423, 2010.

[39] Kenneth T Christensen, Steven M Soloff, and Ronald J Adrian. Piv sleuth: integrated particle image velocimetry interrogation/validation software. Technical report, Department of Theoretical and Applied Mechanics. College of Engineering . . . , 2000.

[40] W Chung and CB1203 Devaud. Buoyancy-corrected k–ε models and large eddy simulation applied to a large axisymmetric helium plume. *International journal for numerical methods in fluids*, 58(1):57–89, 2008.

[41] Thomas Coratger, Gabriel Farag, Song Zhao, Pierre Boivin, and Pierre Sagaut. Large-eddy lattice-boltzmann modelling of transonic flows. *Physics of Fluids*, 33(11):115112, 2021.

[42] Christophe Coreixas, Gauthier Wissocq, Guillaume Puigt, Jean-François Boussuge, and Pierre Sagaut. Recursive regularization step for high-order lattice boltzmann methods. *Physical Review E*, 96(3):033306, 2017.

[43] Christophe Guy Coreixas. *High-order extension of the recursive regularized lattice Boltzmann method*. PhD thesis, Institut National Polytechnique de Toulouse, 2018.

[44] Geoffrey Cox and DD Drysdale. *Combustion fundamentals of fire*. Academic press London, 1995.

[45] Z. Dai, L.K. Tseng, and G.M. Faeth. Structure of round, fully-developed, buoyant turbulent plumes. *J. Heat Transf.*, 116:409–417, 1994.

[46] Michael A Delichatsios. Air entrainment into buoyant jet flames and pool fires. *Combustion and Flame*, 70(1):33–46, 1987.

[47] Paul J Dellar. Bulk and shear viscosities in lattice boltzmann equations. *Physical Review E*, 64(3):031203, 2001.

[48] Kenneth L. Denman. Fischer, h. b., e. j. list, r. c. y. koh, j. imberger, and n. a. brooks. 1979. mixing in inland and coastal waters. academic press, inc., new york, xiv + 483 p. $35.00. *Limnology and Oceanography*, 27(3):593–594, 1982.

[49] PAUL E DESJARDIN. Modeling of conditional dissipation rate for flamelet models with application to large eddy simulation of fire plumes. *Combustion science and technology*, 177(10):1883–1916, 2005.

[50] Paul E DesJardin, Timothy J O'Hern, and Sheldon R Tieszen. Large eddy simulation and experimental measurements of the near-field of a large turbulent helium plume. *Physics of fluids*, 16(6):1866–1883, 2004.

[51] Dominique d'Humières. Generalized lattice-boltzmann equations. *Rarefied gas dynamics*, 1992.

[52] Giovanni Di Ilio, Benedikt Dorschner, Gino Bella, Sauro Succi, and Iliya V Karlin. Simulation of turbulent flows with the entropic multirelaxation time lattice boltzmann method on body-fitted meshes. *Journal of Fluid Mechanics*, 849:35–56, 2018.

[53] Norbert Didden and Chih-Ming Ho. Unsteady separation in a boundary layer produced by an impinging jet. *Journal of Fluid Mechanics*, 160:235–256, 1985.

[54] Hang Ding, Peter DM Spelt, and Chang Shu. Diffuse interface model for incompressible two-phase flows with large density ratios. *Journal of Computational Physics*, 226(2):2078–2095, 2007.

[55] Stefan Paul Domino, Vernon F Nicolette, Timothy John O'Hern, Sheldon R Tieszen, and Amalia Rebecca Black. A turbulence model for buoyant flows based on vorticity generation. Technical report, Sandia National Laboratories (SNL), Albuquerque, NM, and Livermore, CA ..., 2005.

[56] Dougal Drysdale. *An introduction to fire dynamics*. John Wiley & Sons, 2011.

[57] François Dubois and Pierre Lallemand. Towards higher order lattice boltzmann schemes. *Journal of Statistical mechanics: theory and experiment*, 2009(06):P06006, 2009.

[58] F Ducros, F Nicoud, and Thierry Poinsot. Wall-adapting local eddy-viscosity models for simulations in complex geometries. *Numerical Methods for Fluid Dynamics VI*, pages 293–299, 1998.

[59] Alexandre Ern and Vincent Giovangigli. *Multicomponent transport algorithms*, volume 24. Springer Science & Business Media, 1994.

[60] Alexandre Ern and Vincent Giovangigli. Fast and accurate multicomponent transport property evaluation. *Journal of Computational Physics*, 120(1):105–116, 1995.

[61] Gerald GJ Ernst, R Stephen J Sparks, Steven N Carey, and Marcus I Bursik. Sedimentation from turbulent jets and plumes. *Journal of Geophysical Research: Solid Earth*, 101(B3):5575–5589, 1996.

[62] Ivar S Ertesvåg and Bjørn F Magnussen. The eddy dissipation turbulence energy cascade model. *Combustion science and technology*, 159(1):213–235, 2000.

[63] DD Esch, A Siripong, and RW Pike. Thermodynamic properties in polynomial form for carbon, hydrogen, nitrogen, and oxygen systems from 300 to 15000 k. Technical report, 1970.

[64] G Farag, S Zhao, T Coratger, Pierre Boivin, G Chiavassa, and Pierre Sagaut. A pressure-based regularized lattice-boltzmann method for the simulation of compressible flows. *Physics of Fluids*, 32(6):066106, 2020.

[65] Gabriel Farag, Thomas Coratger, Gauthier Wissocq, Song Zhao, Pierre Boivin, and Pierre Sagaut. A unified hybrid lattice-boltzmann method for compressible flows: bridging between pressure-based and density-based methods. *Physics of Fluids*, 33(8), 2021.

[66] Yong-Liang Feng, Shao-Long Guo, Wen-Quan Tao, and Pierre Sagaut. Regularized thermal lattice boltzmann method for natural convection with large temperature differences. *International Journal of Heat and Mass Transfer*, 125:1379–1391, 2018.

[67] Yongliang Feng, Pierre Boivin, Jérôme Jacob, and Pierre Sagaut. Hybrid recursive regularized lattice boltzmann simulation of humid air with application to meteorological flows. *Phys. Rev. E*, 100:023304, Aug 2019.

[68] Yongliang Feng, Pierre Boivin, Jérôme Jacob, and Pierre Sagaut. Hybrid recursive regularized thermal lattice boltzmann model for high subsonic compressible flows. *Journal of Computational Physics*, 394:82–99, 2019.

[69] Yongliang Feng, S Guo, Jérôme Jacob, and Pierre Sagaut. Solid wall and open boundary conditions in hybrid recursive regularized lattice boltzmann method for compressible flows. *Physics of Fluids*, 31(12):126103, 2019.

[70] Yongliang Feng, Pierre Sagaut, and Wen-Quan Tao. A compressible lattice boltzmann finite volume model for high subsonic and transonic flows on regular lattices. *Computers & Fluids*, 131:45–55, 2016.

[71] Yongliang Feng, Pierre Sagaut, and Wenquan Tao. A three dimensional lattice model for thermal compressible flow on standard lattices. *Journal of Computational Physics*, 303:514–529, 2015.

[72] S Ferraris, JX Wen, and S Dembele. Large-eddy simulation of a large-scale methane pool fire. *Fire Safety Science*, 8:963–974, 2005.

[73] O Filippova and D Hänel. Lattice-bgk model for low mach number combustion. *International Journal of Modern Physics C*, 9(08):1439–1445, 1998.

[74] Olga Filippova and Dieter Hänel. A novel lattice bgk approach for low mach number combustion. *Journal of Computational Physics*, 158(2):139–160, 2000.

[75] BEA Fisher. Predicting cooling tower plume dispersion. *Proceedings of the Institution of Mechanical Engineers, Part A: Journal of Power and Energy*, 211(4):291–297, 1997.

[76] U FRISCH, B HASSLACHER, and Y POMEAU. Lattice-gas automata for the navier-stokes equation. *Physical review letters*, 56(14):1505–1508, 1986.

[77] Aurel Galántai. The theory of newton's method. *Journal of Computational and Applied Mathematics*, 124(1-2):25–44, 2000.

[78] Eric Garnier, Nikolaus Adams, and Pierre Sagaut. *Large eddy simulation for compressible flows*. Springer Science & Business Media, 2009.

[79] Benjamin Gebhart, Yogesh Jaluria, Roop L Mahajan, and Bahgat Sammakia. Buoyancy-induced flows and transport. 1988.

[80] Martin Geier, Martin Schönherr, Andrea Pasquali, and Manfred Krafczyk. The cumulant lattice boltzmann equation in three dimensions: Theory and validation. *Computers & Mathematics with Applications*, 70(4):507–547, 2015.

[81] William K George Jr, Ronald L Alpert, and Francesco Tamanini. Turbulence measurements in an axisymmetric buoyant plume. *International Journal of Heat and Mass Transfer*, 20(11):1145–1154, 1977.

[82] Massimo Germano, Ugo Piomelli, Parviz Moin, and William H Cabot. A dynamic subgrid-scale eddy viscosity model. *Physics of Fluids A: Fluid Dynamics*, 3(7):1760–1765, 1991.

[83] Irina Ginzburg, Frederik Verhaeghe, and Dominique d'Humieres. Two-relaxation-time lattice boltzmann scheme: About parametrization, velocity, pressure and mixed boundary conditions. *Communications in computational physics*, 3(2):427–478, 2008.

[84] V Giovangigli. Multicomponent flow modeling birkhäuser, boston, 1999.

[85] Harold Grad. On the kinetic theory of rarefied gases. *Communications on pure and applied mathematics*, 2(4):331–407, 1949.

[86] J-L Guermond and Luigi Quartapelle. A projection fem for variable density incompressible flows. *Journal of Computational Physics*, 165(1):167–188, 2000.

[87] S Guo, Y Feng, J Jacob, F Renard, and P Sagaut. An efficient lattice boltzmann method for compressible aerodynamics on d3q19 lattice. *Journal of Computational Physics*, page 109570, 2020.

[88] Zhaoli Guo and Chang Shu. *Lattice Boltzmann method and its applications in engineering*, volume 3. World Scientific, 2013.

[89] Zhaoli Guo, Chuguang Zheng, and Baochang Shi. Discrete lattice effects on the forcing term in the lattice boltzmann method. *Physical review E*, 65(4):046308, 2002.

[90] Zhaoli Guo, Chuguang Zheng, Baochang Shi, and TS Zhao. Thermal lattice boltzmann equation for low mach number flows: Decoupling model. *Physical Review E*, 75(3):036704, 2007.

[91] Farzaneh Hajabdollahi and Kannan N Premnath. Symmetrized operator split schemes for force and source modeling in cascaded lattice boltzmann methods for flow and scalar transport. *Physical Review E*, 97(6):063303, 2018.

[92] Wang Han, Jianhong Lin, Guan H Yeoh, and Evatt R Hawkes. Les/pdf modelling of a one-meter diameter methane fire plume. *Proceedings of the Combustion Institute*, 38(3):4943–4951, 2021.

[93] Xiaoyi He, Shiyi Chen, and Gary D Doolen. A novel thermal model for the lattice boltzmann method in incompressible limit. *Journal of computational physics*, 146(1):282–300, 1998.

[94] Xiaoyi He, Shiyi Chen, and Raoyang Zhang. A lattice boltzmann scheme for incompressible multiphase flow and its application in simulation of rayleigh–taylor instability. *Journal of Computational Physics*, 152(2):642–663, 1999.

[95] Xiaoyi He, Gary D Doolen, and T Clark. Comparison of the lattice boltzmann method and the artificial compressibility method for navier–stokes equations. *Journal of Computational Physics*, 179(2):439–451, 2002.

[96] Xiaoyi He, Raoyang Zhang, Shiyi Chen, and Gary D Doolen. On the three-dimensional rayleigh–taylor instability. *Physics of Fluids*, 11(5):1143–1152, 1999.

[97] G. Heskestad. Engineering relations for fire plumes. *Fire Safety J.*, 7:25–32, 1984.

[98] G Heskestad. Dynamics of the fire plume. *Philosophical Transactions of the Royal Society of London. Series A: Mathematical, Physical and Engineering Sciences*, 356(1748):2815–2833, 1998.

[99] G. Heskestad. Dynamics of the fire plume. *Phil. Trans. R. Soc. Lond. A*, 356:2815–2833, 1998.

[100] Gunnar Heskestad. Fire plume air entrainment according to two competing assumptions. In *Symposium (international) on combustion*, volume 21, pages 111–120. Elsevier, 1988.

[101] John B Heywood. *Internal combustion engine fundamentals*. McGraw-Hill Education, 2018.

[102] Seyed Ali Hosseini, Amir Eshghinejadfard, N Darabiha, and Dominique Thévenin. Weakly compressible lattice boltzmann simulations of reacting flows with detailed thermo-chemical models. *Computers & Mathematics with Applications*, 79(1):141–158, 2020.

[103] Seyed Ali Hosseini, Hesameddin Safari, and Dominique Thevenin. Lattice boltzmann solver for multiphase flows: Application to high weber and reynolds numbers. *Entropy*, 23(2):166, Jan 2021.

[104] Ming Hu, ACY Yuen, S Chi Pok Cheung, Petros Lappas, WK Chow, and GH Yeoh. Modelling of temporal combustion behaviour in a large-scale buoyant pool fire with detailed chemistry consideration. In *International Congress on Modelling and Simulation, Adelaide, Australia*, 2013.

[105] Haibo Huang, Manfred Krafczyk, and Xiyun Lu. Forcing term in single-phase and shan-chen-type multiphase lattice boltzmann models. *Physical Review E*, 84(4):046710, 2011.

[106] Dominique d' Humières, Irina Ginzburg, Manfred Krafczyk, Pierre Lallemand, and Li-Shi Luo. Multiple–relaxation–time lattice Boltzmann models in three dimensions. *Phil. Trans. R. Soc. Lond. A*, 360:437–451, 2002.

[107] Morgan J Hurley, Daniel T Gottuk, John R Hall Jr, Kazunori Harada, Erica D Kuligowski, Milosh Puchovsky, John M Watts Jr, CHRISTOPHER J WIECZOREK, et al. *SFPE handbook of fire protection engineering*. Springer, 2015.

[108] Jérôme Jacob, Orestis Malaspinas, and Pierre Sagaut. A new hybrid recursive regularised bhatnagar–gross–krook collision model for lattice boltzmann method-based large eddy simulation. *Journal of Turbulence*, 19(11-12):1051–1076, 2018.

[109] Jérôme Jacob and Pierre Sagaut. Wind comfort assessment by means of large eddy simulation with lattice boltzmann method in full scale city area. *Building and Environment*, 139:110–124, 2018.

[110] Anchal Jatale, Philip J Smith, Jeremy N Thornock, Sean T Smith, Jennifer P Spinti, and Michal Hradisky. Application of a verification, validation and uncertainty quantification framework to a turbulent buoyant helium plume. *Flow, Turbulence and Combustion*, 95(1):143–168, 2015.

[111] Hunt' JCR, AA Wray, and P Moin. Eddies, streams, and convergence zones in turbulent flows. *Studying Turbulence Using Numerical Simulation Databases-I1*, page 193, 1988.

[112] Xi Jiang and Kai H Luo. Spatial dns of flow transition of a rectangular buoyant reacting free-jet. *Journal of Turbulence*, 2(1):015, 2001.

[113] Xi Jiang and KH Luo. Spatial direct numerical simulation of the large vortical structures in forced plumes. *Flow, turbulence and combustion*, 64(1):43–69, 2000.

[114] Xi Jiang and KH Luo. Dynamics and structure of transitional buoyant jet diffusion flames with side-wall effects. *Combustion and flame*, 133(1-2):29–45, 2003.

[115] David RU Johansen and Bjarne P Husted. Implementation of improved eddy dissipation concept (edc) combustion model in fire dynamics simulator (fds). In *Proceedings of the thirteenth international conference. Interscience Communications. Interflam*, pages 389–94, 2013.

[116] E. Kaminski, S. Tait, and G. Carazzo. Turbulent entrainment in jets with arbitrary buoyancy. *Journal of Fluid Mechanics*, 526:361–376, 2005.

[117] Shin K Kang and Yassin A Hassan. The effect of lattice models within the lattice boltzmann method in the simulation of wall-bounded turbulent flows. *Journal of Computational Physics*, 232(1):100–117, 2013.

[118] Smadar Karni. Hybrid multifluid algorithms. *SIAM Journal on Scientific Computing*, 17(5):1019–1039, 1996.

[119] Takeshi Kataoka and Michihisa Tsutahara. Lattice boltzmann model for the compressible navier-stokes equations with flexible specific-heat ratio. *Physical review E*, 69(3):035701, 2004.

[120] Wiliam M Kays. Turbulent prandtl number. where are we? *ASME Journal of Heat Transfer*, 116(2):284–295, 1994.

[121] Robert J Kee, Graham Dixon-Lewis, Jürgen Warnatz, Michael E Coltrin, and James A Miller. A fortran computer code package for the evaluation of gas-phase multicomponent transport properties. *Sandia National Laboratories Report SAND86-8246*, 13:80401–1887, 1986.

[122] Andrey Nikolaevich Kolmogorov. The local structure of turbulence in incompressible viscous fluid for very large reynolds numbers. *Cr Acad. Sci. URSS*, 30:301–305, 1941.

[123] Heeseok Koo, Robert C Knaus, John C Hewson, and Stefan P Domino. Model sensitivities in les predictions of buoyant methane fire plumes. Technical report, Sandia National Lab.(SNL-NM), Albuquerque, NM (United States), 2017.

[124] Jonathan Koomey, Stephen Berard, Marla Sanchez, and Henry Wong. Implications of historical trends in the electrical efficiency of computing. *IEEE Annals of the History of Computing*, 33(3):46–54, 2010.

[125] Nikolas E Kotsovinos. Turbulence spectra in free convection flow. *Physics of Fluids A: Fluid Dynamics*, 3(1):163–167, 1991.

[126] Timm Krüger, Halim Kusumaatmaja, Alexandr Kuzmin, Orest Shardt, Goncalo Silva, and Erlend Magnus Viggen. *The Lattice Boltzmann Method: Principles and Practice*. Springer, 2016.

[127] Timm Krüger, Halim Kusumaatmaja, Alexandr Kuzmin, Orest Shardt, Goncalo Silva, and Erlend Magnus Viggen. The lattice boltzmann method. *Springer International Publishing*, 10(978-3):4–15, 2017.

[128] Anand Kumar. Isotropic finite-differences. *Journal of Computational Physics*, 201(1):109–118, 2004.

[129] AJC Ladd and R Verberg. Lattice-boltzmann simulations of particle-fluid suspensions. *Journal of statistical physics*, 104(5):1191–1251, 2001.

[130] Pierre Lallemand and Li-Shi Luo. Hybrid finite-difference thermal lattice boltzmann equation. *International Journal of Modern Physics B*, 17(01n02):41–47, 2003.

[131] Pierre Lallemand and Li-Shi Luo. Theory of the lattice boltzmann method: Acoustic and thermal properties in two and three dimensions. *Physical review E*, 68(3):036706, 2003.

[132] Jonas Latt and Bastien Chopard. Lattice boltzmann method with regularized non-equilibrium distribution functions. *arXiv preprint physics/0506157*, 2005.

[133] Jonas Latt and Bastien Chopard. Lattice boltzmann method with regularized pre-collision distribution functions. *Mathematics and Computers in Simulation*, 72(2-6):165–168, 2006.

[134] Jonas Latt, Bastien Chopard, Orestis Malaspinas, Michel Deville, and Andreas Michler. Straight velocity boundaries in the lattice boltzmann method. *Physical Review E*, 77(5):056703, 2008.

[135] Van Minh Le, Alexis Marchand, Salman Verma, Rui Xu, James White, Andre Marshall, Thomas Rogaume, Franck Richard, Jocelyn Luche, and Arnaud Trouvé. Simulations of a turbulent line fire with a steady flamelet combustion model coupled with models for non-local and local gas radiation effects. *Fire Safety Journal*, 106:105–113, 2019.

[136] Long Lee. A class of high-resolution algorithms for incompressible flows. *Computers & fluids*, 39(6):1022–1032, 2010.

[137] Q Li, KH Luo, YJ Gao, and YL He. Additional interfacial force in lattice boltzmann models for incompressible multiphase flows. *Physical Review E*, 85(2):026704, 2012.

[138] Qing Li, YL He, Yong Wang, and WQ Tao. Coupled double-distribution-function lattice boltzmann method for the compressible navier-stokes equations. *Physical Review E*, 76(5):056705, 2007.

[139] Qing Li and KH Luo. Effect of the forcing term in the pseudopotential lattice boltzmann modeling of thermal flows. *Physical Review E*, 89(5):053022, 2014.

[140] A Lingens, M Reeker, and M Schreiber. Instability of buoyant diffusion flames. *Experiments in Fluids*, 20(4):241–248, 1996.

[141] Li-Shi Luo. Theory of the lattice boltzmann method: Lattice boltzmann models for nonideal gases. *Physical Review E*, 62(4):4982, 2000.

[142] L Ma, F Nmira, and JL Consalvi. Large eddy simulation of medium-scale methanol pool fires - effects of pool boundary conditions. *Combustion and Flame*, 222:336–354, 2020.

[143] L Ma, F Nmira, and JL Consalvi. Exploring subgrid-scale variance models in les of lab-scale methane fire plumes. *Combust. Theor. model.*, 25:44–72, 2021.

[144] L Ma, F Nmira, and JL Consalvi. Modelling extinction/re-ignition processes in fire plumes under oxygen-diluted conditions using flamelet tabulation approaches. *Combust. Theor. model.*, 26:613–636, 2022.

[145] Li Ma, Fatiha Nmira, and Jean-Louis Consalvi. Verification and validation of a variable–density solver for fire safety applications. *Numerical Heat Transfer, Part B: Fundamentals*, 76(3):107–129, 2019.

[146] Bjørn F Magnussen and Bjørn H Hjertager. On mathematical modeling of turbulent combustion with special emphasis on soot formation and combustion. In *Symposium (international) on Combustion*, volume 16, pages 719–729. Elsevier, 1977.

[147] Andfrew Majda and James Sethian. The derivation and numerical solution of the equations for zero mach number combustion. *Combustion science and technology*, 42(3-4):185–205, 1985.

[148] Orestis Malaspinas. Increasing stability and accuracy of the lattice boltzmann scheme: recursivity and regularization. *arXiv preprint arXiv:1505.06900*, 2015.

[149] Orestis Malaspinas, Bastien Chopard, and Jonas Latt. General regularized boundary condition for multi-speed lattice boltzmann models. *Computers & Fluids*, 49(1):29–35, 2011.

[150] Georgios Maragkos and Bart Merci. Large eddy simulations of ch4 fire plumes. *Flow, Turbulence and Combustion*, 99(1):239–278, 2017.

[151] Georgios Maragkos and Bart Merci. Towards predictive simulations of gaseous pool fires. *Proceedings of the Combustion Institute*, 37:3927–3934, 2019.

[152] Georgios Maragkos and Bart Merci. On the use of dynamic turbulence modelling in fire applications. *Combustion and Flame*, 216:9–23, 2020.

[153] Georgios Maragkos, Pieter Rauwoens, and Bart Merci. Application of fds and firefoam in large eddy simulations of a turbulent buoyant helium plume. *Combustion Science and Technology*, 184(7-8):1108–1120, 2012.

[154] Georgios Maragkos, Pieter Rauwoens, Yi Wang, and Bart Merci. Large eddy simulations of the flow in the near-field region of a turbulent buoyant helium plume. *Flow, turbulence and combustion*, 90(3):511–543, 2013.

[155] G Marjanovic, GN Taub, and S Balachandar. On the evolution of the plume function and entrainment in the near-source region of lazy plumes. *Journal of Fluid Mechanics*, 830:736–759, 2017.

[156] Nicos S Martys, Xiaowen Shan, and Hudong Chen. Evaluation of the external force term in the discrete boltzmann equation. *Physical Review E*, 58(5):6855, 1998.

[157] Keijo K Mattila, Paulo C Philippi, and Luiz A Hegele Jr. High-order regularization in lattice-boltzmann equations. *Physics of Fluids*, 29(4):046103, 2017.

[158] Bonnie J McBride. *Coefficients for calculating thermodynamic and transport properties of individual species*, volume 4513. National Aeronautics and Space Administration, Office of Management ..., 1993.

[159] Bernard J McCaffrey and Purely Buoyant Diffusion Flames. Some experimental results. *Nbsir*, 1979.

[160] Kevin McGrattan, Simo Hostikka, Randall McDermott, Jason Floyd, Craig Weinschenk, and Kristopher Overholt. Fire dynamics simulator user's guide. *NIST special publication*, 1019(6):1–339, 2013.

[161] Brian J Meacham and Brian J Meacham. *The evolution of performance-based codes and fire safety design methods*. Society of Fire Protection Engineers, 1996.

[162] S Menow and M Rizk. Large-eddy simulations of forced three-dimensional impinging jets. *International journal of computational fluid dynamics*, 7(3):275–289, 1996.

[163] Bart Merci, José L Torero, and Arnaud Trouve. Call for participation in the first workshop organized by the iafss working group on measurement and computation of fire phenomena. *Fire Safety Journal*, 82:146–147, 2016.

[164] Bart Merci, José L Torero, and Arnaud Trouvé. Iafss working group on measurement and computation of fire phenomena. *Fire technology*, 52(3):607–610, 2016.

[165] Lucie Merlier, Jérôme Jacob, and Pierre Sagaut. Lattice-boltzmann large-eddy simulation of pollutant dispersion in street canyons including tree planting effects. *Atmospheric Environment*, 195:89–103, 2018.

[166] Lucie Merlier, Jérôme Jacob, and Pierre Sagaut. Lattice-boltzmann large-eddy simulation of pollutant dispersion in complex urban environment with dense gas effect: Model evaluation and flow analysis. *Building and Environment*, 148:634–652, 2019.

[167] Alfons Michalke. Survey on jet instability theory. *Progress in Aerospace Sciences*, 21:159–199, 1984.

[168] AA Mohamad. *Lattice boltzmann method*, volume 70. Springer, 2011.

[169] BR Morton. Buoyant plumes in a moist atmosphere. *Journal of Fluid Mechanics*, 2(2):127–144, 1957.

[170] BR Morton and Jason Middleton. Scale diagrams for forced plumes. *Journal of Fluid Mechanics*, 58(1):165–176, 1973.

[171] BR Morton, Geoffrey Ingram Taylor, and John Stewart Turner. Turbulent gravitational convection from maintained and instantaneous sources. *Proceedings of the Royal Society of London. Series A. Mathematical and Physical Sciences*, 234(1196):1–23, 1956.

[172] BR 1959 Morton. Forced plumes. *Journal of Fluid mechanics*, 5(1):151–163, 1959.

[173] H Nakagome and M Hirata. The structure of turbulent diffusion in an axisymmetrical thermal plume. In *Proc. 1976 ICHMT Seminar on Turbulent Buoyant Convection*, pages 361–372, 1977.

[174] S. Nam and R. G. Jr. Bill. Numerical simulation of thermal plumes. *Fire Safety J.*, 21:213–256, 1993.

[175] Patrick Nathen, Daniel Gaudlitz, Mathias J Krause, and Nikolaus A Adams. On the stability and accuracy of the bgk, mrt and rlb boltzmann schemes for the simulation of turbulent flows. *Commun Comput Phys*, 23(3):1–31, 2018.

[176] Franck Nicoud, Hubert Baya Toda, Olivier Cabrit, Sanjeeb Bose, and Jungil Lee. Using singular values to build a subgrid-scale model for large eddy simulations. *Physics of fluids*, 23(8):085106, 2011.

[177] Xiaobo Nie, Xiaowen Shan, and Hudong Chen. A lattice-boltzmann/finite-difference hybrid simulation of transonic flow. In *47th AIAA Aerospace Sciences Meeting Including the New Horizons Forum and Aerospace Exposition*, page 139, 2009.

[178] F Nmira, A Bouffard, JL Consalvi, and Y Wang. Large-eddy simulation of lab-scale ethylene buoyant diffusion flames: Effects of subgrid turbulence/soot production interaction and radiation models. *Proc. Combust. Inst.*, 39:1–10, 2023.

[179] F Nmira and JL Consalvi. Local contributions of resolved and subgrid turbulence-radiation interaction in les/presumed fdf modelling of large-scale methanol pool fires. *Int. J. Heat Mass Transf.*, 190:122746, 2022.

[180] F Nmira, L Ma, and JL Consalvi. Assessment of subfilter-scale turbulence radiation interaction in non-luminous pool fires. *Proceedings of the Combustion Institute*, 221:4927–4934, 2020.

[181] F Nmira, L Ma, and JL Consalvi. Influence of gas radiative property models on large eddy simulation of 1 m methanol pool fires. *Combustion and Flame*, 221:352–363, 2020.

[182] William D Nordhaus. Two centuries of productivity growth in computing. *The Journal of Economic History*, 67(1):128–159, 2007.

[183] TJ O'hern, EJ Weckman, AL Gerhart, SR Tieszen, and RW1154 Schefer. Experimental study of a turbulent buoyant helium plume. *Journal of Fluid Mechanics*, 544:143–171, 2005.

[184] Nasreddine Ouertatani, Nader Ben-Cheikh, Brahim Beya, and Taieb Lili. Numerical simulation of two-dimensional rayleigh–bénard convection in an enclosure. *Comptes Rendus Mécanique*, 336:464–470, 05 2008.

[185] C.S. Pant and A. Bhattacharya. Evaluation of an energy consistent entrainment model for volumetrically forced jets using large eddy simulations. *Physics of Fluids*, 30:105107, 2018.

[186] Samuel Paolucci. Filtering of sound from the navier-stokes equations. *NASA STI/Recon Technical Report N*, 83:26036, 1982.

[187] Panos N. Papanicolaou and E. John List. Investigations of round vertical turbulent buoyant jets. *Journal of Fluid Mechanics*, 195:341–391, 1988.

[188] H Pasdarshahri, G Heidarinejad, and K Mazaheri. Large eddy simulation on one-meter methane pool fire using one-equation sub-grid scale model. In *MCS*, volume 7, pages 11–15, 2012.

[189] Minh Vuong Pham, Frédéric Plourde, Son Doan Kim, and S Balachandar. Large-eddy simulation of a pure thermal plume under rotating conditions. *Physics of Fluids*, 18(1):015101, 2006.

[190] Frédéric Plourde, Minh Vuong Pham, Son Doan Kim, and S Balachandar. Direct numerical simulations of a rapidly expanding thermal plume: structure and entrainment interaction. *Journal of Fluid Mechanics*, 604:99, 2008.

[191] T. Poinsot and D. Veynante. *Theoretical and numerical combustion.* RT Edwards, Inc., 2005.

[192] Kannan N Premnath and John Abraham. Three-dimensional multi-relaxation time (mrt) lattice-boltzmann models for multiphase flow. *Journal of Computational Physics*, 224(2):539–559, 2007.

[193] David Pyle. Sparks, r. s. j., bursik, m. i., carey, s. n., gilbert, j. s., glaze, l. s., sigurdsson, h. & woods, a. w. 1997. volcanic plumes. xv 574 pp. chichester, new york, weinheim, brisbane, singapore, toronto: John wiley & sons. price £85.00 (hard covers). isbn 0 471 93901 3. *Geological Magazine*, 135(1):143–158, 1998.

[194] YH Qian. Simulating thermohydrodynamics with lattice bgk models. *Journal of scientific computing*, 8(3):231–242, 1993.

[195] Ruo-Fan Qiu, Yan-Cheng You, Cheng-Xiang Zhu, Rong-Qian Chen, and Jian-Feng Zhu. Three-dimensional coupled double-distribution-function lattice boltzmann models for compressible navier–stokes equations. *Pramana*, 89(6):1–11, 2017.

[196] Ruo-Fan Qiu, Cheng-Xiang Zhu, Rong-Qian Chen, Jian-Feng Zhu, and Yan-Cheng You. A double-distribution-function lattice boltzmann model for high-speed compressible viscous flows. *Computers & Fluids*, 166:24–31, 2018.

[197] James Quintiere. *Fundamentals of Fire Phenomena.* John Wiley & Sons, 2006.

[198] JG Quintiere and BS Grove. A unified analysis for fire plumes. In *Symposium (International) on Combustion*, volume 27, pages 2757–2766. Elsevier, 1998.

[199] Ronald G Rehm and Howard R Baum. The equations of motion for thermally driven, buoyant flows. *Journal of research of the National Bureau of Standards*, 83(3):297, 1978.

[200] Florian Renard, Yongliang Feng, Jean-François Boussuge, and Pierre Sagaut. Improved compressible hybrid lattice boltzmann method on standard lattice for subsonic and supersonic flows. *Computers & Fluids*, 219:104867, 2021.

[201] Hunter Rouse, Co S Yih, and HW Humphreys. Gravitational convection from a boundary source. *Tellus*, 4(3):201–210, 1952.

[202] MH Saadat, SA Hosseini, B Dorschner, and IV Karlin. Extended lattice boltzmann model for gas dynamics. *Physics of Fluids*, 33(4):046104, 2021.

[203] Z. Saeed, E. Weidner, B.E. Johnson, and T. L. Mandel. Buoyancy-modified entrainment in plumes: Theoretical predictions. *Physics of Fluids*, 34:015112, 2022.

[204] Pierre Sagaut. *Large eddy simulation for incompressible flows: an introduction.* Springer Science & Business Media, 2006.

[205] Hermann Schlichting and Klaus Gersten. *Boundary-layer theory.* Springer, 2016.

[206] W Schmidt. Turbulent propagation of a stream of heated air. *Z. angew. math. mech*, 21:265–278, 1941.

[207] Aamir Shabbir and William K George. Experiments on a round turbulent buoyant plume. *Journal of Fluid Mechanics*, 275:1–32, 1994.

[208] Xiaowen Shan, Xue-Feng Yuan, and Hudong Chen. Kinetic theory representation of hydrodynamics: a way beyond the navier–stokes equation. *Journal of Fluid Mechanics*, 550:413–441, 2006.

[209] Goncalo Silva and Viriato Semiao. Truncation errors and the rotational invariance of three-dimensional lattice models in the lattice boltzmann method. *Journal of Computational Physics*, 269:259–279, 2014.

[210] Eric D Skyllingstad and Donald W Denbo. Turbulence beneath sea ice and leads: A coupled sea ice/large-eddy simulation study. *Journal of Geophysical Research: Oceans*, 106(C2):2477–2497, 2001.

[211] Joseph Smagorinsky. General circulation experiments with the primitive equations: I. the basic experiment. *Monthly weather review*, 91(3):99–164, 1963.

[212] Philippe R Spalart. Comments on the feasibility of les for wings, and on a hybrid rans/les approach. In *Proceedings of first AFOSR international conference on DNS/LES*. Greyden Press, 1997.

[213] D Brian Spalding. Development of the eddy-break-up model of turbulent combustion. In *Symposium (International) on Combustion*, volume 16, pages 1657–1663. Elsevier, 1977.

[214] DB Spalding. Mixing and chemical reaction in steady confined turbulent flames. In *Symposium (International) on combustion*, volume 13, pages 649–657. Elsevier, 1971.

[215] Daniel Richard Stull. *JANAF Thermochemical Tables...*, volume 1. Clearinghouse, 1965.

[216] Sauro Succi, Roberto Benzi, and Francisco Higuera. The lattice boltzmann equation: a new tool for computational fluid-dynamics. *Physica D: Nonlinear Phenomena*, 47(1-2):219–230, 1991.

[217] Kazuhiko Suga, Yoshiaki Kuwata, K Takashima, and R Chikasue. A d3q27 multiple-relaxation-time lattice boltzmann method for turbulent flows. *Computers & Mathematics with Applications*, 69(6):518–529, 2015.

[218] Kunhyuk Sung, Jian Chen, Matthew Bundy, and Anthony Hamins. The characteristics of a 1 m methanol pool fire. *Fire Safety Journal*, 120:103121, 2021.

[219] Kunhyuk Sung, Kunhyuk Sung, Jian Chen, Matthew Bundy, Marco Fernandez, and Anthony Hamins. *The thermal character of a 1 m methanol pool fire*. US Department of Commerce, National Institute of Standards and Technology, 2020.

[220] Mostafa Taha, Song Zhao, Aymeric Lamorlette, Jean-Louis Consalvi, and Pierre Boivin. Lattice-boltzmann modeling of buoyancy-driven turbulent flows. *Physics of Fluids*, 34(5):055131, 2022.

[221] Said Taileb, Alejandro Millán-Merino, Song Zhao, and Pierre Boivin. Lattice-boltzmann modeling of lifted hydrogen jet flames: A new model for hazardous ignition prediction. *Combustion and Flame*, 245:112317, 2022.

[222] Muhammad Tayyab. *Development of combustion modelling within lattice Boltzmann framework*. PhD thesis, Aix-Marseille, 2020.

[223] Muhammad Tayyab, Basile Radisson, Christophe Almarcha, Bruno Denet, and Pierre Boivin. Experimental and numerical lattice-boltzmann investigation of the darrieus-landau instability. *Combustion and Flame*, 221:103–109, 2020.

[224] Muhammad Tayyab, Song Zhao, and Pierre Boivin. Lattice-boltzmann modelling of a turbulent bluff-body stabilized flame. *Physics of Fluids*, 33(3):031701, 2021.

[225] Muhammad Tayyab, Song Zhao, Yongliang Feng, and Pierre Boivin. Hybrid regularized lattice-boltzmann modelling of premixed and non-premixed combustion processes. *Combustion and Flame*, 211:173–184, 2020.

[226] Sumesh P Thampi, Santosh Ansumali, Ronojoy Adhikari, and Sauro Succi. Isotropic discrete laplacian operators from lattice hydrodynamics. *Journal of Computational Physics*, 234:1–7, 2013.

[227] Sheldon R Tieszen, Timothy J OHern, Robert W Schefer, and LD Perea. Spatial and temporal resolution of fluid flows: Ldrd final report. Technical report, Sandia National Lab.(SNL-NM), Albuquerque, NM (United States), 1998.

[228] SR Tieszen and LA Gritzo. Transport phenomena that affect heat transfer in fully turbulent fires. In B Sunden and M Faghri, editors, *Transport Phenonema in Fires*, chapter 2, pages 25–63. WIT Press, Boston, 2008.

[229] SR Tieszen, TJ O'hern, EJ Weckman, and RW Schefer. Experimental study of the effect of fuel mass flux on a 1-m-diameter methane fire and comparison with a hydrogen fire. *Combustion and flame*, 139(1-2):126–141, 2004.

[230] SR Tieszen, TJ O'hern, RW Schefer, EJ Weckman, and TK Blanchat. Experimental study of the flow field in and around a one meter diameter methane fire. *Combustion and Flame*, 129(4):378–391, 2002.

[231] Yoshihide Tominaga and Ted Stathopoulos. Turbulent schmidt numbers for cfd analysis with various types of flowfield. *Atmospheric Environment*, 41(37):8091–8099, 2007.

[232] Ali Nassiri Toosi, Mohammadreza Farokhi, and Behrooz Mashadi. Application of modified eddy dissipation concept with large eddy simulation for numerical investigation of internal combustion engines. *Computers & Fluids*, 109:85–99, 2015.

[233] Eleuterio F Toro. *Riemann solvers and numerical methods for fluid dynamics: a practical introduction*. Springer Science & Business Media, 2013.

[234] Grétar Tryggvason. Numerical simulations of the rayleigh-taylor instability. *Journal of Computational Physics*, 75(2):253–282, 1988.

[235] JS Turner. Buoyant plumes and thermals. *Annual Review of Fluid Mechanics*, 1(1):29–44, 1969.

[236] S Ubertini, P Asinari, and S Succi. Three ways to lattice boltzmann: a unified time-marching picture. *Physical Review E*, 81(1):016311, 2010.

[237] Karim Van Maele and Bart Merci. Application of two buoyancy-modified k–ε turbulence models to different types of buoyant plumes. *Fire Safety Journal*, 41(2):122–138, 2006.

[238] M. van Reeuwijk and J. Craske. Energy-consistent entrainment relations for jets and plumes. *Journal of Fluid Mechanics*, 782:333–355, 2015.

[239] S Vilfayeau, N Ren, Y Wang, and A Trouvé. Numerical simulation of under-ventilated liquid-fueled compartment fires with flame extinction and thermally-driven fuel evaporation. *Proc. Combust. Inst.*, 35:2563–2571, 2015.

[240] S Vilfayeau, JP White, PB Sunderland, AW Marshall, and A Trouvé. Large eddy simulation of flame extinction in a turbulent line fire exposed to air-nitrogen co-flow. *Fire Safety J.*, 86:16–31, 2016.

[241] AW Vreman. An eddy-viscosity subgrid-scale model for turbulent shear flow: Algebraic theory and applications. *Physics of fluids*, 16(10):3670–3681, 2004.

[242] Guanxiong Wang, Song Zhao, Pierre Boivin, Eric Serre, and Pierre Sagaut. A new hybrid lattice-boltzmann method for thermal flow simulations in low-mach number approximation. *Physics of Fluids*, 34(4):046114, 2022.

[243] Yi Wang, Prateep Chatterjee, and John L de Ris. Large eddy simulation of fire plumes. *Proceedings of the Combustion Institute*, 33(2):2473–2480, 2011.

[244] Minoru Watari and Michihisa Tsutahara. Possibility of constructing a multispeed bhatnagar-gross-krook thermal model of the lattice boltzmann method. *Physical Review E*, 70(1):016703, 2004.

[245] EJ Weckman and A Sobiesiak. The oscillatory behaviour of medium-scale pool fires. In *Symposium (International) on Combustion*, volume 22, pages 1299–1310. Elsevier, 1989.

[246] EJ Weckman and AB Strong. Experimental investigation of the turbulence structure of medium-scale methanol pool fires. *Combustion and Flame*, 105(3):245–266, 1996.

[247] Elizabeth J Weckman. The structure of the flowfield near the base of a medium-scale pool fire. 1989.

[248] Alexander Thomas White and Chuh Khiun Chong. Rotational invariance in the three-dimensional lattice boltzmann method is dependent on the choice of lattice. *Journal of Computational Physics*, 230(16):6367–6378, 2011.

[249] James Patrick White. *Measurement and simulation of suppression effects in a buoyant turbulent line fire*. PhD thesis, University of Maryland, College Park, 2016.

[250] JP White, ED Link, A Trouvé, PB Sunderland, and AW Marshall. A general calorimetry framework for measurement of combustion efficiency in a suppressed turbulent line fire. *Fire Safety Journal*, 92:164–176, 2017.

[251] JP White, ED Link, AC Trouvé, PB Sunderland, AW Marshall, JA Sheffel, ML Corn, MB Colket, M Chaos, and H-Z Yu. Radiative emissions measurements from a buoyant, turbulent line flame under oxidizer-dilution quenching conditions. *Fire Safety Journal*, 76:74–84, 2015.

[252] JP White, S Vilfayeau, A W Marshall, A Trouvé, and R J McDermott. Modeling flame extinction and reignition in large eddy simulations with fast chemistry. *Fire safety J.*, 90:72–85, 2017.

[253] Karolina Widell, Ilker Fer, and Peter M Haugan. Salt release from warming sea ice. *Geophysical research letters*, 33(12), 2006.

[254] Forman A Williams. *Combustion theory*. CRC Press, 2018.

[255] Nicholas T Wimer, Marcus S Day, Caelan Lapointe, Michael A Meehan, Amanda S Makowiecki, Jeffrey F Glusman, John W Daily, Gregory B Rieker, and Peter E Hamlington. Numerical simulations of buoyancy-driven flows using adaptive mesh refinement: structure and dynamics

of a large-scale helium plume. *Theoretical and Computational Fluid Dynamics*, 35(1):61–91, 2021.

[256] Gauthier Wissocq, Pierre Sagaut, and Jean-François Boussuge. An extended spectral analysis of the lattice boltzmann method: modal interactions and stability issues. *Journal of Computational Physics*, 380:311–333, 2019.

[257] Dieter A Wolf-Gladrow. *Lattice-gas cellular automata and lattice Boltzmann models: an introduction*. Springer, 2004.

[258] Andrew W Woods. Turbulent plumes in nature. *Annual Review of Fluid Mechanics*, 42:391–412, 2010.

[259] J. Worthy, V. Sanderson, and P. Rubini. Comparison of modified k-epsilon turbulence models for buoyant plumes. *Num. Heat Transf. B*, 39:151–165, 2001.

[260] Rui X, Van Minh Le, Alexis Marchand, Salman Verma, Thomas Rogaume, Franck Richard, Jocelyn Luche, and Arnaud Trouvé. Simulations of a turbulent line fire with a steady flamelet combustion model coupled with models for non-local and local gas radiation effects. *Fire Safety Journal*, 120:103101, 2021.

[261] Y Xin, SA Filatyev, K Biswas, JP Gore, RG Rehm, and HR Baum. Fire dynamics simulations of a one-meter diameter methane fire. *Combustion and Flame*, 153(4):499–509, 2008.

[262] Yu Xin, Tang Xuelin, Wang Wuchang, WANG Fujun, CHEN Zhicong, and SHI Xiaoyan. A lattice boltzmann model coupled with a large eddy simulation model for flows around a groyne. *International Journal of Sediment Research*, 25(3):271–282, 2010.

[263] Hui Xu, Orestis Malaspinas, and Pierre Sagaut. Sensitivity analysis and determination of free relaxation parameters for the weakly-compressible mrt–lbm schemes. *Journal of Computational Physics*, 231(21):7335–7367, 2012.

[264] Mitsuru Yaga, Hajime Endo, Tsuyoshi Yamamoto, Hideyuki Aoki, and Takatoshi Miura. Modeling of eddy characteristic time in les for calculating turbulent diffusion flame. *International Journal of Heat and Mass Transfer*, 45(11):2343–2349, 2002.

[265] Z. H. Yan. Large eddy simulations of a turbulent thermal plume. *Heat Mass Transfer*, 43:503–514, 2007.

[266] HZ Yu and N Ren. A methodology for applying the counterflow flame extinction propensity to the flame extinction determination in fire simulations. *Fire Safety J.*, 120:103100, 2021.

[267] Xu Zhou, Kai H Luo, and John JR Williams. Large-eddy simulation of a turbulent forced plume. *European Journal of Mechanics-B/Fluids*, 20(2):233–254, 2001.

[268] Xu Zhou, Kai H Luo, and John JR Williams. Study of density effects in turbulent buoyant jets using large-eddy simulation. *Theoret. Comput. Fluid Dynamics*, 15:95–120, 2001.

[269] YQ Zu and S He. Phase-field-based lattice boltzmann model for incompressible binary fluid systems with density and viscosity contrasts. *Physical Review E*, 87(4):043301, 2013.

[270] EE Zukoski. Properties of fire plumes. 1995.

Appendix A

NS-related appendix

A.1 From total energy to enthalpy

As mentioned in the main text, the transformation between different forms of energy can be found in details in [191]. Here, and for the sake of our investigation, the linking between total energy and the enthalpy equations will be demonstrated. Starting by recalling the total energy equation 2.5:

$$\frac{\partial \rho e_t}{\partial t} + \frac{\partial u_\alpha(\rho e_t + p)}{\partial x_\alpha} = -\frac{\partial q_\alpha}{\partial x_\alpha} + \frac{\partial \Pi_{\alpha\beta} u_\alpha}{\partial x_\beta} + \rho u_\alpha F_\alpha \tag{A.1}$$

The equation of kinetic energy equation can be obtained by multiplying the momentum equation by u_α and exploiting the continuity equation we end up with:

$$\frac{\partial}{\partial t}(\frac{1}{2}u_\alpha u_\alpha) + \frac{\partial}{\partial x_\beta}(\frac{1}{2}\rho u_\alpha u_\alpha u_\beta) + u_\alpha \frac{\partial p\delta_{\alpha\beta}}{\partial x_\beta} = u_\alpha \frac{\partial \Pi_{\alpha\beta}}{\partial x_\beta} + \rho u_\alpha F_\alpha \tag{A.2}$$

Subtracting the previous two equation we end up with the internal energy equation:

$$\frac{\partial \rho e}{\partial t} + \frac{\partial \rho u_\alpha e}{\partial x_\beta} + p\delta_{\alpha\beta}\frac{\partial u_\alpha}{\partial x_\beta} = -\frac{\partial q_\alpha}{\partial x_\alpha} + \Pi_{\alpha\beta}\frac{\partial u_\alpha}{\partial x_\beta} \tag{A.3}$$

The enthalpy h is linked to energy e though $e = h - p/\rho$ which gives:

$$\rho\frac{De}{Dt} = \rho\frac{Dh}{Dt} - \frac{Dp}{Dt} - p\frac{\partial u_\alpha}{\partial x_\alpha} \quad \text{with} \quad \rho\frac{Df}{Dt} = \frac{\partial f}{\partial t} + \frac{\partial \rho u_\beta f}{\partial x_\beta} \tag{A.4}$$

substituting this into the internal energy equation we get finally the enthalpy equa-

tion:

$$\frac{\partial \rho h}{\partial t} + \frac{\partial \rho u_\alpha h}{\partial x_\alpha} = \frac{Dp}{Dt} - \frac{\partial q_\alpha}{\partial x_\alpha} + \Pi_{\alpha\beta}\frac{\partial u_\alpha}{\partial x_\beta} \tag{A.5}$$

A.2 Vorticity transport equation

Helmholtz equation is the transport equation for vorticity, which can be deduced as follows. Starting from writing the momentum equation of incompressible flow, that is $\nabla \cdot \mathbf{u} = 0$, but with a variable density ρ.

$$\frac{\partial \mathbf{u}}{\partial t} + \mathbf{u} \cdot \nabla \mathbf{u} = -\frac{1}{\rho}\nabla p + \frac{1}{\rho}\nabla \cdot \tau + \frac{(\rho - \rho_0)}{\rho}\boldsymbol{g}, \tag{A.6}$$

The convective term $\mathbf{u} \cdot \nabla \mathbf{u}$ can be written in the following form:

$$\mathbf{u} \cdot \nabla \mathbf{u} = \nabla(\mathbf{u}^2/2) + \boldsymbol{\omega} \times \mathbf{u}, \tag{A.7}$$

The following vector identity will be used:

$$\nabla \times (\boldsymbol{\omega} \times \mathbf{u}) = (\mathbf{u} \cdot \nabla)\boldsymbol{\omega} - \underbrace{\mathbf{u}(\nabla \cdot \boldsymbol{\omega})}_{=0} - (\boldsymbol{\omega} \cdot \nabla)\mathbf{u} + \boldsymbol{\omega}(\nabla \cdot \mathbf{u}), \tag{A.8}$$

where $\nabla \cdot \boldsymbol{\omega} \equiv 0$ (vorticity is solenoidal by definition), the vorticity equation can be rearranged as:

$$\underbrace{\frac{\partial \boldsymbol{\omega}}{\partial t} + (\mathbf{u} \cdot \nabla)\boldsymbol{\omega}}_{D\boldsymbol{\omega}/Dt} = (\boldsymbol{\omega} \cdot \nabla)\mathbf{u} - \boldsymbol{\omega}(\nabla \cdot \mathbf{u}) - \nabla \times \left(\frac{1}{\rho}\nabla p\right) + \nabla \times \left(\frac{1}{\rho}\nabla \cdot \tau\right) + \nabla \times \left[(1 - \frac{\rho_0}{\rho})\mathbf{g}\right], \tag{A.9}$$

The pressure term can be written as:

$$\nabla \times \left(\frac{1}{\rho}\nabla p\right) = \nabla\left(\frac{1}{\rho}\right) \times \nabla p + \underbrace{\frac{1}{\rho}\nabla \times (\nabla p)}_{\text{zero}} = -\frac{1}{\rho^2}\left(\nabla \rho \times \nabla p\right), \tag{A.10}$$

Further more for a **homentropic** flow, the pressure is a function of only of density resulting in the alignment of the two vector ∇p and $\nabla \rho$ and consequently the so called baroclinic torque $-\left(\nabla \rho \times \nabla p\right)/\rho^2$ will vanish. By the same manner, the buoyancy

term will be treated:

$$\nabla \times \left[(1-\frac{\rho_0}{\rho})\mathbf{g}\right] = \underbrace{\nabla \times \mathbf{g}}_{\text{zero}} - \nabla \times \left(\frac{\rho_0}{\rho}\mathbf{g}\right) = -\nabla\left(\frac{\rho_0}{\rho}\right) \times \mathbf{g} - \underbrace{\frac{\rho_0}{\rho}(\nabla \times \mathbf{g})}_{\text{zero}} = \frac{\rho_0}{\rho^2}(\nabla\rho \times \mathbf{g}), \tag{A.11}$$

By introducing the material derivative of the vorticity, $D\boldsymbol{\omega}/Dt$, the vorticity equation yields to:

$$\frac{D\boldsymbol{\omega}}{Dt} = \underbrace{(\boldsymbol{\omega}\cdot\nabla)\boldsymbol{u}}_{\text{vortex stretching}} - \underbrace{\boldsymbol{\omega}(\nabla\cdot\boldsymbol{u})}_{\text{vortex dilatation}} + \underbrace{\frac{1}{\rho^2}(\nabla\rho\times\nabla p)}_{\text{baroclinic torque}} + \underbrace{\frac{\rho_0}{\rho^2}(\nabla\rho\times\mathbf{g})}_{\text{gravitational torque}} + \underbrace{\nabla\times\left(\frac{1}{\rho}\nabla\cdot\tau\right)}_{\text{viscous diffusion}}. \tag{A.12}$$

A.3 NASA polynomials

The NASA polynomial is another representation of the heat capacity, enthalpy, and entropy using seven or nine coefficients. In this work, the seven coefficient formula is used. We used this polynomial only in the reactive simulations, otherwise, the heat capacity was taken constant and enthalpy was calculated using this constant value. The polynomials takes the following formulation:

$$\frac{C_{p,k}(T)}{\mathcal{R}} = A_1 + A_2T + A_3T^2 + A_4T^3 + A_5T^4, \tag{A.13}$$

$$\frac{h_k(T)}{\mathcal{R}} = A_1 + A_2\frac{T}{2} + A_3\frac{T^2}{3} + A_4\frac{T^3}{4} + A_5\frac{T^4}{5} + \frac{A_6}{T} \tag{A.14}$$

Table A.1 shows the NASA polynomial coefficients for the species used during our work as well as the corresponding molecular weight:

There exist 14 coefficients, the first 7 ($A_1 \rightarrow A_7$) are to be used for temperature range from 200 to 1000 K while the second 7 ($A_8 \rightarrow A_{14}$) used when temperature falls between 1000 and 6000 K.

	CH_4	O_2	CO_2	H_2O	N_2
$\mathcal{W}_k$	16.043	31.998	44.009	18.015	28.014
A_1	7.4851495E-02	3.28253784E+00	3.85746029E+00	3.03399249E+00	2.92664E+00
A_2	1.33909467E-02	1.48308754E-03	4.41437026E-03	2.17691804E-03	1.4879768e-03
A_3	-5.73285809E-06	-7.57966669E-07	-2.21481404E-06	-1.64072518E-07	-5.68476e-07
A_4	1.22292535E-09	2.09470555E-10	5.23490188E-10	-9.70419870E-11	1.0097038e-10
A_5	-1.0181523E-13	-2.16717794E-14	-4.72084164E-14	1.68200992E-14	-6.753351e-15
A_6	-9.46834459E+03	-1.08845772E+03	-4.8759166E+04	-3.00042971E+04	-9.227977e+02
A_7	1.8437318E+01	5.45323129E+00	2.27163806E+00	4.9667701E+00	5.980528e+00
A_8	5.14987613E+00	3.78245636E+00	2.35677352E+00	4.19864056E+00	3.298677e+00
A_9	-1.36709788E-02	-2.99673416E-03	8.98459677E-03	-2.0364341E-03	1.4082404e-03
A_{10}	4.91800599E-05	9.84730201E-06	-7.12356269E-06	6.52040211E-06	-3.963222e-06
A_{11}	-4.84743026E-08	-9.68129509E-09	2.45919022E-09	-5.48797062E-09	5.64151500e-09
A_{12}	1.66693956E-11	3.24372837E-12	-1.43699548E-13	1.77197817E-12	-2.444854e-12
A_{13}	-1.02466476E+04	-1.06394356E+03	-4.83719697E+04	-3.02937267E+04	-1.0208999e+03
A_{14}	-4.64130376E+00	3.65767573E+00	9.90105222E+00	-8.49032208E-01	3.950372e+00

Table A.1: NASA polynomial coefficients for different species.

Appendix B

LBM related appendix

B.1 Derivation of distribution function

Let's consider having a gas with N particles contained in a certain volume, the number of particles having a velocity in the x-direction between c_x and $c_x + dc_x$ is $Nf(c_x)dc_x$. The function $f(c_x)$ is the percentage of the particles having velocity between c_x and dc_x in the x-direction. Similarly, for the other two directions (i.e. y and z), the velocity distribution function can be defined as before; thus, the probability function of having particles with velocities that lie between c_x and $c_x + dc_x$, c_y and $c_y + dc_y$, and c_z and $c_z + dc_z$ will be:

$$Nf(c_x)f(c_y)f(c_z)dc_xdc_ydc_z. \tag{B.1}$$

If the previous equation was integrated over all possible values of velocities, the result will be the total number of particles N:

$$\iiint f(c_x)f(c_y)f(c_z)dc_xdc_ydc_z = 1, \tag{B.2}$$

From the previous equation, it can be deduced that the distribution function does not depend on the direction, considering that any direction can be x, or y, or z, nevertheless, it depends only on the velocity of the particles. Consequently, we can write:

$$f(c_x)f(c_y)f(c_z) = \Phi(c_x^2 + c_y^2 + c_z^2), \tag{B.3}$$

where the function Φ is another unknown function, that needs to be determined. The distribution function is always positive ranging from zero to unity. That's why the velocities were squared in Eqn. B.3 to avoid any negative values. Given that, the

possible function that can have the same property is is logarithmic or exponential function. It can be shown that the appropriate form for the distribution function takes the following shape:

$$f(c_x) = Ae^{-Bc_x^2}, \tag{B.4}$$

where A and B are constants. Hence, the total distribution function $f(c)$ will be:

$$f(c) = f(c_x)f(c_y)f(c_z) = Ae^{-Bc_x^2}Ae^{-Bc_y^2}Ae^{-Bc_z^2} = A^3e^{-Bc^2}. \tag{B.5}$$

The multiplication of the probability distributions for all three directions gives the distribution in terms of the total particle velocity c. Strictly speaking, the distribution function describes a number of particles having speed between c and $c + dc$. Another way of seeing this, is by visualizing the particles distribution in the velocity space.

Consider having a three-dimensional velocity space (c_x, c_y, c_z), in which each particle is represented by a point with coordinates corresponding to its velocity. Hence, the particles that have the same velocity will be on a sphere surface centered at the origin having a radius corresponding to the velocity magnitude. As a result, the number of particles having speeds between c and $c+dc$ (Fig.B.1)equals the number of points lying between two shells of the spheres having radii of c and $c + dc$. The volume between those two spheres is $4\pi c^2 dc$, the probability distribution function therefore reads:

$$f(c)dc = 4\pi c^2 A^3 e^{-Bc^2} dc, \tag{B.6}$$

To determine the constant A and B, the above equation should be integrated over all possible speeds to find the total number of particles N, and their total energy E.

Giving that a particle traveling at speed c has kinetic energy $\frac{1}{2}mc^2$, one can use the probability distribution function to find the average kinetic energy for each particle, as:

$$\overline{\frac{1}{2}mc^2} = \frac{\int_0^\infty \frac{1}{2}mc^2 f(c)dc}{\int_0^\infty f(c)dc}, \tag{B.7}$$

where the numerator represents the total kinetic energy whereas the denominator is the total number of particles N. Substituting the expression of $f(c)$ in the integral from Eqn. B.5 yields to:

$$\overline{\frac{1}{2}mc^2} = \frac{3m}{4B} \tag{B.8}$$

It can be shown that the kinetic energy (KE) can be written in terms of temperature

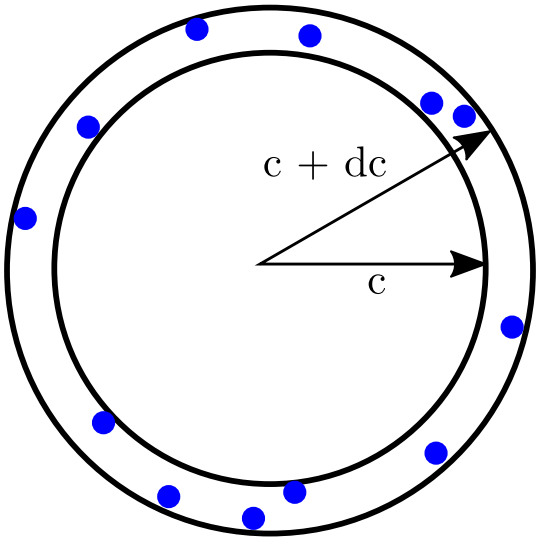

Figure B.1: Schematic showing the velocity phase diagram

by introducing the *Boltzmann constant* $k = 1.38 \times 10^{-23}$J/K, so that: K.E. $= mc^2/2 = (3/2)kT$. Thus, the constant B can be now deduced to be:

$$B = \frac{m}{2kT} \tag{B.9}$$

So the distribution function $f(c)$ will be:

$$f(c) \propto c^2 e^{\frac{-mc^2}{2kT}}, \tag{B.10}$$

The constant of proportionality can be found by integrating over all the velocity space and setting the result to unity (refer to Eqn. B.2). So that the final result will be:

$$f(c) = 4\pi(\frac{m}{2\pi kT})^{\frac{3}{2}} c^2 e^{-\frac{mc^2}{2kT}}, \tag{B.11}$$

B.2 Boltzmann distribution

Boltzmann proved that that the thermodynamic entropy S, of a system having a certain energy E, is related the number W of possible states that it can have $S = klog(W)$, k being the Boltzmann's constant. Determining the number of microscopic possible arrangements was not clear, which was resolved using quantum mechanics. Then Boltz-

mann constructed that for any system (small or large) in thermal equilibrium at temperature T, the probability of being at a specific level of energy E is proportional to $e^{-\frac{E}{kT}}$, in other words:

$$f(E) = Ae^{-\frac{E}{kT}}, \tag{B.12}$$

This is called the *Boltzmann distribution*. Considering that the kinetic energy of a molecule in the x-direction is $E = 1/2mc_x^2$, hence, for a normalized probability function, the integration of the probability function for all the possible values of velocity (from minus to positive infinity) should equal unity:

$$\int_{\infty}^{\infty} Ae^{\frac{mc_x^2}{2kT}} dc = 1 \tag{B.13}$$

So that we can deduce the value of the constant A:

$$A = \sqrt{\frac{m}{2\pi kT}} \tag{B.14}$$

So that, the probability of finding particles with velocity c_x will be:

$$f(c_x) = \sqrt{\frac{m}{2\pi kT}} e^{\frac{mc_x^2}{2kT}} \tag{B.15}$$

Therefore, if we need to find the probability of the three-dimensional velocity $c = c_x^2 + c_y^2 + c_z^2$, the probability of finding particles with velocity c will be the multiplication of the probability of each direction:

$$f(c) = f(c_x)f(c_y)f(c_z), \tag{B.16}$$

which yields to the final form:

$$f(c) = \left(\sqrt{\frac{m}{2\pi kT}}\right)^3 e^{\frac{m(c_x^2+c_y^2+c_z^2)}{2kT}} = \left(\frac{m}{2\pi kT}\right)^{3/2} e^{\frac{mc^2}{2kT}} \tag{B.17}$$

B.3 Derivation of Boltzmann equation

The function $f(\boldsymbol{x}, \boldsymbol{\xi}, t)$ is the number of molecules at time t positioned between $\boldsymbol{x}$ and $\boldsymbol{x} + d\boldsymbol{x}$ possessing velocity between $\boldsymbol{\xi}$ and $\boldsymbol{\xi} + d\boldsymbol{\xi}$, as explained previously. Consider an external force $\mathbf{F}$ acting on a gas molecule of unit mass will change the velocity of the molecule from $\boldsymbol{\xi}$ to $\boldsymbol{\xi} + \mathbf{F}dt$ and its position from $\boldsymbol{x}$ to $\boldsymbol{x} + \boldsymbol{\xi}dt$, depicted in Fig. B.2

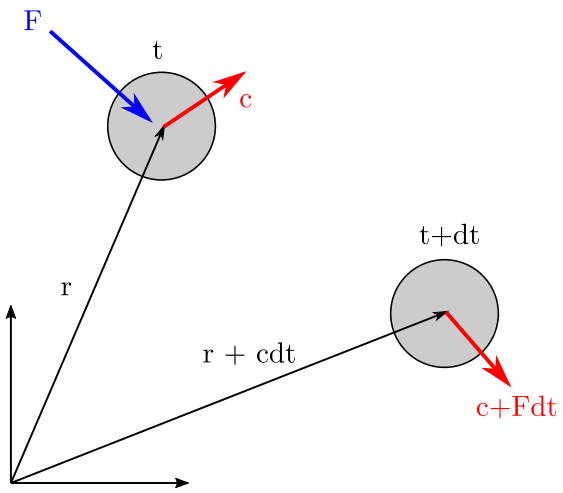

Figure B.2: Change of the position and velocity of a particle after being submitted to external force **F**

The number of the particles remains the same before, $f(\boldsymbol{x}, \boldsymbol{\xi}, t)$, and after applying the force **F**, $f(\boldsymbol{x} + \boldsymbol{\xi}dt, \boldsymbol{\xi} + \mathbf{F}dt, t + dt)$, **if and only if** no collision occurred between the particles. Therefore,

$$f(\boldsymbol{x} + \boldsymbol{\xi}dt, \boldsymbol{\xi} + \mathbf{F}dt, t + dt)d\boldsymbol{x}d\boldsymbol{\xi} - f(\boldsymbol{x}, \boldsymbol{\xi}, t)d\boldsymbol{x}d\boldsymbol{\xi} = 0, \tag{B.18}$$

Nevertheless, if collisions take place between molecules there will be a difference between the number of particles in the interval $d\boldsymbol{x}d\boldsymbol{\xi}$. The rate of change between final and initial state of the distribution function is called the collision operator $\boldsymbol{\Omega}$. So the equation describing the evolution of the number of molecules in such a system will be:

$$f(\boldsymbol{x} + \boldsymbol{\xi}dt, \boldsymbol{\xi} + \mathbf{F}dt, t + dt)d\boldsymbol{x}d\boldsymbol{\xi} - f(\boldsymbol{x}, \boldsymbol{\xi}, t)d\boldsymbol{x}d\boldsymbol{\xi} = \boldsymbol{\Omega}(\boldsymbol{f})d\boldsymbol{x}d\boldsymbol{\xi}dt \tag{B.19}$$

Dividing the previous equation by $d\boldsymbol{x}d\boldsymbol{\xi}dt$ and taking the limit for $dt \to 0$, the difference becomes derivative:

$$\frac{df}{dt} = \Omega(f), \tag{B.20}$$

The previous equation articulate that the total rate of change of the distribution function (number of particles) f is equal to the rate of collision Ω. Since f is function

of $\boldsymbol{x}$, $\boldsymbol{\xi}$ and t, the total derivative can be expanded as:

$$df = \frac{\partial f}{\partial \boldsymbol{x}} d\boldsymbol{x} + \frac{\partial f}{\partial \boldsymbol{\xi}} d\boldsymbol{\xi} + \frac{\partial f}{\partial t} dt, \tag{B.21}$$

Dividing by dt yields to:

$$\frac{df}{dt} = \frac{\partial f}{\partial \boldsymbol{x}} \frac{d\boldsymbol{x}}{dt} + \frac{\partial f}{\partial \boldsymbol{\xi}} \frac{d\boldsymbol{\xi}}{dt} + \frac{\partial f}{\partial t}. \tag{B.22}$$

The bold symbol $\boldsymbol{x}$ signifies the position vector which can be written in 3-D Cartesian coordinate system as $\boldsymbol{x} = x_1\hat{i} + x_2\hat{j} + x_3\hat{k}$, where $\hat{i}$, $\hat{j}$, and $\hat{k}$ are the unit vectors along x, y and z-directions, respectively. In the above equation, the term $\frac{d\boldsymbol{x}}{dt} = \boldsymbol{\xi}$ and $\frac{d\boldsymbol{\xi}}{dt}$ will be assigned to a, and it represents the acceleration that the particle will experience by applying the force $\mathbf{F}$, the acceleration a and the force $\mathbf{F}$ can be linked through *Newton's second law* $\mathbf{F} = ma$. Consequently, the Boltzmann transport equation can be expressed as:

$$\frac{\partial f}{\partial t} + \frac{\partial f}{\partial \boldsymbol{x}} \cdot \boldsymbol{\xi} + \frac{\mathbf{F}}{m} \cdot \frac{\partial f}{\partial \boldsymbol{\xi}} = \Omega(f), \tag{B.23}$$

B.4 Distribution function expansion: Hermite polynomials

In order to discretize and expand the Boltzmann equation, we have first to project our distribution function f on a convenient space to form the basis on which we will continue our analysis. In this context, among the infinite number of different functions and polynomials, one specific set of polynomials used for the discretization of integrals are the *Hermite polynomials* (HPs) which form a well-known class of orthogonal polynomials. They naturally appear in the quantum-mechanical as eigenfunctions of the harmonic oscillator as well as they play an essential role in Gauss-Hermite quadrature in the context of numerical analysis. It was found also that Hermite series basis has the advantage of being mathematically suitable to be a basis for the LB equation besides its ability to recover equations beyond the Navier-Stokes equations. More details about the mathematics behind the Hermite basis can be found in [85].

For any dimension d, the HPs form a complete basis in $\mathbb{R}$, in other words, any sufficiently well-behaved continuous function $f(x) \in \mathbb{R}$ can be represented as a series

of HPs:

$$f(\boldsymbol{x}) = \omega(\boldsymbol{x}) \sum_{n=0}^{\infty} \frac{1}{n!} \boldsymbol{a}^{(n)} : \boldsymbol{\mathcal{H}}^{(n)}(x), \qquad \boldsymbol{a}^{(n)} = \int f(\boldsymbol{x}) \boldsymbol{\mathcal{H}}^{(n)}(\boldsymbol{x}) d^d x \tag{B.24}$$

where $\omega(x)$ is named the *weight function* or *generation function*, and written as:

$$\omega(\boldsymbol{x}) = \frac{1}{(2\pi)^{d/2}} e^{-\frac{|\boldsymbol{x}|^2}{2}}, \tag{B.25}$$

Using the weight function we can construct the HPs of n-th order as:

$$\boldsymbol{\mathcal{H}}^{(n)}(\boldsymbol{x}) = (-1)^n \frac{1}{\omega(\boldsymbol{x})} \nabla^{(n)} \omega(\boldsymbol{x}), \qquad \text{where} \quad n \geq 0 \quad \text{is integer} \tag{B.26}$$

Note that $\boldsymbol{\mathcal{H}}^{(n)}$ and the expansion coefficient $\boldsymbol{a}^{(n)}$ are tensors form rank n, and the dot product $\boldsymbol{a}^{(n)} : \boldsymbol{\mathcal{H}}^{(n)}(x)$ is a full contraction $a^{(n)}_{\alpha_1 \ldots \alpha_n} \mathcal{H}^{(n)}_{\alpha_1 \ldots \alpha_n}$, practically speaking, the full contraction is the summation over all the possible indices.

Applying the Hermite series expansion B.24 to the equilibrium distribution function f^{eq} in $\boldsymbol{\xi}$-space:

$$\begin{aligned} f^{eq}(\boldsymbol{x}, \boldsymbol{\xi}, t) &= \omega(\boldsymbol{\xi}) \sum_{n=0}^{\infty} \frac{1}{n!} \boldsymbol{a}^{(n),eq}(\boldsymbol{x}, t) : \boldsymbol{\mathcal{H}}^{(n)}(\boldsymbol{\xi}), \\ \boldsymbol{a}^{(n),eq} &= \int f^{eq}(\boldsymbol{x}, \boldsymbol{\xi}, t) \boldsymbol{\mathcal{H}}^{(n)}(\boldsymbol{\xi}) d^d \xi, \end{aligned} \tag{B.27}$$

We introduce θ as the non-dimensional temperature defined as:

$$\theta = \frac{rT}{r_0 T_0} = \frac{rT}{c_s^2}, \tag{B.28}$$

where r_0 and T_0 are the reference temperature and reference gas constant associated with a reference velocity (speed of sound) $c_s = \sqrt{r_0 T_0}$. Note that this Hermite expansion covers both isothermal and thermal description, θ will be unity for isothermal

assumption. The Hermite polynomials up to the third order gives:

$$\mathcal{H}^{(0)} = 1, \tag{B.29}$$

$$\mathcal{H}^{(1)}_{\alpha} = \xi_{\alpha}, \tag{B.30}$$

$$\mathcal{H}^{(2)}_{\alpha\beta} = \xi_{\alpha}\xi_{\beta} - c_s^2\delta_{\alpha\beta}, \tag{B.31}$$

$$\mathcal{H}^{(3)}_{\alpha\beta\gamma} = \xi_{\alpha}\xi_{\beta}\xi_{\gamma} - c_s^2\left[\xi_{\alpha}\delta_{\beta\gamma} + \xi_{\beta}\delta_{\gamma\alpha} + \xi_{\gamma}\delta_{\alpha\beta}\right]. \tag{B.32}$$

It is easily noticed that the equilibrium distribution function f^{eq} has the same form as the weight function $\omega(\xi)$ so we can have:

$$f^{\mathrm{eq}}(\rho, \boldsymbol{u}, \theta, \xi) = \frac{\rho}{(2\pi\theta)^{d/2}}\mathrm{e}^{-(\boldsymbol{\xi}-\boldsymbol{u})^2/(2\theta)} = \frac{\rho}{\theta^{d/2}}\omega\left(\frac{\boldsymbol{\xi}-\boldsymbol{u}}{\sqrt{\theta}}\right) \tag{B.33}$$

Thus, the associated coefficients $a^{(n),eq}$ can be proven to be:

$$a^{(0),\mathrm{eq}} = \rho, \tag{B.34}$$

$$a^{(1),\mathrm{eq}}_{\alpha} = \rho u_{\alpha} \tag{B.35}$$

$$a^{(2),\mathrm{eq}}_{\alpha\beta} = \rho\left(u_{\alpha}u_{\beta} + (\theta-1)\delta_{\alpha\beta}\right), \tag{B.36}$$

$$a^{(3),\mathrm{eq}}_{\alpha\beta\gamma} = \rho\left[u_{\alpha}u_{\beta}u_{\gamma} + (\theta-1)\left(\delta_{\alpha\beta}u_{\gamma} + \delta_{\beta\gamma}u_{\alpha} + \delta_{\gamma\alpha}u_{\beta}\right)\right]. \tag{B.37}$$

The coefficients $a^{(n),eq}$ can express isothermal formulation simply by setting θ to 1. In addition, a deeper look into Eqn. B.34 discloses that the coefficients in the Hermite series expansion of the equilibrium distribution function f^{eq} are tied directly to the conserved moments; the first three coefficients are connected to the density, momentum and energy. This is one of the reason why the Hermite series expansion are ideal to deal with the Boltzmann equation; the series coefficient are directly connected to the conserved moments or even match them. The first three coefficients are sufficient to to fulfill the conservation laws and represent the macroscopic equation. To put it simply, To reproduce the the required physics, satisfy the conservation equations in the macroscopic level, we do not need the full expansion of mesoscopic equilibrium or particle distribution functions. Rather, the first three terms of the Hermite series expansion (n = 0, 1, 2) are sufficient to recover the macroscopic laws of hydrodynamics, which reduces the numerical cost significantly.

In the light of previous insights, the Hermite expansion can be limited to the N-th

order, hence, the equilibrium and the particle distribution functions can be expressed as:

$$\begin{aligned} f^{eq}(\boldsymbol{x},\boldsymbol{\xi},t) &\approx \omega(\boldsymbol{\xi})\sum_{n=0}^{N}\frac{1}{n!}\boldsymbol{a}^{(n),eq}(\boldsymbol{x},t):\boldsymbol{\mathcal{H}}^{(n)}(\boldsymbol{\xi}),\\ f(\boldsymbol{x},\boldsymbol{\xi},t) &\approx \omega(\boldsymbol{\xi})\sum_{n=0}^{N}\frac{1}{n!}\boldsymbol{a}^{(n)}(\boldsymbol{x},t):\boldsymbol{\mathcal{H}}^{(n)}(\boldsymbol{\xi}). \end{aligned} \tag{B.38}$$

As we mentioned earlier, we need only the first three terms of the Hermite expansion to recover the physical behaviour. Thus, we can write down equilibrium distribution function truncated after the third moment, i.e. up to the second order in ξ (N = 0):

$$\begin{aligned} f^{eq}(\boldsymbol{x},\boldsymbol{\xi},t) &\approx \omega(\boldsymbol{\xi})\rho\left[1+\xi_\alpha u_\alpha+(u_\alpha u_\beta+(\theta-1)\delta_{\alpha\beta})(\xi_\alpha\xi_\beta-\delta_{\alpha\beta})\right]\\ &= \omega(\boldsymbol{\xi})\rho Q(\boldsymbol{\xi}) \end{aligned} \tag{B.39}$$

where Q is a multi-dimensional polynomial in $\boldsymbol{\xi}$.

B.5 External force Hermite projection

Here, we will revisit briefly without a lot of details this derivation and how we can encompass the external forces into the LB equation. As before, the derivation contains two main steps: first comes the discretization over the velocity space, then comes the spatial and temporal discretization. The following demonstrations is based on [156,208], we recall the continuous Boltzmann equation with forcing term:

$$\frac{\partial f}{\partial t}+\frac{\partial f}{\partial \boldsymbol{x}}\cdot\boldsymbol{\xi}+\frac{\boldsymbol{F}}{\rho}\cdot\frac{\partial f}{\partial \boldsymbol{\xi}}=\Omega(f), \tag{B.40}$$

we recall as well the Hermite polynomials and the expansion of f:

$$f(\boldsymbol{x},\boldsymbol{\xi},t)\approx\omega(\boldsymbol{\xi})\sum_{n=0}^{N}\frac{1}{n!}\boldsymbol{a}^{(n)}(\boldsymbol{x},t):\boldsymbol{\mathcal{H}}^{(n)}(\boldsymbol{\xi}). \tag{B.41}$$

and the derivative property of Hermite polynomials reads:

$$\boldsymbol{\mathcal{H}}^{(n)}(\boldsymbol{\xi}) = \frac{(-1)^n}{\omega(\boldsymbol{\xi})}\nabla_{\boldsymbol{\xi}}^{(n)}\omega(\boldsymbol{\xi}) \tag{B.42}$$

thus, we can write the Hermite expansion of $f(\boldsymbol{\xi}_i)$ as follows:

$$f(\boldsymbol{x}, \boldsymbol{\xi}, t) \approx \sum_{n=0}^{N} \frac{(-1)^n}{n!}\boldsymbol{a}^{(n)} : \nabla_{\boldsymbol{\xi}}^{n}\omega, \tag{B.43}$$

which permits us to simplify and project the forcing term onto the Hermite basis:

$$\begin{aligned} \frac{\boldsymbol{F}}{\rho} \cdot \nabla_{\boldsymbol{\xi}} f &\approx \frac{\boldsymbol{F}}{\rho} \cdot \sum_{n=0}^{N} \frac{(-1)^n}{n!}\boldsymbol{a}^{(n)} \cdot \nabla_{\boldsymbol{\xi}}^{n+1}\omega \\ &\approx -\frac{\boldsymbol{F}}{\rho} \cdot \omega \sum_{n=1}^{N} \frac{1}{n!} n\boldsymbol{a}^{(n-1)} \cdot \boldsymbol{\mathcal{H}}^{(n)} \end{aligned} \tag{B.44}$$

As done in Appendix B.4, we need the Hermite expansion up to the second order to recover the physical behaviour which produces the following projected forcing term:

$$\mathcal{F} = -\frac{\boldsymbol{F}}{\rho} \cdot \frac{\partial f}{\partial \boldsymbol{\xi}} = w(\boldsymbol{\xi}) \left(\xi_\alpha + \left(\xi_\alpha\xi_\beta - \delta_{\alpha\beta}\right) u_\beta\right) F_\alpha, \tag{B.45}$$

where F_α is the applied force field.

B.6 Velocity Sets

The choice of a velocity set $\{\boldsymbol{c}_i\}$ is delicate and requires satisfying some criteria. From one angle, the velocity set must be adequately well-resolved to allow for consistent solution (i.e. minimizing discretization error) for the Navier-Stokes equation, form another angle is to the numerical cost that increases with the number of the velocities. Therefore, it is of great importance to find the a velocity set that has the minimum number of velocities, yet achieving the right physics. For more details about the history and the evolution of of velocity set, one can refer to Chapter 3 and 5 in [257].

Velocity sets are named by its number d of spatial dimensions and the number q of discrete velocity using the notation DdQq. For example D2Q9 is the velocity set in 2D with 9 discrete velocities, while D3Q19 is the velocity set in 3D with 19 discrete velocities. A velocity set is defined by 2 main sets of parameters: the velocities $\{\boldsymbol{c}_i\}$

and the corresponding Gaussian weights $\{w_i\}$, moreover, for each velocity set we should know and define the speed of sound c_s.

Requirements of velocity set

There exist numerous ways to construct a velocity set, one of them is to find general conditions that must be fulfilled by our velocity set. The mass and momentum conservation should be satisfied (as we did previously), but more importantly, which we did not address earlier, is the rotational isotropy of the lattice [76]. This depends on the definition of "sufficiently isotropic lattice". As a rule of thumb, LB is used to solve NSE for which one requires all moments of the weight $w_i$up to the fifth order to be isotropic. Having said that, the following conditions can be written down:

$$\sum_i w_i = 1 \tag{B.46}$$

$$\sum_i w_i c_{i\alpha} = 0 \tag{B.47}$$

$$\sum_i w_i c_{i\alpha} c_{i\beta} = c_s^2 \delta_{\alpha\beta} \tag{B.48}$$

$$\sum_i w_i c_{i\alpha} c_{i\beta} c_{i\gamma} = 0 \tag{B.49}$$

$$\sum_i w_i c_{i\alpha} c_{i\beta} c_{i\gamma} c_{i\mu} = c_s^4 \left(\delta_{\alpha\beta}\delta_{\gamma\mu} + \delta_{\alpha\gamma}\delta_{\beta\mu} + \delta_{\alpha\mu}\delta_{\beta\gamma}\right) \tag{B.50}$$

$$\sum_i w_i c_{i\alpha} c_{i\beta} c_{i\gamma} c_{i\mu} c_{i\nu} = 0 \tag{B.51}$$

In addition, all the weights w_i have to be non-negative (as this will give values for f^{eq} which is negative, which is impossible, recall that the equilibrium distribution is a probability that takes values from Zero to unity). So all in all, any velocity set which is not capable of satisfying the those conditions is not suitable to recover Navier-Stokes from Lattice-Boltzmann.

Most common lattice for 1D and 2D lattices for hydrodynamic simulations are D1Q3 and D2Q9 (see Fig. B.3), respectively. For 3D simulations there are many options that can be found in the literature, the most popular three are the D3Q15, D3Q19 shown in Fig.B.3 and less commonly used D3Q27. The weights $\{w_i\}$ and velocities $\{\boldsymbol{c}_i\}$ are given in Table

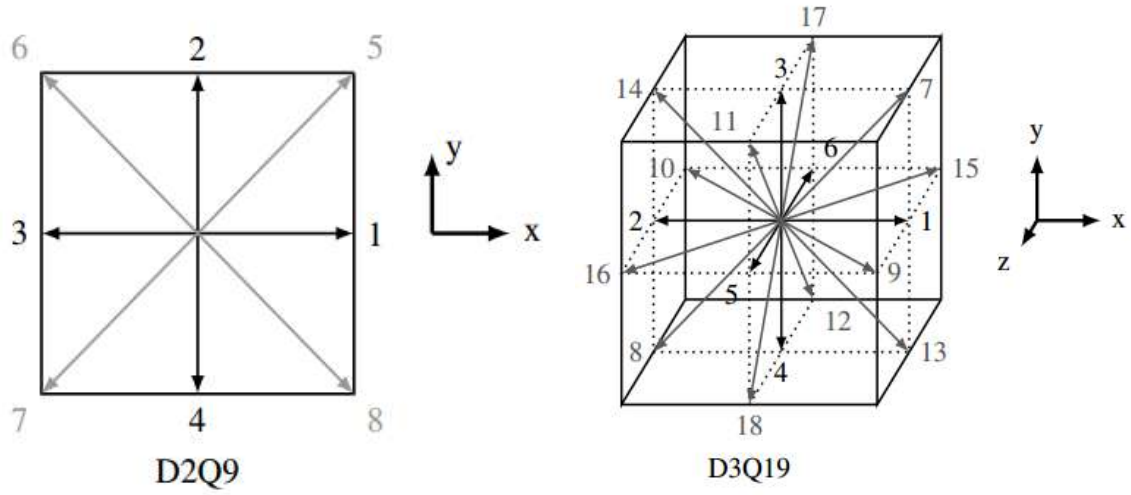

Figure B.3: Representation of velocity sets, D2Q9 on the left and D3Q19 on the right. Figure from [127].

Velocity set	Velocities	No.	Length $\|\boldsymbol{c}_i\|$	Weight w_i
D1Q3	(0)	1	0	2/3
	($\pm$1)	2	1	1/6
D2Q9	(0, 0)	1	0	4/9
	($\pm$1, 0), (0, $\pm$1)	4	1	1/9
	($\pm$1, $\pm$1)	4	$\sqrt{2}$	1/36
D3Q19	(0, 0, 0)	1	0	1/3
	($\pm$1, 0, 0), (0, $\pm$1, 0), (0, 0, $\pm$1)	6	1	1/18
	($\pm$1, $\pm$1, 0), ($\pm$1, 0,$\pm$1), (0, $\pm$1, $\pm$1)	12	$\sqrt{2}$	1/36

Table B.1: Properties of the most popular velocity sets for NS simulations

. The speed of sound of all those velocity sets is $c_s = 1/\sqrt{3}$.

B.7 Chapman-Enskog Expansion

Until now we are mathematically manipulating the transport equation of the velocity distribution function f_i in order to use it as Navier-Stokes solver. Yet, we did not prove that this equation actually is a representation of the NS equations. In that light, the Chapman-Enskog is proposed to clarify this ambiguity and to show how the Boltzmann

equation can reproduce NS equations. There are many ways to introduce the Chapman-Enskog expansion, the one introduced here is the one articulated by [42] where they did the expansion in the Hermite polynomial space. We recall the Hermite tensor that can be written as:

$$\mathcal{H}^{(n)}_{\alpha_1\cdots\alpha_n}(\boldsymbol{\xi}) \equiv \frac{(-rT_0)^n}{\omega(\boldsymbol{\xi})}\left(\partial_{\alpha_1}\cdots\partial_{\alpha_n}\omega(\boldsymbol{\xi})\right), \tag{B.52}$$

and the weighting function $\omega(\boldsymbol{\xi})$ is written as:

$$\omega(\boldsymbol{\xi}) \equiv \frac{1}{(2\pi rT_0)^{D/2}}\exp\left(-\frac{\xi^2}{2rT_0}\right) \tag{B.53}$$

where $\xi^2 \equiv \boldsymbol{\xi}\cdot\boldsymbol{\xi}$, c_s the reference lattice speed of sound:

$$c_s \equiv \sqrt{rT_0}. \tag{B.54}$$

The VDF $f(\boldsymbol{x},\boldsymbol{\xi},t)$ can be projected onto the Hermite polynomial basis:

$$f(\boldsymbol{x},\boldsymbol{\xi},t) = \omega(\boldsymbol{\xi})\sum_{n=0}^{\infty}\frac{1}{(n)!c_s^{2n}}\boldsymbol{a}^{(n)}(\boldsymbol{x},t) : \mathcal{H}^{(n)}(\boldsymbol{\xi}) \tag{B.55}$$

with $\boldsymbol{a}^{(n)}(\boldsymbol{x},t)$ as the Hermite coefficient tensor.

$$a^{(n)}_{\alpha_1\cdots\alpha_n}(\boldsymbol{x},t) \equiv \int f(\boldsymbol{x},\boldsymbol{\xi},t)\mathcal{H}^{(n)}_{\alpha_1\cdots\alpha_n}(\boldsymbol{\xi})d\boldsymbol{\xi}. \tag{B.56}$$

Applying the same procedure on the equilibrium distribution function, one can obtain the equilibrium coefficient tensors. Moreover, projecting the transport equation of f (Eqn. 3.3) with BGK collision model (Eqn. 3.14) to the Hermite space gives:

$$\frac{\partial}{\partial t}a^{(n)}_{\alpha_1\cdots\alpha_n} + \frac{\partial}{\partial x_j}\left(\xi_j a^{(n)}_{\alpha_1\cdots\alpha_n}\right) + \frac{F_\alpha}{\rho}\frac{\partial}{\partial\xi_j}\left(a_{\alpha_1\cdots\alpha_n}\right) = -\frac{1}{\tau}\left(a^{(n)}_{\alpha_1\cdots\alpha_n} - a^{(n),\mathrm{eq}}_{\alpha_1\cdots\alpha_n}\right) \tag{B.57}$$

For simplicity we will remove the force term. Note that this equation is not discretized at all, it is still a continuous equation that was just projected onto the Hermite basis. Note that the index j iterates from 1 to D the spatial dimension. The *Rodrigues*

Recursive relation of the Hermite tensor states:

$$\xi_j \mathcal{H}^{(n)}_{\alpha_1 \cdots \alpha_n}(\boldsymbol{\xi}) = \mathcal{H}^{(n+1)}_{j\alpha_1 \cdots \alpha_n}(\boldsymbol{\xi}) + c_s^2 \sum_{i=1}^{n} \delta_{j\alpha_i} \mathcal{H}^{(n-1)}_{\alpha_1 \cdots \alpha_{i-1}\alpha_{i+1} \cdots \alpha_n}(\boldsymbol{\xi}) \tag{B.58}$$

This relation will be applied to Eqn.B.57 so that it becomes:

$$\partial_t a^{(n)}_{\alpha_1 \cdots \alpha_n} + \partial_j \left(a^{(n+1)}_{j\alpha_1 \cdots \alpha_n} \right) + c_s^2 \sum_{i=1}^{n} \left(\partial_{\alpha_i} a^{(n-1)}_{\alpha_1 \cdots \alpha_{i-1}\alpha_{i+1} \cdots \alpha_n} \right) = -\frac{1}{\tau} \left(a^{(n)}_{\alpha_1 \cdots \alpha_n} - a^{(n),\mathrm{eq}}_{\alpha_1 \cdots \alpha_n} \right). \tag{B.59}$$

The CE analysis will be performed on that equation. In perturbation analysis, the perturbation terms at the two lowest orders together often result in a sufficiently accurate description of the system. Hence, we can assume that only the two lowest order of *Knudsen number* are sufficient to recover the Navier-Stokes equations, the Knudsen number ϵ is expressed as:

$$\epsilon = \frac{l_{mfp}}{l} = \alpha \frac{Re}{Ma}, \tag{B.60}$$

where l_{mfp} is the mean free path and l is the physical length scale. The spatial and temporal projections can be expanded into terms spanning several orders in Knudsen number ϵ:

$$\partial_t = \epsilon \partial_{t_1} + \epsilon^2 \partial_{t_2}; \quad \partial_j = \epsilon \partial_{j_1}, \tag{B.61}$$

we assume that f and $\boldsymbol{a}^{(n)}$ are at equilibrium:

$$\begin{aligned} f^{(n)} &= f^{(n),\mathrm{eq}}, \\ \boldsymbol{a}^{(n)} &= \boldsymbol{a}^{(n),\mathrm{eq}}, \end{aligned} \tag{B.62}$$

Thus, the right hand side of Eqn.B.59 (the collision operator) vanishes and we will end up with:

$$\partial_t a^{(n),\mathrm{eq}}_{\alpha_1 \cdots \alpha_n} + \partial_j \left(a^{(n+1),\mathrm{eq}}_{j\alpha_1 \cdots \alpha_n} \right) + c_s^2 \sum_{i=1}^{n} \left(\partial_{\alpha_i} a^{(n-1),\mathrm{eq}}_{\alpha_1 \cdots \alpha_{i-1}\alpha_{i+1} \cdots \alpha_n} \right) = 0, \tag{B.63}$$

Using Eqn.B.61 to expand the previous equation and separating scales, one attain:

$$\begin{aligned}
&\epsilon\partial_{t_1} a^{(n),\mathrm{eq}}_{\alpha_1\cdots\alpha_n} + \epsilon\partial_{j_1}\left(a^{(n+1),\mathrm{eq}}_{j\alpha_1\cdots\alpha_n}\right) + c_s^2\sum_{i=1}^{n}\left(\epsilon\partial_{\alpha_{i_1}} a^{(n-1),\mathrm{eq}}_{\alpha_1\cdots\alpha_{i-1}\alpha_{i+1}\cdots\alpha_n}\right) = 0 \quad \sim \mathcal{O}\left(\epsilon^1\right)\\
&\epsilon^2\partial_{t_2} a^{(n),\mathrm{eq}}_{\alpha_1\cdots\alpha_n} = 0 \qquad\qquad \sim \mathcal{O}\left(\epsilon^2\right)
\end{aligned} \tag{B.64}$$

Adding all contribution over $n = 0, 1$ we will recover the macroscopic equation of mass and momentum:

$$\begin{aligned}
\frac{\partial\rho}{\partial t} + \frac{\partial\rho u_\alpha}{\partial x_\alpha} &= 0,\\
\frac{\partial\rho u_\alpha}{\partial t} + \frac{\partial\rho u_\alpha u_\beta}{\partial x_\beta} &= -\frac{\partial p}{\partial x_\alpha},
\end{aligned} \tag{B.65}$$

the energy equation (not shown here) can be recovered for $n = 2$. The thermodynamic pressure $p = \rho r T$ is linked to density and temperature via ideal gas law. The assumption that we made earlier where we had f and $\boldsymbol{a}^{(n)}$ at equilibrium, resulted in Euler's set of equations lacking the viscosity term and the stress tensor. Thus, it is indispensable to introduce the non-equilibrium part in order to go beyond the Euler equations and evoke the viscous terms. Consequently, the contribution of order $\mathcal{O}$ is taken into account in the definition of f and $\boldsymbol{a}^{(n)}$:

$$\begin{aligned}
f^{(n)} &= f^{(n),\mathrm{eq}} + \epsilon f^{(n),1}, \ \text{where } f^{(n),\mathrm{eq}} \gg f^{(n),1} \sim \mathcal{O}(\epsilon) \ll 1,\\
\boldsymbol{a}^{(n)} &= \boldsymbol{a}^{(n),\mathrm{eq}} + \epsilon \boldsymbol{a}^{(n),1}, \ \text{where } \boldsymbol{a}^{(n),\mathrm{eq}} \gg \boldsymbol{a}^{(n),1} \sim \mathcal{O}(\epsilon) \ll 1,
\end{aligned} \tag{B.66}$$

So we do the same procedure where we insert Eqns. B.61 and B.66 into the original equation B.59 and separating scales we end up with:

$$\begin{aligned}
&\epsilon\partial_{t_1} a^{(n),\mathrm{eq}}_{\alpha_1\cdots\alpha_n} + \epsilon\partial_{j_1}\left(a^{(n+1),\mathrm{eq}}_{j\alpha_1\cdots\alpha_n}\right) + c_s^2\sum_{i=1}^{n}\left(\epsilon\partial_{\alpha_{i_1}} a^{(n-1),\mathrm{eq}}_{\alpha_1\cdots\alpha_{i-1}\alpha_{i+1}\cdots\alpha_n}\right) = -\frac{1}{\tau} a^{(n),1}_{\alpha_1\cdots\alpha_n}\\
&\epsilon^2\partial_{t_2} a^{(n),\mathrm{eq}}_{\alpha_1\cdots\alpha_n} + \epsilon\partial_{t_1} a^{(n),1}_{\alpha_1\cdots\alpha_n} + \epsilon\partial_{j_1}\left(a^{(n+1),1}_{j\alpha_1\cdots\alpha_n}\right) + c_s^2\sum_{i=1}^{n}\left(\epsilon\partial_{\alpha_{i_1}} a^{(n-1),1}_{\alpha_1\cdots\alpha_{i-1}\alpha_{i+1}\cdots\alpha_n}\right) =\\
&\epsilon^2\partial_{t_2} a^{(n),1}_{\alpha_1\cdots\alpha_n} = 0
\end{aligned} \tag{B.67}$$

Adding up the contributions of all orders, we end up with the macroscopic equations which reads:

$$\partial_t \rho + \partial_\alpha \left(\rho u_\alpha\right) = 0, \tag{B.68}$$

$$\partial_t \left(\rho u_\alpha\right) + \partial_\beta \left(\rho u_\alpha u_\beta + p\delta_{\alpha\beta}\right) = -\partial_\beta a^{(2),1}_{\alpha\beta}, \tag{B.69}$$

$$\begin{aligned}&\partial_t \left(\rho u_\alpha u_\beta + p\delta_{\alpha\beta} - \rho c_s^2 \delta_{\alpha\beta}\right) + \partial_\gamma \left[\rho u_\gamma u_\alpha u_\beta + \left(p - \rho c_s^2\right)\left(\boldsymbol{u\delta}\right)_{\gamma\alpha\beta}\right] \\ &+ c_s^2 \left[\partial_\alpha \left(\rho u_\beta\right) + \partial_\beta \left(\rho u_\alpha\right)\right] + \partial_t a^{(2),1}_{\alpha\beta} + \partial_\gamma a^{(3),1}_{\gamma\alpha\beta} = -\frac{1}{\tau} a^{(2),1}_{\alpha\beta}.\end{aligned} \tag{B.70}$$

The first equation gives the mass conservation, the second equation is the momentum conservation equation with an unknown term $a^{(2),1}_{\alpha\beta}$. An explicit expression for this term is essential to reveal the viscous stress tensor into the momentum equation. Combining Eqns. B.68 and B.69 we can retrieve a transport equation for the $\rho u_\alpha u_\beta$:

$$\partial_t \left(\rho u_\alpha u_\beta\right) + \partial_\gamma \left(\rho u_\alpha u_\beta u_\gamma\right) + \left(\partial_\alpha p\right) u_\beta + \left(\partial_\beta p\right) u_\alpha = -u_\beta \partial_\gamma a^{(2),1}_{\alpha\gamma} - u_\alpha \partial_\gamma a^{(2),1}_{\beta\gamma} \tag{B.71}$$

inserting this equation back to Ean. B.70, we get:

$$\delta_{\alpha\beta}\left[\partial_t p + \partial_\gamma \left(u_\gamma p\right)\right] + 2pS_{\alpha\beta} \underbrace{-u_\beta \partial_\gamma a^{(2),1}_{\alpha\gamma} - u_\alpha \partial_\gamma a^{(2),1}_{\beta\gamma} + \partial_t a^{(2),1}_{\alpha\beta} + \partial_\gamma a^{(3),1}_{\gamma\alpha\beta}}_{\text{neglected}} = -\frac{1}{\tau} a^{(2),1}_{\alpha\beta}, \tag{B.72}$$

where $S_{\alpha\beta} = \frac{1}{2}(\partial_\beta u_\alpha + \partial_\alpha u_\beta)$ is the strain rate. Neglecting terms of order $\mathcal{O}$ we end up with:

$$a^{(2)}_{1,\alpha\beta} = -2p\tau S_{\alpha\beta} - \tau\delta_{\alpha\beta}\left[\partial_t p + \partial_\gamma \left(u_\gamma p\right)\right], \tag{B.73}$$

where the second term can be neglected for low-mach numbers, for this reason it is usually said that LBM is only valid for weakly compressible phenomena, in contrast with the strongly compressible phenomena which occur for transonic and supersonic flows where Ma reaches unity or even surpass it. Setting $\mu = \tau/p$, we can recover the viscous stress tensor without the bulk viscosity term. The bulk viscosity is important in high speed flows where compressibility effects are important, this viscosity can be added through a forcing term.

B.8 Hermite polynomials for the HRR-$\mathcal{P}$ solver

In regularized LBM, distribution functions will be constructed using an orthogonal polynomial basis. The basis of the D3Q19r lattice used in the current study consists of 19 polynomials, read [65]

$$\mathcal{H}_{i}^{(0)} \equiv 1, \quad \mathcal{H}_{i,\alpha}^{(1)} \equiv c_{i\alpha}, \quad \mathcal{H}_{i,\alpha\beta}^{(2)} \equiv c_{i\alpha}c_{i\beta} - c_s^2\delta_{\alpha\beta}, \tag{B.74}$$

$$\mathcal{H}_{i,1}^{(3r)} \equiv \mathcal{H}_{i,xxy}^{(3)} + \mathcal{H}_{i,yzz}^{(3)}, \tag{B.75}$$

$$\mathcal{H}_{i,2}^{(3r)} \equiv \mathcal{H}_{i,xzz}^{(3)} + \mathcal{H}_{i,xyy}^{(3)}, \tag{B.76}$$

$$\mathcal{H}_{i,3}^{(3r)} \equiv \mathcal{H}_{i,yyz}^{(3)} + \mathcal{H}_{i,xxz}^{(3)}, \tag{B.77}$$

$$\mathcal{H}_{i,4}^{(3r)} \equiv \mathcal{H}_{i,xxy}^{(3)} - \mathcal{H}_{i,yzz}^{(3)}, \tag{B.78}$$

$$\mathcal{H}_{i,5}^{(3r)} \equiv \mathcal{H}_{i,xzz}^{(3)} - \mathcal{H}_{i,xyy}^{(3)}, \tag{B.79}$$

$$\mathcal{H}_{i,6}^{(3r)} \equiv \mathcal{H}_{i,yyz}^{(3)} - \mathcal{H}_{i,xxz}^{(3)}, \tag{B.80}$$

$$\mathcal{H}_{i,1}^{(4r)} \equiv \frac{4}{9}\left(3+2\sqrt{3}\right)\mathcal{D}_{i,xyz}^{(4)} + \frac{4}{9}\left(3-\sqrt{3}\right)\mathcal{D}_{i,xzy}^{(4)} + \frac{4}{9}\left(3-\sqrt{3}\right)\mathcal{D}_{i,zyx}^{(4)}, \tag{B.81}$$

$$\mathcal{H}_{i,2}^{(4r)} \equiv \frac{4}{9}\left(3+2\sqrt{3}\right)\mathcal{D}_{i,xzy}^{(4)} + \frac{4}{9}\left(3-\sqrt{3}\right)\mathcal{D}_{i,xyz}^{(4)} + \frac{4}{9}\left(3-\sqrt{3}\right)\mathcal{D}_{i,zyx}^{(4)}, \tag{B.82}$$

$$\mathcal{H}_{i,3}^{(4r)} \equiv \frac{4}{9}\left(3+2\sqrt{3}\right)\mathcal{D}_{i,zyx}^{(4)} + \frac{4}{9}\left(3-\sqrt{3}\right)\mathcal{D}_{i,xzy}^{(4)} + \frac{4}{9}\left(3-\sqrt{3}\right)\mathcal{D}_{i,xyz}^{(4)}, \tag{B.83}$$

where the superscript (r) denotes regularized, furthermore we have:

$$\mathcal{H}_{i,\alpha\beta\gamma}^{(3)} \equiv c_{i\alpha}c_{i\beta}c_{i\gamma} - c_s^2[c_{i\alpha}\delta_{\beta\gamma} + c_{i\beta}\delta_{\gamma\alpha} + c_{i\gamma}\delta_{\alpha\beta}], \tag{B.84}$$

$$\mathcal{D}_{i,\alpha\beta\gamma}^{(4)} \equiv \mathcal{H}_{i,\alpha\alpha\beta\beta}^{(4)} + \frac{c_s^2}{2}\mathcal{H}_{i,\gamma\gamma}^{(2)}, \tag{B.85}$$

$$\begin{aligned}\mathcal{H}_{i,\alpha\beta\gamma\delta}^{(4)} \equiv\ & c_{i\alpha}c_{i\beta}c_{i\gamma}c_{i\delta} + c_s^4(\delta_{\alpha\beta}\delta_{\gamma\delta} + \delta_{\beta\gamma}\delta_{\delta\alpha} + \delta_{\delta\alpha}\delta_{\beta\gamma}) \\ & - c_s^2(c_{i\alpha}c_{i\beta}\delta_{\gamma\delta} + c_{i\beta}c_{i\gamma}\delta_{\delta\alpha} + c_{i\gamma}c_{i\delta}\delta_{\alpha\beta} + c_{i\delta}c_{i\alpha}\delta_{\beta\gamma} + c_{i\gamma}c_{i\alpha}\delta_{\beta\delta} + c_{i\beta}c_{i\delta}\delta_{\alpha\gamma}).\end{aligned} \tag{B.86}$$

The Hermite coefficients will read:

$$a^{(0),\mathrm{eq}} = \rho\theta \ , \quad a^{(1),\mathrm{eq}}_{\alpha} = \rho u_{\alpha} \ , \quad a^{(2),\mathrm{eq}}_{\alpha\beta} = \rho u_{\alpha} u_{\beta} \tag{B.87}$$

$$a^{(3r),\mathrm{eq}}_{1} = 3(\rho u_x u_x u_y + \rho u_y u_z u_z) \ , \tag{B.88}$$

$$a^{(3r),\mathrm{eq}}_{2} = 3(\rho u_x u_z u_z + \rho u_x u_y u_y) \ , \tag{B.89}$$

$$a^{(3r),\mathrm{eq}}_{3} = 3(\rho u_y u_y u_z + \rho u_x u_x u_z) \ , \tag{B.90}$$

$$a^{(3r),\mathrm{eq}}_{4} = \rho u_x u_x u_y - \rho u_y u_z u_z \ , \tag{B.91}$$

$$a^{(3r),\mathrm{eq}}_{5} = \rho u_x u_z u_z - \rho u_x u_y u_y \ , \tag{B.92}$$

$$a^{(3r),\mathrm{eq}}_{6} = \rho u_y u_y u_z - \rho u_x u_x u_z \ , \tag{B.93}$$

$$a^{(4r),\mathrm{eq}}_{1} = -\rho c_s^2 \left[\frac{-4\sqrt{3}-6}{9} u_z^2 + \frac{2\sqrt{3}-6}{9} \left(u_x^2 + u_y^2 \right) \right] \ , \tag{B.94}$$

$$a^{(4r),\mathrm{eq}}_{2} = -\rho c_s^2 \left[\frac{-4\sqrt{3}-6}{9} u_y^2 + \frac{2\sqrt{3}-6}{9} \left(u_x^2 + u_z^2 \right) \right] \ , \tag{B.95}$$

$$a^{(4r),\mathrm{eq}}_{3} = -\rho c_s^2 \left[\frac{-4\sqrt{3}-6}{9} u_x^2 + \frac{2\sqrt{3}-6}{9} \left(u_y^2 + u_z^2 \right) \right] \ . \tag{B.96}$$

where θ is the the non-dimensional temperature related to the mass fractions as:

$$\theta = \frac{\overline{r}T}{c_s^2} = \frac{\mathcal{R}T}{c_s^2} \sum_k \frac{Y_k}{W_k}, \tag{B.97}$$

it is note worthy that the fourth order coefficients $[a^{(4),\mathrm{eq}}]$ are included in order to enhance the isotropicity of the lattice.

B.9 Forcing Terms

Depending on the order of the Gauss-Hermite quadrature [127] used in the LB model, an adequate forcing term should be added to achieve a correct viscous stress tensor:

$$a^{\mathrm{neq}}_{\alpha\beta} \approx -\Pi_{\alpha\beta} = -\mu\left(\frac{\partial u_{\alpha}}{\partial x_{\beta}} + \frac{\partial u_{\beta}}{\partial x_{\alpha}} - \frac{2}{D}\frac{\partial u_{\gamma}}{\partial x_{\gamma}}\delta_{\alpha\beta}\right), \tag{B.98}$$

with D the spatial dimension. For the D3Q19r basis, the projected forcing term reads as:

$$a_{\alpha\beta}^{F^E} = c_s^2 u_\alpha \left[\frac{\partial(\rho(1-\theta))}{\partial x_\beta}\right] + c_s^2 u_\beta \left[\frac{\partial(\rho(1-\theta))}{\partial x_\alpha}\right] + \delta_{\alpha\beta}\rho c_s^2 \frac{2}{D}\frac{\partial u_\gamma}{\partial x_\gamma} - a_{\alpha\beta}^{\text{cor}} + a_{\alpha\beta}^{F_D} \tag{B.99}$$

where $a_{\alpha\beta}^{\text{cor}}$ is a correction tensor due to the deflection of second order moments of the population introduced by the modification of the mass equation, which can be evaluated as:

$$a_{\alpha\beta}^{\text{cor}} \equiv c_s^2 \delta_{\alpha\beta} \frac{\partial(\rho(1-\theta))}{\partial t} \approx c_s^2 \delta_{\alpha\beta} \left(\frac{\rho(\boldsymbol{x}, t+\delta_t)[1-\theta(\boldsymbol{x}, t+\delta_t)] - \rho(\boldsymbol{x}, t)[1-\theta(\boldsymbol{x}, t)]}{\delta_t} \right), \tag{B.100}$$

which can be discretized using a backward Euler operator and $a_{\alpha\beta}^{F_D}$ the correction tensor due to the defect of the lattice at third order:

$$a_{\alpha\beta}^{F_D} = -\begin{pmatrix} (\rho u_x^3)_{,x} & (\rho u_x u_y u_z)_{,z} & (\rho u_x u_y u_z)_{,y} \\ (\rho u_x u_y u_z)_{,z} & (\rho u_y^3)_{,y} & (\rho u_x u_y u_z)_{,x} \\ (\rho u_x u_y u_z)_{,y} & (\rho u_x u_y u_z)_{,x} & (\rho u_z^3)_{,z} \end{pmatrix} \tag{B.101}$$

where all the differential operations are performed using first order upwind FD except for the divergence operator for which a second order centered FD scheme was employed. The final expression of the forcing term is then

$$F_i^E = \frac{\omega_i}{2c_s^4} \mathcal{H}_{i,\alpha\beta}^{(2)} a_{\alpha\beta}^{F^E} + F_i^g, \tag{B.102}$$

where F_i^g is the gravity force term defined as:

$$F_i^g = \omega_i \left[\frac{\rho g_\alpha \mathcal{H}_{i,\alpha}^{(1)}}{c_s^2} + \frac{(\rho u_\alpha g_\beta + \rho u_\beta g_\alpha)\mathcal{H}_{i,\alpha\beta}^{(2)}}{2c_s^4} \right], \tag{B.103}$$

where g_α is the gravity acceleration in the direction α.

B.10 Recursive construction of third order off-equilibrium tensor

The third-order off-equilibrium terms are reconstructed recursively from the second-order non-equilibrium tensor as:

$$
\begin{aligned}
a^{(3),\mathrm{neq}}_{\alpha\beta\gamma} &= u_\alpha a^{(2),\mathrm{neq}}_{\beta\gamma} + u_\beta a^{(2),\mathrm{neq}}_{\alpha\gamma} + u_\gamma a^{(2),\mathrm{neq}}_{\alpha\beta} \\
a^{(3r),\mathrm{neq}}_{1} &\equiv a^{(3),\mathrm{neq}}_{xxy} + a^{(3),\mathrm{neq}}_{yzz} \\
a^{(3r),\mathrm{neq}}_{2} &\equiv a^{(3),\mathrm{neq}}_{xzz} + a^{(3),\mathrm{neq}}_{xyy} \\
a^{(3r),\mathrm{neq}}_{3} &\equiv a^{(3),\mathrm{neq}}_{yyz} + a^{(3),\mathrm{neq}}_{xxz} \\
a^{(3r),\mathrm{neq}}_{4} &\equiv a^{(3),\mathrm{neq}}_{xxy} - a^{(3),\mathrm{neq}}_{yzz} \\
a^{(3r),\mathrm{neq}}_{5} &\equiv a^{(3),\mathrm{neq}}_{xzz} - a^{(3),\mathrm{neq}}_{xyy} \\
a^{(3r),\mathrm{neq}}_{6} &\equiv a^{(3),\mathrm{neq}}_{yyz} - a^{(3),\mathrm{neq}}_{xxz}
\end{aligned}
\tag{B.104}
$$

Physics of Fluids

Lattice-Boltzmann modeling of buoyancy-driven turbulent flows

Cite as: Phys. Fluids **34**, 055131 (2022); https://doi.org/10.1063/5.0088409
Submitted: 16 February 2022 • Accepted: 04 May 2022 • Accepted Manuscript Online: 06 May 2022 • Published Online: 27 May 2022

M. Taha, S. Zhao (赵崧), A. Lamorlette, et al.

Physics of Fluids ARTICLE scitation.org/journal/phf

Lattice-Boltzmann modeling of buoyancy-driven turbulent flows

Cite as: Phys. Fluids **34**, 055131 (2022); doi: 10.1063/5.0088409
Submitted: 16 February 2022 · Accepted: 4 May 2022 ·
Published Online: 27 May 2022

M. Taha,[1] S. Zhao (赵崧),[1] A. Lamorlette,[2] J. L. Consalvi,[2] and P. Boivin[1,a)]

AFFILIATIONS

[1]Aix Marseille Univ., CNRS, Centrale Marseille, M2P2, Marseille, France
[2]Aix Marseille Univ., CNRS, IUSTI, Marseille, France

Note: This paper is part of the Special Issue on the Lattice Boltzmann Method.
[a)]**Author to whom correspondence should be addressed:** pierre.boivin@univ-amu.fr

ABSTRACT

The pressure-based hybrid lattice-Boltzmann method presented by Farag *et al.* ["A pressure-based regularized lattice-Boltzmann method for the simulation of compressible flows," Phys. Fluids **32**, 066106 (2020)] is assessed for the simulation of buoyancy driven flows. The model is first validated on Rayleigh–Benard and Rayleigh–Taylor two-dimensional cases. A large-eddy simulation of a turbulent forced plume is then carried out, and results are validated against experiments. Good overall agreement is obtained, both for mean and fluctuation quantities, as well as global entrainment. The self-similarity characteristic of the plume in the far-field is also recovered.

I. INTRODUCTION

Lattice Boltzmann Methods (LBM) are a powerful tool for the simulation of fluid dynamics.[1] Due to their attractive computational cost,[2] its capacities for massively parallel computing, and the ease to deal with complex geometries using multi-level Cartesian grids, these methods have attracted growing interest both in the academic and industrial spheres in the past decade.[3–5]

LBM being initially designed to tackle isothermal flows, extension to thermal flows is today an active topic of investigation in the community. In achieving that goal, the numerical stability of the collision operator, at the heart of the method, used to be a major issue. The single relaxation time Bhatnagar–Gross–Krook model,[6] probably the most popular model, lacks stability for shear flows, but more recent models such as multiple relaxation collision[7] or regularized kernels[8,9] significantly improved stability. Another issue is the resolution of energy or temperature equation, which cannot be straightforwardly achieved on low-order lattices.[5] Two main options are available in the literature. The first is the double distribution function (DDF) option that consists in coupling the LBM solver with a second distribution function, whose main order corresponds to either temperature, energy, or enthalpy (see, e.g., Refs. 10 and 11, for recent studies). A second option is to couple directly LBM with a scalar (temperature, energy, enthalpy), solved in a coupled finite difference solver. This second option was found attractive as it allows us, for a reasonable cost,[2] to include an arbitrary number of additional scalar equations. Following recent successful applications to compressible,[12–17] atmospheric,[14,18–21] or reactive flows,[22–24] the second option, often referred to as hybrid LBM, is retained for this study. This work aims at investigating their applicability to buoyancy driven flows, such as those encountered in fire-related problems.[25]

The far field of turbulent, axisymmetric, free-plumes in a quiescent, unstratified environment, where a buoyancy-driven plume exhibits self-similar behavior, plays a significant role in various fluid flows of environmental and technological importance, including thermal plumes that arise due to the convective heating on the Earth's surface,[26–28] fire protection engineering with problems associated with fire detection, smoke filling rates of indoor spaces, fire venting, fire heating of structural elements of buildings,[29] wildland fires,[30,31] dispersal of volcanic eruptions,[32–34] sea ice plumes,[35,36] smoke stacks,[37] and cooling tower plume dispersion.[38] Forced plumes or buoyant jets represent a canonical configuration to study such plumes. They consist of releasing the plumes from a source with some initial momentum. The flow can be decomposed into three regions: (i) a region featuring a jet-like behavior near the source, (ii) a transitional region, and (iii) further downstream, the far-field fully developed buoyancy-driven plume.[39]

The first far-field plume theories[40–42] assumed a turbulent flow, a point source of buoyancy, the Boussinesq approximation, and a dynamic similarity of the mean and turbulent motion at all elevations. Morton *et al.*[42] developed an integral formulation by assuming both

"top-hat" radial profiles for both velocity and temperature (density) and a point source, and by introducing an entrainment coefficient, α, defined as the ratio of radial velocity at the edge of the plume to the vertical velocity within the plume. Their model predicts correctly the scaling laws for the plume radius that increases linearly with height, z, as well as for both velocity and temperature rise above the ambient that decay as $z^{-1/3}$ and $z^{-5/3}$, respectively. The weak plume formulation of Morton *et al.*[42] was extended to "strong plumes" by removing both the Boussinesq approximation and the point source assumption through the introduction of a virtual origin and by considering more realistic Gaussian profiles for both velocity and temperature.[29] This in conjunction with experiments in fire plumes above the flames[43] provided expressions for plume radius and centerline velocity and temperature consistent with experimental data.[44–46] Another important feature of buoyant plumes is that the radial profiles of dimensionless mean velocity and temperature and dimensionless rms turbulent fluctuations of velocity and temperature exhibit a self-similar behavior with $\eta = r/z$ as a self-similar variable, where r is the radial coordinate.[46–48] Progress was also made in the understanding of the role of buoyancy in the entrainment process and the flow behavior. In particular, Saeed *et al.* found that buoyancy contributes to enhance not only the mean kinetic energy budget but also the momentum flux.[49]

The computational fluid dynamics (CFD) modeling of forced plumes was also a very active research area. A significant amount of Reynolds-averaged Navier–Stokes simulations were reported with different formulations of the k−ϵ model.[50–53] On the other hand, Zhou *et al.*[54] and Yan[55] showed the capability of Large Eddy Simulation (LES) to predict well the puffing, self-preserving, and spreading of the plume. LES of forced jet were also performed[56] to evaluate the energy-consistent approach for modeling entrainment rate coefficient, α, developed by Kaminski *et al.*[57] and van Reeuwijk and Craske.[58] Direct numerical simulation (DNS) and LES of thermal plumes were also reported.[59–62] These studies focused mainly on the generation and growth of buoyancy-induced instabilities in the near field that governs the transition from laminar to turbulence. In particular, it was shown that these instabilities have to be fully resolved to capture the dynamics of such purely buoyant thermal plumes.[59] In addition, the DNS was found to be in good agreement with experimental data in the far field.[60]

This literature survey reveals that all the numerical investigations were performed by using a low Mach-formulation of the Navier–Stokes equation. To the best knowledge of the authors, no attempt to consider lattice-Boltzmann method was reported.

The goal in the current work is to assess the ability of the pressure-based lattice-Boltzmann method proposed by Farag *et al.*[16] to correctly predict the behavior of a forced plume in the self-similarity region away from the source. This manuscript is organized as follows: Sec. II recalls the target macroscopic equations, as well as the lattice-Boltzmann algorithm proposed. Section III presents a number of 2D canonical flow validations, including Rayleigh–Benard and Rayleigh–Taylor instabilities. Section IV presents a large eddy simulation of the plume experimentally described by Shabbir and George,[46] along with comparisons with the large eddy simulation presented by Zhou *et al.*[54] and the theoretical model of Morton.[27,42] All the simulations were performed using the compressible ProLB code.[63]

II. LATTICE-BOLTZMANN MODEL FOR COMPRESSIBLE FLOWS

A. Macroscopic governing equations

The flow mass, momentum, and energy conservation equations are introduced as follows:

$$\frac{\partial \rho}{\partial t} + \frac{\partial \rho u_i}{\partial x_i} = 0, \tag{1}$$

$$\frac{\partial \rho u_i}{\partial t} + \frac{\partial \rho u_i u_j + \delta_{ij} p}{\partial x_j} = \frac{\partial \Pi_{ij}}{\partial x_j} + \rho g_i \quad (i = 1, 2, 3), \tag{2}$$

$$\rho \frac{\partial h}{\partial t} + \rho u_j \frac{\partial h}{\partial x_j} = \frac{Dp}{Dt} - \frac{\partial q_j}{\partial x_j} + \Pi_{ij} \frac{\partial u_i}{\partial x_j}, \tag{3}$$

where ρ is the mass volume, u_i is the velocity vector, p is the pressure, g_i is the gravitational acceleration, h is the mass enthalpy, and δ_{ij} is the Kronecker delta symbol. Throughout this manuscript, we neglect the pressure work $\frac{Dp}{Dt} = \frac{\partial p}{\partial t} + u_j \frac{\partial p}{\partial x_j} \approx 0$ in the energy equation, a reasonable approximation for buoyancy driven flows. The stress tensor Π_{ij} in Eqs. (2) and (3) reads

$$\Pi_{ij} = \mu \left(\frac{\partial u_i}{\partial x_j} + \frac{\partial u_j}{\partial x_i} - \delta_{ij} \frac{2}{3} \frac{\partial u_k}{\partial x_k} \right), \tag{4}$$

with μ the dynamic viscosity. Finally, the heat flux q_i in the energy equation reads

$$q_i = -\lambda \frac{\partial T}{\partial x_i}, \tag{5}$$

where T is the temperature, and λ is the heat conductivity, obtained assuming constant Prandtl number,

$$\mathrm{Pr} = \frac{c_p \mu}{\lambda} = \frac{\nu}{\alpha}, \tag{6}$$

where ν is the kinematic viscosity defined as $\nu = \mu/\rho$, while α is the thermal diffusivity defined as $\alpha = \lambda/\rho c_p$. The system of Eqs. (1)–(3) is fully closed by the choice of an equation of state,

$$p = \rho \cdot r \cdot T, \quad h = c_p \cdot T, \tag{7}$$

with c_p the mass heat capacity at constant pressure, and $r = 287\,\mathrm{J\,kg^{-1}K^{-1}}$ is the gas constant for air per unit mass. Note that we assume c_p to be constant since the temperature in the test cases presented does not exceed 600 K.

B. Turbulence modeling

For the large eddy simulation presented in Sec. IV, a Vreman eddy-viscosity subgrid scale model is used.[64] The filtered expressions for Eqs. (1)–(3) are widely reported in the literature (see, e.g., Ref. 65) and not recalled here. Applying the subgrid-scale model numerically comes down to modifying the viscosity μ through the addition of a turbulent viscosity μ_t obtained as follows:

$$\mu_t = \rho C \sqrt{\frac{B_\beta}{\alpha_{ij}\alpha_{ij}}}, \tag{8}$$

with

$$\alpha_{ij} = \frac{\partial u_j}{\partial x_i}, \tag{9}$$

$$\beta_{ij} = \Delta_m^2 \alpha_{mi}\alpha_{mj}, \tag{10}$$

$$B_\beta = \beta_{11}\beta_{22} - \beta_{12}^2 + \beta_{11}\beta_{33} - \beta_{13}^2 + \beta_{22}\beta_{33} - \beta_{23}^2. \tag{11}$$

The constant C is related to the Smagorinsky constant C_s as $C = 2.5C_s^2$. Δ_m is the local mesh size. The model is simple to implement and compute as it only requires the local filter width (i.e., mesh size) and the first order derivatives of the velocity field. In our simulation, $C_s = 0.1$, following Vreman's recommendation,[64] which was also adopted in the forced plume large eddy simulation by Zhou *et al.*[54] The heat flux takes into account the subgrid contribution via a turbulent Prandtl number Pr_t.

C. Numerical method: Lattice Boltzmann solver

For a complete description of the numerical method, the reader is referred to Farag et al.[16,17] Lattice-Boltzmann methods are derived from a space, time, and velocity discretization of the Boltzmann equation.[5] In the present model, the probability density function f_i is solved at each point x via the Boltzmann equation discretized as follows:

$$f_i(x + c_i\delta t, t + \delta t) = f_i^{\mathrm{eq}}(x,t) + \left(1 - \frac{\delta t}{\tau}\right) f_i^{\mathrm{neq}}(x,t) + \frac{\delta t}{2} F_i^E(x,t), \tag{12}$$

where δt is the time step, c_i is the ith discrete velocity of the D3Q19 lattice,[66] and F_i^E is a volume force including gravity and correcting terms, as defined in the Appendix. The equilibrium and off-equilibrium populations (f_i^{eq},f_i^{neq}) are to be defined in Eqs. (14) and (16).

In Eq. (12), the relaxation time τ is related to the dynamic viscosity as follows:

$$\tau = \frac{\mu}{\rho c_s^2} + \frac{\delta_t}{2}, \tag{13}$$

where $c_s = \delta x/\left(\sqrt{3}\delta t\right)$ is the characteristic velocity of the D3Q19 lattice.[66]

The equilibrium function is obtained as

$$f_i^{\mathrm{eq}} = \omega_i \left(\rho\theta + \frac{\mathcal{H}_{i,\alpha}^{(1)}}{c_s^2}\rho u_\alpha + \frac{\mathcal{H}_{i,\alpha\beta}^{(2)}}{2c_s^4}\rho u_\alpha u_\beta + a^{(3)} + a^{(4)}\right), \tag{14}$$

where ω_i is the D3Q19 weight of discrete velocity c_i, $\mathcal{H}_i$ are the discrete Hermite polynomials, defined in the Appendix, and $a^{(3)}$ and $a^{(4)}$ are third and fourth order terms also provided in the Appendix. The reduced temperature θ reads

$$\theta = \frac{rT}{c_s^2}. \tag{15}$$

The off-equilibrium counterpart f^{neq} is obtained as

$$f_i^{\mathrm{neq}} = \omega_i \left[\frac{\mathcal{H}_{i,\alpha\beta}^{(2)}}{2c_s^4} a_{\alpha\beta}^{(2),\mathrm{neq}} + \frac{\mathcal{H}_{i,\gamma}^{(3r)}}{6c_s^6} a_\gamma^{(3r),\mathrm{neq}}\right], \tag{16}$$

with

$$a_{\alpha\beta}^{(2),\mathrm{neq}} \equiv a_{\alpha\beta}^{*(2),\mathrm{neq}} - \frac{\delta_{\alpha\beta}}{3} a_{\gamma\gamma}^{*(2),\mathrm{neq}}, \tag{17}$$

$$a_{\alpha\beta}^{*(2),\mathrm{neq}} = \sum_i \left[\left(f_i - f_i^{\mathrm{eq}} + \frac{\delta t}{2} F_i^E\right)\mathcal{H}_{i,\alpha\beta}^{(2)}\right], \tag{18}$$

and the third-order contribution is defined in the Appendix.

Finally, the macroscopic variables are reconstructed from f_i as

$$\rho(t + \delta_t, x) = \sum_i f_i(t + \delta_t, x) - (\rho\theta)(t,x) + \rho(t,x), \tag{19}$$

$$\rho u_i(t + \delta_t, x) = \sum_i c_i \left(f_i(t + \delta_t, x) + \frac{\delta_t}{2} F_i^g\right), \tag{20}$$

where F_i^g is the gravity force term defined in the Appendix. The enthalpy equation (3) is solved at the same time using a finite difference discretization under non-conservative form, exactly as presented by Tayyab *et al.*[23,24] Second-order consistency to the macroscopic equations (1)–(3) can be shown via Chapman–Enskog,[5] or Taylor[67,68] expansions.

III. CANONICAL 2D VALIDATIONS

This section provides canonical validations of the numerical method presented above. It focuses on two gravity-driven configurations: the Rayleigh–Benard and Rayleigh–Taylor instabilities since the properties of the flow solver are already validated in a large number of compressible flow configurations in the absence of gravity.[2,16,17,19,23,24,69]

A. Rayleigh–Benard Instability

The Rayleigh–Benard instability is a configuration involving natural convection and heat transfer.[70]

Figure 1 depicts the configuration to be simulated. It consists of a square box of dimension $1 \times 1\,\mathrm{m}^2$, initially filled with quiescent air and surrounded by adiabatic walls on the left and right, and isothermal top and bottom walls, respectively, at $T_C = 299.5$ and $T_H = 300.5$K.

The Rayleigh number, Ra, describes, on the one hand, the balance between buoyancy vs viscous forces in the momentum equation and, on the other hand, the balance between conductive vs convective transfer in the energy equation. It is assumed that convective heat transfer takes place with the velocity obtained by the balance in the momentum equation, and it is defined as

$$\mathrm{Ra} = \frac{g\beta(T_H - T_C)H^3}{\alpha\nu} = \mathrm{Pr}\frac{g\beta(T_H - T_C)H^3}{\nu^2}, \tag{21}$$

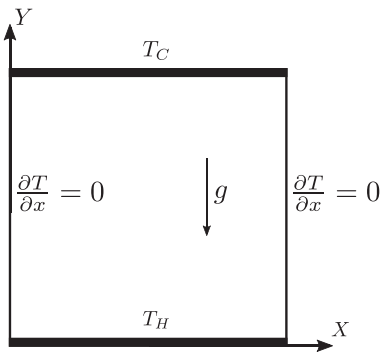

FIG. 1. Schematic of Rayleigh–Benard test case.

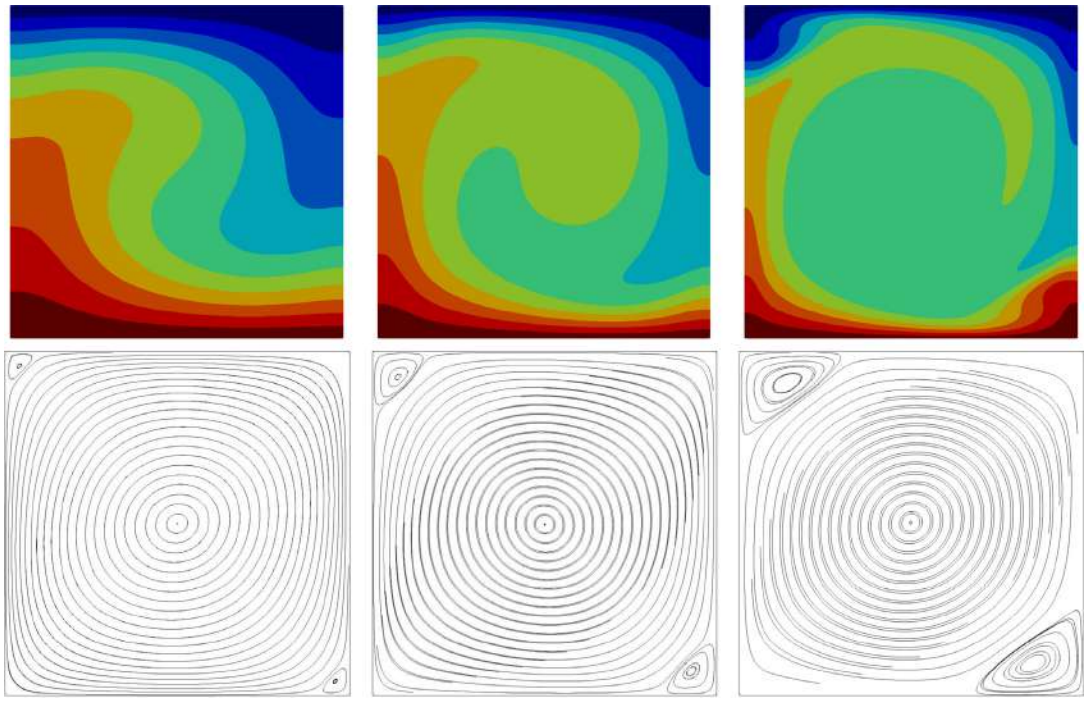

FIG. 2. Rayleigh–Benard instability: Temperature contours (top) and streamlines (bottom), for three Rayleigh numbers (10^4, 10^5, 10^6), from left to right.

where $g = 9.81\,\mathrm{m\,s^{-2}}$ is the gravitational acceleration and $H = 1$ m is the domain size. β is the thermal expansion coefficient that is equal to $1/T_{ref}$ for an ideal gas with isobaric expansion (i.e., at constant pressure). In the present study, T_{ref} is taken equal to T_H. Setting $\mathrm{Pr} = 0.71$, the viscosity can be deduced from the target Rayleigh numbers [Eq. (21)] of 10^4, 10^5, and 10^6, while the thermal conductivity, λ, in the energy equation is obtained from Eq. (6).

The domain is discretized with a uniform grid with 256×256 cells. The flow is then uniformly initialized as $u_0 = 0$, $T_0 = 300$ K, $\rho_0 = 1.17\,\mathrm{kg\,m^{-3}}$, and $p = p_0 + \rho_0 g y$. The simulation is then carried out until convergence using a time step, $\delta_t = 6.5 \times 10^{-6}$ s.

Figure 2 presents temperature contours as well as streamline patterns, showing good qualitative agreement with the literature (see, e.g., Ref. 71), for $\mathrm{Ra} = 10^4$, the flow is symmetric and dominated by the recirculation in the core region with small eddies near the corner. When increasing the Raleigh number, secondary eddies near the top left and bottom right corners appear and become larger.

The quantitative agreement is shown in Fig. 3, presenting velocity profiles along the centerlines. The present numerical results are compared with the benchmark solution provided by Ouertatani *et al.*[71] For further validation, the local Nusselt number Nu is calculated at the bottom wall as

$$\mathrm{Nu} = \left.\frac{\partial T}{\partial y}\right|_{y=0}. \tag{22}$$

It can be observed that both velocity and Nusselt number profiles are in excellent agreement with the reference solutions.

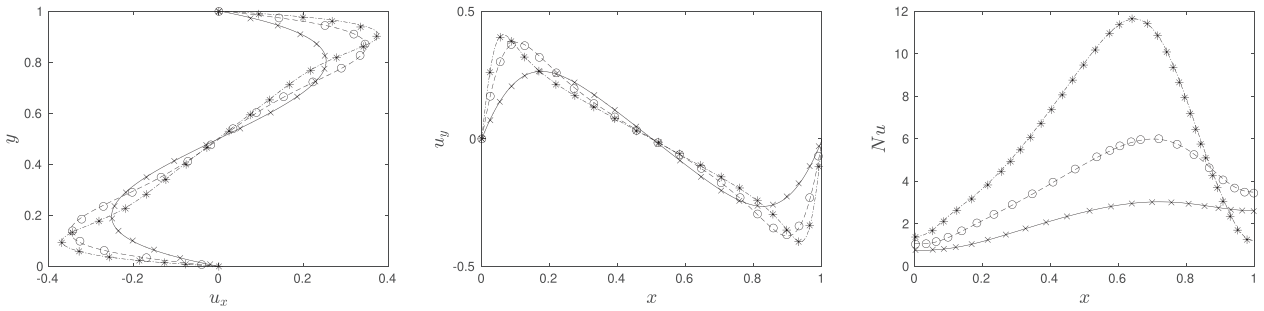

FIG. 3. Rayleigh–Benard instability. u_x along the vertical centerline, u_y along the horizontal centerline, and Nusselt number along the bottom wall (from left to right) for $\mathrm{Ra} = 10^4$ (solid), $\mathrm{Ra} = 10^5$ (dashed), and $\mathrm{Ra} = 10^6$ (dotted-dashed). Symbols indicate the reference data.[71]

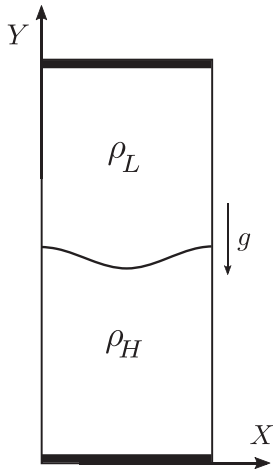

FIG. 4. Schematic of Rayleigh–Taylor instability.

B. Rayleigh–Taylor instability

The Rayleigh–Taylor instability is another classical test case for buoyancy-driven flows due to its practical and fundamental importance. It was investigated extensively in the literature by different numerical methods.[72–81] It consists of two layers of fluids of different densities (ρ_H, ρ_L) at rest under gravitational field, as illustrated in Fig. 4.

The dynamics of this problem is governed by the Atwood (At) and Reynolds (Re) numbers,

$$\mathrm{At} = \frac{\rho_H - \rho_L}{\rho_H + \rho_L}, \quad \mathrm{Re} = \frac{U^* L_x}{\nu}, \tag{23}$$

where L_x is the dimension of the domain in the horizontal direction and $U^* = \sqrt{gL_x}$ is a reference velocity.

The investigated configuration was previously studied in the literature[73–75] with two target Reynolds numbers of 256 and 2048. The domain size is $L_x \times 4L_x$, discretized with 256×1024 (fine mesh) or 128×512 grid points (coarse mesh). The heavy (index H) and light (index L) fluids are initially separated by a perturbed interface given by the following equation:

$$y_i(x) = \frac{L_x}{10}\cos\left(\frac{2\pi x}{L_x}\right) + 2L_x. \tag{24}$$

The fluids initial densities are set to $\rho_H = 3$ and $\rho_L = 1\,\mathrm{kg\,m^{-3}}$, corresponding to $\mathrm{At} = 0.5$. The pressure was initialized to account for the gravity field as follows:

$$p = \begin{cases} p_0 + \rho_L g y, & 0 \le y \le y_i(x), \\ p_0 + \rho_L g y_i(x) + \rho_H g(y - y_i(x)), & y_i(x) < y, \end{cases} \tag{25}$$

where p_0 is the pressure at $y = 0$. Finally, the domain size and gravity are set to $L_x = 0.25\mathrm{m}$ and $g = 20\mathrm{m\,s^{-2}}$. The fluid viscosity is obtained from the target Reynolds numbers of 256 and 2048.

Figure 5 represents the density contours obtained for the two Reynolds numbers of 256 and 2048 using the finer mesh. The diagrams of the right of the figure represent the time evolution of the bubble and spike positions. Numerical predictions are compared to reference numerical simulation,[72] showing excellent agreement.

To investigate the robustness of the method, simulations were carried out on the coarser mesh. Excellent agreement is also obtained with a maximum error less than 2%.

IV. LARGE EDDY SIMULATION OF A THERMAL PLUME

This section presents a large eddy simulation of a buoyant plume, generated by a vertical jet of hot air into a quiescent atmosphere. The source conditions correspond to the experiments of Shabbir and George,[46] summarized in Table I. The plume source diameter, D, the exit mean velocity, U_0, the hot air temperature, T_0, and the ambient air temperature, T_a, are 6.35 cm, 0.98 m/s, 568 K and 300 K, respectively. The corresponding Reynolds number, Re, based on inflow mean injection velocity, source diameter, and kinematic viscosity, is 1273. The specific momentum, M_0, buoyancy, F_0, mass, Q_0, and the Morton length scale, L_M, are defined as

$$\begin{aligned} F_0 &= 2\pi g \int_0^\infty U_z \frac{\Delta T}{T} r dr, \quad M_0 = 2\pi \int_0^\infty U_z^2 r dr, \\ Q_0 &= 2\pi \int_0^\infty U_z r dr, \quad L_M = \frac{M_0^{3/4}}{F_0^{1/2}}, \end{aligned} \tag{26}$$

where r is the radial coordinate. Morton[27] and Morton and Middleton[82] introduced the source parameter Γ_0 that characterizes the plume as being either lazy ($\Gamma_0 > 1$), pure ($\Gamma_0 = 1$), or forced ($0 < \Gamma_0 < 1$),

$$\Gamma_0 = \frac{5Q_0^2 F_0}{8\sqrt{\pi}\alpha M_0^{5/2}} \tag{27}$$

with α the entrainment coefficient explained in detail later on. The value of Γ_0 in our simulation is around 0.9, which indicates a forced plume, having a value of Γ_0 near unity says that the plume is forced but not too much; as a result, the buoyancy is significant near the source, which explains the acceleration zone detailed later.

A. Numerical setup

The computational domain is a box of size $9\,\mathrm{D} \times 9\mathrm{D} \times 18\mathrm{D}$. A uniform mesh, composed of $150 \times 150 \times 300$ cells, is considered. The simulation was performed with ProLB on 280 processors. The time step, based on the sound speed, is $\delta_t = 4.5 \times 10^{-6}$ s. In accordance with previous LES of this configuration,[54] the Vreman turbulence model, described in Sec. II B, is applied with a turbulent Prandtl number of $\mathrm{Pr}_t = 0.3$.

The boundary conditions are as follows: at the outlet, a Dirichlet condition is considered for pressure, whereas a Neumann condition is applied for other variables with a clip for the axial velocity to prevent any backflow of the plume. Typical inflow/outflow boundary conditions are considered for the vertical sides.

At the inlet, temperature and velocity were imposed to represent a plume source.

For the inlet boundary condition, we followed the strategy of Zhou *et al.*[54,83] to ensure a transition from laminar to turbulence at a very short distance of the exit, consistently with the experimental observations of Shabbir and George.[46] This kind of fluctuations work more as perturbations with artificial nature so, they are not divergence free. However, this does not represent an important issue because the

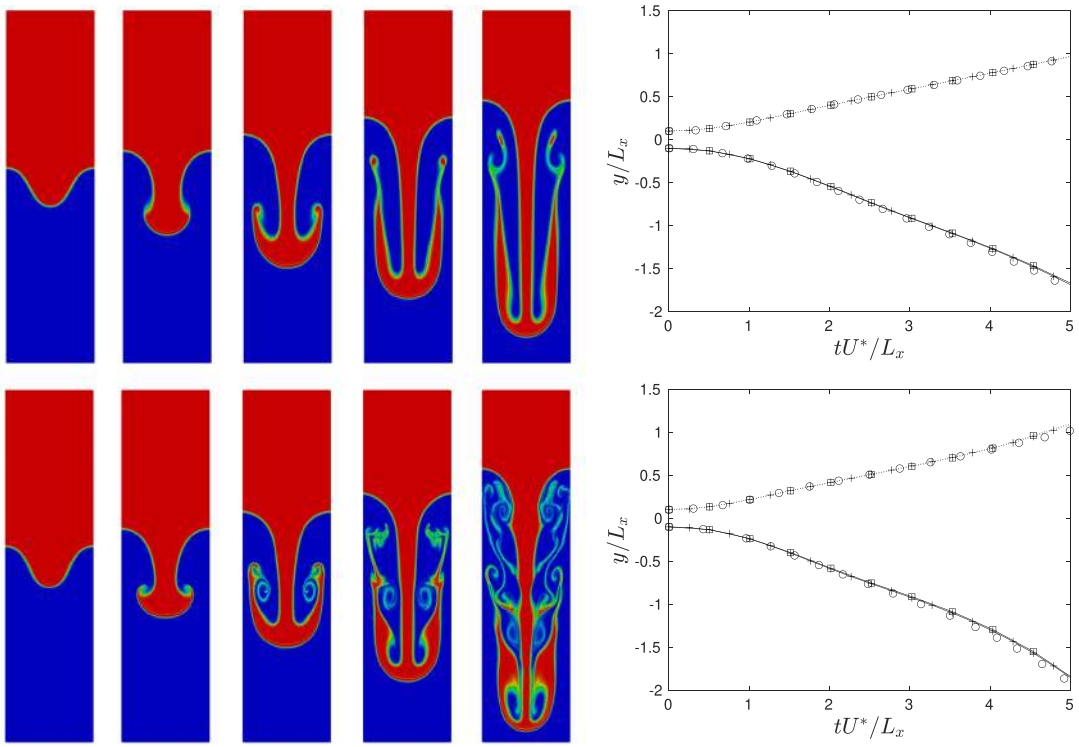

FIG. 5. Rayleigh–Taylor instability for Re = 256 (top) and Re = 2048 (bottom). Left: Density contours at different normalized times $t.U^*/L = 1, 2, 3, 4, 5$ obtained for the fine mesh. Right: Time evolution of the position of both bubble (solid) and spike (dashed). (□) The coarse mesh, (+) the fine mesh, and (○) the reference from He *et al.*[72]

associated timescale is large compared to the flow turbulent time scales (the fastest timescale of our injection is around 0.2 s). As a consequence, the impact of this synthetic injection vanishes few diameters away from the inlet where we start performing our analysis. It consists of superimposing azimuthal disturbances,

$$u'(r) = AU_0(r)\left[\left(1-\frac{r}{D}\right)\sum_{n=1}^{N}\sin(2\pi ft/n)+\frac{r}{D}\sum_{n=1}^{N}\sin(2\pi ft/n+\theta)\right], \tag{28}$$

to a mean flow $U_0(r)$ corresponding to a pipe profile,

$$U_0(r) = \frac{1}{2}U_0[1-\tanh(b_2(2r/D-D/2r))], \tag{29}$$

where A is the amplitude of the forcing and $N=6$ is the number of the modes. f is the frequency of the forcing that is determined by the jet preferred mode corresponding to a Strouhal number, $\mathrm{St} = fD/U_0$, of 0.3, leading to $f = 4.629$ Hz. In the mean pipe flow profile, θ is the azimuthal angle and $b_2 = 6.25$.[84]

Note that Eq. (28) was slightly modified from the original formulation,[85,86] which presented a singularity at the center. The forcing amplitude $A = 0.2/\sqrt{3}$ corresponds to a RMS fluctuations of 20% for the axial velocity and $A = 0.01/\sqrt{3}$ corresponds to a RMS fluctuations of 1% for the other two components.

The time-averaged statistics (mean, rms) presented hereafter were collected over 15 forcing cycles = 20 s once a statistical steady state was reached. The forcing cycle is defined by the longest period of the sine series in Eq. (28) = 1.3 s.

TABLE I. Source parameters of the plume.

D (m)	T_a (K)	T_0 (K)	U_0 (m/s)	F_0 (m^4/s^3)	M_0 (m^4/s^3)	$\mathrm{Re} = \frac{U_0 D}{\nu}$	$\mathrm{Fr} = \frac{U_0^2}{gD}$
0.0635	300	568	0.98	0.0127	0.003	1273	1.54

B. Results and discussion

1. Qualitative description

Figure 6 illustrates the transition process through a snapshot of the three dimensional iso-surface for the Q-criterion[87] along with temperature and density fields. The Q-criterion is defined as

$$Q = \frac{1}{2}(||\Omega||^2 - ||S||^2), \tag{30}$$

where S and Ω are the strain rate and the vorticity tensor, respectively,

$$\Omega = \frac{1}{2}(\nabla\mathbf{u} + \nabla\mathbf{u}^T), \tag{31}$$

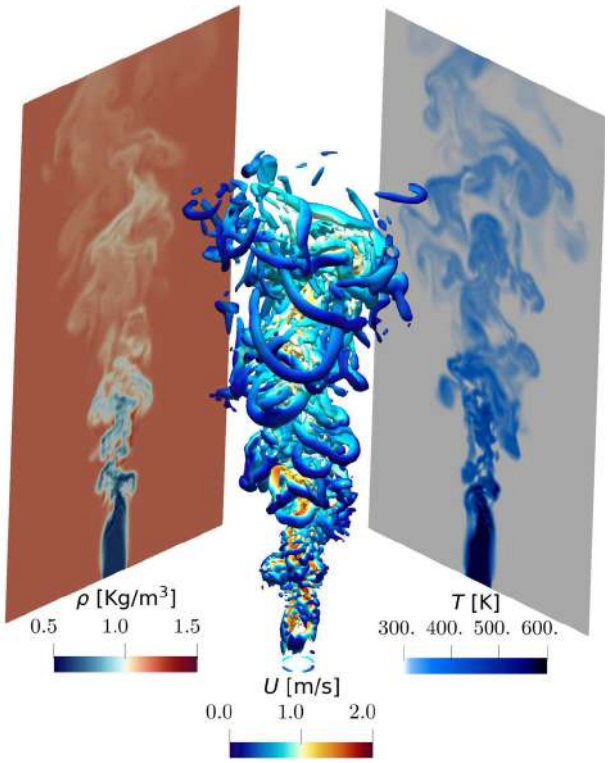

FIG. 6. Instantaneous 3D Q-criterion colored by velocity magnitude alongside density and temperature fields.

$$S = \frac{1}{2}(\nabla \mathbf{u} - \nabla \mathbf{u}^T). \tag{32}$$

The Q-criterion defines the areas where the vorticity magnitude is larger than the magnitude of the strain rate, such that $Q > 0$ indicates the existence of a vortex. The potential core of the plume becomes rapidly turbulent after few diameters from the source, which is consistent with the experimental observations of Shabbir and George.[46] The transition occurs due to the growth of azimuthal instabilities that form large coherent energy containing structures, which eventually break down to generate small-scale turbulence.

Figure 7 shows the energy spectrum based on the axial velocity at distance $z/D = 4$; it shows the energy cascading reported by the theory of Kolmogorov[88] and that we have the correct power law of $-5/3$ in the inertial range, and also the dissipation range was detected at higher frequencies. In addition, in Fig. 7 the spectrum for temperature fluctuations is shown, and the spectrum initially shows the $-5/3$ power law in the so-called inertial-convection region. Afterwards, a region is expected where the spectrum decays sharply and follows a -3 power law, which is a unique characteristic of the forced plumes, and it belongs to the inertial-diffusive subrange proposed by Papanicolaou and List.[45] Kostovinos[89] argued experimentally that the slope change from $-5/3$ to -3 is due to strong energy feeding as a result of the large plume vortices driven by buoyancy force. This region cannot be clearly identified on the spectrum of temperature fluctuations in Fig. 7.

2. Axial mean quantities

Figure 8 compares the centerline time-averaged axial velocity U_c and temperature T_c to the experimental data of Shabbir and George,[46] who proposed the following correlation in the plume-like region:

$$U_c = A_U z^{-1/3} F_0^{1/3}, \quad \frac{T_a}{T_c} = 1 - A_T z^{-5/3} F_0^{2/3}/g, \tag{33}$$

where $A_T = 9.4$ and $A_U = 3.4$ were fitted from the experimental results (see also in Table II). The centerline velocity in Fig. 8 increases rapidly from its initial value at the inlet to a maximum value of about 1.8 at $z/D \approx 2.5$ and then decreases afterwards rapidly to reach values lower than the inflow velocity after about six diameters. This behavior was also observed by Lingens *et al.*[90] who experimentally investigated buoyant jet diffusion flame. The initial acceleration in the near field is due to the large buoyancy force resulting from large temperature (density) difference between the plume core and the ambient. The rapid deceleration after the peak results from the turbulent mixing of the plume with the surrounding fluid, which decreases the temperature. The rapid decrease in temperature downstream the potential core is clearly evidenced in Fig. 8. The location of the transition from jet-like

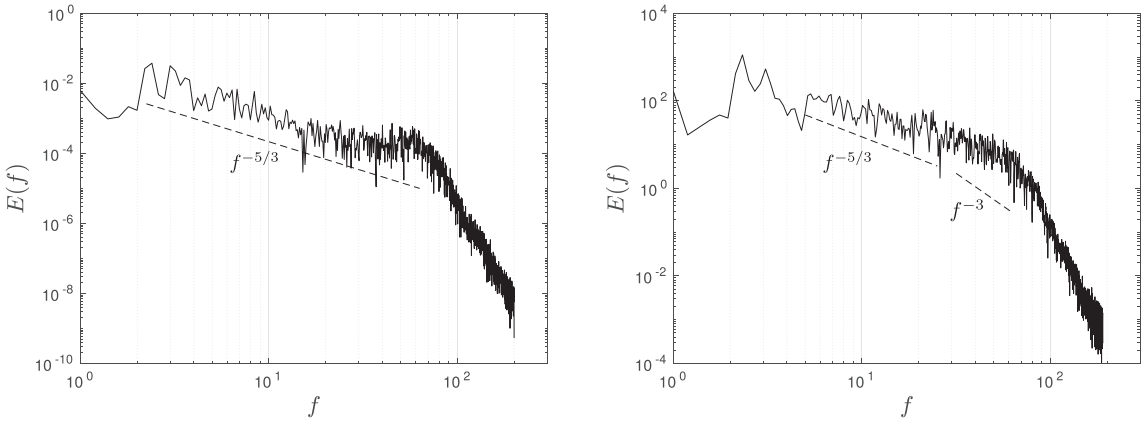

FIG. 7. Temporal energy spectrum at $z/D = 4$ for axial velocity (left) and temperature (right). Dashed lines indicate the expected characteristic slopes.

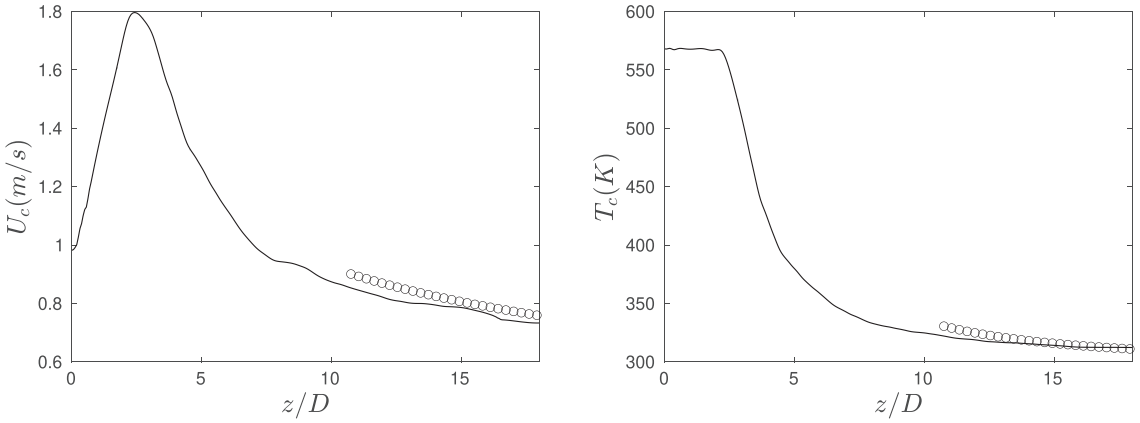

FIG. 8. Centerline means axial velocity (left) and temperature (right) profiles. Solid line for the simulation and symbols for experimental data of Shabbir and George.[46]

TABLE II. Summary of mean flow parameters and turbulence intensities for different experiments.

Reference	A_T	A_U	B_T	B_U	$\overline{(T'^2)}^{1/2}/\overline{\Delta T_c}$	$\overline{(u_z'^2)}^{1/2}/\overline{U_c}$	$\overline{u_z'T'}/\overline{(u_z'^2)}^{1/2}\overline{(T'^2)}^{1/2}$
Shabbir and George[46]	9.4	3.4	68	58	0.4	0.33	0.67
George *et al.*[44]	9.1	3.4	65	55	0.38	0.28	0.67
Papanicolaou and List[45]	14.28	3.85	80	90	0.42	0.25	0.51
Nakagome and Hirata[47]	11.5	3.89	48.1	63	0.36	0.25	0.46

to plume-like behavior can be identified through the rates of decrease that have to scale with $z^{-1/3}$ and $z^{-5/3}$ for velocity and temperature, respectively. The numerical model predicts the transition at $z/D \approx 10$–11, which is consistent with the experiments of Shabbir and Georges[46] where it was estimated to occur at $z/D = 10.5$. In the plume-like region, the model reproduces quantitatively the evolution of both axial velocity and temperature with z/D although U_c is on the whole slightly underestimated.

The non-dimensional mean axial velocity $U_c z/\sqrt{M_0}$ is plotted as a function of the non-dimensional axial distance $\xi = z/L_M$ in Fig. 9. The transition to the plume-like region (i.e., the slope change) is predicted around $\xi = 4$–5, which is consistent with the finding of Morton *et al.*[42] who reported that a forced plume will reach a pure plume behavior for $z/L_M > 5$. In addition, our simulation exhibits good agreement with the experimental profile obtained from the correlation of Shabbir and George[46] [see Eq. (33)] in the plume-like region.

Forced plumes becomes plume-like far away from the source in homogeneous environment even if the injected momentum flux is large when the function Γ changes from a value smaller than 1 at the source to a value of 1 in the far field. Four regions were identified in the present simulation: (1) a non-buoyant region where momentum dominates the flow, (2) an acceleration region where the plume is accelerated due to gravity, (3) an intermediate region where influence of initial momentum weakens, and (4) the plume-like region (i.e., self-similarity region) where the plume dynamics is dominated solely by the buoyancy forces. This picture is consistent with the descriptions of Gebhart *et al.*[91] and Chen and Rodi[92] although they did not report the acceleration region (i.e., region 2). Note that the limits of each region in Fig. 9 are defined using the velocity inflection points, consistently with the global behavior of the plume.

3. Fluctuations quantities

In this section, the axial evolution of the rms values of axial velocity and temperature fluctuations and the cross correlation between velocity and temperature fluctuations are discussed and compared with experiments,[44–47] for which the fitting parameters are reported in Table II.

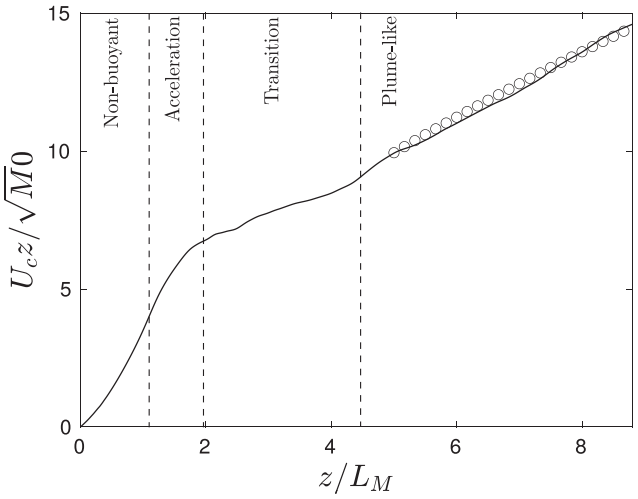

FIG. 9. Centerline means the non-dimensional axial velocity profile. Solid line for the simulation and symbols for the experiment of Shabbir and George.[46]

Figure 10 presents the rms values of axial velocity and temperature fluctuations. As expected, the velocity fluctuations are about 20% at vicinity of the inflow plane and correspond to the imposed disturbance level. The velocity fluctuations decrease in the potential core region of the plume before starting to increase very abruptly in the laminar to turbulence transition region, and the initial drop in velocity fluctuations is due to the artificial nature of the fluctuations imposed at the inlet. These artificial fluctuations, without a proper cascade, are dissipated very quickly; however, they constitute the seed for a correct transition to turbulence with a realistic energy cascade in the far field where we perform our analysis. In the plume-like region, both velocity and temperature fluctuations decrease at a same rate as mean velocity and temperature to ensure constant ratio of $\overline{u'^2}^{1/2}/U_c$ and $\overline{T'^2}^{1/2}/(T_c - T_a)$. The predicted velocity-based turbulence intensity in the plume-like region is lower than those of 0.28 and 0.33 reported by George *et al.*[44] and Shabbir and George,[46] respectively. It is in better agreement with those of 0.25 reported by Papanicolaou and List[45] and Nakagome and Hirata[47] On the other hand, Fig. 10 shows that the temperature-based turbulence intensity is also consistent with the available data.

Figure 10 shows the evolution of the cross correlation between velocity and temperature fluctuations, $\overline{u'T'}/(\overline{(u'^2)}^{1/2}\overline{(T'^2)}^{1/2})$, along the centerline. It can be clearly observed that velocity and temperature fields are positively correlated in this type of flows with a predicted nearly constant value in the plume-like region of about 0.55. This value is lower than those reported by George and co-workers[44,46] in the range 0.6–0.7, averaged to 0.67 (see Table II), and in closer agreement with those of 0.46 and 0.51 reported by Nakagome and Hirata[47] and Papanicolaou and List,[45] respectively.

4. Self-similarity

An important feature of the mean flow in the fully developed region of turbulent positively buoyant plumes is the "self-similarity" or "self-preserving" behavior. The radial mean velocity and temperature profiles follow a Gaussian shape and become wider as the plume rises. The profiles collapse on the same curve when considering appropriate dimensionless variables,

$$\frac{U_z}{U_c} = \exp\left\{\left(-B_u \frac{r^2}{z^2}\right)\right\}, \quad \frac{T - T_a}{T_c - T_a} = \exp\left\{\left(-B_T \frac{r^2}{z^2}\right)\right\}. \quad (34)$$

The coefficients B_u and B_T are unknown empirical constants that can be obtained by assuming a linear growth of the plume width b,[42]

$$\frac{b}{z} = \frac{6}{5}\alpha = const. \quad (35)$$

The coefficients will then be calculated using $B_u = \sqrt{z/b_u}$ and $B_T = \sqrt{z/b_T}$, where b_u and b_T are the plume width defined by the distance from the centerline to the point at which we have $1/e$ of the centerline values of velocity and temperature, respectively. George *et al.*[44] determined by experiments those coefficients as $B_u = 55$ and $B_T = 65$.

The radial profiles of mean velocity and temperature from our LES at $z/D = 10, 12, 14, 16$ and the profiles of George *et al.*[44] form are plotted in Fig. 11. The velocity and the temperature rise above the ambient are normalized by the centerline value. The profiles are plotted vs the non-dimensional radial coordinate $r/(z + z_0)$ where z_0 is the virtual origin of the plume. Empirical relationships were reported to estimate the location of the virtual origin.[54] As pointed out by Yang,[55] the location of virtual origin predicted in the simulation can be different from that estimated by empirical formula. Indeed, this location is significantly affected by the transition from laminar to turbulent whose the prediction is a difficult task in LES mainly due to its sensitivity to the source inflow condition of the plume. In the present study, the virtual origin was estimated to collapse the radial profiles in the fully developed region to a single dimensionless Gaussian profile following the methodology proposed by Yan,[55] giving z_0 set equal to $2.3D$. It can be observed in Fig. 11 that the self-similarity is well preserved in the simulation and the predicted self-similarity profiles agree well with those reported by Georges *et al.*[44]

Following Shabbir and George,[46] the radial profiles of rms values of axial velocity and temperature and of the cross correlation between velocity and temperature fluctuations are plotted in terms of the similarity variables in Fig. 12. The predicted profiles clearly exhibit a self-similar behavior. The agreement with the experimental data is reasonable although, consistently with Fig. 10, both rms values of axial velocity fluctuations and the cross correlation between velocity and temperature fluctuations are overall underestimated.

5. Entrainment

The mechanism of turbulent mixing that brings air into the buoyant plume is called entrainment. The ideal plume theory is based

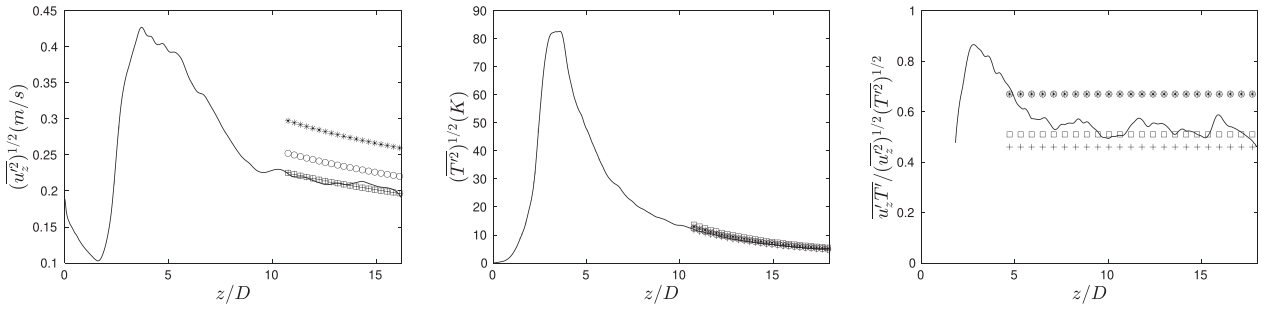

FIG. 10. Center line profiles of rms of axial velocity (left), temperature (center), and the cross correlation of velocity and temperature fluctuations (right). Solid line for simulation, (∗) for Shabbir and George,[46] (○) for Geroge *et al.*,[44] (□) for Papanicolaou and List,[45] and (+) for Nakagome and Hirata.[47]

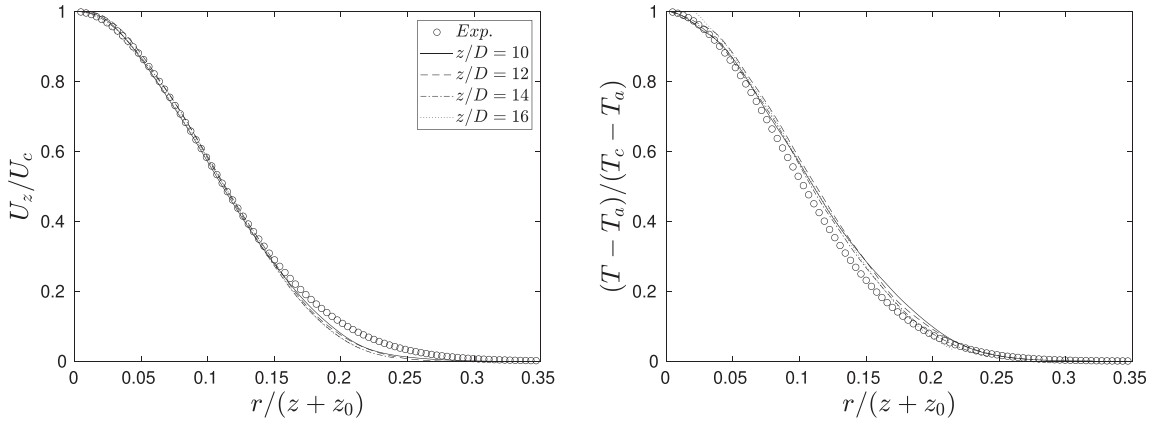

FIG. 11. Radial profiles of mean axial velocity (left) and mean temperature (right) at four axial positions compared to the experiments of George *et al.*[44]

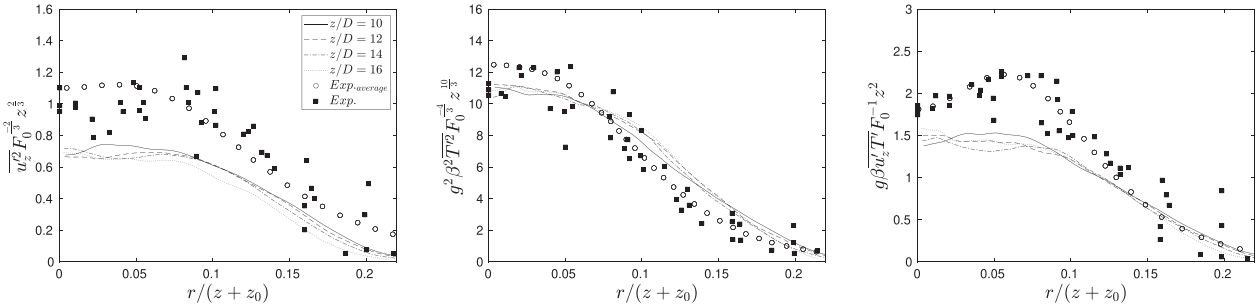

FIG. 12. Radial profiles at $z/D = 10, 12, 14, 16$ for normalized rms of axial velocity fluctuation (left), rms of temperature fluctuations (middle), and cross correlation of both velocity and temperature fluctuations (right).

on both Boussinesq and top-hat radial-profile assumptions and assumes that the mean entrained flux across the edge of the plume E (entrainment rate) is proportional to the local upward velocity W. An air entrainment coefficient is then defined as

$$\alpha = \frac{E}{bW}, \tag{36}$$

where E, W, b are known as the top-hat variables of entrainment rate, local vertical velocity, and plume width defined by Turner,[93]

$$b^2 W = \int_0^\infty U_z r dr, \quad b^2 W^2 = \int_0^\infty U_z^2 r dr, \quad E = \frac{d}{dz}\left(\int_0^\infty U_z r dr\right). \tag{37}$$

The plume width, b, can be calculated as the value at which velocity or temperature reaches a value of $1/e$ of the centerline value as indicated by Morton *et al.*[42] This will be referred to as (*method 1*) hereafter. It can be also obtained from Eq. (37) as $b^2 W/\sqrt{b^2 W^2}$. This second method will referred to as (*method 2*) hereafter. Figure 13 compares the two methods. The experimental slope obtained by George *et al.*[44] and the numerical prediction obtained by Zhou *et al.*[54] are also plotted in Fig. 13. Both the present predicted velocity and temperature half-widths decrease first due to the "necking" process in the near field, as observed experimentally by Cetegen,[94] before, as expected, increasing almost linearly in plume region. The two methods provide on the whole consistent predictions that agree with both the experimental slope and the numerical results obtained by Zhou *et al.*[54]

The entrainment coefficient, α, can be calculated using Eq. (35). This method requires the knowledge the width of b, along the plume axis. It can be obtained either from temperature and velocity radial profiles (*method 1*) or from Eq. (37) (*method 2*), as discussed previously. Another method was adopted by Zhou *et al.*[54] from Eqs. (36) and (37), leading to $\alpha = E/\sqrt{b^2 W^2}$. This method will be referred to as (*method 3*). Figure 13 shows that the three methods provide consistent results in the far-field. Our results agree well with the LES of Zhou *et al.*,[54] which settles on a constant value in the far-field, $\alpha = 0.09$–0.1. Our predictions of α in the plume region are also close to the value of 0.116 adopted by Morton in his plume model[27] and the experimental value 0.108 reported by George *et al.*[44]

Integrating radially the momentum and energy equations across the flow introduces two fundamental quantities.[46] The first is the momentum flux, M, that can be normalized by the inflow momentum flux, M_0 (see Table I),

$$M = 2\pi \int_0^\infty (U_z^2 + \overline{u_z'^2} - \overline{v'^2}) r dr. \tag{38}$$

The moment flux ratio increases with the height according to the following relationship:[95]

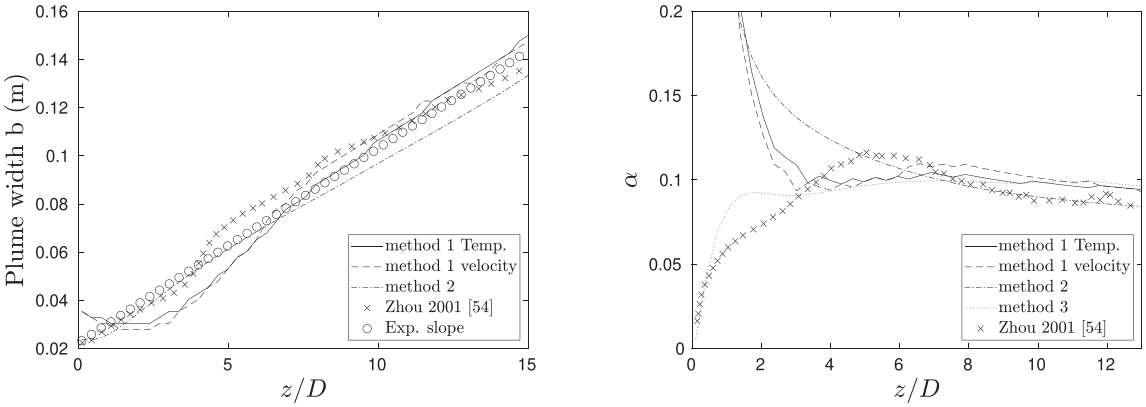

FIG. 13. Evolution with the height of (left) the plume width and (right) the entrainment coefficient α.

$$\frac{M}{M_0} = k\left(\frac{x}{L_M}\right)^{4/3}. \tag{39}$$

Different values of 0.35,[95] 0.34,[46] and 0.29[45] were reported for the coefficient k. Figure 14 compares our result to these experimental results. Model predictions are in good agreement with the experiments of Shabbir and George[46] and Fisher[95] but overpredict that of Papanicolaou and List.[45]

The second is the buoyancy flux F that has to be conserved along the plume height,

$$F = 2\pi g \int_0^\infty \left(U_z \frac{\Delta T}{T} + \frac{\overline{u_z' T'}}{T}\right) r dr. \tag{40}$$

The buoyancy flux is normalized by its injection value, F_0. Figure 14 shows the evolution of F/F_0 along the plume height. The simulated normalized buoyancy flux evolves around unity, consistently with the theory (solid line). It appears clearly by comparing the solid and dashed lines that the turbulent contribution is essential. When it is disregarded, the buoyancy flux decreases with the axial distance and is no more conserved. The turbulence contribution is predicted around 15% − 20% as also noted by Shabbir and George,[46] while George *et al.*[44] and Papanicolaou and List[45] found the contribution to be about 15%.

V. CONCLUDING REMARKS

A recursive regularized pressure based LBM solver (ProLB) was tested for buoyancy driven flows.

The solver was able to correctly validate the Rayleigh–Bénard cavity test case for different Rayleigh numbers $Ra = 10^4, 10^5, 10^6$; vertical and horizontal velocity profiles as well as Nusselt number profiles at the bottom wall were all in good agreement with the reference.

As for the Rayleigh–Taylor test case, we were able to correctly predict the instantaneous evolution of the positions of bubble and spike for two different Reynolds numbers Re = 256, 2048. In addition, the test case was run on a coarser mesh to test the robustness of the solver, and the results were abundantly satisfying.

For the 3D forced plume simulation, which is a critical test case in which the buoyancy is highly coupled with momentum and turbulent mixing, the solver was able to anticipate the correct physics of a thermal plume from numerous aspects listed below:

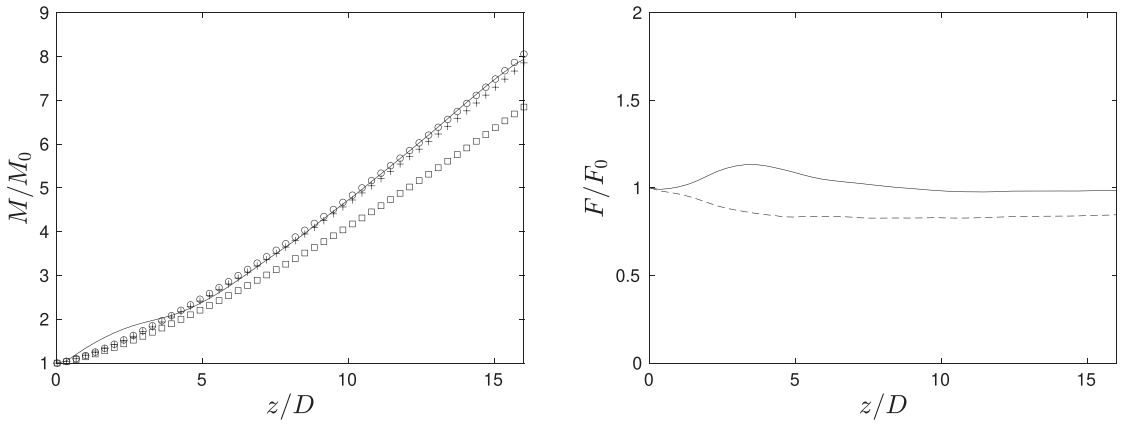

FIG. 14. Axial profile of momentum flux ratio (left). The solid line represents the present LES, whereas the symbols represent the experimental data of Denman[95] (○), (+) for Shabbir and George,[46] and (□) for Papanicolaou and List.[45] Axial profile of buoyancy flux ratio (right), solid line includes the turbulent heat flux while dashed line does not.

- The velocity energy spectrum follows the Kolmogorov theoretical slope of $-5/3$, indicating a proper resolution of the turbulence energy cascading as reported in the literature.
- Axial profiles of mean velocity and temperature were in good agreement with the experimental data.
- Our forced-plume reaches a plume-like region at around $z/L_m = 4$–5, which is consistent with the findings in the literature.
- The axial profiles of rms for velocity and temperature were also in good agreement with the experiments; we should emphasize that we did not take into account the experimental errors, which are significant especially for the second order statistics.
- The cross-correlation between velocity and temperature has a high positive value, which compares well with the reported values from experiments and indicates a strong coupling between the velocity and temperature fluctuations due to gravity.
- Self-similarity profiles in the far field (i.e., plume-like region) were achieved for both mean and rms of velocity and temperature.
- The growth rate of the plume was examined through the spatial evolution of the plume width. The growth of the plume compared very well with experimental and numerical references.
- The entrainment of fluid form the surrounding was correctly predicted by examining the entrainment coefficient α, and the predictions were in good agreement with the theoretical, experimental, and numerical references.
- Integral quantities, mainly buoyancy flux and momentum flux, were compared with the experiments and both were in good agreement. We emphasize about the finding that the turbulent heat flux participates by around 20% in the total buoyancy flux, which is consistent with the experiments.

From all the previous points, we can conclude that our solver is capable of reproducing the physics of a thermal plume correctly whether the mean values, the second order statistics, or even integral quantities through the plume, and that our code can handle any type of flows with variable densities regardless of their complexity.

ACKNOWLEDGMENTS

Centre de Calcul Intensif d'Aix-Marseille and GENCI-TGCC/CINES (Grant Nos. 2021-A0092B11951 and 2021-A0092A07679) are acknowledged for granting access to their high performance computing resources.

AUTHOR DECLARATIONS

Conflict of Interest

The authors have no conflicts to disclose.

DATA AVAILABILITY

The data that support the findings of this study are available from the corresponding author upon reasonable request.

APPENDIX: EXPRESSIONS FOR THE LBM SOLVER

In regularized LBM, distribution functions will be constructed using an orthogonal polynomial basis. The basis of the D3Q19r lattice used in the current study consists of 19 polynomials, read[17]

$$\mathcal{H}_i^{(0)} \equiv 1\,, \quad \mathcal{H}_{i,\alpha}^{(1)} \equiv c_{i\alpha}\,, \quad \mathcal{H}_{i,\alpha\beta}^{(2)} \equiv c_{i\alpha}c_{i\beta} - c_s^2\delta_{\alpha\beta}, \tag{A1}$$

$$\mathcal{H}_{i,1}^{(3r)} \equiv \mathcal{H}_{i,xxy}^{(3)} + \mathcal{H}_{i,yzz}^{(3)}, \tag{A2}$$

$$\mathcal{H}_{i,2}^{(3r)} \equiv \mathcal{H}_{i,xzz}^{(3)} + \mathcal{H}_{i,xyy}^{(3)}, \tag{A3}$$

$$\mathcal{H}_{i,3}^{(3r)} \equiv \mathcal{H}_{i,yyz}^{(3)} + \mathcal{H}_{i,xxz}^{(3)}, \tag{A4}$$

$$\mathcal{H}_{i,4}^{(3r)} \equiv \mathcal{H}_{i,xxy}^{(3)} - \mathcal{H}_{i,yzz}^{(3)}, \tag{A5}$$

$$\mathcal{H}_{i,5}^{(3r)} \equiv \mathcal{H}_{i,xzz}^{(3)} - \mathcal{H}_{i,xyy}^{(3)}, \tag{A6}$$

$$\mathcal{H}_{i,6}^{(3r)} \equiv \mathcal{H}_{i,yyz}^{(3)} - \mathcal{H}_{i,xxz}^{(3)}, \tag{A7}$$

$$\mathcal{H}_{i,1}^{(4r)} \equiv \frac{4}{9}\left(3+2\sqrt{3}\right)\mathcal{D}_{i,xyz}^{(4)} + \frac{4}{9}\left(3-\sqrt{3}\right)\mathcal{D}_{i,xzy}^{(4)} + \frac{4}{9}\left(3-\sqrt{3}\right)\mathcal{D}_{i,zyx}^{(4)}, \tag{A8}$$

$$\mathcal{H}_{i,2}^{(4r)} \equiv \frac{4}{9}\left(3+2\sqrt{3}\right)\mathcal{D}_{i,xzy}^{(4)} + \frac{4}{9}\left(3-\sqrt{3}\right)\mathcal{D}_{i,xyz}^{(4)} + \frac{4}{9}\left(3-\sqrt{3}\right)\mathcal{D}_{i,zyx}^{(4)}, \tag{A9}$$

$$\mathcal{H}_{i,3}^{(4r)} \equiv \frac{4}{9}\left(3+2\sqrt{3}\right)\mathcal{D}_{i,zyx}^{(4)} + \frac{4}{9}\left(3-\sqrt{3}\right)\mathcal{D}_{i,xzy}^{(4)} + \frac{4}{9}\left(3-\sqrt{3}\right)\mathcal{D}_{i,xyz}^{(4)}, \tag{A10}$$

where

$$\mathcal{H}_{i,\alpha\beta\gamma}^{(3)} \equiv c_{i\alpha}c_{i\beta}c_{i\gamma} - c_s^2[c_{i\alpha}\delta_{\beta\gamma} + c_{i\beta}\delta_{\gamma\alpha} + c_{i\gamma}\delta_{\alpha\beta}], \tag{A11}$$

$$\mathcal{D}_{i,\alpha\beta\gamma}^{(4)} \equiv \mathcal{H}_{i,\alpha\alpha\beta\beta}^{(4)} + \frac{c_s^2}{2}\mathcal{H}_{i,\gamma\gamma}^{(2)}, \tag{A12}$$

$$\begin{aligned}\mathcal{H}_{i,\alpha\beta\gamma\delta}^{(4)} \equiv\ & c_{i\alpha}c_{i\beta}c_{i\gamma}c_{i\delta} + c_s^4(\delta_{\alpha\beta}\delta_{\gamma\delta} + \delta_{\beta\gamma}\delta_{\delta\alpha} + \delta_{\delta\alpha}\delta_{\beta\gamma}) \\ & - c_s^2(c_{i\alpha}c_{i\beta}\delta_{\gamma\delta} + c_{i\beta}c_{i\gamma}\delta_{\delta\alpha} + c_{i\gamma}c_{i\delta}\delta_{\alpha\beta} + c_{i\delta}c_{i\alpha}\delta_{\beta\gamma} \\ & + c_{i\gamma}c_{i\alpha}\delta_{\beta\delta} + c_{i\beta}c_{i\delta}\delta_{\alpha\gamma}).\end{aligned} \tag{A13}$$

Any distribution function in the D3Q19r lattice can be written as a (weighted) sum of the contributions from each base polynomial. For instance, the equilibrium distribution in Eq. (14) reads

$$\begin{aligned}f_i^{\mathrm{eq},19r} = \omega_i\Bigg\{ & a^{(0),\mathrm{eq}} + \frac{\mathcal{H}_{i,\alpha}^{(1)}}{c_s^2}a_\alpha^{(1),\mathrm{eq}} + \frac{\mathcal{H}_{i,\alpha\beta}^{(2)}}{2c_s^4}a_{\alpha\beta}^{(2),\mathrm{eq}} \\ & + \frac{\mathcal{H}_{i,\gamma}^{(3r)}}{6c_s^6}a_\gamma^{(3r),\mathrm{eq}} + \frac{\mathcal{H}_{i,\delta}^{(4r)}}{24c_s^8}a_\delta^{(4r),\mathrm{eq}}\Bigg\},\end{aligned} \tag{A14}$$

where

$$a^{(0),\mathrm{eq}} = \rho\theta\,, \quad a_\alpha^{(1),\mathrm{eq}} = \rho u_\alpha\,, \quad a_{\alpha\beta}^{(2),\mathrm{eq}} = \rho u_\alpha u_\beta \tag{A15}$$

$$a_1^{(3r),\mathrm{eq}} = 3(\rho u_x u_x u_y + \rho u_y u_z u_z), \tag{A16}$$

$$a_2^{(3r),\mathrm{eq}} = 3(\rho u_x u_z u_z + \rho u_x u_y u_y), \tag{A17}$$

$$a_3^{(3r),\mathrm{eq}} = 3(\rho u_y u_y u_z + \rho u_x u_x u_z), \tag{A18}$$

$$a_4^{(3r),\mathrm{eq}} = \rho u_x u_x u_y - \rho u_y u_z u_z, \tag{A19}$$

$$a_5^{(3r),\mathrm{eq}} = \rho u_x u_z u_z - \rho u_x u_y u_y, \tag{A20}$$

$$a_6^{(3r),\mathrm{eq}} = \rho u_y u_y u_z - \rho u_x u_x u_z, \tag{A21}$$

$$a_1^{(4r),\mathrm{eq}} = -\rho c_s^2\left[\frac{-4\sqrt{3}-6}{9}u_z^2 + \frac{2\sqrt{3}-6}{9}\left(u_x^2+u_y^2\right)\right], \tag{A22}$$

$$a_2^{(4r),\mathrm{eq}} = -\rho c_s^2\left[\frac{-4\sqrt{3}-6}{9}u_y^2 + \frac{2\sqrt{3}-6}{9}\left(u_x^2+u_z^2\right)\right], \quad \text{(A23)}$$

$$a_3^{(4r),\mathrm{eq}} = -\rho c_s^2\left[\frac{-4\sqrt{3}-6}{9}u_x^2 + \frac{2\sqrt{3}-6}{9}\left(u_y^2+u_z^2\right)\right]. \quad \text{(A24)}$$

It is worth noting that the fourth-order coefficients $[a^{(4),\mathrm{eq}}]$ are added to improve the isotropicity of the lattice, which could be quite important considering the round jet simulation in the current study.

The third-order off-equilibrium terms are reconstructed recursively from the second-order non-equilibrium tensor as

$$\begin{aligned} a_{\alpha\beta\gamma}^{(3),\mathrm{neq}} &= u_\alpha a_{\beta\gamma}^{(2),\mathrm{neq}} + u_\beta a_{\alpha\gamma}^{(2),\mathrm{neq}} + u_\gamma a_{\alpha\beta}^{(2),\mathrm{neq}}, \\ a_1^{(3r),\mathrm{neq}} &\equiv a_{xxy}^{(3),\mathrm{neq}} + a_{yzz}^{(3),\mathrm{neq}}, \\ a_2^{(3r),\mathrm{neq}} &\equiv a_{xzz}^{(3),\mathrm{neq}} + a_{xyy}^{(3),\mathrm{neq}}, \\ a_3^{(3r),\mathrm{neq}} &\equiv a_{yyz}^{(3),\mathrm{neq}} + a_{xxz}^{(3),\mathrm{neq}}, \\ a_4^{(3r),\mathrm{neq}} &\equiv a_{xxy}^{(3),\mathrm{neq}} - a_{yzz}^{(3),\mathrm{neq}}, \\ a_5^{(3r),\mathrm{neq}} &\equiv a_{xzz}^{(3),\mathrm{neq}} - a_{xyy}^{(3),\mathrm{neq}}, \\ a_6^{(3r),\mathrm{neq}} &\equiv a_{yyz}^{(3),\mathrm{neq}} - a_{xxz}^{(3),\mathrm{neq}}. \end{aligned} \quad \text{(A25)}$$

Depending on the order of the Gauss–Hermite quadrature[66] used in the LB model, an adequate forcing term should be added to achieve a correct viscous stress tensor,

$$a_{\alpha\beta}^{\mathrm{neq}} \approx -\Pi_{\alpha\beta} = -\mu\left(\frac{\partial u_\alpha}{\partial x_\beta} + \frac{\partial u_\beta}{\partial x_\alpha} - \frac{2}{D}\frac{\partial u_\gamma}{\partial x_\gamma}\delta_{\alpha\beta}\right), \quad \text{(A26)}$$

with D the spatial dimension. For the D3Q19r basis, the projected forcing term reads as

$$\begin{aligned} a_{\alpha\beta}^{F^E} = c_s^2 u_\alpha\left[\frac{\partial(\rho(1-\theta))}{\partial x_\beta}\right] + c_s^2 u_\beta\left[\frac{\partial(\rho(1-\theta))}{\partial x_\alpha}\right] + \delta_{\alpha\beta}\rho c_s^2\frac{2}{D}\frac{\partial u_\gamma}{\partial x_\gamma} \\ - a_{\alpha\beta}^{\mathrm{cor}} + a_{\alpha\beta}^{F_D}, \end{aligned} \quad \text{(A27)}$$

where $a_{\alpha\beta}^{\mathrm{cor}}$ is a correction tensor due to the deflection of second order moments of the population introduced by the modification of the mass equation, which can be evaluated as

$$a_{\alpha\beta}^{\mathrm{cor}} \equiv c_s^2\delta_{\alpha\beta}\frac{\partial(\rho(1-\theta))}{\partial t}, \quad \text{(A28)}$$

which can be discretized using a backward Euler operator and $a_{\alpha\beta}^{F_D}$ the correction tensor due to the defect of the lattice at third order,

$$a_{\alpha\beta}^{F_D} = -\begin{pmatrix} (\rho u_x^3)_{,x} & (\rho u_x u_y u_z)_{,z} & (\rho u_x u_y u_z)_{,y} \\ (\rho u_x u_y u_z)_{,z} & (\rho u_y^3)_{,y} & (\rho u_x u_y u_z)_{,x} \\ (\rho u_x u_y u_z)_{,y} & (\rho u_x u_y u_z)_{,x} & (\rho u_z^3)_{,z} \end{pmatrix}, \quad \text{(A29)}$$

where all the differential operations are performed using first order upwind FD except for the divergence operator for which a second order centered FD scheme was employed. The final expression of the forcing term is then

$$F_i^E = \frac{\omega_i}{2c_s^4}\mathcal{H}_{i,\alpha\beta}^{(2)}a_{\alpha\beta}^{F^E} + F_i^g, \quad \text{(A30)}$$

where F_i^g is the gravity force term defined as

$$F_i^g = \omega_i\left[\frac{\rho g_\alpha\mathcal{H}_{i,\alpha}^{(1)}}{c_s^2} + \frac{(\rho u_\alpha g_\beta + \rho u_\beta g_\alpha)\mathcal{H}_{i,\alpha\beta}^{(2)}}{2c_s^4}\right], \quad \text{(A31)}$$

where g_α is the gravity acceleration in the direction α.

REFERENCES

[1] S. Chen and G. D. Doolen, "Lattice Boltzmann method for fluid flows," Annu. Rev. Fluid Mech. **30**, 329–364 (1998).
[2] P. Boivin, M. Tayyab, and S. Zhao, "Benchmarking a lattice-Boltzmann solver for reactive flows: Is the method worth the effort for combustion?," Phys. Fluids **33**, 071703 (2021).
[3] S. Succi, R. Benzi, and F. Higuera, "The lattice Boltzmann equation: A new tool for computational fluid-dynamics," Phys. D **47**, 219–230 (1991).
[4] Z. Guo and C. Shu, *Lattice Boltzmann Method and Its Applications in Engineering* (World Scientific, 2013), Vol. 3.
[5] T. Krüger, H. Kusumaatmaja, A. Kuzmin, O. Shardt, G. Silva, and E. M. Viggen, *The Lattice Boltzmann Method: Principles and Practice* (Springer, 2016).
[6] P. L. Bhatnagar, E. P. Gross, and M. Krook, "A model for collision processes in gases. I. Small amplitude processes in charged and neutral one-component systems," Phys. Rev. **94**, 511 (1954).
[7] D. d. Humières, I. Ginzburg, M. Krafczyk, P. Lallemand, and L.-S. Luo, "Multiple–relaxation–time lattice Boltzmann models in three dimensions," Philos. Trans. R. Soc. London A **360**, 437–451 (2002).
[8] O. Malaspinas, "Increasing stability and accuracy of the lattice Boltzmann scheme: Recursivity and regularization," arXiv:1505.06900 (2015).
[9] J. Jacob, O. Malaspinas, and P. Sagaut, "A new hybrid recursive regularised Bhatnagar–Gross–Krook collision model for lattice Boltzmann method-based large eddy simulation," J. Turbul. **19**, 1051–1076 (2018).
[10] S. A. Hosseini, A. Eshghinejadfard, N. Darabiha, and D. Thévenin, "Weakly compressible lattice Boltzmann simulations of reacting flows with detailed thermo-chemical models," Comput. Math. Appl. **79**, 141–158 (2020).
[11] M. Saadat, S. Hosseini, B. Dorschner, and I. Karlin, "Extended lattice Boltzmann model for gas dynamics," Phys. Fluids **33**, 046104 (2021).
[12] Y. Feng, P. Sagaut, and W. Tao, "A three dimensional lattice model for thermal compressible flow on standard lattices," J. Comput. Phys. **303**, 514–529 (2015).
[13] Y. Feng, P. Sagaut, and W.-Q. Tao, "A compressible lattice Boltzmann finite volume model for high subsonic and transonic flows on regular lattices," Comput. Fluids **131**, 45–55 (2016).
[14] Y. Feng, P. Boivin, J. Jacob, and P. Sagaut, "Hybrid recursive regularized thermal lattice Boltzmann model for high subsonic compressible flows," J. Comput. Phys. **394**, 82–99 (2019).
[15] S. Guo, Y. Feng, J. Jacob, F. Renard, and P. Sagaut, "An efficient lattice Boltzmann method for compressible aerodynamics on d3q19 lattice," J. Comput. Phys. **418**, 109570 (2020).
[16] G. Farag, S. Zhao, T. Coratger, P. Boivin, G. Chiavassa, and P. Sagaut, "A pressure-based regularized lattice-Boltzmann method for the simulation of compressible flows," Phys. Fluids **32**, 066106 (2020).
[17] G. Farag, T. Coratger, G. Wissocq, S. Zhao, P. Boivin, and P. Sagaut, "A unified hybrid lattice-Boltzmann method for compressible flows: Bridging between pressure-based and density-based methods," Phys. Fluids **33**, 086101 (2021).
[18] I. Cheylan, S. Zhao, P. Boivin, and P. Sagaut, "Compressible pressure-based lattice-Boltzmann applied to humid air with phase change," Appl. Therm. Eng. **191**, 116868 (2021).
[19] J. Jacob and P. Sagaut, "Wind comfort assessment by means of large eddy simulation with lattice Boltzmann method in full scale city area," Build. Environ. **139**, 110–124 (2018).
[20] L. Merlier, J. Jacob, and P. Sagaut, "Lattice-Boltzmann large-eddy simulation of pollutant dispersion in street canyons including tree planting effects," Atmos. Environ. **195**, 89–103 (2018).
[21] L. Merlier, J. Jacob, and P. Sagaut, "Lattice-Boltzmann large-eddy simulation of pollutant dispersion in complex urban environment with dense gas effect: Model evaluation and flow analysis," Build. Environ. **148**, 634–652 (2019).

[22]M. Tayyab, B. Radisson, C. Almarcha, B. Denet, and P. Boivin, "Experimental and numerical lattice-Boltzmann investigation of the Darrieus–Landau instability," Combust. Flame **221**, 103–109 (2020).
[23]M. Tayyab, S. Zhao, Y. Feng, and P. Boivin, "Hybrid regularized lattice-Boltzmann modelling of premixed and non-premixed combustion processes," Combust. Flame **211**, 173–184 (2020).
[24]M. Tayyab, S. Zhao, and P. Boivin, "Lattice-Boltzmann modelling of a turbulent bluff-body stabilized flame," Phys. Fluids **33**, 031701 (2021).
[25]S. P. Domino, J. Hewson, R. Knaus, and M. Hansen, "Predicting large-scale pool fire dynamics using an unsteady flamelet- and large-eddy simulation-based model suite," Phys. Fluids **33**, 085109 (2021).
[26]B. Morton, "Buoyant plumes in a moist atmosphere," J. Fluid Mech. **2**, 127–144 (1957).
[27]B. Morton, "Forced plumes," J. Fluid Mech. **5**, 151–163 (1959).
[28]A. W. Woods, "Turbulent plumes in nature," Annu. Rev. Fluid Mech. **42**, 391–412 (2010).
[29]G. Heskestad, "Engineering relations for fire plumes," Fire Saf. J. **7**, 25–32 (1984).
[30]M. D. Fromm and R. Servranckx, "Transport of forest fire smoke above the tropopause by supercell convection," Geophys. Res. Lett. **30**, 1542, https://doi.org/10.1029/2002GL016820 (2003).
[31]R. A. Kahn, Y. Chen, D. L. Nelson, F.-Y. Leung, Q. Li, D. J. Diner, and J. A. Logan, "Wildfire smoke injection heights: Two perspectives from space," Geophys. Res. Lett. **35**, L04809, https://doi.org/10.1029/2007GL032165 (2008).
[32]D. Pyle, "Sparks, R. S. J., Bursik, M. I., Carey, S. N., Gilbert, J. S., Glaze, L. S., Sigurdsson, H. and Woods, A. W. 1997. Volcanic Plumes. XV 574 pp. Chichester, New York, Weinheim, Brisbane, Singapore, Toronto: JOHN Wiley and Sons. Price £85.00 (hard covers). ISBN 0 471 93901 3," Geol. Mag. **135**, 143–158 (1998).
[33]G. G. Ernst, R. S. J. Sparks, S. N. Carey, and M. I. Bursik, "Sedimentation from turbulent jets and plumes," J. Geophys. Res.: Solid Earth **101**, 5575–5589, https://doi.org/10.1029/95JB01900 (1996).
[34]G. Carazzo, E. Kaminski, and S. Tait, "On the rise of turbulent plumes: Quantitative effects of variable entrainment for submarine hydrothermal vents, terrestrial and extra terrestrial explosive volcanism," J. Geophys. Res.: Solid Earth **113**, B09201, https://doi.org/10.1029/2007JB005458 (2008).
[35]E. D. Skyllingstad and D. W. Denbo, "Turbulence beneath sea ice and leads: A coupled sea ice/large-eddy simulation study," J. Geophys. Res.: Oceans **106**, 2477–2497, https://doi.org/10.1029/1999JC000091 (2001).
[36]K. Widell, I. Fer, and P. M. Haugan, "Salt release from warming sea ice," Geophys. Res. Lett. **33**, L12501, https://doi.org/10.1029/2006GL026262 (2006).
[37]G. A. Briggs, "Chimney plumes in neutral and stable surroundings," Atmos. Environ. **6**, 507–510 (1972).
[38]B. Fisher, "Predicting cooling tower plume dispersion," Proc. Inst. Mech. Eng., Part A **211**, 291–297 (1997).
[39]C. J. Chen and W. Rodi, *Vertical Buoyant Jets: A Review Experimental Data* (Pergamon, 1980).
[40]W. Schmidt, "Turbulent propagation of a stream of heated air," Z. Angew. Math. Mech. **21**, 265–278 (1941).
[41]H. Rouse, C. S. Yih, and H. Humphreys, "Gravitational convection from a boundary source," Tellus **4**, 201–210 (1952).
[42]B. Morton, G. I. Taylor, and J. S. Turner, "Turbulent gravitational convection from maintained and instantaneous sources," Proc. R. Soc. London, Ser. A **234**, 1–23 (1956).
[43]G. Heskestad, "Dynamics of the fire plume," Philos. Trans. R. Soc. London A **356**, 2815–2833 (1998).
[44]W. K. George, Jr., R. L. Alpert, and F. Tamanini, "Turbulence measurements in an axisymmetric buoyant plume," Int. J. Heat Mass Transfer **20**, 1145–1154 (1977).
[45]P. N. Papanicolaou and E. J. List, "Investigations of round vertical turbulent buoyant jets," J. Fluid Mech. **195**, 341–391 (1988).
[46]A. Shabbir and W. K. George, "Experiments on a round turbulent buoyant plume," J. Fluid Mech. **275**, 1–32 (1994).
[47]H. Nakagome and M. Hirata, "The structure of turbulent diffusion in an axisymmetrical thermal plume," in *Proceedings of the 1976 ICHMT Seminar Turbulent Buoyant Convection* (1977), pp. 361–372.
[48]Z. Dai, L. Tseng, and G. Faeth, "Structure of round, fully-developed, buoyant turbulent plumes," J. Heat Transfer **116**, 409–417 (1994).
[49]Z. Saeed, E. Weidner, B. Johnson, and T. L. Mandel, "Buoyancy-modified entrainment in plumes: Theoretical predictions," Phys. Fluids **34**, 015112 (2022).
[50]S. Nam and R. G. J. Bill, "Numerical simulation of thermal plumes," Fire Saf. J. **21**, 213–256 (1993).
[51]J. Worthy, V. Sanderson, and P. Rubini, "Comparison of modified k-epsilon turbulence models for buoyant plumes," Num. Heat Transfer, Part B **39**, 151–165 (2001).
[52]C. P. Brescianini and M. Delichatsios, "New evaluation of the k-epsilon turbulence model for free buoyant plumes," Num. Heat Transfer, Part A **43**, 731–751 (2003).
[53]Z. H. Yan, "Application of two buoyancy modified k-epsilon turbulence models to different types of buoyant plumes," Fire Saf. J. **41**, 122–138 (2006).
[54]X. Zhou, K. H. Luo, and J. J. Williams, "Large-eddy simulation of a turbulent forced plume," Eur. J. Mech. B **20**, 233–254 (2001).
[55]Z. H. Yan, "Large eddy simulations of a turbulent thermal plume," Heat Mass Transfer **43**, 503–514 (2007).
[56]C. Pant and A. Bhattacharya, "Evaluation of an energy consistent entrainment model for volumetrically forced jets using large eddy simulations," Phys. Fluids **30**, 105107 (2018).
[57]E. Kaminski, S. Tait, and G. Carazzo, "Turbulent entrainment in jets with arbitrary buoyancy," J. Fluid Mech. **526**, 361–376 (2005).
[58]M. van Reeuwijk and J. Craske, "Energy-consistent entrainment relations for jets and plumes," J. Fluid Mech. **782**, 333–355 (2015).
[59]M. V. Pham, F. Plourde, S. D. Kim, and S. Balachandar, "Large-eddy simulation of a pure thermal plume under rotating conditions," Phys. Fluids **18**, 015101 (2006).
[60]F. Plourde, M. V. Pham, S. D. Kim, and S. Balachandar, "Direct numerical simulations of a rapidly expanding thermal plume: Structure and entrainment interaction," J. Fluid Mech. **604**, 99 (2008).
[61]C. H. Chen and K. Bhaganagar, "New findings in vorticity dynamics of turbulent buoyant plumes," Phys. Fluids **33**, 115104 (2021).
[62]K. Bhaganagar and S. R. Bhimireddy, "Numerical investigation of starting turbulent buoyant plumes released in neutral atmosphere," J. Fluid Mech. **900**, A32 (2020).
[63]CS Communication and Systèmes, ProLB (2017).
[64]A. Vreman, "An eddy-viscosity subgrid-scale model for turbulent shear flow: Algebraic theory and applications," Phys. Fluids **16**, 3670–3681 (2004).
[65]T. Poinsot and D. Veynante, *Theoretical and Numerical Combustion* (RT Edwards, Inc., 2005).
[66]T. Krüger, H. Kusumaatmaja, A. Kuzmin, O. Shardt, G. Silva, and E. M. Viggen, *The Lattice Boltzmann Method* (Springer International Publishing, 2017), Vol. 10, pp. 4–15.
[67]G. Farag, S. Zhao, G. Chiavassa, and P. Boivin, "Consistency study of lattice-Boltzmann schemes macroscopic limit," Phys. Fluids **33**, 037101 (2021).
[68]G. Wissocq and P. Sagaut, "Hydrodynamic limits and numerical errors of isothermal lattice Boltzmann schemes," J. Comput. Phys. **450**, 110858 (2022).
[69]T. Coratger, G. Farag, S. Zhao, P. Boivin, and P. Sagaut, "Large-eddy lattice-Boltzmann modelling of transonic flows," Phys. Fluids **33**, 115112 (2021).
[70]P. Bergé and M. Dubois, "Rayleigh–Bénard convection," Contemp. Phys. **25**, 535–582 (1984).
[71]N. Ouertatani, N. Ben-Cheikh, B. Beya, and T. Lili, "Numerical simulation of two-dimensional Rayleigh–Bénard convection in an enclosure," C. R. Méc. **336**, 464–470 (2008).
[72]X. He, S. Chen, and R. Zhang, "A lattice Boltzmann scheme for incompressible multiphase flow and its application in simulation of Rayleigh–Taylor instability," J. Comput. Phys. **152**, 642–663 (1999).
[73]D. Chiappini, G. Bella, S. Succi, F. Toschi, and S. Ubertini, "Improved lattice Boltzmann without parasitic currents for Rayleigh–Taylor instability," Commun. Comput. Phys. **7**, 423 (2010).
[74]S. A. Hosseini, H. Safari, and D. Thevenin, "Lattice Boltzmann solver for multiphase flows: Application to high Weber and Reynolds numbers," Entropy **23**, 166 (2021).

[75]H. Ding, P. D. Spelt, and C. Shu, "Diffuse interface model for incompressible two-phase flows with large density ratios," J. Comput. Phys. **226**, 2078–2095 (2007).
[76]X. He, R. Zhang, S. Chen, and G. D. Doolen, "On the three-dimensional Rayleigh–Taylor instability," Phys. Fluids **11**, 1143–1152 (1999).
[77]Q. Li, K. Luo, Y. Gao, and Y. He, "Additional interfacial force in lattice Boltzmann models for incompressible multiphase flows," Phys. Rev. E **85**, 026704 (2012).
[78]G. Tryggvason, "Numerical simulations of the Rayleigh–Taylor instability," J. Comput. Phys. **75**, 253–282 (1988).
[79]J.-L. Guermond and L. Quartapelle, "A projection fem for variable density incompressible flows," J. Comput. Phys. **165**, 167–188 (2000).
[80]L. Lee, "A class of high-resolution algorithms for incompressible flows," Comput. Fluids **39**, 1022–1032 (2010).
[81]Y. Zu and S. He, "Phase-field-based lattice Boltzmann model for incompressible binary fluid systems with density and viscosity contrasts," Phys. Rev. E **87**, 043301 (2013).
[82]B. Morton and J. Middleton, "Scale diagrams for forced plumes," J. Fluid Mech. **58**, 165–176 (1973).
[83]X. Zhou, K. H. Luo, and J. J. Williams, "Study of density effects in turbulent buoyant jets using large-eddy simulation," Theor. Comput. Fluid Dyn. **15**, 95–120 (2001).
[84]A. Michalke, "Survey on jet instability theory," Prog. Aerosp. Sci. **21**, 159–199 (1984).
[85]N. Didden and C.-M. Ho, "Unsteady separation in a boundary layer produced by an impinging jet," J. Fluid Mech. **160**, 235–256 (1985).
[86]S. Menow and M. Rizk, "Large-eddy simulations of forced three-dimensional impinging jets," Int. J. Comput. Fluid Dyn. **7**, 275–289 (1996).
[87]H. JCR, A. Wray, and P. Moin, "Eddies, streams, and convergence zones in turbulent flows," in *Proceedings of the 1988 Summer Program Studying Turbulence Using Numerical Simulation Databases–II* (1988), p. 193.
[88]A. N. Kolmogorov, "The local structure of turbulence in incompressible viscous fluid for very large Reynolds numbers," Cr. Acad. Sci. URSS **30**, 301–305 (1941).
[89]N. E. Kotsovinos, "Turbulence spectra in free convection flow," Phys. Fluids A **3**, 163–167 (1991).
[90]A. Lingens, M. Reeker, and M. Schreiber, "Instability of buoyant diffusion flames," Exp. Fluids **20**, 241–248 (1996).
[91]B. Gebhart, Y. Jaluria, R. L. Mahajan, and B. Sammakia, *Buoyancy-Induced Flows and Transport* (1988).
[92]C. J. Chen and W. Rodi, "Vertical turbulent buoyant jets: A review of experimental data," NASA STI/Recon Tech. Rep. A **80**, 23073 (1980).
[93]J. Turner, "Buoyant plumes and thermals," Annu. Rev. Fluid Mech. **1**, 29–44 (1969).
[94]B. M. Cetegen, "Behavior of naturally unstable and periodically forced axisymmetric buoyant plumes of helium and helium-air mixtures," Phys. Fluids **9**, 3742–3753 (1997).
[95]K. L. Denman, "Fischer, H. B., E. J. List, R. C. Y. Koh, J. Imberger, and N. A. Brooks, 1979. Mixing in inland and coastal waters. Academic Press, Inc., New York, xiv + 483 p. $35.00," Limnol. Oceanogr. **27**, 593–594 (1982).